Institut für Wasserbau · Universität Stuttgart

Mitteilungen

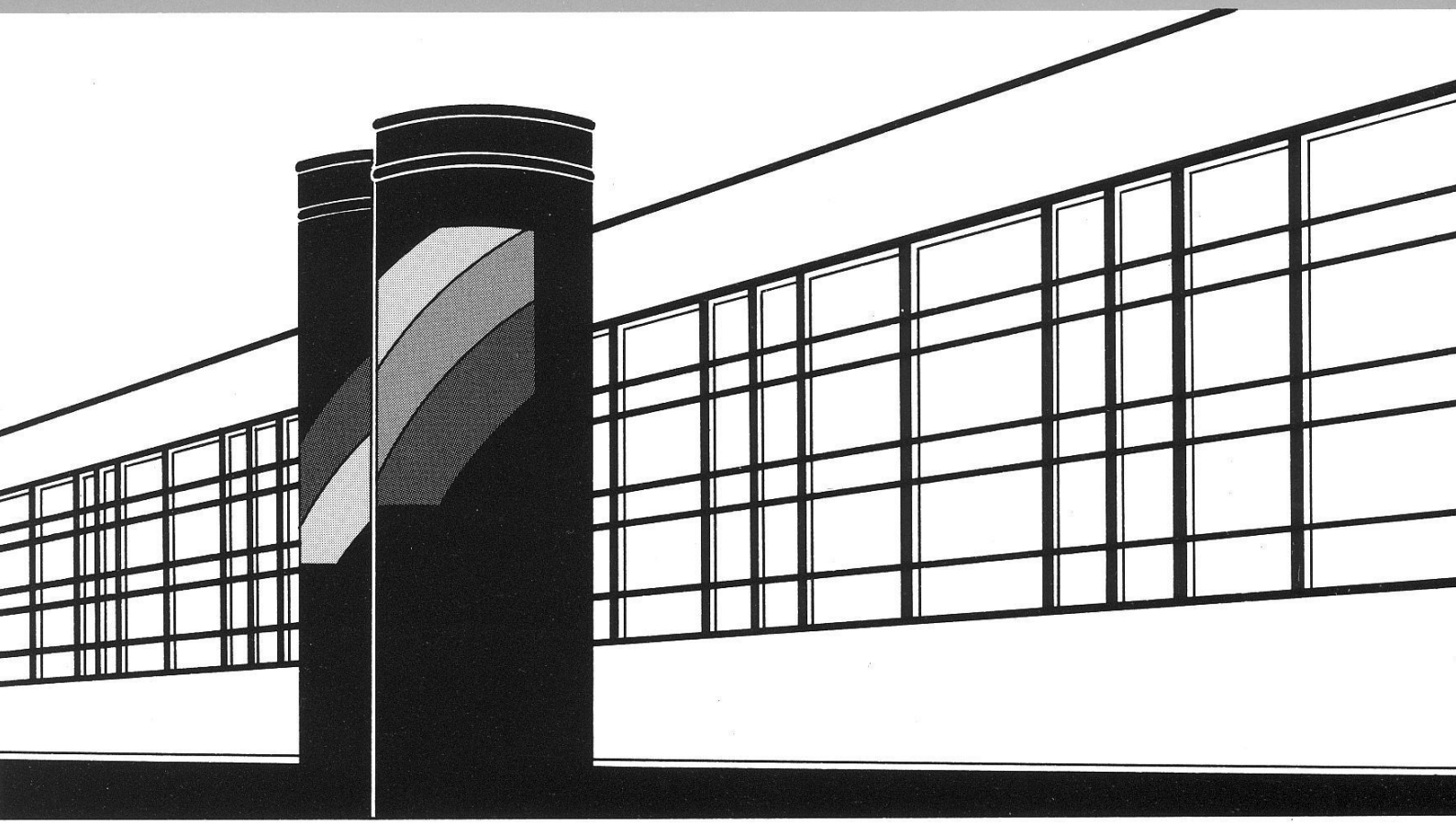

Heft 173 Sven Wagner

Water Balance in a Poorly Gauged Basin in West Africa Using Atmospheric Modelling and Remote Sensing Information

Water Balance in a Poorly Gauged Basin in West Africa Using Atmospheric Modelling and Remote Sensing Information

Von der Fakultät Bau- und Umweltingenieurwissenschaften der Universität Stuttgart zur Erlangung der Würde eines Doktor-Ingenieurs (Dr.-Ing.) genehmigte Abhandlung

Vorgelegt von

Sven Wagner

aus Weingarten

Hauptberichter:	Prof. Dr. rer. nat. Dr.-Ing. habil. András Bárdossy
Mitberichter:	Prof. Dr. rer. nat. habil. Wolfgang Seiler

Tag der mündlichen Prüfung: 30. April 2008

Institut für Wasserbau der Universität Stuttgart
2008

Heft 173

Water Balance in a Poorly Gauged Basin in West Africa Using Atmospheric Modelling and Remote Sensing Information

von
Dr.-Ing.
Sven Wagner

Eigenverlag des Instituts für Wasserbau der Universität Stuttgart

D93 Water Balance in a Poorly Gauged Basin in West Africa Using Atmospheric Modelling and Remote Sensing Information

Titelaufnahme der Deutschen Bibliothek

Wagner, Sven:
Water Balance in a Poorly Gauged Basin in West Africa Using Atmospheric Modelling and Remote Sensing Information / von Sven Wagner. Institut für Wasserbau, Universität Stuttgart. - Stuttgart: Inst. für Wasserbau, 2008

(Mitteilungen / Institut für Wasserbau, Universität Stuttgart: H. 173)
Zugl.: Stuttgart, Univ., Diss., 2008)
ISBN 3-933761-77-8
NE: Institut für Wasserbau <Stuttgart>: Mitteilungen

Herausgegeben 2008 vom Eigenverlag des Instituts für Wasserbau
Druck: Document Center S. Kästl, Ostfildern

Acknowledgements

I sincerely thank Dr. Harald Kunstmann (IMK-IFU) for proposing the topic, his guidance and continuous support throughout this work.

I am very grateful to Prof. András Bárdossy (University Stuttgart) for the excellent supervision, invaluable suggestions and guidance.

My sincere gratitude to Prof. Wolfgang Seiler (IMK-IFU) for giving me the opportunity to work at the Institute for Meteorology and Climate Research (IMK-IFU) in Garmisch-Partenkirchen, his support and accepting to co-supervise my thesis.

This work is part of the research project *GLOWA*-Volta funded by the BMBF (German Ministry of Education and Research). Many thanks to all co-workers and partners of the *GLOWA*-Volta project for the good atmosphere and cooperation; especially to Dr. Marc Andreini and Dr. Bouboucar Barry, the project coordinators in Ghana, for their great support during the field campaigns. The collaboration with the Hydrological- and Meteorological Services Department in Ghana is gratefully acknowledged.

Many thanks to Dr. Christopher Conrad and Dr. Rene R. Colditz (University Wuerzburg) for the good cooperation on the assimilation of satellite derived land surface properties in hydrological modelling.

A big thank you to Dr. Andreas Marx (IMK-IFU), Sabine Pakosch (UniBw Munich) and Claudia Mende for proofreading the manuscript, giving valuable suggestions and the help with the English language.

I wish to express special thanks to all colleagues at IMK-IFU for the overall good working atmosphere, indispensable coffee breaks and their manifold help during this work; especially to the co-workers Dr. Gerlinde Jung (now at IIA-CNR) and Patrick Laux for their support within the *GLOWA*-Volta project.

Finally, I am extremely grateful to my family and my partner Sabine for their understanding and support/encouragement at all time.

Contents

List of Figures

List of Tables

List of Abbreviations

Abbreviation	Meaning
AEJ	African Easterly Jet
BMBF	Federal Ministry for Education and Research of Germany (Bundesministerium für Bildung und Forschung)
D	Domain
DEM	Digital Elevation Model
DSS	Decision Support System
EDK	External Drift Kriging
FAO	United Nations Food and Agriculture Organization
FDDA	Four Dimensional Data Assimilation
GCM	General Circulation Model
GFS	Global Forecasting System
GLOWA	Global change and the hydrological cycle (Globaler Wandel des WAsserkreislaufs)
GPCC	Global Precipitation Climatology Centre
IDW	Inverse Distance Weighting
ITCZ	Inter Tropical Convergence Zone
LAI	Leaf Area Index
LAM	Limited Area Model
MM5	Mesoscale Meteorological Model
MODIS	MODerate resolution Imaging Spectroradiometer
NCAR	National Centre for Atmospheric Research
NCEP	National Centers for Environmental Prediction
NSE	Nash-Sutcliffe model Efficiency
NWP	Numerical Weather Predictions
OK	Ordinary Kriging
OSU-LSM	Oregon-State-University Land-Surface-Model
PBL	Planetary Boundary Layer
RT	Real Time
SST	Sea Surface Temperature
SVAT	Soil-Vegetation-Atmosphere-Transfer
TEJ	Tropical Easterly Jet
TiSeG	Time Series Generator
TRMM	Tropical Rainfall Measuring Mission
TOVAS	TRMM Online Visualization and Analysis System
WaSiM	Water balance Simulation Model

Abstract

Sustainable water resources management under increasing water demands and changing climate conditions is a central, socio-political challenge, in particular in climate sensitive regions. Decisions in sustainable water resources management require scientifically sound information of the current water resources and fluxes and future water availability.

The first objective of this work is to provide estimations of the current water resources and fluxes in a poorly gauged basin. This is a central task to support water management authorities and stakeholders in operational irrigation, water supply and running hydro-power strategies. To allow investigations in ungauged or poorly gauges basins, these instruments and methods should be applicable world wide, cost-effective and preferably public domain. In poorly gauged basins without automatic data recorders and online transmission other meteorological data sources for near real time estimations of the terrestrial water balance have to be used to overcome the temporal delay and/or the insufficient spatial resolution. Therefore, a joint atmospheric-hydrological modelling system is developed which is able to provide near real time water balance estimations with a delay of 48 h. Additionally to meteorological modelling results and observation data, a *TRMM* product, which is available with approximately one month delay, is applied as precipitation data source.

Besides meteorological driving data, land surface properties are essential input data for distributed hydrological modelling. Land surface properties information is usually taken from standard literature values and incorporated into hydrological modelling through tables depending on the land use. The second objective of this work is to increase the level of detail in the spatial and temporal dimension of land surface properties in hydrological modelling using satellite derived land surface properties and to investigate the impact on hydrological modelling results. In this study, products of the MODerate resolution Imaging Spectroradiometer (*MODIS*) remote sensing system for albedo and leaf area index *LAI* are imported into the hydrological model and investigated.

For sustainable decisions in water resources management, additionally to the modelling result itself, the reliability or uncertainty of the result has to be quantified. Due to the fact that the spatial variability of rainfall is often termed as the major source of error in investigations of rainfall-runoff processes and modelling, the propagation of uncertainties, resulting from the calculation of areal precipitation from point measurements in water balance estimations, are

investigated as third objective of this work. Therefore, different spatial interpolation methods, including external drift kriging, for areal precipitation are applied, and their impact on water balance estimates is analysed. Furthermore, geostatistical simulations using the turning band method for areal precipitation are performed in order to investigate the propagation of uncertainties in water balance estimations. These results provide ranges of the temporal and spatial distribution of water balance variables as consequence of uncertainties from the calculation of areal precipitation from station data.

Zusammenfassung

"Süßwasser ist eine endliche und verletzliche Ressource, die absolut notwendig ist für Leben, Entwicklung und Umwelt" (Unesco, 1992). Diese endliche Süßwassermenge ist auf der Erde ungleichmäßig verteilt. Zusätzlich steigt der Wasserbedarf permanent, insbesondere in Ländern mit einer schnell wachsenden Bevölkerung und/oder Volkswirtschaft. Dabei wird laut Unesco der globale Bedarf an Süßwasser die Verfügbarkeit ab 2030 übersteigen. In Afrika werden viele Länder auf Grund ihrer aktuellen Bevölkerungsentwicklung und ihres steigenden Wasserbedarfs die Grenzen ihrer wirtschaftlich nutzbaren Wasserressourcen vor 2025 übertreffen (Ipcc, 2007; Ashton, 2002). Die Klimaänderung und -variabilität verschärfen zusätzlich die Wasserverfügbarkeit, -zugänglichkeit und -bedarf.

Auf Grund der steigenden Nachfrage und mit der globalen Erwärmung verbundenen Änderung des Wasserdargebots ist nachhaltiges Wassermanagement insbesondere in klimasensitiven Regionen eine zentrale, gesellschaftspolitisch relevante Herausforderung. Nachhaltige Wassermanagemententscheidungen erfordern wissenschaftlich fundierte Informationen über die aktuell verfügbaren Wasserressourcen und zukünftige Wasserverfügbarkeit. In dieser Arbeit wurden Instrumente und Methoden für die Abschätzung der aktuell verfügbaren Wasserressourcen entwickelt und angewendet. Dabei wurden öffentlich zugängliche, weltweit erhältliche und kostengünstige Methoden und Datensätze verwendet.

Die Arbeit ist eingegliedert in das vom BMBF geförderte Projekt *GLOWA*-Volta. Das übergeordnete Ziel von *GLOWA* (Globaler Wandel des Wasserkreislaufs) ist die Entwicklung integrierter Strategien für eine nachhaltige Bewirtschaftung von Wasser und Gewässern im regionalen Maßstab. Das zentrale Ziel des *GLOWA*-Volta-Projekts ist die Analyse der physischen und sozioökonomischen Bedingungen des Wasserkreislaufs im Voltabecken und die diesbezüglichen Auswirkungen des globalen Wandels. Darauf aufbauend soll ein wissenschaftlich fundiertes System zur Entscheidungshilfe (*Decision Support System - DSS*) im Bereich des Wasserressourcenmanagements entwickelt werden.

Ein zentrales Instrument zur Entscheidungsunterstützung für nachhaltiges Wassermanagement ist die hydrologische Modellierung, die Informationen über die räumliche und zeitliche Veränderung von Wasserhaushaltsgrößen liefert. Die hydrologische Modellierung benötigt meteorologische Eingangsdaten, deren Verfügbarkeit in ausreichender zeitlicher und räumlicher Auflösung insbesondere in infrastrukturschwachen Einzugsgebieten eine große Herausfor-

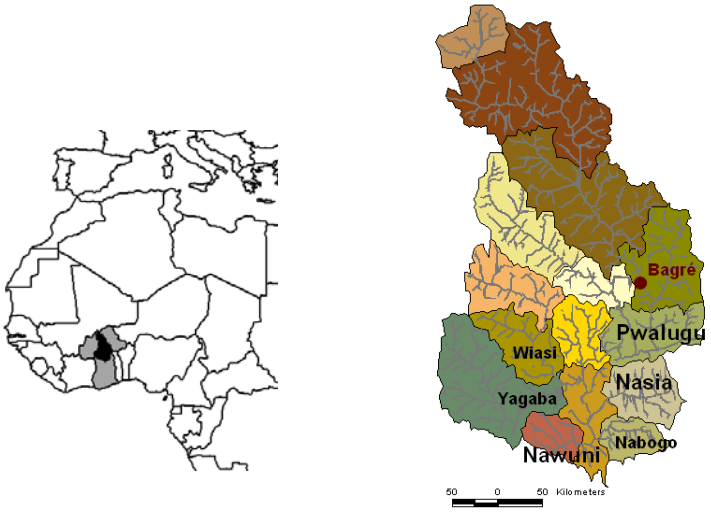

(a) (b)

Abbildung 0.1: Lage des Einzugsgebiets der Weißen Volta in West Afrika (a); Abgrenzung der Teileinzugsgebiete und Lage der Pegel mit verfügbaren Messdaten und des Staudamms in Bagré (b)

derung darstellt. Darüber hinaus sind Stationsdaten oft nur mit einer beträchtlichen zeitlichen Verzögerung verfügbar und damit ungeeignet für kurzfristige Wassermanagemententscheidungen, z.B. für operationelle Bewässerungs-, Wasserversorgungs- oder Wasserkraftanlagenstrategien. Vor diesem Hintergrund wurde in dieser Arbeit untersucht, inwieweit, zusätzlich zu Stationsdaten, meteorologische Modelle in der Lage sind, meteorologische Felder mit ausreichender Genauigkeit für die flächendifferenzierte Wasserhaushaltsmodellierung zu liefern. Als weitere Datenquelle für den Niederschlag wurde das skalierte *TRMM* Produkt 3B42 verwendet, das mit einer zeitlichen Verzögerung von ungefähr einem Monat verfügbar ist.

Das Untersuchungsgebiet: Das Untersuchungsgebiet (siehe Abbildung 0.1) ist das Einzugsgebiet der Weißen Volta (94000 km^2), ein großes Teilgebiet des Volta Einzugsgebiets in Westafrika. Die Weiße Volta entspringt im Norden von Burkina Faso und mündet in den 9000 km^2 großen Voltasee in Ghana, der durch den Akosombo Damm aufgestaut und seit 1965 zur Energieerzeugung genutzt wird.

Das Klima im Einzugsgebiet ist semi-arid im Norden bis sub-humid im Süden. Die mittlere Jahrestemperatur liegt im nördlichen Teil zwischen 27°C und 36°C und im Südlichen zwischen 24°C und 30°C (Hayward and Oguntoyinbo, 1987). Die mittleren Jahresniederschlagssummen weisen einen großen Nord-Süd-Gradienten (mit 300 mm im Norden und bis zu 1500 mm im Süden) und zusätzlich eine hohe räumliche Variabilität auf. Ungefähr 80% der Gesamtnie-

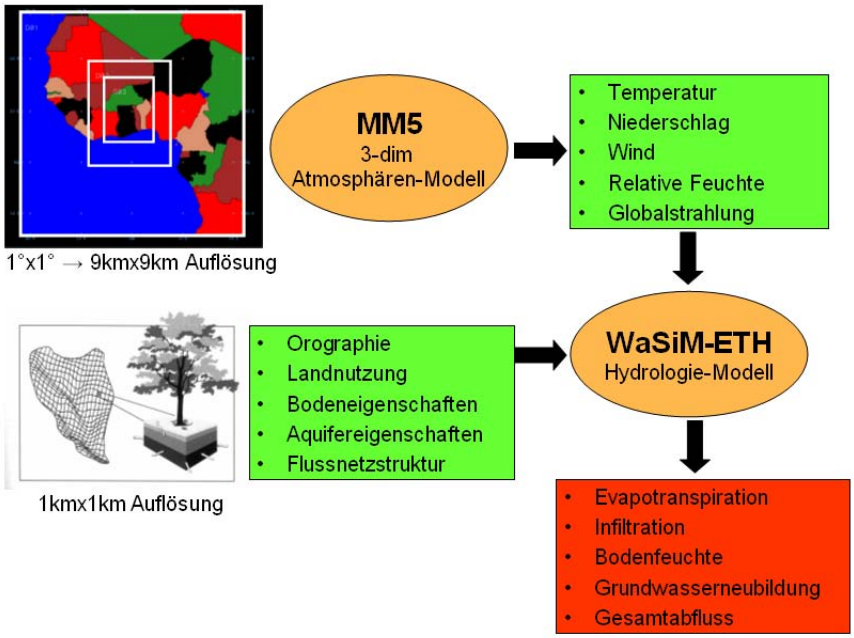

Abbildung 0.2: Ein-Wege-Strategie bei der Kopplung des meteorologischen (*MM5*) und hydrologischen (*WaSiM*) Modells

derschlagsmenge fallen während der Regenzeit zwischen Juli und September, wovon wiederum etwa 80% verdunstet.

Das Einzugsgebiet ist charakterisiert durch eine flache Topographie insbesondere im südlichen Teil. Guinea-Savanne im südlichen und Sudan-Savanne im nördlichen Teil des Einzugsgebiets sind die vorherrschenden Landnutzungstypen. Das natürliche Fließverhalten der Weißen Volta wird durch ein großes Staudammprojekt in Bagré im Süden von Burkina Faso, das im Jahre 1993 fertig gestellt wurde und zur Energieerzeugung und Bewässerung verwendet wird, gestört.

Auf Grund dieser Zweiteilung des Einzugsgebietes, der Datenverfügbarkeit und die vom *GLOWA*-Volta-Projekt durchgeführten interdisziplinären Messkampagnen, insbesondere in der Upper East Region im Norden von Ghana, liegt der Fokus dieser Arbeit im ghanaischen Teil des Einzugsgebiets der Weißen Volta.

Gekoppelte Meteorologie-Hydrologie-Simulationen: Insbesondere in infrastrukturschwachen Regionen mit Messgeräten ohne online Datentransfer sind die Ergebnisse eines regionalen meteorologischen Modells oft die einzige verfügbare Datenquelle für zeitnahe Abschätzungen des terrestrischen Wasserhaushalts. Dies führt zu dem in Abbildung 0.2 dargestellten Ein-Wege-Kopplungsschema des meteorologischen (*MM5*) und hydrologischen (*WaSiM*) Modells.

Der Einsatz eines hydrologischen Modells zur Abschätzungen des terrestri-

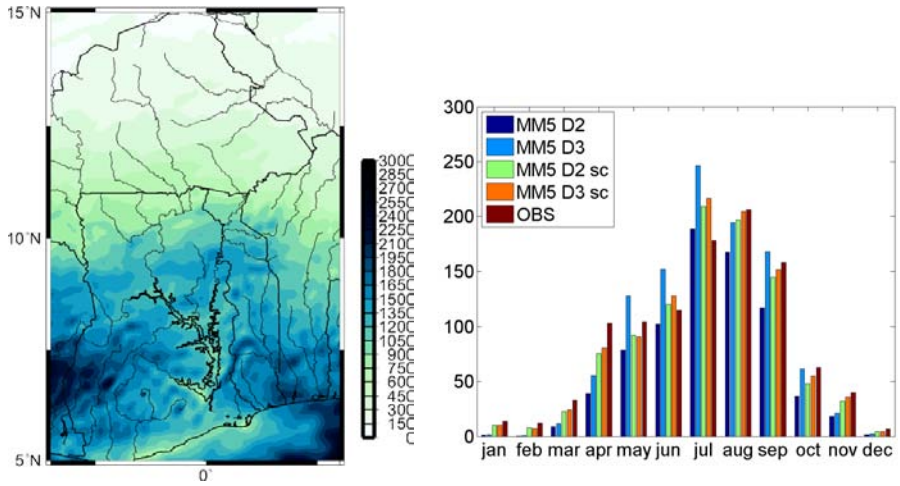

(a) (b)

Abbildung 0.3: Räumliche Darstellung des simulierten Jahresniederschlags (*MM5* Domain 3) für 2004 (a) und Vergleich des simulierten und gemessenen (22 Stationen) Jahresgang für 2004 (b); *MM5* Ergebnisse für Domain 2 und Domain 3 (Echtzeit und skaliert)

schen Wasserhaushalts erfordert zuvor eine detaillierte Kalibrierung und Validierung des Modells. Dafür werden insbesondere in unerforschten und messdatenarmen Einzugsgebieten möglichst lange hydrometeorologische Zeitreihen benötigt. Die Kalibrierung und Validierung erfolgte mit historischen Beobachtungen, die darüber hinaus flächendifferenzierte, langjährige (1961-2000) und kontinuierliche Abschätzungen des terrestrischen Wasserhaushalts liefern. Dies ist insbesondere in Einzugsgebieten mit wenigen und lückenhaften Daten, für langfristige Untersuchungen der Wasserhaushaltsbilanzen, wie zum Beispiel Dürren, eine wichtige Informationsquelle.

Für zeitnahe Abschätzungen des terrestrischen Wasserhaushalts wurden mit dem mesoskaligen meteorologischen Modell *MM5* (Grell et al., 1995) globale, meteorologische Analysedaten in drei Schritten mit horizontalen Auflösungen von 81 x 81 km^2 (Domain 1), 27 x 27 km^2 (Domain 2) und 9 x 9 km^2 (Domain 3) dynamisch regionalisiert. Als globaler Datensatz wurden Analysedaten von *NCEP* (National Centers for Environmental Prediction) mit einer zeitlichen Auflösung von 6 h verwendet. In Domain 1 wurden zusätzlich verfügbare Radiosondenmessdaten in die Modellrechnungen assimiliert. Die meteorologischen Simulationen wurden im "ex-post hindcasting" Modus durchgeführt. Dies bedeutet, dass nur Daten, die in Echtzeit verfügbar sind, eingesetzt werden, obwohl Zeiträume in der Vergangenheit simuliert werden. Demzufolge kann dieses Setup leicht in den operationellen Betrieb für zeitnahe Abschätzungen des terrestrischen Wasserhaushalts transferiert werden. Zusätzlich zu den meteorologischen Simulationen wurden für den Niederschlag zu Validierungs- und Vergleichszwecken das skalierte Produkt 3B42 von der "Tropical Rainfall Mea-

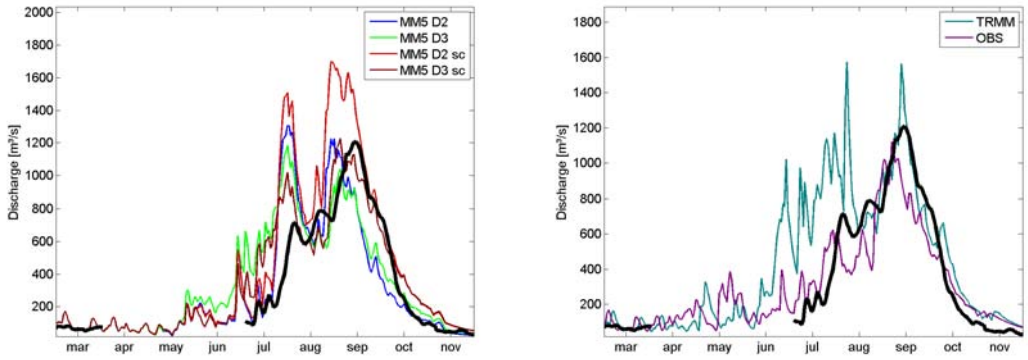

(a) Nawuni MM5

(b) Nawuni TRMM & OBS

Abbildung 0.4: Gemessene (schwarz) und simulierte Abflüsse für den Pegel Nawuni unter Verwendung von (a) Echtzeit (MM5 D2 und MM5 D3) und skalierten (MM5 D2 sc und MM5 D3 sc) *MM5* Ergebnisse sowie (b) dem skalierten *TRMM* Produkt 3B42 und Beobachtungsdaten (OBS)

suring Mission" (*TRMM*) verwendet, das auf Grund der Skalierung mit beobachteten Monatsniederschlägen mit einer Verzögerung von ungefähr einem Monat zur Verfügung steht.

Die Ergebnisse der *MM5* Simulationen sind zufrieden stellend und vergleichbar mit denen des skalierten *TRMM* Produkts 3B42, sowohl in der räumlichen Verteilung der Jahresniederschlagssummen als auch beim Jahresgang (siehe Abbildung 0.3 für 2004). Eine Skalierung der *MM5* Simulationen mit beobachteten Monatsniederschlägen, führt zu etwas verbesserten Ergebnissen. Die für eine zeitnahe Abschätzung des terrestrischen Wasserhaushalts erforderlichen gekoppelten atmosphärisch-hydrologischen Simulationen liefern im "expost hindcast" Modus für 2004 gute Ergebnisse und für 2005 auf Grund einer Überschätzung der Niederschlagssummen eine Überschätzung des Abflusses. Die Verwendung der skalierten *MM5* Simulationen für 2005 verbessert die gekoppelten Simulationsergebnisse erheblich. Die Ergebnisse der hydrologischen Simulationen mit Niederschlagsinput von dem skalierten *TRMM* Produkt 3B42 sind gut, jedoch etwas schlechter im Vergleich zu den gekoppelten atmosphärisch-hydrologischen Simulationen in Echtzeit für 2004 und skaliert für 2004 und 2005. Die Verwendung von Stationsdaten für die erforderlichen, meteorologischen Eingangsdaten in hydrologischen Simulationen führt zu guten und insgesamt zu den besten Ergebnissen. In Abbildung 0.4 sind die Abflussganglinien am Pegel Nawuni für 2004 für alle verwendeten Datenquellen der meteorologischen Eingangsgrößen gezeigt. Anstatt der flächendifferenzierten Verwendung von *MM5* and *TRMM* Ergebnissen, können diese auch nur an den Stationsstandorten als meteorologische Eingangsdaten in hydrologischen Simulationen verwendet werden. Diese

Methode liefert in den meisten Fällen die besten Simulationsergebnisse, obwohl ein Großteil der flächendifferenzierten Informationen nicht berücksichtigt wird.

Die Validierung der hydrologischen Simulationen basiert auf Grund der Datenverfügbarkeit ausschließlich auf dem Vergleich mit beobachteten Abflüssen. Die Anwendung der gekoppelten atmosphärisch-hydrologischen Simulationen liefert zusätzlich zum Abfluss zeitnahe Informationen über die räumliche und zeitliche Verteilung weiterer wichtiger Wasserhaushaltsgrößen, wie z.B. potentielle und reale Evapotranspiration, Bodenfeuchte oder Grundwasserneubildung.

Assimilierung von Landoberflächenparametern aus Satellitendaten in die hydrologische Modellierung: Neben meteorologischer Antriebsdaten sind Landoberflächenparameter, wie z.B. Albedo und Blattflächenindex (LAI), zentrale Eingangsdaten für die flächendifferenzierte hydrologische Modellierung. In den hydrologischen Modellen werden normalerweise Standardliteraturwerte für die Landoberflächenparameter verwendet, die als Tabellenwerte abhängig von der Landnutzung abgeleitet werden. Für eine detailliertere räumliche und zeitliche Beschreibung der Landoberflächenparameter wurden in dieser Arbeit die Möglichkeiten untersucht, Albedo und Blattflächenindex LAI aus multispektralen Fernerkundungsdaten abzuleiten. Dabei wurde der Einfluss der dynamischen Abschätzungen von Landoberflächenparameter aus Fernerkundungsdaten, im Vergleich zu statischen Tabellenwerten, auf die Ergebnisse der hydrologischen Simulationen untersucht.

Als spektrale Fernerkundungsdaten wurden *MODIS* Produkte verwendet. Die in dieser Arbeit verwendeten *MODIS* Produkte für Albedo (MOD43B3) und LAI (MOD15A2) liegen als 16- bzw. 8-Tageskomposits vor. Die *MODIS* Produkte wurden am Lehrstuhl für Fernerkundung der Universität Würzburg vorverarbeitet (siehe z.B. Wagner et al., 2007) und anschließend zu Monatswerten aggregiert, um die Anzahl der ungültigen Pixel auf Grund von Bewölkung zu reduzieren und gleichzeitig die Dynamik zu erhalten. Der Jahresgang der *MODIS* Produkte für Albedo und LAI sowie des Niederschlags ist in Abbildung 0.5 für das Einzugsgebiet der Weißen Volta und das Jahr 2004 dargestellt. Bei der hydrologischen Modellierung beeinflussen Albedo und LAI die potentielle Verdunstung, die in dieser Arbeit nach dem Ansatz von Penman-Monteith berechnet wurde. Der Vergleich zwischen den statischen Standardliteraturwerten und dynamischen *MODIS* Abschätzungen zeigt für Albedo eine ähnliche räumliche Verteilung. *MODIS* Daten erhöhen jedoch den räumlichen Detaillierungsgrad. Für den LAI kann die Dynamik mit zwei Jahreszeiten und statischen Standardliteraturwerten nicht zufrieden stellend nachgezeichnet werden. Im Vergleich zu den dynamischen *MODIS* Abschätzungen werden die LAI Werte während der Trockenzeit über- und während der Regenzeit im südlichen Teil des Einzugsgebiets unterschätzt. Der Einfluss der dynamischen *MODIS* Abschätzungen für Albedo und LAI ist im Vergleich zu statischen Tabellenwerten gering in Bezug auf Zeitreihen räumlich aggregierter Wasserhaushaltsgrößen, wie potentielle und reale Verdunstung oder Gesamtabfluss.

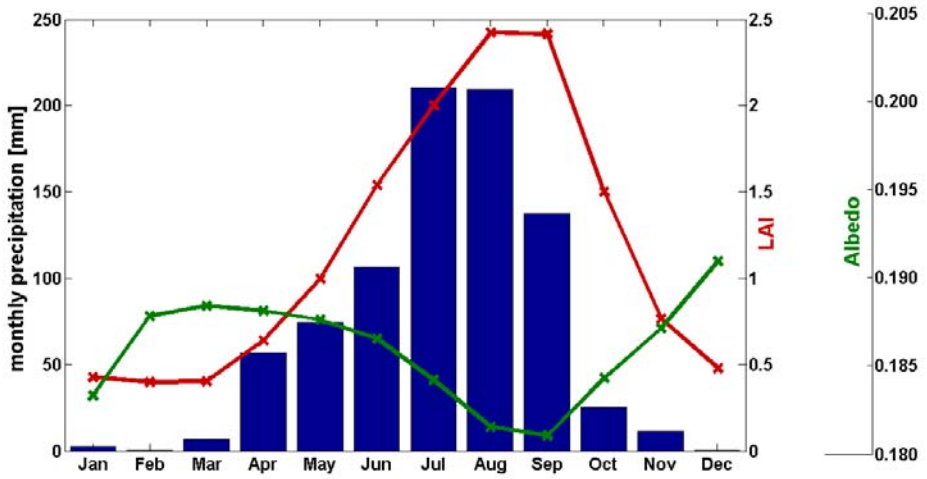

Abbildung 0.5: Jahresgang des Niederschlags [mm/Monat], Blattflächenindex *LAI* und Albedo für das Einzugsgebiet der Weißen Volta für 2004

Auf die räumliche Verteilung der Wasserhaushaltsgrößen ist der Einfluss jedoch klar erkennbar. Dies ist beispielhaft in Abbildung 0.6 für die räumliche Verteilung der Jahressumme der potentiellen Evapotranspiration gezeigt. Die berechneten Unterschiede zu den Simulationsergebnissen mit Standardliteraturwerten sind für alle Wasserhaushaltsgrößen sehr heterogen über das gesamte Einzugsgebiet verteilt. Insgesamt wurden mittels dynamischen *MODIS* Abschätzungen etwas höhere Verdunstungs- und Abflusswerte im nördlichen Teil und etwas niedrigere im südlichen Teil des Einzugsgebiets der Weißen Volta simuliert. Des Weiteren wurden niedrigere Standardabweichungen für die Verdunstungs- und Abflusssummen auf Teil- und Gesamteinzugsgebiets-mit dynamischen *MODIS* Abschätzungen der Landoberflächenparameter berechnet. Die zwischenjährliche (2004 und 2005) Variabilität von Albedo und *LAI* wirkt sich ebenso geringer auf räumlich aggregierte Zeitreihen im Vergleich zur räumliche Verteilung der Wasserhaushaltsgrößen aus.

Auswirkungen der Niederschlagsunsicherheiten auf die Ergebnisse der hydrologischen Modellierung: Zur Entscheidungsunterstützung für nachhaltiges Wassermanagement ist zusätzlich zu den Modellierungsergebnissen eine Quantifizierung der Zuverlässigkeit bzw. Unsicherheit dieser Ergebnisse erforderlich. Unsicherheitsquellen in der hydrologischen Modellierung sind insbesondere (i) Fehler bei den Antriebsdaten und eine ungenügende Repräsentativität der Variabilität (Grayson und Blöschl, 2000), (ii) die Verwendung einer unvollständigen Modellstruktur und (iii) nicht optimaler Modellparameter sowie (iv) Fehler bei den Messdaten, die für die Kalibrierung verwendet werden (Rosbjerg und Madsen, 2005). Dabei wird die richtige Abschätzung der räumlichen Variabilität des Niederschlags oft als Hauptfehlerquelle bei Un-

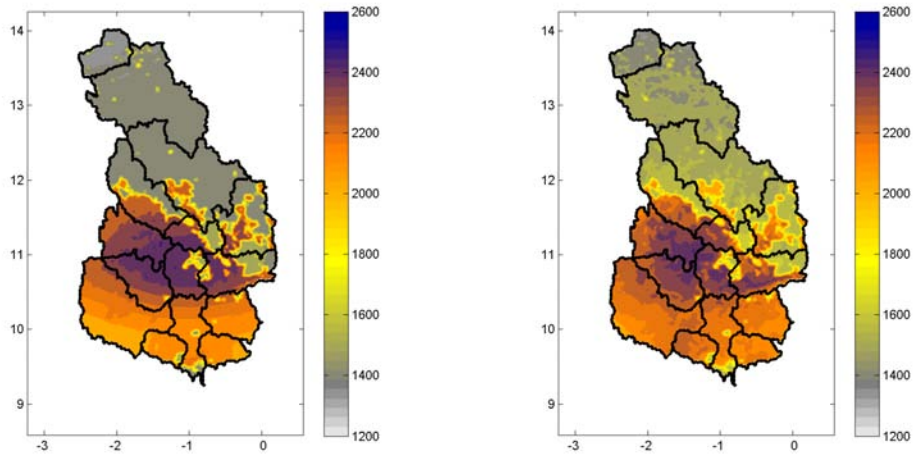

(a) (b)

Abbildung 0.6: Räumliche Darstellung der simulierten Jahressumme der potentiellen Verdunstung [mm] für das Einzugsgebiet der Weißen Volta für 2004 unter Verwendung von (a) statischen Tabellenwerten bzw. (b) dynamischen *MODIS* Abschätzungen für Albedo and *LAI*

tersuchungen der Niederschlags-Abfluss-Prozesse sowie deren Modellierung genannt (z.B. O'Loughling et al., 1996; Syed et al., 2003). Die zeitlich und räumlich sehr variable Niederschlagsverteilung ist bedingt durch die sehr komplexen physikalischen Prozesse bei der Niederschlagsbildung, die von Natur aus nichtlinear sind und sehr stark auf Veränderungen reagieren (Bárdossy und Plate, 1992). Demzufolge wurden in dieser Arbeit die Auswirkungen der Niederschlagsunsicherheiten, die sich aus der erforderlichen räumlichen Interpolation von Stationsdaten (Punktmessungen) ergeben, auf die Ergebnisse der hydrologischen Modellierung untersucht. Insbesondere in Regionen, wo wenige Beobachtungsdaten zur Verfügung stehen, und somit die Dichte des Messnetzes sehr gering ist, ist die räumliche Interpolation mit großen Unsicherheiten behaftet. Zur Untersuchung der Auswirkungen dieser Unsicherheiten auf die Ergebnisse der hydrologischen Modellierung wurden in dieser Arbeit verschiedene räumliche Interpolationsmethoden zur Ermittlung des Gebietsniederschlages aus Stationsdaten angewendet und deren Einfluss auf die hydrologischen Simulationsergebnisse untersucht. Zusätzlich zu den in *WaSiM* definierten abstandsgewichteten Interpolationsmethoden wurde der Gebietsniederschlag mittels "ordinary-" und "external drift kriging" berechnet. Die Ergebnisse zeigen, dass die Berücksichtigung geeigneter Zusatzinformationen beim "external drift kriging" die räumliche Interpolation unterstützt. Insbesondere die räumliche Verteilung des langjährigen Mittelwerts der Jahresniederschlagssummen liefert, vor allem in messdatenarmen Regionen, eine wichtige Zusatzinformation bei der räumlichen Interpolation von Stationsdaten. Die Kreuzvalidierungsergebnisse zeigen, dass die Krigingmethoden im Vergleich zu den Standardin-

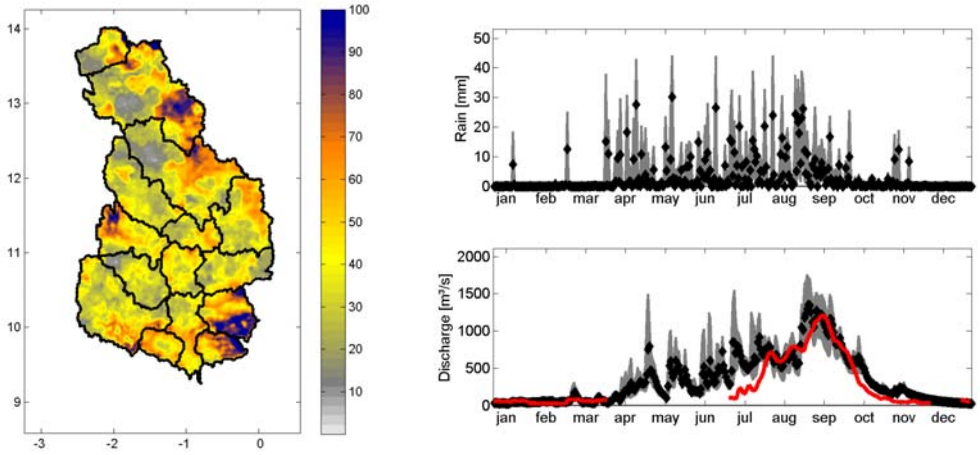

(a) std Gesamtabfluss (b) Nawuni

Abbildung 0.7: Ergebnisse der hydrologischen Simulationen mit "Turning Band" simuliertem Niederschlag für 2004: (a) Räumliche Verteilung der Standardabweichung des Gesamtabflusses [mm] und (b) Zeitreihen der Spannbreite (grau) und Mittelwerts (schwarz) für Niederschlag und Abfluss für Nawuni

terpolationsverfahren vorzuziehen sind. Beim "external drift kriging" bleibt, im Gegensatz zu den restlichen Interpolationsverfahren, die räumliche Variabilität der Stationsdaten erhalten. Der Einfluss der gewählten räumlichen Interpolationsmethode auf die Ergebnisse der hydrologischen Simulationen ist für räumlich aggregierte Variablen und die dazugehörigen Zeitreihen gering. Die Interpolationsmethode beeinflusst jedoch die räumliche Verteilung der Wasserhaushaltsgrößen. Insbesondere die gewählte Zusatzinformation beim "external drift kriging" ist in den räumlichen Darstellungen deutlich zu erkennen.

Zusätzlich zu den verschieden Interpolationsverfahren wurden Niederschlagsdaten mittels bedingter Simulationen generiert. Hierfür wurde die "Turning Band" Methode (Matheron, 1973) angewendet. Die bedingten, räumlichen Niederschlagssimulationen zeigen eine signifikant größere Variabilität des Niederschlags, behalten aber die räumlichen Hauptstrukturen bei. Die mit den generierten, gleichwahrscheinlichen Niederschlagsfeldern durchgeführten hydrologischen Simulationen liefern Spannbreiten der zeitlichen und räumlichen Verteilung der Wasserhaushaltsgrößen. Diese Spannbreiten beinhalten die Unsicherheiten, die auf die Berechnung des Gebietsniederschlags zurückzuführen sind. In Abbildung 0.7 ist die Fortpflanzung dieser Unsicherheiten auf die räumliche und zeitliche Verteilung des Gesamtabflusses gezeigt. Die räumliche Darstellung der Standardabweichungen ermöglicht z.B. die Detektion von Regionen, die mit größeren Unsicherheiten behaftet sind. Die Fortpflanzung der Unsicherheiten im Niederschlag auf den Abfluss ist am Pegel Nawuni (Gesamtauslass des Ein-

zugsgebiets) deutlich zu sehen. Der Vergleich mit anderen Teileinzugsgebieten zeigt, dass die Spannbreite wesentlich von der Lage (siehe Abbildung 0.7(a)) und den Unsicherheiten der flussaufwärts liegenden Gebiete abhängt.

Zusammenfassend wurde in dieser Arbeit für zeitnahe Abschätzungen der verfügbaren Wasserressourcen in einer messdatenarmen Region ein Ein-Wege-Modellsystem des meteorologischen (*MM5*) und hydrologischen (*WaSiM*) Modells technisch realisiert und dessen Funktions- und Leistungsfähigkeit demonstriert. Zusätzlich zu den *MM5* Ergebnissen wurden hydrologische Simulationen mit dem skalierten *TRMM* Produkt 3B42 sowie Stationsdaten angetrieben. Beide Datenquellen eignen sich jedoch nicht für die Abschätzung der aktuellen Wasserverfügbarkeit. Die Einbindung aus Satellitendaten abgeleiteter Landoberflächenparameter in die hydrologische Modellierung hat gezeigt, dass eine detailliertere räumliche und zeitliche Beschreibung der Landoberflächenparameter insbesondere die räumliche Verteilung der Wasserhaushaltsgrößen unterstützt. Das Potential der Wasserhaushaltssimulationen als zentrales Instrument zur Entscheidungsunterstützung für nachhaltiges Wassermanagement wurde demonstriert. Die Quantifizierung der Unsicherheiten der Wasserhaushaltsgrößen auf Grund der Berechnung des Gebietsniederschlags aus Stationsmessungen liefert insbesondere in messdatenarmen Regionen wichtige Zusatzinformationen für nachhaltige Wassermanagemententscheidungen.

1 Introduction

1.1 Motivation and objectives

"Fresh water is a finite and vulnerable resource, essential to sustain life, development and the environment" (Unesco, 1992). From the total world water reserves only 3% are fresh water, whereof the majority of approximately 69% is locked up in glaciers and ice caps. The remaining freshwater resource is mainly groundwater (30%). Surface and atmospheric water contribute to the last 1% of the fresh water resource (e.g. Unesco, 1978). The spatial distribution of these finite fresh water resources on Earth is extremely variable. Less than 10 countries possess 60% of the world's available fresh water supply. Water demand increases permanently, especially in countries with a fast growing population and/or economy. According to Unesco, by 2030 global demands for fresh water will exceed the supply. Furthermore, changing climate conditions will impact the water availability. A warmer climate will intensify the hydrological cycle with an increasing frequency of extreme events, i.e. heavy rainfall and droughts.

In Africa, between 75 and 250 million people are projected to be exposed to increased water stress due to climate change by 2020. Furthermore, agricultural production is projected to be severely compromised by climate variability and change, with reductions of yields from rain-fed agriculture up to 50% by 2020 in some countries (Ipcc, 2007). The water sector is strongly influenced by, and sensitive to, changes in climate. Hence, climate change and variability have the potential to impose additional pressures on water availability, water accessibility and water demand in Africa. Even in the absence of climatic change, present population trends and patterns of water use indicate that more African countries will exceed the limits of their economically usable, land-based water resources before 2025 (Ipcc, 2007; Ashton, 2002).

Hence, sustainable water resources management under increasing water demands and changing climate conditions is a central, socio-political challenge, in particular in climate sensitive regions. Decisions in sustainable water resources management require scientifically sound information of the

- current water resources and fluxes and
- future water availability.

In this work, methods and instruments are developed and applied to investigate the current water resources and fluxes. To allow investigations in ungauged or poorly gauges basins, these instruments and methods should be applicable world wide, cost-effective and preferably public domain.

Central support for decisions in sustainable water resources management arises from hydrological modelling, which provides spatial and temporal changes of water balance variables. Hydrological modelling depends strongly on meteorological input data because the atmosphere is the primary driving force for all hydrological processes. Thus, the availability of spatially and temporally reliable hydrometeorological information remains a critical issue in many hydrological studies. This applies particularly to developing countries where observation networks are extremely coarse and the vulnerability to droughts and extreme hydrological events is large (Boegh et al., 2007). Furthermore, station data are only available with a considerable temporal delay and therefore unsuitable for specific questions in water resources management, where basin-wide and short-term monitoring is required to support stakeholders and water management authorities in e.g. operational irrigation, water supply, or running hydro-power strategies. Therefore, other data sources for the meteorological driving information for hydrological simulations have to be used. In this study, three meteorological data sources, available with different temporal delays, are investigated with special focus on precipitation, which is the basic input component of the water balance. First, for near real time estimations, joint atmospheric-hydrological simulations are performed, where the output of the mesoscale meteorological model *MM5* is used as meteorological input data source. The second data source is a product of the Tropical Rainfall Measuring Mission (*TRMM*), which is available with approximately one month delay. Third, station data are used as meteorological data source. The time of availabilities of the applied meteorological input data sources are summarized in Figure 1.1.

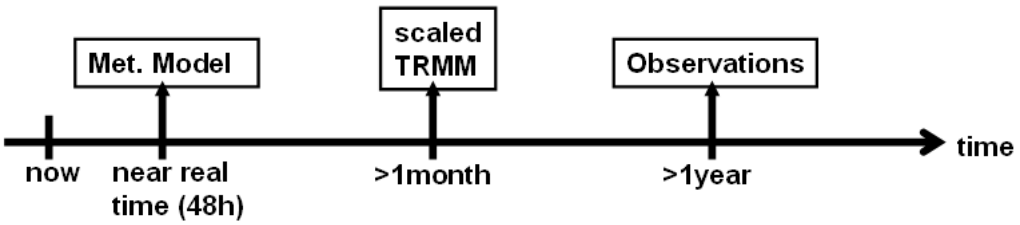

Figure 1.1: Time of availability of applied meteorological data sources

Besides meteorological driving data, land surface properties, like albedo and leaf area index (*LAI*), are essential input data for distributed hydrological modelling. In Chapter 6, the impact using different data sources for land surface

properties on hydrological simulations is investigated. Land surface properties information is usually taken from standard literature values and incorporated into hydrological modelling through tables depending on the land use. This means that the spatial distribution of the land use grid with static land surface properties has a high influence on the hydrological modelling result. However, space-borne remote sensing systems such as MODerate resolution Imaging Spectroradiometer (*MODIS*) acquire full global coverage of a large suite of land surface properties with a high spatial and temporal resolution. In this study, the *MODIS* products of albedo (MOD43B3) and *LAI* (MOD15A2) are imported into the hydrological model. This means that static parametrizations of albedo and *LAI* are substituted by dynamic estimates. The use of dynamic estimates leads to a more "detailed" spatial and temporal distribution of these parameters in the basin.

The reliability of hydrological modelling results has to be quantified to enable sustainable decisions in water resources management. The main sources of uncertainty in hydrological modelling are related to (i) errors in the model forcings and inadequate representativeness of the variability (Grayson and Blöschl, 2000), (ii) use of an incomplete model structure, (iii) use of nonoptimal model parameters, and (iv) errors in the measurements used for model calibration (Rosbjerg and Madsen, 2005). The spatial variability of rainfall is often termed as the major source of error in investigations of rainfall-runoff processes and modelling (e.g. O'Loughling et al., 1996; Syed et al., 2003). The spatial variation of the distribution pattern of precipitation is caused, by or largely attributable to, the general circulation, the temperature distribution, the non-uniform land-ocean distribution, and orographic conditions. The high spatial and temporal distribution of precipitation has a large impact on vegetation, droughts, and flooding (Quante and Matthias, 2006), i.e. on the terrestrial water balance. Hence, in Chapter 7, the impact of the uncertainties from the spatial interpolation of precipitation measurements (point observations) to areal information on hydrological modelling results is investigated. Particularly in developing countries where observation networks are coarse, the spatial interpolation is afflicted with uncertainties. Therefore, the geostatistical interpolation methods of inverse distance weighting and kriging as well as turning band simulations are applied for the areal estimation of precipitation. Their impacts on the spatial and temporal distribution of hydrological simulations are investigated in a region with only little hydro-meteorological information.

In summary, this work intends to show the application and performance of hydrological simulations driven by

1. different meteorological input data sources:
   (i) mesoscale meteorological model results,
   (ii) the satellite *TRMM* product, and
   (iii) ground based stations;

2. different land surface data sources:
   (i) tabulated, static standard literature, and
   (ii) multi-temporal *MODIS* remote sensing data;

3. different interpolation and simulation methods for areal precipitation.

The study area is the White Volta basin (94000 km^2) in West Africa, a main tributary of the Volta basin, which is described in Chapter 2. This work was funded and performed within the *GLOWA*-Volta project, which is shortly described in Section 1.3.

1.2 Innovation

Innovative work, performed within the scope of this thesis includes:

- Development of a joint atmospheric-hydrological modelling system, which is driven by public domain data sources and models only and can be applied for near real time water balance estimations in a data sparse environment. Performance analysis of this modelling system for a large basin (White Volta: 94000 km^2) with an extremely coarse observation network, in a comparable fine resolution (1 km).

- The potential of an increased level of detail in the spatial and temporal dimension of land surface properties in hydrological models using satellite derived estimations (instead of static, standard literature values depending on the land use) has not been exploited so far for large and poorly gauged basins, and is investigated here for the White Volta basin in West Africa.

- Due to coarse observation networks, areal precipitation calculations from station data (point measurements) are afflicted with significant uncertainties, which impact the results of water balance estimations. The impact of different geostatistical interpolation and simulation methods on water balance estimations is investigated, hence providing reliability estimations.

1.3 The GLOWA-Volta project

GLOWA-Volta is one of five *GLOWA* projects. *GLOWA* stands for Global Change and the Hydrological Cycle, an example of integrative interdisciplinary and application oriented global change research. It is financed by the Federal Ministry for Education and Research, with additional funding from the Ministry of Science and Research of North Rhine - Westphalia. The *GLOWA*-Volta project investigates sustainable water use under changing land use patterns, rainfall reliability and water demand in the Volta Basin. The central objective of the *GLOWA*-Volta project is the analysis of the physical and socio-economic determinants of the hydrological cycle in the Volta Basin in the face of global change. Based on this, the project aims at the establishment of a scientifically sound Decision Support System (*DSS*) for water resource management that has been adequately tested. The knowledge and tools developed are intended to serve two purposes: (i) to advance the scientific understanding of the complex linkages between atmosphere, land use, human settlement and economic activities and the hydrological cycle, and (ii) to support economically and ecologically sound water management decision-making in the Volta Basin (http://www.glowa-volta.de).

In this work, a model-based, operational water flow and balance system for the White Volta basin is developed. It provides the primary physical components of the integrated analysis of the hydrological cycle, including atmospheric processes. This system provides important support for decisions in operational water management and agricultural planning. It is the short-term part of the hydro-meteorological decision support in sustainable water management (Kunstmann et al., 2007).

In the next chapter a short description of the Volta basin is given with special focus on the study area; the White Volta basin.

2 The study area

2.1 The Volta basin

The Volta Basin is situated in a semi-arid to sub-humid environment in West Africa. It covers an area of 414000 km^2 and stretches approximately from latitude 5°30' N to 14°30' N and longitude 5°30' W to 2°00' E (see Figure 2.1). The Volta basin is shared by six riparian countries. Burkina Faso (42.07%) and Ghana (40.25%) encompass 80% of the basin's drainage. Further riparian countries are Togo, Benin, Mali and Ivory Coast. Main tributaries of the Volta basin are the Black Volta (called Mohoun in Burkina Faso), the White Volta (Nakanbé) and the Oti (Pendjari) river. All three tributaries originate in Burkina Faso and drain into the Volta Lake in Ghana. The study focuses on the White Volta basin, located North of Lake Volta between latitude 9°30' N to 14°00' N and longitude 2°30 W to 0°30 E. The Volta Lake is still one of the largest artificial lakes in the world with a surface area of about 8500 km^2, an average depth of about 18.8 m and a shoreline of about 5500 km. Lake Volta is the result of the construction of a dam at Akosombo in the South of Ghana in 1965, not long after Ghana reached independence as the first West African state in 1957. The dam was created primarily for hydroelectric power generation. Additionally, Lake Volta is used for transportation, fishery, water supply, tourism and irrigation. At Akosombo, 912 Megawatt of electricity can be produced at its maximum operating capacity (Barry et al., 2005). The Akosombo dam generates 80% of the power produced in Ghana. Therewith it is of strategic importance for the economy in Ghana. It supplies energy and water demanding industries like aluminium production with cheap electricity. This lead to a fast economic development compared to other West African countries. Today the annual Gross Domestic Product *GDP* of Ghana amounts to 10.7 billion US$ (2005) with an annual growth of 5.8%. The structure of the economy consists of 38.8% agriculture, 24.6% industry and 36.6% services (Worldbank, 2006). For Burkina Faso *GDP* amounts to 5.2 billion US$ (2005) with an annual growth of 4.8%. The structure of the economy consists of 30.6% agriculture, 19.8% industry and 49.6% services (Worldbank, 2006). Burkina Faso has 13.2 million inhabitants and an average annual population growth (1999-2005) of 3.5%. The numbers for Ghana are 22.1 million inhabitants and an average annual population growth of 2.2% (Worldbank, 2006). These numbers and in particular the growth rates show that the demand for water supply, food and energy production is increasing permanently, which

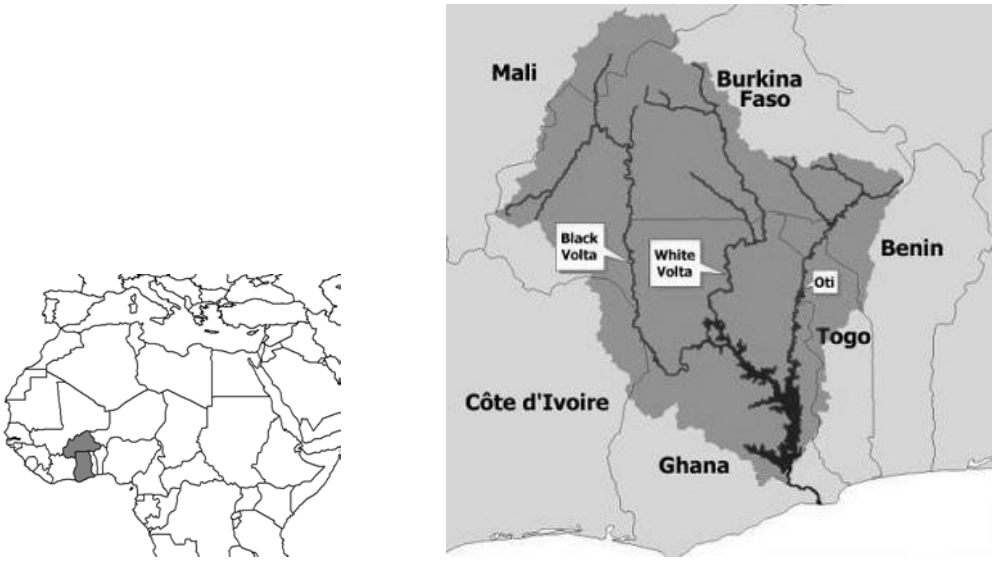

(a) Ghana and Burkina Faso (b) Volta basin

Figure 2.1: Location of (a) Ghana and Burkina Faso, and (b) the Volta Basin basin in West Africa

leads to competition or even conflicts between the different consumers and/or the riparian countries (transboundary conflicts). The potential for conflict is larger in dry years, which occur periodically, because precipitation intensities and annual amounts show a strong inter-annual, inter-decadal and even intra-seasonal variability due to climatic conditions in West Africa (see Section 2.2). The variability affects in particular the rural population whose major source of livelihood is rain-fed agriculture.

Due to the above mentioned reasons, the estimation of rainfall, in particular of rainfall variability, and the spatial and temporal changes of the terrestrial water balance are of crucial importance for sustainable decisions in water resources management, for example in operational irrigation, water supply or running hydro-power strategies.

2.2 Climate of the White Volta basin

Large scale dynamics: The general climate characteristics like e.g. the annual cycle of temperature and rainfall, are primarily controlled by the large scale dynamics of the atmosphere. The global circulation system is formed as a consequence of the latitudinal dependence of solar insolation. It transports the thermal energy polewards, and thus reduces the resulting equator-to-pole temperature contrast. The basic structure of the atmospheric circulation remains fairly constant, but it is seasonally modulated by the altitude of the sun showing weak year-to-year variability. Within this global circulation, the Hadley

circulation, which is the mean meridional circulation in lower latitudes and the Walker circulation which is the mean zonal circulation along the meteorological equator are the dominating factors determining West African dynamics and its variability. The Hadley cell is a thermally driven circulation pattern that dominates the tropical atmosphere, with rising motion near the equator, poleward flow 10-15 km above the surface, descending motion in the subtropics, and equator-ward flow near the surface. The Inter Tropical Convergence Zone (*ITCZ*) is a boundary zone between the two Hadley-type cell circulations of the two hemispheres and influences most flow characteristics in West Africa. It separates humid maritime air masses from dry continental air masses from the Sahara; the Harmattan. Following an annual cycle, the *ITCZ* moves northwards up to 25° N - 30° N in boreal summer. The wet south-westerly flow moves into the inner continent as a function of pressure and thermal gradients that settle between the relatively cool ocean and the heated desert. During the rainy season from May to approximately November, a thermally induced low pressure cell is prevailing over the Sahara with its axis located between 18° N and 22° N and a subtropical anticyclone intensifies and extends equator-wards. As a function of the pressure gradients between these two cells an unstable wet and cold south-westerly flow (south-west monsoon) penetrates deep into the inner continent and reaches latitudes of 20° N - 22° N in August. During the dry season the prevailing flow is the Harmattan. Regions in the southern part of West Africa experience two rainy seasons, whereas regions in the north just show one season. In higher levels, monsoonal winds and Harmattan are overlain by the *AEJ* at approximately 600-700 hPa and the *TEJ* at 200 hPa, both also related to the *ITCZ*. Strength and location affect the climatic conditions in West Africa and are discussed for the White Volta basin in the following paragraphs (Jung, 2006).

Precipitation: Mean annual precipitation ranges from less than 400 mm (North) to more than 1500 mm in the South-East, whereof around 80% falls between July and September with the monsoonal rains. Additionally to the strong North-South gradient a West-East gradient is present in the spatial distribution of precipitation especially along the coast in the South of Ghana. The spatial distribution of annual precipitation is depicted in Figure 2.2 where long-term mean annual precipitation data (1961-1999) of 29 stations in Burkina Faso and Ghana are spatially interpolated applying external drift kriging (see Section 7.3.2). Furthermore, the small scale rainfall variability is very high.

Temperature: Mean annual temperature lies between 27°C and 36°C with a daily variation of 8-14°C in the northern and between 24°C and 30°C with a daily variation of 3-5°C in the southern part (Oguntunde, 2004; Hayward and Oguntoyinbo, 1987). The seasonal variation in temperature is characterised by four periods: two extremely hot and two relatively cool periods. The first hot period is in March-April. The second, which is not as hot as the first

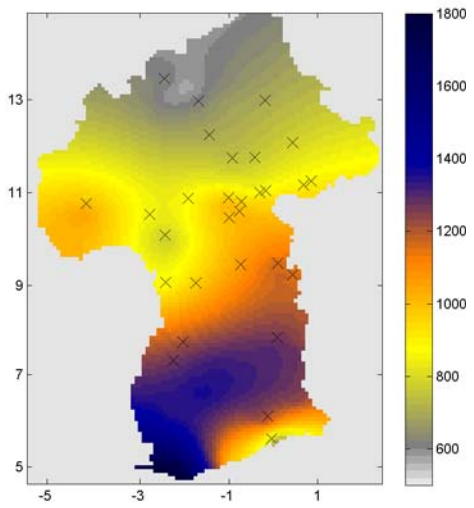

Figure 2.2: Long-term (1961-2000) mean annual precipitation [mm] for Burkina Faso and Ghana

one, occurs directly after the rainy season. The first cooler period occurs in December-January during Harmattan and the second one coincides with the rainy season (Barry et al., 2005).

Evapotranspiration: The range of mean annual potential evapotranspiration (1961-1990) for the White Volta basin in Ghana is between 1650 mm and 1968 mm (Barry et al., 2005). In the Burkinabé part of the basin mean annual values increase up to 2300 mm in the North of Burkina Faso. Approximately 80% of the precipitation amount evapotranspirates during the rainy season (Oguntunde, 2004).

Humidity: Relative humidity can reach up to 80% in August which is the wettest month during the rainy season. During Harmattan relative humidity can be as low as 20-30% (Barry et al., 2005).

Precipitation variability: Precipitation variability is of crucial importance for investigations of the terrestrial water balance, but also for the livelihood of the population in West Africa. Variability occurs on inter-annual and inter-decadal temporal scale. Observations suggest that inter-annual variability can be partly explained by a connection of Hadley and Walker circulation. According to Burpee (1972) stronger Hadley circulation could be observed during dry years, whereas stronger Walker circulation occurs during wetter years. Furthermore, for example, Bader (2005) identified the influence of sea surface temperature (SST) in the eastern tropical Atlantic and Indian ocean on rainfall anomalies in West Africa. Additionally to SST variation, the influence of bio-geophysical feedback-mechanisms, e.g. land use change, on rainfall

regimes or soil moisture-rainfall interactions for West Africa were investigated (e.g. NICHOLSON, 1993; KUNSTMANN and JUNG, 2003).

Climate change footprints: A linear trend analysis was performed for the Volta Basin by NEUMANN et al. (2007). The results for temperature, precipitation and runoff time series in Ghana and Burkina Faso can be summarized as follows.

- Temperature: The time series show a clear and significant trend of an increase over the last decades.
- Precipitation: For precipitation time series both negative and positive trends are calculated but only a small number of trends are significant. Due to the fact that almost all significant trends are negative, a weak trend towards a decrease in precipitation is concluded.
- Runoff: No linear relationship between the trend in precipitation and river discharge is found, revealing the non-linearity of the response of the discharge signal to the signal in precipitation.

2.3 Hydrology of the White Volta basin

Discharge: The White Volta is one of the main tributaries of the Volta basin (see Figure 2.1b). Mean annual runoff of the White Volta is 9565 x 10^6 m^3, whereof 3492 x 10^6 m^3 are generated in Burkina Faso and 6037 x 10^6 m^3 in Ghana (MWH, 1998). The White Volta begins as the Nakanbé river in Burkina Faso. The main tributaries of the White Volta are the Red Volta, referred to as Nazinon in Burkina Faso, and Sissili. Discharge observations without dam influence show a high seasonal variability. Mean runoff during the driest month is approximately 240 times less than mean peak flows (ANDREINI et al., 2000). Except for the White Volta itself the tributaries usually run dry during the dry season. During the rainy season large areas of adjacent flood plains are subject to shallow flooding of less than one meter (VAN DE GIESEN, 2001). The runoff coefficient RC [%] defined as

$$RC = 100 \cdot \frac{Q}{P} \tag{2.1}$$

with runoff Q and precipitation P, calculates the percentage of precipitation which becomes runoff. For the White Volta basin RC is 7.1%. The high nonlinearity of the rainfall-runoff process is demonstrated by ANDREINI et al. (2000). A mean variation coefficient of 7% for precipitation faces 57% for runoff. Furthermore, approximately 340 km^3 of rainfall are required before significant runoff can be generated. This indicates the high sensitivity of runoff with respect to precipitation and implies that relatively small changes in annual

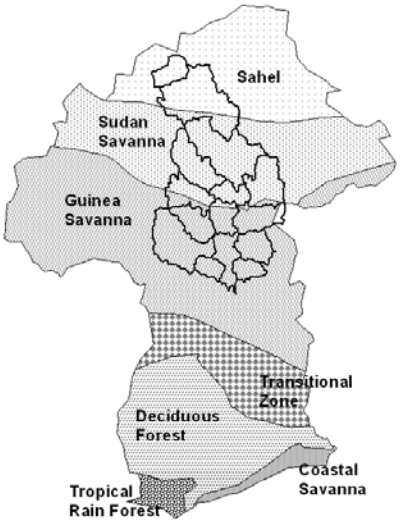

Figure 2.3: Agroecological zones of Ghana and Burkina Faso with the subcatchments of the White Volta basin and its subcatchments

precipitation may cause large changes in annual runoff (Obeng-Asiedu, 2004). It is worth mentioning that since 1993 the White Volta catchment is disturbed by a dam and hydro-power generation in Bagré in the South of Burkina Faso.

Land use: Land use in the White Volta Basin is dominated by savannah type vegetation. The agroecological zones for Ghana and Burkina Faso with the outline of the White Volta basin are depicted in Figure 2.3. From South to North a transition from Guinea savannah via Sudan savannah to Sahel occurs. Several studies demonstrate the high influence of the type of land use on runoff processes. Chevallier and Planchon (1993), for example, investigated runoff processes in the small Booro-Borotou basin, a savannah environment in Ivory Coast, and detected a dominant influence of the vegetation on the high variability of infiltration. In this study, the assimilation of satellite-derived land surface properties in hydrological modelling is investigated in detail (see Section 6).

Soil: The soils of Burkina Faso are predominantly of lateritic type. In the southern part of the basin, the soils are mainly lixisols. These are strongly weathered soils with predominantly kaolinite clays and high contents of iron, aluminium and titanium oxide. The aggregate stability at the surface is low and soils are prone to erosion if vegetation cover is removed (Adams et al., 1996). The other main group of soils in the Volta Basin are the arenosols, mainly found in the northern, arid part of the basin. The basis is sand, coated with iron oxides, which gives the soil its specific reddish colour. These soils are characterized by high infiltration rates. A study on soil properties by Agyare (2004) at two

sites in the Ghanaian Volta Basin revealed high discrepancies between subsoil and topsoil due to less soil disturbance in the subsoil. Saturated hydraulic conductivity (K_{sat}) turned out to be highly variable in space for both soil layers considered.

Geology and groundwater: The dominant geological systems of the basin are a Precambrian platform and a sedimentary layer. The Ghanaian sedimentary layer, which underlies the Volta Basin, is known as the Voltaian formation. A detailed description of the geohydrology can be found in VAN DER SOMMEN and GEIRNAERT (1988), and, with a special emphasis on the Ghanaian part of the basin, in AGYARE (2004). Burkina Faso is dominated by crystalline and metamorphic rocks of the West African shield, formed primarily from Precambrian platform rocks, which are essentially impermeable. Fractures and channels, which enable the transmission and storage of groundwater, are only developed through tectonic movements (SHAHIN, 2002). The basement and the overlying weathered zone form a two-layer aquifer that reaches from 25 m to 65 m below ground. The average depth of the decomposed zone in the Ghanaian part of the Precambrian platform is given with 40 m and aquifers are characterized through low transmissivities (7.5-30 m^2/d) and low storativities (0.003-0.008). A detailed geohydrological map of the Volta Basin was set up and analysed by MARTIN and VAN DE GIESEN (2005). The groundwater aquifer system is characterized by two different types of aquifer. One is of the reservoir type, meaning a weathered mantle of high porosity, but low permeability. This type provides the main aquifer storage (ADAMS et al., 1996). The other type, developed in fractured bedrock has low porosity and high permeability. It is generally assumed, that the aquifer systems in the basin are highly discontinuous with individual compartments in which isolated groundwater circulation occurs (AMISIGO, 2005). Surface water and groundwater are regarded as separate resources with little or no interaction. Groundwater flow to rivers in the basin is regarded as insignificant. Groundwater recharge was found to be spatially very heterogeneous and seems to derive largely from excess rainfall (VAN DER SOMMEN and GEIRNAERT, 1988). According to MARTIN and VAN DE GIESEN (2005), recharge is comparably low and no recharge at all is observed below an annual rainfall of 170 mm for sandstone aquifers and below 380 mm for weathered rock aquifers.

3 Joint atmospheric-hydrological modelling

Sustainable decisions in water resources management require scientifically sound information on water availability, which includes the quantification of the spatial and temporal changes of water balance variables. Central support in hydrological decision making arises from hydrological modelling which, in turn, depends on meteorological input. In poorly gauged basins, this task is hampered by the fact that only little hydro-meteorological information is available. Station data are only available with a considerable temporal delay and therefore unsuitable for specific questions in water resources management, where basin-wide and near real time monitoring is required to support stakeholders and water management authorities in operational irrigation, water supply, or running hydro-power strategies. Therefore, other data sources for the meteorological driving information for hydrological simulations have to be used. For near real time estimations of current water resources and fluxes a model based water balance monitoring system, based on a joint atmospheric-hydrological model system, is applied. For the meteorological simulations, the mesoscale meteorological model *MM5* (Grell et al., 1995) is used. An interface developed at *IMK-IFU* is used to transform the results of the meteorological simulations to meteorological input data for hydrological simulations, which are performed using the Water Balance Simulation Model *WaSiM* (Schulla and Jasper, 2000). In the following sections the theory and application of meteorological and hydrological modelling in the White Volta basin are described.

3.1 Regional atmospheric modelling

For numerical weather predictions (*NWP*) two kinds of meteorological models are applied: the general circulation model (*GCM*) and the limited area model (*LAM*). The first *GCM*'s were pure atmospheric models, where oceans were parametrized as "swamp oceans". Newer models are mostly atmosphere ocean general circulation models (*AOGCM*), where the atmosphere model is coupled to an ocean one. Nowadays, *GCM*'s are applied additionally to numerical weather predictions as global climate models. Providing global coverage, the horizontal resolution of *GCM*'s is limited due to computation time. *GCM*'s are able to model large scale atmospheric phenomena, but it is not possible to achieve an explicit representation of mesoscale forcings, like land use, oro-

graphy or land-sea interactions because mesoscale forcings require higher horizontal resolutions. Thus, different downscaling approaches exist to improve the simulations of mesoscale forcings compared to *GCM*'s.

Downscaling approaches: It can be distinguished between two downscaling approaches: (i) statistical and (ii) dynamical downscaling. The aim of all approaches is the simulation of small scale meteorological fields derived from *GCM* simulation results.

- Statistical downscaling determines statistical relations between large-scale and regional or local variables, e.g. observations (Giorgi et al., 2001). Therefore, a variety of statistical methods, e.g. weather generators, weather typing through classification of circulation patterns (Stehlik and Bárdossy, 2002) or transfer functions like linear and nonlinear regression, artificial neural networks, empirical orthogonal functions (*EOF*) or canonical correlation analysis (*CCA*) are applied.

- Dynamical downscaling uses *LAM*s for the numerical solution of atmospheric equations of motion, energy and momentum balance for a spatially limited area on the globe. Initial, lower and lateral boundary conditions are provided by *GCM* output fields which indicates the dependency of the *LAM* results on the *GCM* output.

In this study, the dynamical downscaling approach is applied to consider the mesoscale forcings. Although dynamical downscaling requires substantial CPU and storage capacities, this approach has been selected due to the following reasons. The main reason is the scarcity of observation data, which is a mandatory prerequisite for the development of statistical transfer functions between large-scale and regional or local variables. Furthermore, in the *GLOWA*-Volta project *NWP*'s are simulated for the Volta basin. These results shall be linked to the hydrological simulations.

Mesoscale forcings in the Volta basin
In the Volta basin the following mesoscale forcings have to be considered:

- Topographic influences: Due to a higher resolved topography, lee effects and an orographic enhancement of convection are accounted for in more detail in the smaller scale simulations. In the Volta basin this applies in particular for the mountain range along the border between Togo and Ghana.

- Land cover: A high resolution of land cover is also essential for small scale dynamics, as land-atmosphere interactions are not only a large-scale phenomenon.

- Convective precipitation: Although convection is triggered by large scale forcing, small and mesoscale convective systems are observed in West Africa. This means that convective processes happen predominantly below grid scale in coarser resolved simulations. In coarsely resolved simulations, convective parametrization schemes, although required, provide only a limited representation of small scale rainfall processes, and are one of the largest sources of uncertainty in meteorological modelling.

- Land-sea interaction: Furthermore, land-sea interactions are of major importance for small scale climate conditions in the Volta Basin. For example the precipitation distribution along the coast in this region, known as Togo-gap, is strongly dependent on small scale *SST* fluctuation, like the up-welling of cold water along the coast. These phenomena cannot be represented unless the regional climate model is coupled to a mesoscale ocean model.

These mesoscale, and even smaller scale forcings, have to be represented properly. This requires the application of a regional meteorological model.

3.1.1 Mesoscale meteorological model MM5

For the meteorological simulations the mesoscale meteorological model *MM5* (Grell et al., 1995) is used. *MM5* is a community model which was developed at the National Centre for Atmospheric Research (*NCAR*) and the Pennsylvania State University (*PSU*) (Dudhia et al., 2003). Being designed to broaden applications, *MM5* includes (i) a multiple-nest capability, (ii) nonhydrostatic dynamics, (iii) a four-dimensional data assimilation capability, (iv) an increased number of physics options, and (v) portability to a wider range of computer platforms, including *OpenMP* and *MPI* systems (Dudhia et al., 2003). The large user community applied and validated *MM5* intensively under different conditions around the world.

To find an optimal *MM5* parametrization scheme for the Volta region, Kunstmann and Jung (2003) compared precipitation data measured at 28 stations from July 15, 1998 to August 14, 1998 with model simulations for domain 3 with 9 x 9 km spatial resolution. This model setup used *NCEP* reanalysis data. The chosen episode extends from the first maximum of the bimodal rainy season to the intermediate minimum of the "Little Dry Season" in August. An entire set of 16 simulations was performed to determine the optimal model configuration. This configuration is described shortly in the following section, based mainly on Grell et al. (1995), and Dudhia et al. (2003).

Horizontal discretization: The horizontal discretization scheme of *MM5* uses an Arakawa-B-grid staggering. Scalar variables are defined in the centre of the grid cell, whereas the horizontal velocity components are calculated in the corners. This allows a larger maximum time step compared to other methods.

Vertical discretization: The vertical discretization is performed in a sigma-pressure system, with respect to the hydrostatic reference pressure p_0. As a result, the pressure levels are height dependent, which makes this vertical sigma-pressure coordinate equivalent to terrain-following height coordinates (Grell et al., 1995). In this study 25 layers up to 30 hPa are defined. To account for the higher tropopause level in the tropics the top level is set to 30 hPa instead of the standard value of 100 hPa. Scalar variables and horizontal velocity components are defined in the middle of each vertical model layer. The vertical velocity component is defined at full sigma levels.

Temporal discretization: A second order leapfrog scheme is used for temporal discretization of temperature, moisture, and the slow terms of pressure and momentum. Sound waves, as components of the nonhydrostatic equations of motion, must be calculated with a shorter time step within the nonhydrostatic model for reasons of numeric stability. This is done using a semi-implicit time splitting scheme following Klemp and Wilhelmson (1978), in which vertically propagating sound waves are treated implicitly, whereas horizontally propagating sound waves are treated explicitly and time centred. A horizontal divergence damping technique according to Skamarok and Klemp (1994) is applied. This leads to the short time step being solely dependent on the horizontal and independent of the vertical resolution.

Nonhydrostasy: Given the purposes of this study, nonhydrostasy is of major importance, as the hydrostatic equation can only be a good estimate of the atmospheric state at a larger scale, specifically as long as the scale of vertical circulation features is smaller than the horizontal patterns' scale (Pichler, 1997). In order to simulate the Volta Basin meteorology with a reasonably high resolution, nonhydrostatic dynamics must be considered. This includes the use of the fully compressible mass continuity equation. The adiabatic heating term within the pressure tendency equation is the only term that is neglected. In general, the hydrostatic assumption does not hold below a resolution of 10 km (Kalnay, 2003).

Lateral boundary conditions: A relaxation procedure is induced to "relax" the model's predicted variables at the lateral boundary towards the large-scale analysis. This is accomplished using a relaxation function that decreases linearly from the lateral boundary (Grell et al., 1995). Vertical velocity is not nudged. A zero gradient condition is defined for cloud water, rain water, snow, and ice on outflow, and additionally no inflow of these variables occurs.

Lower boundary conditions: Originally *MM5* used fixed lower boundary conditions for *SST*, soil moisture, and soil temperature. *MM5* version 3.5 introduced the option of using variable lower boundary conditions. In this context the introduction of a variable *SST* is very important for West Africa, because a large portion of climatic variability is connected to *SST* anomalies. Another

improvement was the coupling of a land surface model to the lower boundary to account for feedback mechanisms between soil, vegetation, and atmosphere, which requires a soil-vegetation-atmosphere-transfer (*SVAT*) model. Therefore, *MM5* is applied with the Oregon-State-University Land-Surface-Model (*OSU-LSM*) (Chen and Dudhia, 2001). The *OSU-LSM* is a fully developed one-dimensional *SVAT* model, able to account for the feedback mechanisms between soil, vegetation and planetary boundary layer. The *OSU-LSM* is capable of predicting soil moisture and temperature in four layers (10, 30, 60, and 100 cm thick), as well as canopy moisture and water equivalent snow depth. Soil temperature is derived by solving the diffusion equation, including heat capacity and thermal conductivity as a function of soil moisture. The *OSU-LSM* also computes surface and underground runoff accumulations. It makes use of vegetation and soil type when handling evapotranspiration and accounts for effects such as soil conductivity and gravitational flux of moisture. Temperature at the lower boundary of the model is defined as the mean of the annual cycle and assumed to be found at three meters below surface. The *OSU-LSM* takes surface-layer exchange coefficients as input along with radiative forcing, precipitation rate and outputs the surface fluxes back to the PBL scheme. The simulation of feedback mechanisms between soil moisture and precipitation using *MM5/OSU-LSM* and the importance of these feedbacks especially for West Africa and the Volta region was demonstrated by Kunstmann and Jung (2003).

Planetary boundary layer (PBL): In combination with the *OSU-LSM* *SVAT*-model the *MRF-PBL* scheme (Hong and Pan, 1996) is the only choice for the parametrization of the planetary boundary layer. The Hong-Pan *PBL* scheme is based on a nonlocal boundary layer vertical diffusion scheme of Troen-Mahrt. The largest difference between this non-local K approach and the local K approach is that the transport of mass and momentum in the planetary boundary layer is determined by the bulk properties of the *PBL*, rather than the local properties. This is important because these transports strongly depend on large eddies in the *PBL*. Within this *PBL* scheme, vertical diffusion is simulated using an implicit scheme to allow a longer time step (Dudhia et al., 2003).

Radiation: The applied cloud-radiation scheme incorporates short wave and long wave interactions with clear sky and explicit clouds (Grell et al., 1995). Interaction with cloudy skies is simulated by a cloud parametrization scheme. An upper radiative boundary condition that allows wave energy to pass through unreflected was developed (Klemp and Durran, 1983; Bougeault, 1983).

Gridscale (explicit) precipitation and clouds: For the calculation of gridscale precipitation, microphysical processes that influence precipitation formation and conversion processes between the different phases of water must be parametrized. This scheme is activated as soon as saturation at a grid point is

reached. The Reisner Graupel scheme is used within the present study. This scheme is based on the Reisner mixed phase scheme (Reisner et al., 1998), and includes the calculation of cloud water, cloud ice, rain water, snow, super cooled water, melting of snow, graupel and ice particle number concentration.

Sub-gridscale (implicit) precipitation: The sub-gridscale precipitation scheme, often referred to as the cumulus parametrization, produces precipitation before gridscale saturation is reached, to account for sub-gridscale processes as well as grid-scale instability associated with a saturated conditionally unstable atmosphere (Betts, 1986). The Grell scheme used here (Grell and Kuo, 1991) includes updraft and downdraft. No entrainment and no detrainment are considered along the cloud edges. Therefore, mixture of clouds and surrounding air only takes place at the top and the bottom of the circulations. A constant mass flux with height is assumed. In addition, no cloud water is produced. All condensate water immediately falls out as rain/snow. The closure scheme relates the amount of convection to the destabilization rate in the environment. A quasi-equilibrium between destabilization by the large-scale environment and stabilization by convection is assumed.

Shallow convection: Additionally, a shallow convection scheme is implemented to account for shallow, non precipitating convection that is forced by sub-grid scale processes (Grell et al., 1995).

3.1.2 Setup of MM5 for the White Volta basin

In this section the setup of the regional meteorological model *MM5* applied for the Volta basin is described.

Global Forecasting System: As already mentioned in Section 3.1, a *LAM* requires input data from a *GCM*. In this study, global analysis fields are obtained from the Global Forecasting System (*GFS*) from the National Centers for Environmental Prediction (*NCEP*). The *GFS* provides forecasting and analysis data with a temporal resolution of 6 hours. In this study, the *GFS* analysis data are applied. These incorporate available observation data at initialization time.

Nesting: *LAM*s dynamically downscale (see Section 3.1) global atmospheric fields stepwise from the coarse resolution of the *GCM* to higher spatial and temporal resolutions in the area of interest. In the tropics, lateral boundary forcing is generally weak and, when using large *LAM* domains, it is more likely that *LAM* simulations develop a circulation that differs from that of the *GCM*. Whether or not this is an advantage for the credibility of the *LAM* simulations has been widely discussed. Therefore, domain settings are a widely discussed issue, whether the circulation of the *LAM* should not differ significantly from that of the *GCM* (Jones, 1995) or large domains should be used in regional

meteorological modelling to allow modifications of the atmospheric circulation by the *LAM* at spatial scales which are not well represented by the *GCM* (Wang et al., 2004). Additionally, it is advisable to avoid placing *LAM* lateral boundaries over regions with known *GCM* biases (Wang et al., 2004) or erroneous moisture transport which occur mainly over the ocean. Therefore, the lateral boundaries over the ocean for domain 2 and domain 3 are positioned far away from the area of interest, as has been recommended, for example, by Warner et al. (1997).

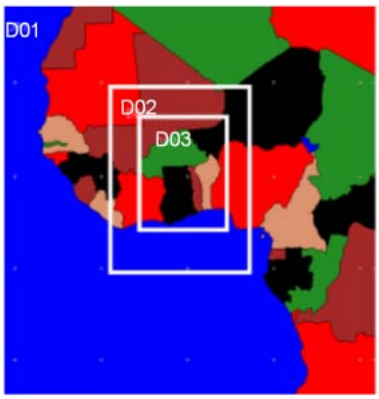

Figure 3.1: Nesting strategy for the meteorological modelling with *MM5* for the White Volta basin (D01: domain 1; D02: domain 2; D03: domain 3)

In this study, global atmospheric analysis fields with a resolution of 1° are dynamically downscaled to 9 km using three domains with horizontal resolutions of 81 x 81 km^2 (61 x 61 grid points), 27 x 27 km^2 (85 x 67 grid points) and 9 x 9 km^2 (157 x 121 grid points) (see Figure 3.1). Domain 1 has been selected to be large enough to allow distinct circulations to develop (Jung and Kunstmann, 2007). Lateral and lower boundaries of the model domains are updated every 6 hours for all three domains. For the vertical resolution 25 layers from the surface up to 30 hPa are chosen to account for the high altitude of the tropical tropopause. The time step is between 240 s for model domain 1 and 30 s for the highest resolution in domain 3. For this study, *MM5* version 3.6 in the one-way nesting approach is used. Applying one-way nesting means that boundary conditions are passed only from the coarser to the finer domain without feedback. The output of the *MM5* simulations is saved every 3 hours.

Four dimensional data assimilation: Four dimensional data assimilation (*FDDA*) is a method of running a full-physics model while incorporating observations. Thus, the model equations assure a dynamic consistency while the observations keep the model close to the true conditions. The *MM5* model uses the Newtonian-relaxation or nudging technique (Dudhia et al., 2003). In domain 1, available observations obtained from radiosondes are incorporated into the simulations to include vertical profiles of atmospheric variables into

the modelling process. The number of upper air observations within domain 1 ranges mostly between 0 and 6, maximally up to 16. Within domain 2 the maximal number of upper air observations is 3. Usually however, no measurement data are available for *FDDA*. Therefore, radiosonde observations are incorporated only in domain 1, but through the one-way nesting approach this information is passed on to the following domains.

Parametrizations: Kunstmann and Jung (2003) determined an adequate configuration of the available parametrizations for the Volta basin, which are listed in Table 3.1, and used for this study. The applied *MM5* parametrizations have been described in Section 3.1.1.

	Parametrizations
Soil model	*OSU-LSM* (Chen and Dudhia, 2001)
Planetary boundary layer	*MRF-PBL* scheme (Hong and Pan, 1996)
Radiation physics	Cloud-radiation scheme (Grell et al., 1995)
Gridscale precipitation	Mixed phase Graupel (Reisner et al., 1998)
Sub-gridscale precipitation	Cumulus parameterization (Grell and Kuo, 1991)

Table 3.1: Choice of *MM5* parametrization schemes for the Volta region

3.2 Hydrological modelling

3.2.1 Concepts of hydrological modelling

A hydrological model is a simplified description of nature, developed or adjusted for a specific goal (Rosbjerg and Madsen, 2005). Models can be more or less general, but so far no model can be assumed to be universal. So many processes are involved in the cycling of the water, that only the most important ones can be taken into account in the modelling efforts. In a given application the most important ones will depend on the purpose of modelling. Furthermore, the hydrological cycle covers an immense range of spatial and temporal scales that make a single model approach impossible. Therefore, Rosbjerg and Madsen (2005) introduce the concept of appropriate modelling where the actual purpose of the modelling is governing the scales, sophistication level in process description and parametrization, the calibration and validation procedures and the uncertainty assessment.

Classification according to model development

Depending on the degree of physical considerations involved in the process descriptions, it has been common to divide models into black box (empirical), grey box (conceptual), and white box (physical based) models. The models differ in the way of transforming input into output. The modelling system can

have a firm physical basis built on theories and physical laws. Alternatively, one can analyse the input and output data and build empirical models that describe the observed relations using, for example, deterministic artificial neural networks (*ANN*) or autoregressive-moving average (*ARMA*) linear stochastic models. Between these two approaches, a broad spectrum of modelling systems can be formulated using different process conceptualizations that have a certain degree of physical content, but need observation data to tune or calibrate the model parameters (Rosbjerg and Madsen, 2005).

Classification according to spatial and temporal resolution

A further model classification is based on the spatial resolution. Lumped models do not take into account the spatial variability of processes, input, boundary conditions or system (watershed) geometric characteristics. Distributed models take an explicit account of spatial variability of processes, input, boundary conditions and/or system (watershed) geometric characteristics (Singh, 1995). In real applications of physical based models usually a lumping of small scale physics to the model grid scale occurs (Beven, 1989). Semi-Distributed models subdivide the watershed into response units with similar hydrological characteristics.

In addition to the spatial resolution, models can be also classified according to their temporal regime. It is differentiated between event based or continuous time application.

Hydrological modelling concept for this study

According to Rosbjerg and Madsen (2005), the actual purpose of the modelling is governing the selection of a modelling concept (appropriate modelling). Furthermore, data availability determines the appropriate modelling concept. The purpose of this setup is to support stakeholders and water management authorities in their decisions, like operational irrigation, water supply, or running hydro-power strategies. Therefore, basin-wide, near real time and distributed estimations of the terrestrial water balance are required. In particular in poorly gauged regions where, due to lack of sufficient and current hydro-meteorological observation data, this information cannot be obtained from measurements. A model based water balance monitoring system may overcome this frequently encountered problem. The quantification of spatial and temporal changes of water balance variables requires a distributed hydrological model. The quantification of all relevant water balance variables excludes empirical models, which describe e.g. the rainfall-runoff relationship as a linear transformation of effective rainfall into runoff (unit hydrograph model). Furthermore, empirical models require long and continuous historical records, which are usually not available in poorly gauged regions (Abbott et al., 1986). Compared to empirical models, physically based models require geo-hydrological, soil physical, and vegetation dynamical input data, which leads to increased uncertainties in case of sparse data sources.

Providing basin-wide, near real time and distributed estimations of the terrestrial water balance and advancing the scientific understanding of the hydrological cycle inclusive atmosphere leads to the selection of a distributed, physically based hydrological modelling concept. Furthermore, the impact of vegetation dynamics on hydrological simulations is investigated applying this setup. In this case, satellite derived, instead of tabulated standard literature land surface data, (for example albedo and lead area index LAI) are incorporated into the modelling process (see Section 6). This investigation requires a distributed, physically based hydrological modelling concept, like it is used in the Water Balance Simulation Model *WaSiM*.

3.2.2 Water balance simulation model WaSiM-ETH

WaSiM (Schulla and Jasper, 2000) is a deterministic, fully distributed, modular model for the simulation of the terrestrial water balance using physically based algorithms for the vertical fluxes and lateral groundwater fluxes. Other lateral fluxes like surface runoff and interflow are treated in a lumped manner. *WaSiM* has been developed and primarily applied in small to mesoscale alpine catchments for impact studies of climate or land use change on the terrestrial water balance, and for flood forecasting (Schulla and Jasper, 2000; Kleinn, 2002; Kunstmann et al., 2004; Marx, 2007). The application of *WaSiM* range from event-based to continuous simulations. However, *WaSiM* was not used so far in a semi-arid environment, which requires adaptations concerning the climatic conditions, and the flat topography in the Volta basin. The setup of *WaSiM* for the Volta region was performed in collaboration with Jung (2006) on two scales: the Volta basin (Jung, 2006) and the White Volta basin (Wagner et al., 2006). In the following section the most important components of the hydrological model *WaSiM* and the required adaptations for this study are described, following Schulla and Jasper (2000).

Preprocessing: The topographical analysis (*Tanalys*) derives exposition, slope, flow net structure, flow directions, flow times, and sub catchment boundaries from the digital elevation model (*DEM*).

Interpolation of the meteorological input data: Hydrological models generally require precipitation, temperature, humidity, wind speed, and solar radiation data as the driving meteorological information. Usually this information is available as station data. Consequently, these point measurements have to be interpolated to the predefined regular grid. Applying gridded meteorological data sources, e.g. results of a meteorological model, also require an interpolation to the predefined regular grid. *WaSiM* provides the following interpolation techniques for the calculation of areal precipitation:

- *Inverse distance weighting (IDW) interpolation:* For this interpolation method all stations within a specified search radius are used for the in-

terpolation. Weights are calculated depending on the distances between the location requiring an estimate and the locations of the observations (see Equation 7.1).

- *Thiessen polygon:* Thiessen polygon is a special case of *IDW*, which considers only the nearest observation station per grid point.

- *Altitude-dependent regression:* In mountainous catchments some meteorological parameters, e.g. wind speed and temperature, have a stronger vertical than horizontal dependency. The altitude dependency is calculated by linear regression. For variables with horizontal and altitude dependency a combination of *IDW* and altitude-dependent regression can be selected.

- *Bilinear interpolation:* Applying gridded meteorological data sources, e.g. results of a meteorological model, the bilinear interpolation method is less time consuming and effective.

For this study, externally generated meteorological fields, e.g. results from the meteorological simulations, or geostatistical interpolations and simulations are imported and bilinearly interpolated to the resolution of the predefined grid.

Radiation and temperature adjustment: A radiation and temperature adjustment is required to compensate shadowing effects in mountainous regions. These effects influence the incoming shortwave radiation (Geiger et al., 1987). As sensible heat flux and therefore temperature depend on incoming shortwave radiation, temperatures are also influenced by the shadowing effects. The adjustment of temperature and radiation due to shadowing effects follows an approach by Oke (1987), which calculates a correction factor depending on sunshine duration, incident and zenith angle, and an empirical factor considering diffuse short wave radiation. This correction factor is applied for radiation and temperature.

Potential and actual evapotranspiration: Potential evaporation is calculated using an approach by Penman-Monteith (Monteith, 1975; Brutsaert, 1982), which is described in detail in Chapter 6. Using this approach, additional to meteorological variables, the most important plant properties are taken into consideration, e.g. stomata resistance, root density distribution and depth, leaf area index *LAI*, effective vegetation height and vegetation coverage. The temporal development of plant properties within a year can be considered. To determine real evapotranspiration, the first step is to reduce potential evaporation by the amount of water equal to interception storage. Then, considering soil and plant physiological properties, a further reduction of potential evaporation is performed dependent on the actual suction of the soil. However,

WaSiM does not solve the heat flux balance in the soil. Soil heat flux is considered as constant fraction (10%) of net incoming radiation. Furthermore, the full energy balance at the land surface is not solved.

Interception: For the storage of precipitation on vegetation and ground level a simple bucket approach is used with a capacity depending on the leaf area index *LAI*, the vegetation coverage degree, and the maximum height of the water on the leafs. The extraction of water out of the interception storage by evaporation is assumed to be at a potential rate. If the interception storage is filled, further precipitation will fall directly to the soil surface.

Infiltration and generation of surface runoff: The infiltration model is an integrated part of the soil model. Running *WaSiM* with *Richards*-equation for the unsaturated zone, infiltration is considered in the calculation of the *Richards*-equation. Surface runoff is generated if precipitation intensities are larger than the actual hydraulic conductivity of the soil (Schulla, 2006).

Unsaturated zone: Applying *WaSiM* with *Richards*-equation for the unsaturated zone (Richards, 1931) the vertical fluxes in the unsaturated zone are modelled as follows:

$$\frac{\partial \Theta}{\partial t} = \frac{\partial q}{\partial z} = \frac{\partial}{\partial z}\left(-k(\Theta)\frac{\partial \Psi(\Theta)}{\partial z}\right) \tag{3.1}$$

with	Θ	$[m^3/m^3]$	water content
	t	$[s]$	time
	k	$[m/s]$	hydraulic conductivity
	Ψ	$[m]$	hydraulic head as sum of the suction ψ and geodetic altitude
	q	$[m/s]$	specific flux
	z	$[m]$	vertical coordinate

WaSiM calculates the *Richards*-equation in the spatially and temporally discretized form for each grid cell. Hydraulic conductivity and hydraulic head, which are functions of the water content, are parametrized through an approach by Van Genuchten (1976). Through the introduction of a recession constant k_{rec} for describing the recession of the saturated hydraulic conductivity k_s with depth z

$$k_{s,z} = k_s \cdot k_{rec}^z \tag{3.2}$$

the generation of interflow q_{ifl} for soil layer m

$$q_{ifl} = k_s(\Theta_m) \cdot \Delta z \cdot d_r \cdot tan\beta \tag{3.3}$$

is enabled with the drainage density d_r, which is a scaling parameter to consider river density. β is the local slope angle. Groundwater recharge in *WaSiM* is defined as the remaining vertically percolating water.

Using the *Richards*-equation it is assumed that matrix flow dominates macropore flow. The *Richards*-equation is interpreted as a combination of mass balance and *Darcy* equation, due to the fact that a horizontal resolution of 1 km is much larger than the original lab scale. Hence, the corresponding parameters are not fully comparable to laboratory ones. In addition, they consider natural heterogeneities within the horizontal resolution and therefore must be interpreted as effective lumped parameters.

Saturated zone: A horizontally two-dimensional groundwater model is coupled to the unsaturated zone. The unsaturated zone module calculates the flux between unsaturated zone and groundwater. With these boundary fluxes the lateral fluxes are calculated using the groundwater model, which is based on the mass balance equation and Darcy's law. Interactions between surface water and subsurface water are simulated using the leakage principle. Therefore, baseflow, which is the portion of river discharge derived from groundwater, can only be generated when groundwater levels reach the river bed or lake bottom level. Re-infiltration of surface water into groundwater occurs if groundwater drops below river water level. This is an advantage when simulating the hydrology of semi-arid regions.

Discharge routing: Direct runoff and interflow are routed to the subcatchment outlet by subdividing the catchment into flow time zones which are calculated with the preprocessor *Tanalys*. Discharge routing in the river bed channel is performed by a kinematic wave approach using different flow velocities for different water levels in the channel. After the translation of the wave, a single linear storage is applied accounting for diffusion and retention (see Equation 5.2). Finally, discharges from different subbasins are superposed.

3.2.3 Setup of WaSiM for the White Volta basin

In this section the setup of the hydrological model *WaSiM* for the application in the White Volta basin is described. As already mentioned in Section 3.2.2, *WaSiM* was so far not used in a semi-arid environment. This requires additional to the calibration, adaptations concerning the climatic conditions and the flat topography in the Volta basin (see Figure 3.2(a)).

Temporal resolution: The temporal resolution is restricted to the availability of measurement data during the calibration period. Due to the fact that only daily observation data are available, a time step of 24 hours is selected. Due to the large catchment size and long flow time zones, a daily time step is adequate.

Spatial resolution: The spatial resolution used in this study is 1 x 1 km^2, which results in a regular grid of 411 x 631 grid points for the White Volta basin.

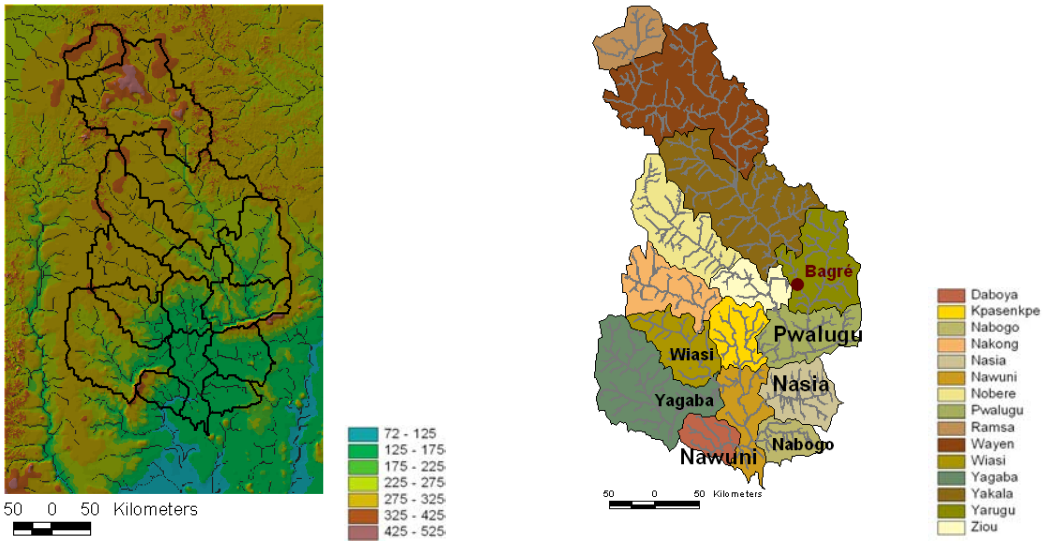

(a) DEM (b) subcatchments

Figure 3.2: *WaSiM* setup: digital elevation model [m], derived river network and the boundaries of the White Volta basin and its subcatchments

Subcatchments: The White Volta catchment is subdivided into 15 subcatchments. The outlets of the subcatchments are located at past, present, and planned, future hydrological stations, so that simulated discharges can be compared to available measurements. In this study only observation data at 6 river gauges are available. However, the setup contains all possible gauges if more data, in particular discharge data from Burkina Faso, become available. Furthermore, the subdivision into several subcatchments allows investigations of the differences which occur within the basin. The outlet of the model setup is not Lake Volta but the station Nawuni. This is due to backwater effects from Lake Volta into the White Volta, which cannot be calculated by the model. Figure 3.2(b) depicts the White Volta catchment with all 15 subcatchments and the names and locations of the stations with observation data for this study.

Land use: Land use data (see Figure 3.3(a)) are derived from project partners (Vescovi, 2001). With the land use grid, regular grids of tabulated albedo, surface resistance, *LAI*, vegetation height, and covering degree, as well as root depth values are generated. The tabulated parameters are obtained from Grell et al. (1995) and Schulla and Jasper (2000). *WaSiM* allows, except for albedo, to consider the phenological development within a year by introducing seasons. The definition of "season" in Europe does not hold for the White Volta basin, where only two main seasons can be distinguished: a rainy season (approximately May-October) and a dry season (approximately November-April). Therefore, the number of seasons is reduced to two.

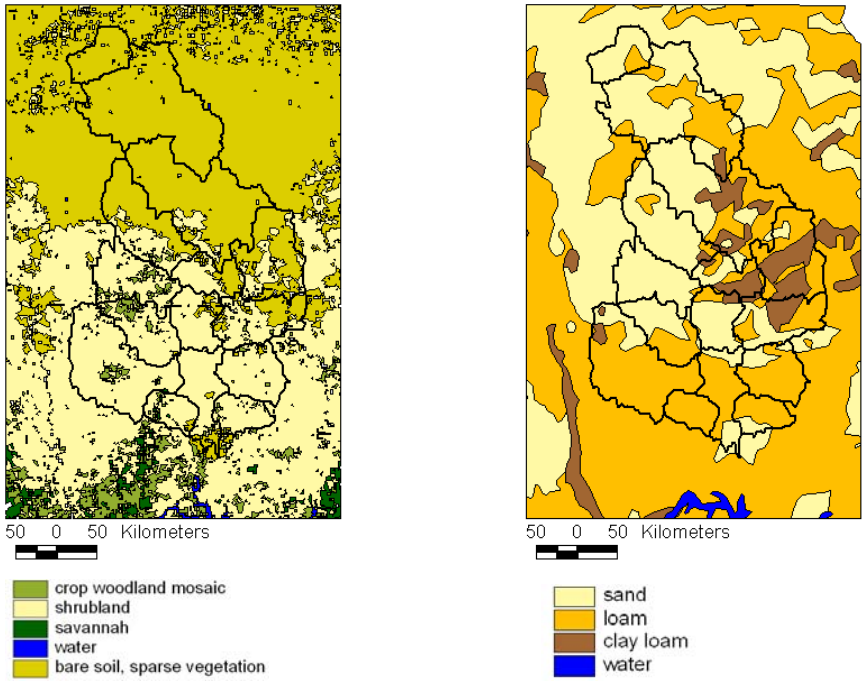

(a) Land use (b) Soil

Figure 3.3: *WaSiM* setup: Land use and soil texture discretization for the White Volta basin

Soil: Soil texture (see Figure 3.3(b)) is derived from the global *FAO* (United Nations Food and Agriculture Organization) soil map (FAO, 1971-81). The van Genuchten parameters for tropical soils are derived from Hodnet and Tomasella (2002). The remaining soil hydraulic properties are either derived from Maidment (1993), or Schulla and Jasper (2000). With the soil grid, regular grids of tabulated wilting points and saturation soil moistures, saturated hydraulic conductivities, van Genuchten parameters, recession constants k_{rec}, fillable porosities, as well as the number and thickness of soil layers are generated. Vertically, the soil is represented by 20 equidistant layers of 1 m thickness each.

Hydrogeology: Applying *WaSiM* with the groundwater model requires hydrogeological information. A hydrogeological grid is derived from Martin and van de Giesen (2005). This grid is based on various hydrogeological maps and sources of information from Ghana and Burkina Faso. Information on horizontal hydraulic conductivities, storage coefficients, and aquifer thickness are classified for each hydrogeological unit. The values of hydraulic conductivities, as well as the aquifer thicknesses, are provided by Martin and van de Giesen (2005). Storage coefficients values are taken from standard literature (Maidment, 1993). These values are implemented in *WaSiM* as regular grids.

River network properties: To account for the extremely flat terrain in the White Volta Basin, with a slope of less than 0.1% in the southern part, a few modifications are required for the preprocessing tool *Tanalys*. The minimum slope is set to 0.0001 instead of 0.001 and the minimum flow velocity is reduced from 0.1 to 0.01 m/s. Without these modifications, the slopes of several subcatchments reach the originally minimum value of 0.1 m/s, which leads to shorter flow times in these subcatchments and finally to time shifts in the discharge curves. Furthermore, the Manning-roughness parameter for surface runoff of M=10 $m^{1/3}s^{-1}$ is changed to M=5 $m^{1/3}s^{-1}$ following Maidment (1993). Additionally, *WaSiM* has a default ratio of channel width to channel depth of 1/10, which is typical for mountainous catchment. With this ratio however, the river depths in the White Volta basin are too high. Therefore, this ratio has to be smaller. A value of 1/30, based on personal, on-site estimations, is chosen.

Meteorological input data: The required meteorological input data come from different sources with different characteristics. Here, the application of meteorological observation data, which are used for calibration and validation of *WaSiM*, is described. Observation data are provided from the meteorological services in Ghana and Burkina Faso for the *GLOWA*-Volta project. As interpolation method for observation data the inverse distance weighting method (IDW) is selected. Due to the flat topography in the catchment and elevation independent vegetation dynamics in the White Volta basin, altitude-dependent regression is not considered in this study.

Anisotropy: To account for the strong latitudinal dependence of precipitation distribution (see Section 2.2), *WaSiM* allows the introduction of an anisotropy factor. With the anisotropy, which is defined as ratio between the main and short axis of an ellipsoid, the weights of observations along the main axis are increased compared to observations along the short axis. Additionally to the ratio, the slope of the main axis against the horizontal can be defined. For the White Volta basin a length ratio of 0.5 between the long and short axis and a slope of zero is selected. The introduction of anisotropy is very important for the application in the White Volta basin due to the following reason. In data sparse regions, where long distances between observation stations occur, a comparatively large search radius has to be selected to cover each grid point of the catchment. For the White Volta basin, this means that without anisotropy for example for grid points in the drier northern part, observations from the wetter South are considered with the same weights as observations from the North with similar distance and vice versa. Including anisotropy, observations in the same latitudinal range are preferred for the interpolation, which leads to a more realistic areal precipitation field.

Potential evapotranspiration after Penman-Monteith: In *WaSiM*, daily potential evapotranspiration is calculated as the sum of day and night

potential evapotranspiration. This requires the calculation of mean day and mean night temperatures from mean daily temperatures. Therefore, monthly differences between day and night average temperatures referring to sea level are needed, which are in proportion to sunshine duration added for day and subtracted for night potential evapotranspiration. The estimation of the monthly differences between day and night average temperatures (see Table 3.2) was performed for the Volta basin by Jung (2006) based on field measurements from the *GLOWA*-Volta project.

Month	Jan	Feb	Mar	Apr	May	Jun
ΔT_{sea}	3.98	3.77	3.57	3.21	2.43	1.99
Month	Jul	Aug	Sep	Oct	Nov	Dec
ΔT_{sea}	1.60	3.10	2.84	2.30	2.57	3.51

Table 3.2: Monthly differences between day and night average temperatures, referring to sea level, estimated for Volta basin (from Jung, 2006)

Furthermore, Jung estimated the value of a recession constant, which is required for the calculation of monthly differences at specific altitudes with an exponential regression equation, to 625 m compared to 1654 m as *WaSiM* standard value.

3.3 Joint atmospheric-hydrological modelling for the White Volta basin

Joint atmospheric-hydrological simulations are performed in a one-way approach by passing results of a meteorological model as input data to hydrological modelling (see Figure 3.4). Therefore, an interface, which has been developed and applied already at IMK-IFU by Kunstmann et al. (2004) and Jung (2006), is further generalized to export only results of the region of interest.

WaSiM requires the following meteorological input data: precipitation, temperature, horizontal wind velocity, global radiation, and relative humidity, which are generated from the results of the meteorological model *MM5* as follows:

- *MM5* simulates two precipitation components, one for subgrid and one for gridscale precipitation processes, which have to be summed for total precipitation amount.

- *MM5* simulates temperature in 2 m height.

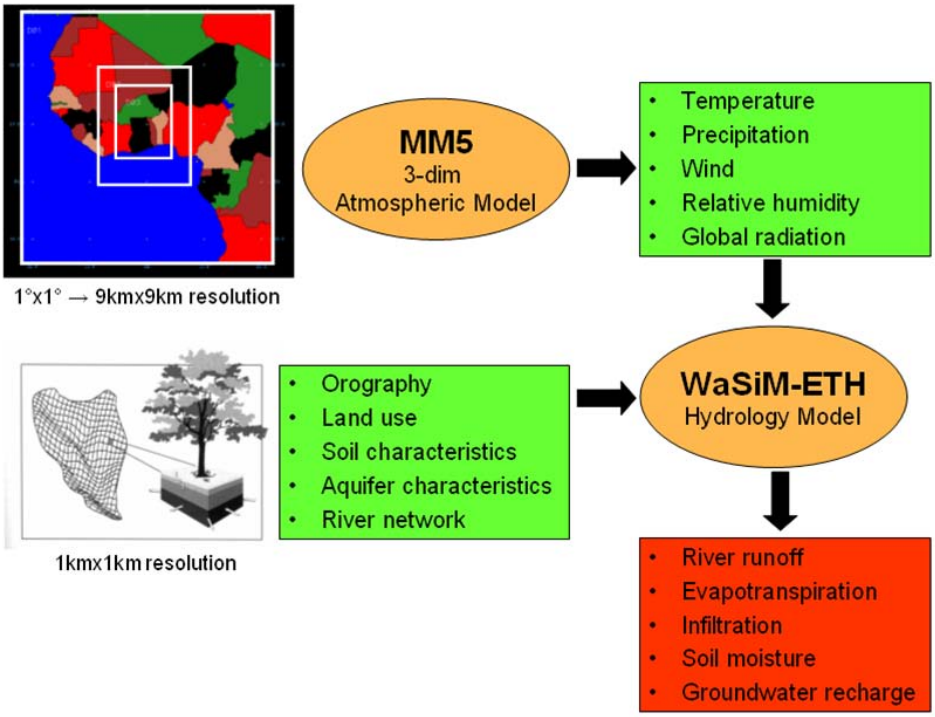

Figure 3.4: Coupling strategy for using atmospheric information in hydrological modelling

- With the horizontal wind vectors $\vec{u}$ and $\vec{w}$ the horizontal wind velocity v_h is calculated by:

$$v_h^2 = \vec{u}^2 + \vec{w}^2$$

- Global radiation is defined in *WaSiM* as shortwave direct and diffuse radiation. Therefore *MM5* shortwave radiation is used.

- The calculation of relative humidity requires the mass mixing ratio of water vapour w_v [kg/kg], temperature T [K] and surface pressure P_a [hPa] (Jacobson, 2005):

$$f_r = 100\% \cdot \frac{w_v}{w_{v,s}} \tag{3.4}$$

with the saturation mass mixing ratio of $w_{v,s}$ [kg/kg]

$$w_{v,s} = \frac{0.622 \cdot P_{v,s}}{P_a - P_{v,s}} \tag{3.5}$$

and the saturation vapour pressure of water over a liquid surface

$$P_{v,s} = 6.112 \cdot exp\left(\frac{17.67 \cdot (T - 273.15)}{T - 29.65}\right) \tag{3.6}$$

In this study, *MM5* output is stored every 3 hours, but the temporal resolution of WaSiM is 24 hours, which requires daily averages for all variables except for rainfall, which requires daily sums. Each grid point of the meteorological model is treated as a "virtual" meteorological station in the hydrological model (see Figure 3.5). Therefore, the results have to be in tabular form with time series for each "virtual" station and each variable. Within the resolutions of the meteorological model, which are 27 x 27 km^2 for domain 2 and 9 x 9 km^2 for domain 3, the meteorological variables are interpolated bilinearily to the 1 x 1 km^2 resolution of the hydrological model.

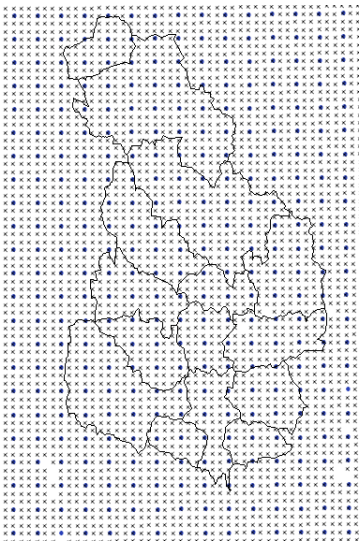

Figure 3.5: Section of virtual meteorological station using *MM5* results of domain 2 (dots) and domain 3 (crosses) for hydrological modelling of the White Volta basin

In cases where both models, *MM5* and *WaSiM* need the same input data (e.g. land use and soil properties) the same data sets are used for both, as far as possible. This includes land use parameters like *LAI*, albedo, etc., as well as soil characteristics like wilting point and saturated soil moisture content. These are taken from the *MM5* land use and soil table if available. In case *WaSiM* needs supplementary parameter inputs, these are derived from literature. Land use data and classification (Vescovi, 2001) are based on the same data source in *WaSiM* and *MM5*.

4 Data basis and field campaign

4.1 Historical hydro-meteorological observations

The calibration and validation process of a hydrological model requires meteorological and hydrological observation data with a long and ideally continuous time series. Thus, historical data records are required for this purpose. The *GLOWA*-Volta project collects historical data from different institutions, for example from the hydrological and meteorological services departments. During my stays in Ghana I collected daily historical meteorological and hydrological data from the respective departments in Ghana. Thus, during phase 2 and 3 of the *GLOWA*-Volta project further data became available allowing long-term 40-year (1961-2000) water balance simulations. Unfortunately, meteorological information from 2001 on are still not available for Burkina Faso to continue the simulations up to the present moment.

The available historical data record consists of approximately 40 precipitation stations between 1961 and 1984 and 17 stations between 1985 and 2001 within the rectangle applied for the simulation of the White Volta catchment (see Figure 3.2). In Figure 4.1 the mean number of available precipitation observations per year are shown. The break between 1985 and 1986 is due to an abrupt decrease in observation data in Burkina Faso. Thus, data for approximately one precipitation station per 6000 km^2 between 1961 and 1984 and one station per 15000 km^2 between 1985 and 2001 are available. The number of stations providing the further required meteorological data like temperature, wind speed, humidity, is by far smaller, in general less than 10. Discharge measurements for

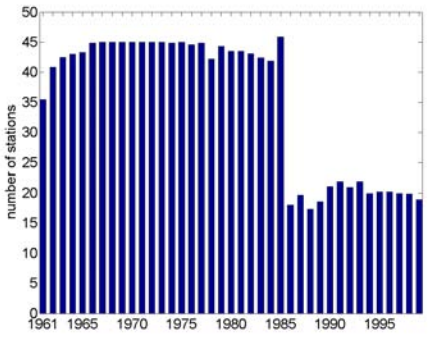

Figure 4.1: Mean number of available precipitation stations per year for the White Volta basin

the White Volta basin are only available for stations in Ghana. Additionally to the two main stations along the White Volta, Pwalugu and Nawuni, discharge measurements of two source basins; Nasia and Nabogo, which are all shown in Figure 3.2(b), are partially available. For all four stations the time series are never complete. For Nawuni data gaps are short, but for other stations gaps up to ten years between 1975 and 1985 occur (see black stars in Figure 5.13).

4.2 Current hydro-meteorological observations

The years 2004 and 2005 are selected for current hydrological simulations. For these two years different meteorological input data sources are applied, whose time of availability differ. As already mentioned in Chapter 1 this work investigates in particular the current water resources and fluxes.

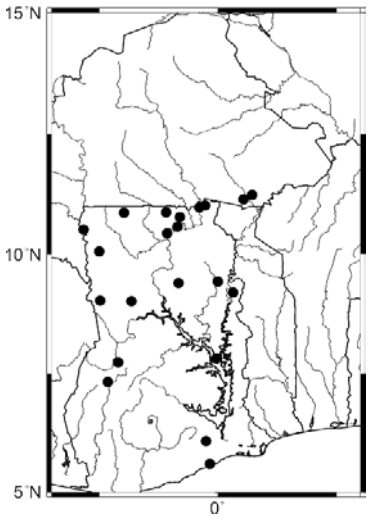

Figure 4.2: Location of available station data in Ghana and Burkina Faso

The first meteorological data source are observation data. For 2004 and 2005 data from synoptical stations are available only for Ghana and the South of Burkina Faso (see Figure 4.2). The data sources are the meteorological services department in Ghana and *GLOWA*-Volta stations. However, in regions with weak infrastructure observation data are only available with a considerable temporal delay. In particular if no automatic data recorders are used, the delay can increase up to one year or more until the data are collected, digitized, and become available to the public. Therefore, these station data are unsuitable for specific questions in water resources management, where basin-wide and near real time, as well as short term monitoring, is required. Thus, additional to observation data other meteorological data sources have to be chosen.

For near real time hydrological simulations the output of a meteorological model is required. Using this setup, water balance estimations are available

within two days. Results of the joint atmospheric-hydrological simulations are shown in Section 5.3. This method requires substantial CPU and storage capacities as well as meteorological expertise which may be a limitation in the application in developing countries.

Because of the limitations of the first two data sources, a product of the Tropical Rainfall Measuring Mission (*TRMM*) is chosen as third meteorological data source. The *TRMM* product 3B42, which is described in the following section, is available with approximately one month delay.

4.3 The TRMM product 3B42

TRMM is a joint mission between *NASA* and the Japan Aerospace Exploration Agency (*JAXA*), dedicated to measure tropical and subtropical rainfall through microwave and visible infrared sensors. It includes space-borne rain radar. Since August 2001 the average operating altitude for *TRMM* is 403 km. In this study the *TRMM* product 3B42 (V6) - TRMM Merged high quality HQ / infrared (*IR*) Precipitation - is used (http://trmm.gsfc.nasa.gov/3b42.html; Huffman et al., 1995). These gridded estimates of precipitation are on a 3 hour temporal resolution and a 0.25° by 0.25° spatial resolution in a global belt extending from 50° South to 50° North latitude. The 3B42 estimates are available in real time *RT* and with a temporal delay of a month and a few days. The real time product 3B42-RT is produced by a combination of the microwave and IR estimates. In a second step these estimates are scaled to match the monthly rain gauge analyses used in another *TRMM* product 3B43. The 3B43 product combines the estimates generated by 3B42 and global gridded rain gauge data from the Climate Assessment and Monitoring System (*CAMS*), produced by NOAA's Climate Prediction Centre and/or global rain gauge product, produced by the Global Precipitation Climatology Centre (*GPCC*). The output is rainfall for 0.25° x 0.25° grid boxes for each month. The scaling of the 3 hour product 3B42 to match the monthly rain gauge analyses product leads to a delay of at least one month until this product is available. Additionally to the delay, the *TRMM* products only provide precipitation data for the hydrological simulations, and not all required meteorological fields.

Besides using the *TRMM* products as precipitation input for hydrological modelling, the data set can be used as basis for validation purposes of the meteorological simulations, especially for the spatial distribution.

4.4 Hydro-meteorological field campaign

Within the *GLOWA*-Volta intensified measurements and surveys of all disciplines are carried out in the Upper East Region in the North of Ghana. To refine

the hydro-meteorological data in the Upper East region, water level and precipitation gauges have been installed during my two field campaigns in 2004 and 2005 in close collaboration with the hydrological services department (*HSD*). Furthermore, rating curves for the determination of river discharge from the water level measurements are performed for new and updated for existing gauges from the *HSD*. At two gauges along the White Volta in Yarugu and Pwalugu, *HydroArgos* systems are installed for water level measurements, which allow online monitoring of the water level due to a daily transmission via satellite. In particular for the station Yarugu the online monitoring will be required for near real time water balance simulations, because Yarugu is the first gauge downstream of the Bagré dam and as long as dam management and outflow data are not available, simulation results have to be replaced by measured ones at Yarugu. The field campaign leads to the higher density of observation stations in the North of Ghana in Figure 4.2. As an example of the field campaign, measured water levels in Yarugu are shown in Figure 4.3 for 2004 until 2007. The figure shows that since the beginning of the field campaign in May 2004

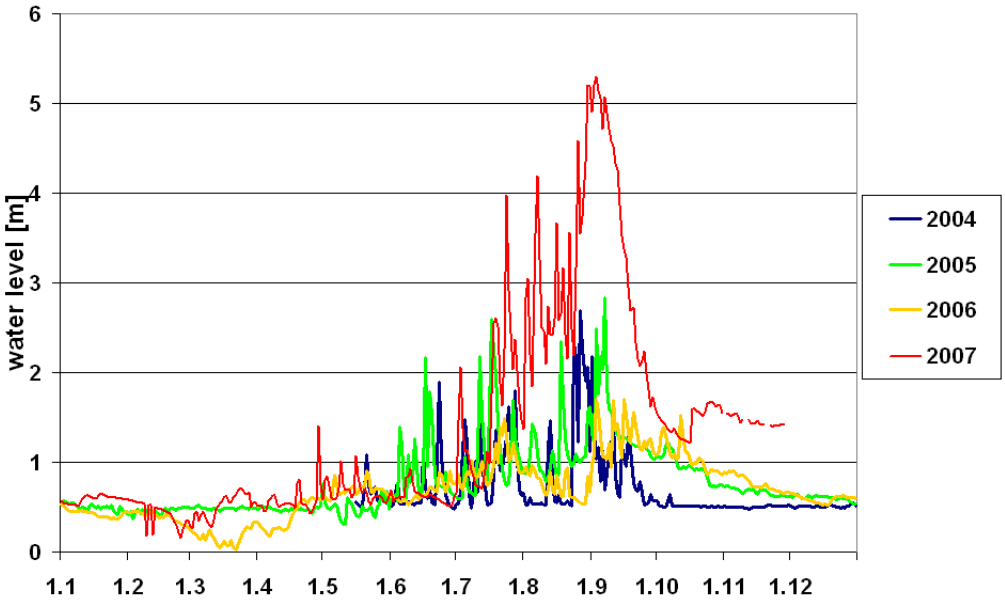

Figure 4.3: Measured water level [m] at Yarugu from 2004 until 2007

almost continuous measurements of the water level at Yarugu are available. The parallel use of the Hydro Argos and another pressure sensor with a data logger allows to bridge time gaps of failure of one of the two systems. For control purposes, the water level is additionally read manually three times per day.

The water level time series show a high inter-annual variability. For 2006, the water level at Yarugu and Lake Volta was so low that hydro-power generation

had to be reduced, which lead to daily shut-downs of power in Ghana. In 2007, West Africa and in particular Ghana was affected by severe floods. In Ghana 20 people died. In total more than 400 million people were affected by the floods. Furthermore, most of the crops were lost and fertile farmland was washed away.

5 Performance of meteorological, hydrological and joint modelling

In the first section of this chapter, results of meteorological simulations are discussed and compared to observations, and the *TRMM* product 3B42, which has been introduced in Section 4.3. In Section 5.2 the hydrological model *WaSiM* is calibrated and validated for the White Volta basin with historical station data as meteorological input. Furthermore, long-term (1961-2000) hydrological simulations are performed. In Section 5.3, joint atmospheric-hydrological simulations are performed and compared to hydrological simulations driven by *TRMM* and station data.

5.1 Performance of meteorological simulations

When near real time estimations of the terrestrial water balance are required, the output of a regional meteorological model is often the only possible data source, in particular in poorly gauged basins where no automatic data recorders with online transmission are available. For the meteorological simulations, the mesoscale meteorological model *MM5* (Grell et al., 1995) is applied in non-hydrostatic mode to dynamically downscale the global atmospheric fields stepwise using three domains with horizontal resolutions of 81 x 81 km^2 (61 x 61 grid points), 27 x 27 km^2 (85 x 67 grid points) and 9 x 9 km^2 (157 x 121 grid points). The *MM5* setup is described in detail in Section 3.1.2.

Meteorological simulations are performed for 2004 and 2005 in the ex-post hindcasting mode. This means that, although past years are simulated, only information is applied, which is available at real time. Thus, this setup can be transferred in operational mode, which finally allows simulation of the terrestrial water balance in near real time. For 2004 and 2005 the performance of near real time *MM5* simulations for the Volta basin is investigated.

Four dimensional data assimilation: FDDA

For 2004, the meteorological simulations are performed with and without FDDA to analyse the influence of running the model with forcing terms that nudge it towards the observations. Observations (available radiosonde data) are incorporated only in domain 1. Through the one-way nesting approach however, this information is passed on to the following domains. Figure 5.1 shows the spatial distribution of annual precipitation for 2004 for all three domains

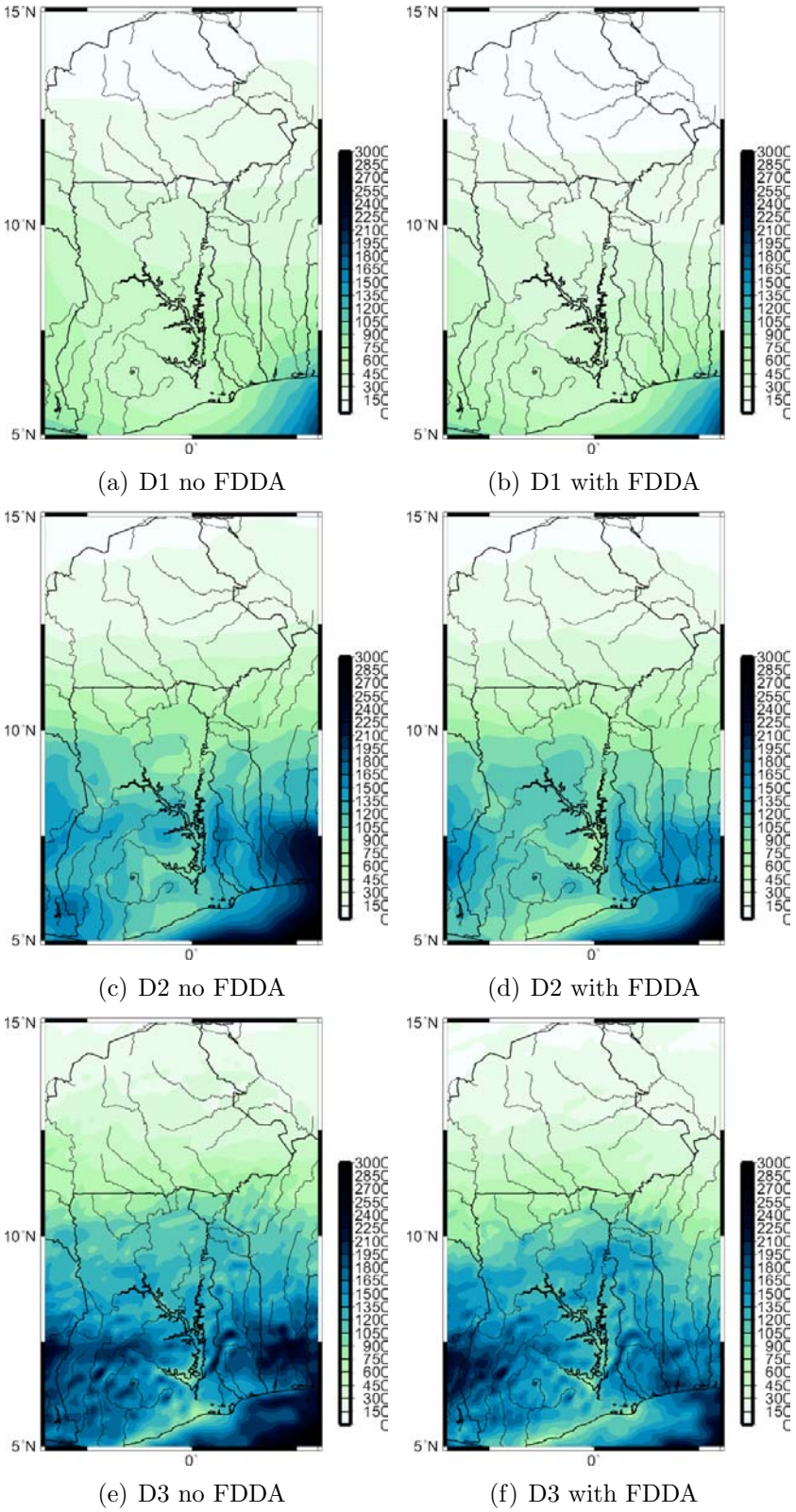

(a) D1 no FDDA (b) D1 with FDDA

(c) D2 no FDDA (d) D2 with FDDA

(e) D3 no FDDA (f) D3 with FDDA

Figure 5.1: Simulated annual precipitation for 2004 [mm] for the Volta basin; *MM5* results of (a) D1 no FDDA, (b) D1 FDDA, (c) D2 no FDDA, (d) D2 FDDA, (e) D3 no FDDA, (f) D3 FDDA

without and with the incorporation of radiosonde observations via FDDA in domain 1. The precipitation distribution shows a North-South gradient in all domains with increasing magnitude in higher domains. The simulation results of domain 2 and 3 show higher annual sums compared to the results of domain 1. The general spatial distributions of annual precipitation in domain 2 and domain 3 are comparable with the strong North-South gradient and an additional minimum along the shore South of Lake Volta. Compared to the results of domain 2, the patterns are refined in domain 3. In general, the patterns of domain 2 and domain 3 are in good agreement with the results of ORSTOM (1996). The simulation results show the importance of the downscaling process, especially in regions with predominantly convective precipitation, like in the Volta basin where convective precipitation accounts for approximately 80% of the total amount. Compared to the differences between the domains, the effect of incorporating radiosonde information is minor but present. In general, for all three domains the annual precipitation sums are slightly lower over the complete area using FDDA. The patterns remain almost the same. In the following, this work focuses on simulation results with incorporation of radiosonde observations via FDDA, because (1) this information is available at real time and free of charge, and (2) it supports the meteorological simulations with observations.

Validation of meteorological simulations

For validation of the meteorological simulations scatter plots of the monthly precipitation amounts for domain 2 and domain 3 versus the observed monthly sums at 22 available stations (see Figure 4.2) are shown in Figure 5.2. The

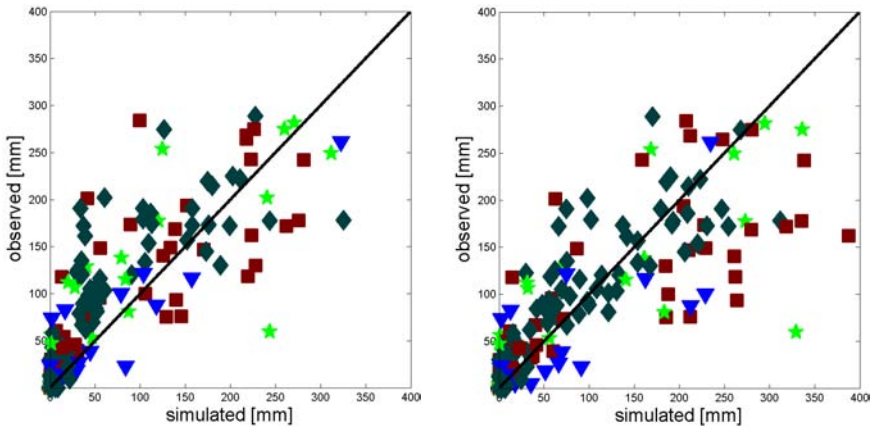

(a) D2 (b) D3

Figure 5.2: Scatter plots of simulated vs. observed monthly precipitation for 2004. The 22 stations are subdivided into 4 regions: the coast (blue triangles), between latitude 7.5° and 8° (green stars), North of Lake Volta between latitude 8.5° and 9.5° (brown squares) and North Ghana together with South Burkina Faso between latitude 10.0° and 11.5° (grey diamonds)

22 stations are subdivided into 4 regions: the coast, between latitude 7.5° and 8°, North of Lake Volta between latitude 8.5° and 9.5°, and North Ghana together with South Burkina Faso between latitude 10.0° and 11.5°. For the calculation of the simulated precipitation at each station, the results of four neighbouring grid points are interpolated using the inverse distance weighting method. The scatter plots of domain 2 and domain 3 in Figure 5.2 show a fairly good agreement with partly under- and overestimations of the monthly precipitation sums. Compared to domain 2, domain 3 tends toward slightly higher values. Additionally to the scatter plots, coefficients of determination R^2, which are defined as square of Pearson correlation coefficient

$$R^2 = \frac{COV(X,Y)^2}{VAR(X) \cdot VAR(Y)} \tag{5.1}$$

between simulated and measured monthly precipitation amounts, are calculated. In Table 5.1, the mean and range of R^2 is given for all four regions

	$\mathbf{R^2}$			
	D2 FDDA		**D3 FDDA**	
Latitude	**mean**	**range**	**mean**	**range**
10.0° - 11.5°	0.75	0.52 - 0.92	0.83	0.58 - 0.98
8.5° - 9.5°	0.72	0.51 - 0.95	0.68	0.44 - 0.89
7.5° - 8.0°	0.71	0.46 - 0.85	0.69	0.44 - 0.82
5.5° - 6.5°	0.83	0.75 - 0.92	0.74	0.56 - 0.92

Table 5.1: Mean and range (of stations) of coefficients of determination (R^2) for the *MM5* results subdivided into 4 regions for 2004

for 2004. The R^2-values indicate a better simulation result for domain 3 in the northernmost region, but for the remaining area domain 2 provides better performance. The results, which are shown in this section, are based on the four neighbouring grid points of each observation and on aggregated monthly sums. As a general remark, correlation and validation results depend on the selected spatial and temporal scale.

For the investigation of the performance of *MM5* to represent the annual cycle of precipitation, spatially (22 stations) and monthly averaged simulated values are compared to measured ones for 2004 in Figure 5.3. Additionally to the real time simulation results (*MM5* D2 and *MM5* D3), modified *MM5* results, which are scaled with gridded observations on a monthly scale (see Section 5.1.2), are added (*MM5* D2 sc and *MM5* D3 sc). The results in Figure 5.3 indicate a good and sufficient accuracy of the *MM5* simulation results to represent the annual cycle of precipitation. In general, the higher resolution of domain 3 leads to larger monthly precipitation sums. Furthermore, the scaled *MM5* products improve the representation of the annual cycle of precipitation.

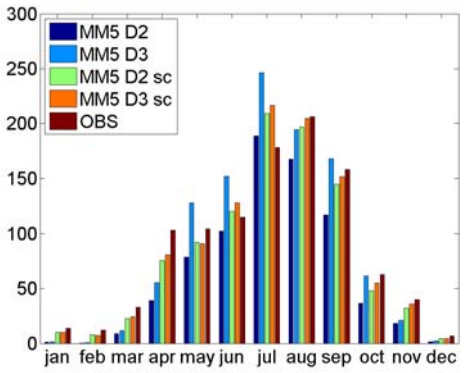

Figure 5.3: Spatially (22 stations) and monthly averaged simulated vs. observed precipitation for 2004; *MM5* simulation results are shown for domain 2 and domain 3 (real time and scaled)

It is worth mentioning that for the comparison of simulation results derived from meteorological models with point measurements (stations), it has to be considered that models are only able to simulate precipitation averages on a scale that is two to four times the model's resolution (Pielke, 2002). Furthermore, a spatial and/or temporal displacement in rainfall predictions is very probable in meteorological simulations. This is particularly relevant for regions with a high spatial variability such as the Volta catchment. Therefore, the performance of the meteorological simulations is satisfying.

Performance and validation of meteorological simulations for 2005

With respect to the above mentioned results, the meteorological simulations for 2005 are performed only with *FDDA*. Figure 5.4(a) and (b) show the spatial distribution of annual precipitation for 2005 for domain 2 and domain 3. For both domains the distribution shows a North-South gradient, except for the region along the coast, known as the Togo gap. Compared to the simulation results for 2004, the patterns are similar in the northern part with slightly higher amounts for 2005. In the southern part, in particular along the eastern and western boundaries, lower amounts are simulated for 2005. Scatter plots of monthly precipitation amounts versus available measurements are depicted in Figure 5.4(c) and (d). For 2005, only 16 observation stations in Ghana are available for validation. Compared to the scatter plots for 2004, the *MM5* simulation results for 2005 tend toward overestimating observed values. The corresponding mean and range of R^2-values are given in Table 5.2. The results for domain 2 are, except for the region between latitude 7.5° and 8.0°, better than for domain 3. Compared to the results for 2004 the R^2-values increase for both domains for the region between latitude 7.5° and 8.0°, whereas for the northernmost region the R^2-values increase for domain 2, but decrease for domain 3.

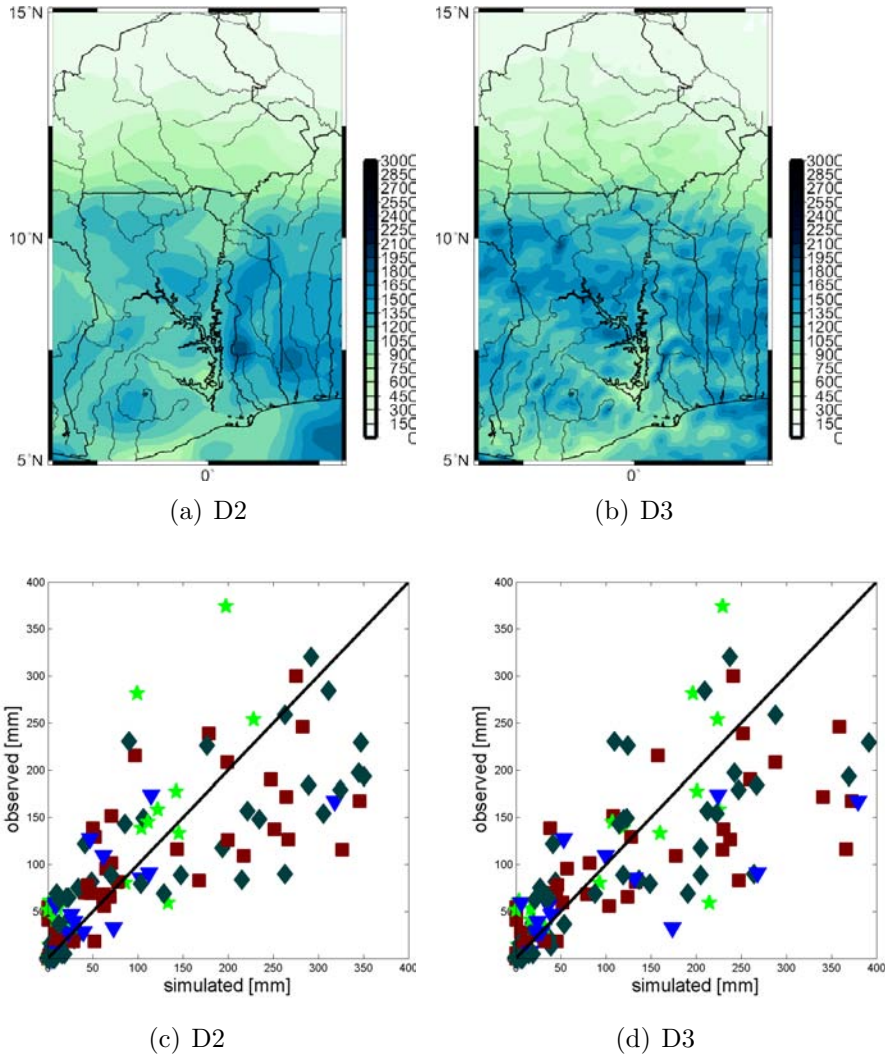

(a) D2 (b) D3

(c) D2 (d) D3

Figure 5.4: Simulated annual precipitation for 2005 [mm]: (a) D2 FDDA, (b) D3 FDDA; scatter plots simulated vs. observed monthly precipitation for (c) D2 FDDA, and (d) D3 FDDA. The 16 stations are subdivided into 4 regions: the coast (blue triangles), between latitude 7.5° and 8° (green stars), North of Lake Volta between latitude 8.5° and 9.5° (brown squares) and North Ghana together with South Burkina Faso between latitude 10.0° and 11.5° (grey diamonds)

For the investigation of the performance of *MM5* to represent the annual cycle of precipitation for 2005, spatially (16 stations) and monthly averaged simulated values are compared to measured ones in Figure 5.5. As already indicated in the scatter plots in Figure 5.4, the real time simulation results (*MM5* D2 and *MM5* D3) overestimate the observations in the rain intensive months June to August. For this period, the scaled MM5 products improve the monthly values considerable. For the remaining months *MM5* is able to

	R^2			
	D2 FDDA		D3 FDDA	
Latitude	**mean**	**range**	**mean**	**range**
10.0° - 11.5°	0.80	0.66 - 0.92	0.75	0.50 - 0.95
8.5° - 9.5°	0.74	0.44 - 0.93	0.70	0.51 - 0.94
7.5° - 8.0°	0.82	0.59 - 0.99	0.84	0.63 - 0.99
5.5° - 6.5°	0.74	0.58 - 0.90	0.70	0.50 - 0.90

Table 5.2: Mean and range (of stations) of coefficients of determination (R^2) for the *MM5* results subdivided into 4 regions for 2005

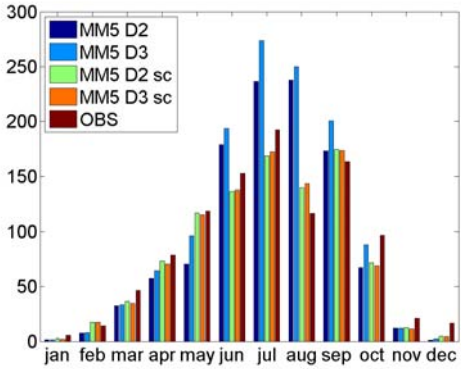

Figure 5.5: Spatially (16 stations) and monthly averaged simulated vs. observed precipitation for 2005; *MM5* simulation results are shown for domain 2 and domain 3 (real time and scaled)

represent the seasonal development of precipitation. The higher resolution of domain 3 leads again to larger monthly precipitation sums.

5.1.1 Performance of the real time and scaled TRMM product 3B42

According to the results of meteorological simulations, the spatial distribution of annual precipitation (see Figure 5.6), as well as scatter plots and R^2-values of monthly precipitation amounts (see Figure 5.7), are presented for both the unscaled *TRMM* product 3B42-RT and for the scaled product, which is available with approximately 1 month delay. The comparison of the spatial distribution of annual precipitation between the unscaled and scaled *TRMM* product shows, in particular for 2004, a large overestimation of the unscaled product. This occurs over the entire section but most notably in the region North of Lake Volta. In general, the spatial distributions of the *TRMM* products (0.25° x 0.25°) are comparable to the *MM5* results of domain 2. They are approximately on the same scale, but North of Lake Volta and in Burkina Faso annual

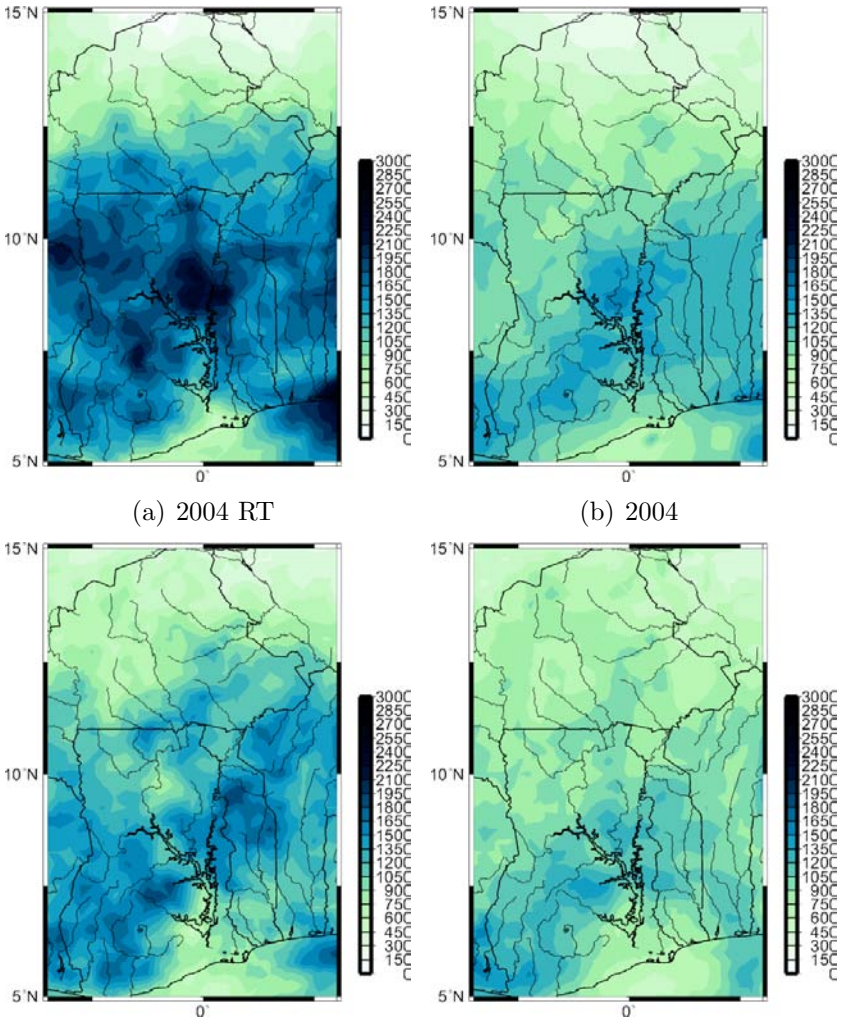

(a) 2004 RT (b) 2004

(c) 2005 RT (d) 2005

Figure 5.6: *TRMM* annual precipitation [mm] available at real time (*RT*) for 2004 (a) and 2005 (c) and as scaled product with one month delay for 2004 (b) and 2005 (d)

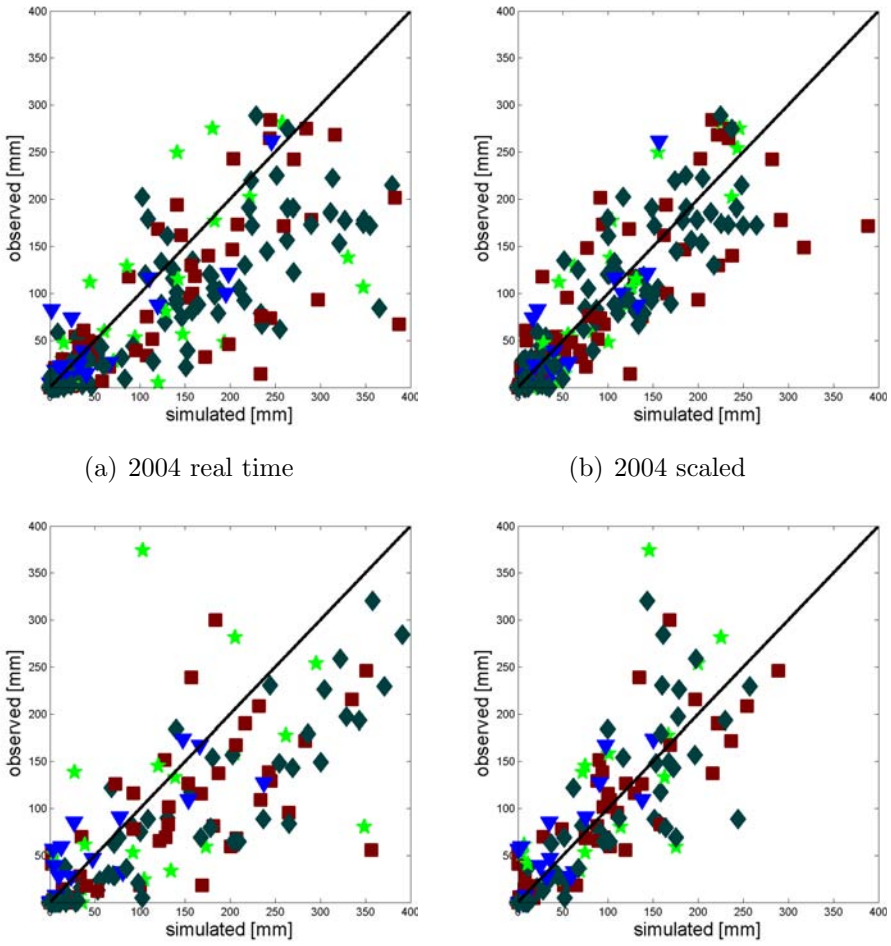

(a) 2004 real time

(b) 2004 scaled

(c) 2005 real time

(d) 2005 scaled

Figure 5.7: Scatter plots of *TRMM* monthly precipitation for 2004 and 2005 available in real time (a), respectively (c), and with one month delay (b), respectively (d). The 22 or 16 stations are subdivided into 4 regions: the coast (blue triangles), between latitude 7.5° and 8° (green stars), North of Lake Volta between latitude 8.5° and 9.5° (brown squares) and North Ghana together with South Burkina Faso between latitude 10.0° and 11.5° (grey diamonds)

(a) 2004

	R^2			
	TRMM RT		**TRMM**	
Latitude	**mean**	**range**	**mean**	**range**
10.0° - 11.5°	0.71	0.22 - 0.97	0.86	0.75 - 0.94
8.5° - 9.5°	0.56	0.36 - 0.83	0.67	0.53 - 0.76
7.5° - 8.0°	0.57	0.21 - 0.86	0.84	0.81 - 0.87
5.5° - 6.5°	0.86	0.84 - 0.88	0.92	0.89 - 0.95

(b) 2005

	R^2			
	TRMM RT		**TRMM**	
Latitude	**mean**	**range**	**mean**	**range**
10.0° - 11.5°	0.86	0.75 - 0.99	0.75	0.57 - 0.86
8.5° - 9.5°	0.60	0.38 - 0.77	0.82	0.71 - 0.88
7.5° - 8.0°	0.51	0.23 - 0.99	0.77	0.59 - 0.99
5.5° - 6.5°	0.80	0.68 - 0.93	0.72	0.55 - 0.88

Table 5.3: Mean and range (of stations) of coefficients of determination (R^2) for *TRMM* results subdivided into 4 regions for 2004 and 2005

precipitation amounts are higher. The scatter plots in Figure 5.7(a) and (c) also indicate this trend of overestimation of the unscaled product in particular for 2004. Scaling improves the results significantly for 2004. For 2005, scaling reduces the number of overestimations, but generates some large underestimations. The R^2 values in Table 5.3 confirm the results from Figure 5.7. For 2004, scaling leads to increased means and decreased ranges of R^2 values. For 2005, the impact of scaling on the R^2 values is ambiguous.

The performance of the unscaled and scaled *TRMM* products to represent the annual cycle of precipitation for 2004 and 2005 is shown in Figure 5.8 on a monthly scale. For both years it is clearly visible that the unscaled *TRMM* product 3B42-RT highly overestimates the measured precipitation sums, in particular between March and July. The performance od the scaled *TRMM* product 3B42 to represent the annual cycle of precipitation is noticeably better for both years.

Furthermore, the application of the unscaled *TRMM* product is discussed in literature as follows: Ebert (2005) found that on a monthly scale, the *TRMM* Multisatellite Precipitation analysis (*TMPA*) performs best in relatively heavy, convective, warm-season regimes, while they perform more poorly in relatively light, cool-season regimes. Moving to shorter time scales (daily/subdaily), the *TMPA* estimates show considerably more uncertainty, in common with other short-interval precipitation estimates (Huffman et al., 2007). They summarize that *TMPA* provides reasonable performance at monthly scales, although

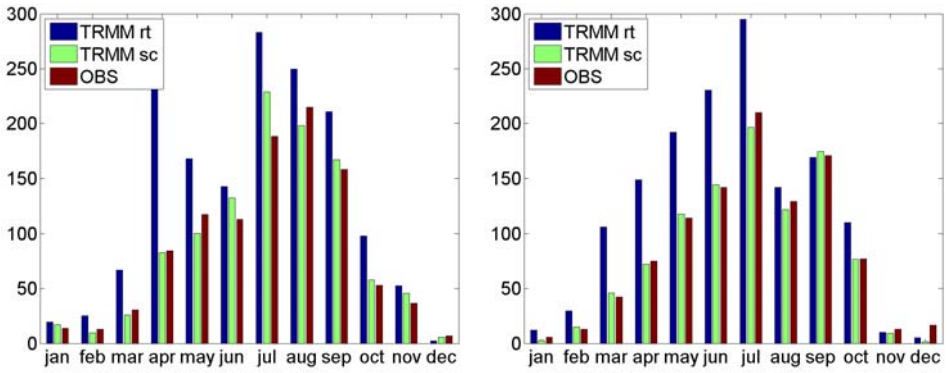

(a) 2004 annual cycle (b) 2005 annual cycle

Figure 5.8: Spatially (22 or 16 stations) and monthly averaged *TRMM* vs. observed precipitation for 2004 and 2005; *TRMM* results are shown for the unscaled, real time (3B42-RT) and scaled (3B42) product

it is shown to have a precipitation rate-dependent low bias. Second, *TMPA* has lower skill in correctly specifying moderate and light event amounts on short time intervals, in common with other finescale estimators.

Due to the results shown in Figure 5.6 and Figure 5.7, as well as the documentations in literature, this study only uses the scaled *TRMM* product 3B42 as meteorological input data source for hydrological modelling, which is available with approximately one month delay.

5.1.2 MM5 results scaled with GPCC

For the purpose of comparison and application in hydrological simulations, the results of the meteorological simulations for domain 2 and domain 3 are scaled similar to the *TRMM* product:

- The global rain gauge product of the Global Precipitation Climatology Centre (*GPCC*) provides global observation data. The data sets are area averaged and time integrated precipitation fields based on surface rain gauge measurements. An interim database of about 6700 meteorological stations is defined. Surface rain gauge based on monthly precipitation data from these stations are analysed over land areas and a gridded data set is created (e.g. Rudolf, 1996) using a spatial objective analysis method. The final product has a spatial resolution of one degree providing monthly gridded area mean rainfall totals. It can be downloaded for example from the *TRMM* Online Visualization and Analysis System (*TOVAS*) (http://disc2.nascom.nasa.gov/Giovanni/tovas).

- Applying these data as a reference source to scale the precipitation results of the meteorological simulations the one degree, gridded data are first

refined to each grid point of domain 2, and domain 3 respectively, using the bilinear interpolation method.

- For each grid point in both domains, scaling factors, defined as the ratio of simulated and *GPCC* precipitation sum, are calculated on a monthly time resolution.
- Daily simulated precipitation fields are rescaled based on the calculated monthly scaling factors. Due to the described scaling method the spatial distribution of the scaled annual precipitation field is the same for domain 2 and domain 3 (see Figure 5.9 for 2004 and 2005).

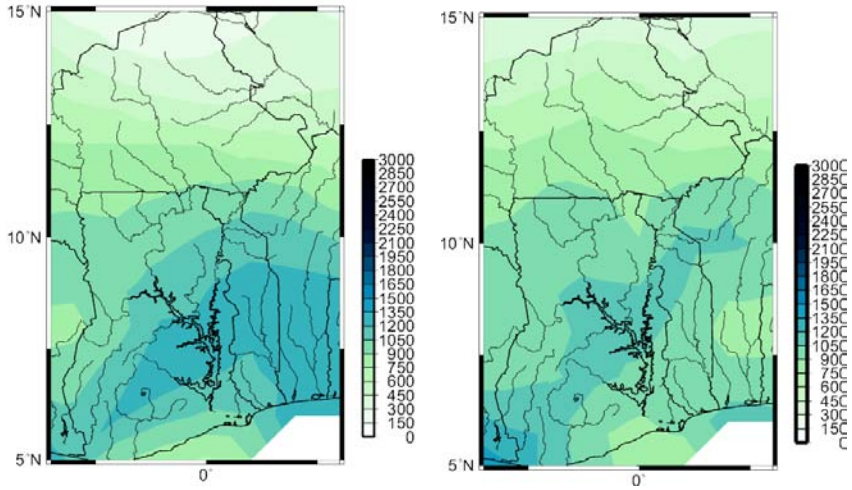

(a) 2004 (b) 2005

Figure 5.9: Spatial distribution of the scaled *MM5* annual precipitation fields, which are identical for domain 2 and domain 3, for 2004 and 2005

Although the scaled precipitation field is the same for both methods, the scatter plots and R^2-values of the monthly precipitation amounts differ slightly. This is due to the different grid sizes of the domains and thus different neighbour grid points for the calculation. The results are shown in Figure 5.10 and Table 5.4. Scaling improves the results for both domains significantly for 2004. For 2005, scaling reduces the number of overestimations, but generates some large underestimations. The R^2-values in Table 5.4 confirm the results in Figure 5.10. In general, scaling leads to partly significantly increased means and decreased ranges of R^2-values for both years.

In this section the performance of a meteorological model and the *TRMM* product $3B42$ have been investigated and compared to available ground measurements of precipitation. In total, three meteorological data sources with different temporal delay of availability are used in the following sections as input for hydrological simulations.

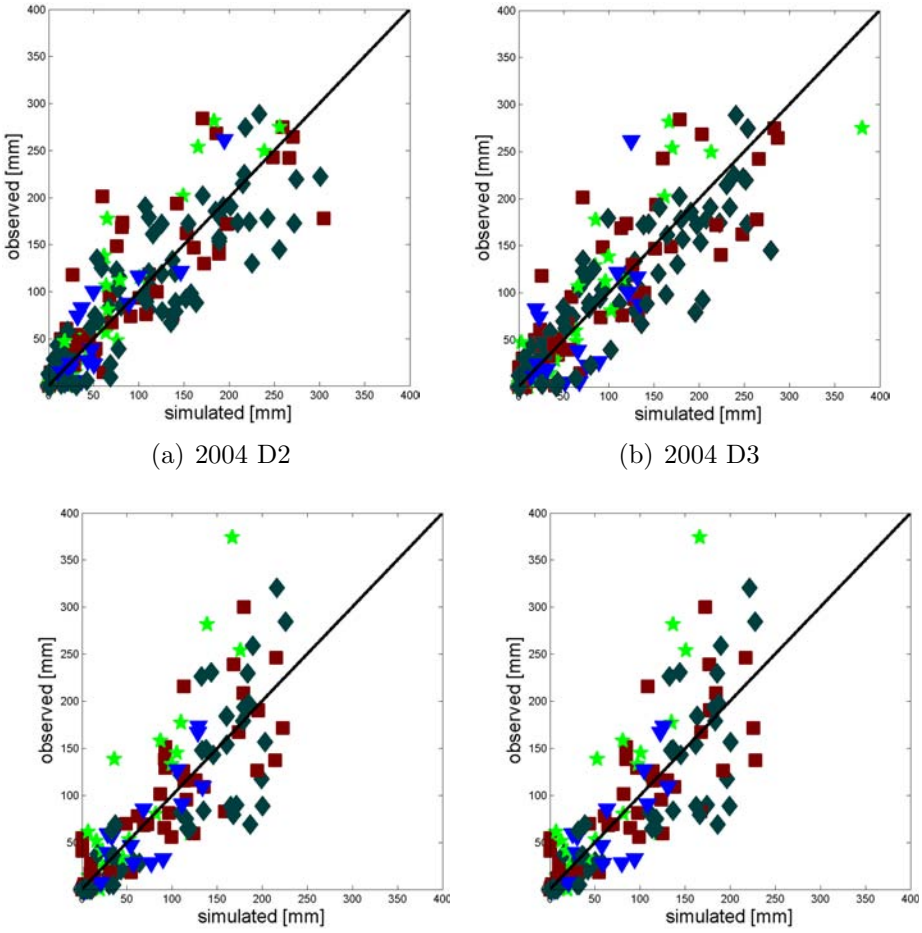

(a) 2004 D2 (b) 2004 D3

(c) 2005 D2 (d) 2005 D3

Figure 5.10: Scatter plots of the (*GPCC*) scaled *MM5* simulations vs. observed monthly precipitation for 2004 and 2005. The 22 or 16 stations are subdivided into 4 regions: the coast (blue triangles), between latitude 7.5° and 8° (green stars), North of Lake Volta between latitude 8.5° and 9.5° (brown squares) and North Ghana together with South Burkina Faso between latitude 10.0° and 11.5° (grey diamonds)

(a) 2004

	$\mathbf{R^2}$			
	D2 scaled		**D3 scaled**	
Latitude	**mean**	**range**	**mean**	**range**
10.0° - 11.5°	0.85	0.78 - 0.94	0.88	0.77 - 0.97
8.5° - 9.5°	0.78	0.63 - 0.99	0.79	0.61 - 0.99
7.5° - 8.0°	0.88	0.82 - 0.97	0.91	0.88 - 0.95
5.5° - 6.5°	0.85	0.74 - 0.96	0.81	0.69 - 0.94

(b) 2005

	$\mathbf{R^2}$			
	D2 scaled		**D3 scaled**	
Latitude	**mean**	**range**	**mean**	**range**
10.0° - 11.5°	0.76	0.53 - 0.92	0.77	0.54 - 0.93
8.5° - 9.5°	0.84	0.67 - 0.92	0.82	0.64 - 0.92
7.5° - 8.0°	0.86	0.70 - 0.97	0.87	0.71 - 0.98
5.5° - 6.5°	0.80	0.67 - 0.97	0.78	0.61 - 0.96

Table 5.4: Mean and range (of stations) of coefficients of determination (R^2) for (*GPCC*) scaled *MM5* results subdivided into 4 regions for 2004 and 2005.

5.2 Performance of hydrological simulations

Before a hydrological model can be used for the estimation of the terrestrial water balance, a detailed calibration and validation process is required. This demands, in particular in large and less investigated basins, long and dense meteorological and hydrological observation data. Thus, calibration and validation is performed in a first step with historical observation data. This is described in Section 5.2.1 and Section 5.2.2 and provides in addition distributed and long-term estimations of the terrestrial water balance.

5.2.1 Calibration and validation

As mentioned in Section 3.2.2, *WaSiM* was so far not used in a semi-arid environment. This requires for the climatic adaptation and the calibration of a hydrological model as much meteorological and hydrological input information in sufficient temporal resolution as possible. Especially in regions with weak infrastructure this is the most important criteria (Jung, 2006). Therefore, the year 1968 has been selected as the calibration period. For this time period both meteorological and hydrological observation data are available for both countries; Burkina Faso and Ghana. Another reason for the selection of this early time period is that the flow regime of the White Volta was quite natural compared to nowadays where dams, irrigation, and water supply impact the natural flow regimes.

Main calibration parameters

WaSiM is calibrated specifically for each subcatchment if observation data is available. Otherwise calibration parameters of downstream or surrounding subcatchments are transferred. The main calibration parameters are listed in Table 5.5.

K_D	[h]	recession constant for direct runoff
K_I	[h]	recession constant for interflow
d_r	$[m^{-1}]$	drainage density
K_{rec}	[-]	recession constant for saturated hydraulic conductivity with depth

Table 5.5: Main calibration parameters of *WaSiM*

Considering retention, single linear storage approaches are applied to direct runoff and interflow, which require the calibration of the recession constants K_D and K_I. Applying a single linear storage approach, the runoff component Q_t at time t is calculated by runoff component Q_{t0} at time t_0 and the corresponding recession constants K:

$$Q_t = Q_{t0} \cdot e^{-\frac{\Delta t}{K}} \tag{5.2}$$

with $\Delta t = t - t_0$.

Furthermore, the empirical scaling parameter drainage density d_r, which linearly controls the strength of interflow, has to be calibrated (see Equation 3.3). For the unsaturated zone, the calibration of the recession constant K_{rec}, which describes the reduction of the saturated hydraulic conductivity with depth (see Equation 3.2), is required. Furthermore, the initialization of the groundwater level in a specific soil layer can be selected.

Performance criteria

For the mathematical quantification of the model's results on the basis of observations, there exist several performance criteria for hydrological model assessment (e.g. Krause et al., 2005). Nash-Sutcliffe model efficiencies NSE (Nash and Sutcliffe, 1970) are widely-used in hydrological modelling:

$$NSE = 1 - \frac{\sum_{i=1}^{n}(Q_{i,sim} - Q_{i,obs})^2}{\sum_{i=1}^{n}(Q_{i,obs} - \overline{Q_{i,obs}})^2} \tag{5.3}$$

The range of NSE values is $[-\infty...1]$. The assumption underlying the application of NSE is that the simulated and the observed runoff data are Gaussian and that their variances are constant (homoskedastic). The fact that runoff data usually does not fulfil these theoretical requirements, leads to an overestimation of the impact of flood events on the performance calculation. Therefore, NSE values can be additionally calculated for the logarithms of the runoff values, which places more emphasis on the entire flow spectrum.

Calibration procedure and results

The calibration of a hydrological model requires meteorological and hydrological observations. For poorly gauged basins the spatial interpolation of coarse-resolution meteorological point observations are afflicted with uncertainties. These are transferred to the hydrological simulations and therefore hamper the calibration process. The uncertainties in simulated water balances due to uncertain precipitation estimations are investigated in Chapter 7.

Moreover, no discharge data are available for the Burkinabé part of the White Volta. Therefore, this study focuses on the Ghanaian part of the White Volta basin. *WaSiM* calculates the *NSE* performance criteria at the end of each simulation, but only for complete time series. Here the problem arises, that runoff time series in poorly gauged basins are usually not complete and contain large data gaps which can not be easily interpolated.

Due to these limitations, model calibration is performed manually based on subjective (visual) and objective (performance calculation) criteria. As performance criteria mainly *NSE* of logarithmic runoff values are calculated for time periods with available measurements.

Figure 5.11 shows the daily time series of the calibration results for the two main stations along the White Volta in Ghana, Pwalugu and Nawuni. It can be seen that the general discharge hydrograph can be simulated fairly well.

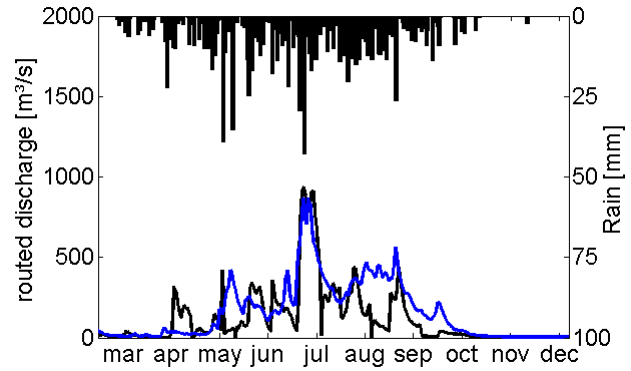

(a) Pwalugu

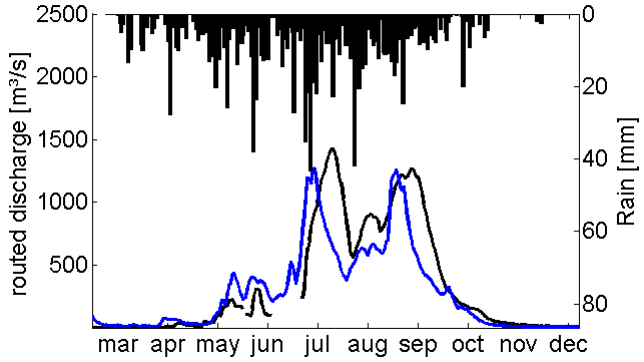

(b) Nawuni

Figure 5.11: Calibration results for the two main gauges along the White Volta in Ghana (a) Pwalugu and (b) Nawuni for 1968 (simulated: blue; observed: black)

	Nakong	Nasia	Nawuni	Pwalugu	Yagaba
$linNSE$	0.68	0.28	0.77	0.49	0.78
$logNSE$	0.49	0.47	0.72	0.47	0.67

Table 5.6: Nash-Sutcliffe efficiencies of linear and logarithmic runoff values of all gauges with discharge measurements in Ghana for the calibration period 1968

Nash-Sutcliffe efficiencies for all gauges with discharge measurements are given in Table 5.6 for both linear and logarithmic runoff values. Table 5.6 shows that best results are obtained for Nawuni, the outlet of the entire White Volta basin. The anthropogenic impact on the simulation results can not be quantified due to missing information. Although it can be assumed to be quite small for this time period, it is a factor of uncertainty in the hydrological simulations.

Validation results

The validation of the hydrological model is performed for the period 1961 to 1967. The fact that at the beginning of the calibration process only observations for the year 1968 with a daily temporal resolution have been available, leads to the applied division of the calibration and validation period.

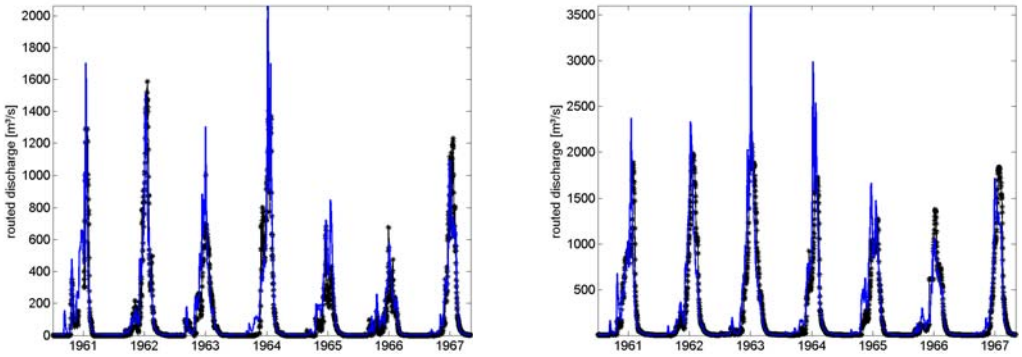

(a) Pwalugu (b) Nawuni

Figure 5.12: Validation results for Pwalugu and Nawuni, the two main station along the the White Volta in Ghana for 1961-1967 (simulated: blue; observed: black)

	Nakong	Nasia	Nawuni	Pwalugu	Yagaba
$linNSE$	-	0.58	0.73	0.81	0.32
$logNSE$	-	0.72	0.81	0.68	0.56

Table 5.7: Nash-Sutcliffe efficiencies of linear and logarithmic runoff values of all gauges with discharge measurements in Ghana for the validation period 1961-1967

Figure 5.12 again shows the daily time series of the validation results for the two main stations along the White Volta in Ghana; Pwalugu and Nawuni. The performance is comparable to the one of the calibration period. For Pwalugu it is even better, which is also reflected in the model efficiencies in Table 5.7. For the head and smaller basins (Nasia and Yagaba) model performances vary in both directions between calibration and validation period. For the complete basin (Nawuni) model efficiencies are in the same range.

5.2.2 Long-term hydrological simulations

During phase 2 and 3 of the *GLOWA*-Volta project, further daily historical meteorological and few hydrological data from the respective departments in Burkina Faso and Ghana became available. Therefore, long-term, 40-year (1961-2000) water balance simulations, are performed using these data sets and the setup described in Section 5.2.1. Unfortunately, meteorological information from 2001 on is still not available for Burkina Faso to continue the simulations up to the present moment. However, these simulations provide long-term, spatially distributed estimations of all relevant water balance variables, and possible changes in the water balance within this time period can be investigated.

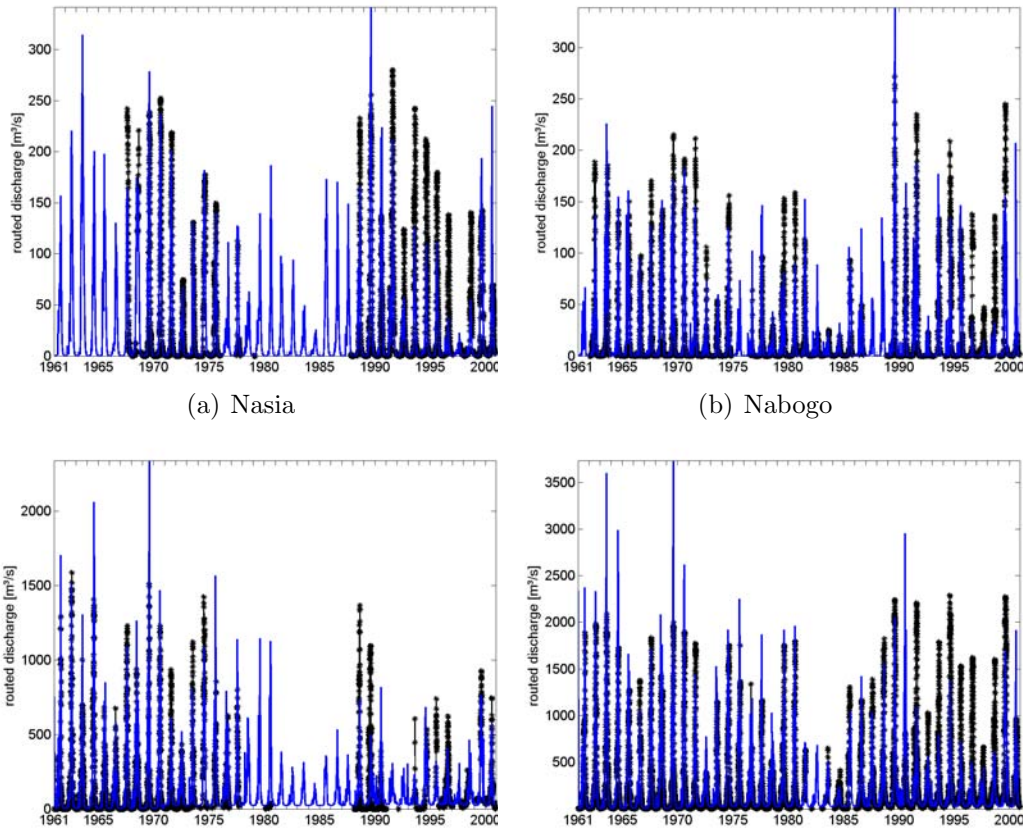

(a) Nasia (b) Nabogo

(c) Pwalugu (d) Nawuni

Figure 5.13: Simulated (blue) vs. observed (black) discharge $[m^3/s]$ of long-term (1961-2000) hydrological simulations for two head basins, Nasia and Nabogo, and the two main stations along the White Volta in Ghana

Like in Section 5.2.1, discharge measurements are only available for stations in Ghana. Additionally to the two main stations along the White Volta; Pwalugu and Nawuni, discharge measurements of two source basins; Nasia and

(a) lin NSE

	61-00	60s	70s	80s	90s
Nasia	0.66	0.70	0.79	0.79	0.53
Nabogo	0.57	0.52	0.63	0.74	0.50
Wiasi	0.56	0.59	0.66	-	0.40
Yagaba	0.39	0.36	0.42	-	-
Pwalugu	0.68	0.76	0.62	0.39	0.78
Nawuni	0.60	0.66	0.61	0.65	0.51

(b) log NSE

	61-00	60s	70s	80s	90s
Nasia	0.37	0.57	0.64	0.79	0.10
Nabogo	0.41	0.55	0.44	-0.18	0.51
Wiasi	0.52	0.45	0.73	-	0.36
Yagaba	0.54	0.60	0.39	-	-
Pwalugu	0.55	0.69	0.33	0.21	0.55
Nawuni	0.70	0.81	0.53	0.64	0.68

Table 5.8: Linear and logarithmic Nash-Sutcliffe efficiencies NSE of long-term (1961-2000) hydrological simulations of all available stations with discharge measurements in Ghana

Nabogo, are partially available. For all four stations the time series are never complete. For Nawuni, data gaps are short. For the other stations gaps however, up to ten years, between 1975 and 1985, occur. The data gaps emphasises the need of long-term water balance simulations which provide continuous estimations of discharge and further water balance variables. The results of the simulation for the discharge hydrographs at the four stations are good considering the limited data availability (see Figure 5.13). In Table 5.8 the corresponding Nash-Sutcliffe model efficiencies are given for the complete time series and for each decade separately. The linear and logarithmic NSE values vary between the stations and the considered time periods. Except for Pwalugu, linear NSE-values for the decade 1991–2000 are the lowest. A reason for that may be the increasing anthropogenic water use for water supply and irrigation, which started especially around Tamale, and had an effect on the surrounding subcatchments Nawuni, Nabogo and Nasia. A further disturbance of the natural flow regime are dams, whereof the Bagré dam in the South of Burkina Faso, built in the early 1990's, is the most important.

Although observed discharge is the only validation variable, the modelling system is designed to provide long-term information on the spatial and temporal distribution of the terrestrial water balance, which includes the different runoff components, evapotranspiration, groundwater recharge and soil moisture. First, this is illustrated in the following figures for the meteorological

variables precipitation, temperature and relative humidity in Figure 5.14. The time series of annual precipitation in Figure 5.14(a) shows relatively high amounts in the 1960s followed by approximately 15 years of drier conditions and, in the 1990s, slightly increasing amounts, but less compared to the 1960s. Figure 5.14(c) shows a trend of increasing annual temperatures for the complete time series. Mean annual relative humidity in Figure 5.14(e) follows approximately the course of the precipitation time series. These long-term simulation estimations are in good agreement with the results found in literature, where decreasing rainfall amounts and increasing temperatures have been observed in West Africa over the past decades and analysed in a variety of studies (Le Barbé and Lebel, 1997; Amani, 2001; Nicholson, 1993; Nicholson, 2001; Hulme et al., 2001; Le Barbé et al., 2002). A striking decrease in annual rainfall in the Sahel region was observed after 1968, with a decrease of around 20% to 40% from 1931–60 to 1968–97 by Nicholson (2001). According to Nicholson (1993), the 1980s were the driest period of the 20th century in West Africa. A weak increase in rainfall occurred in the 1990s, but never reached values comparable to those of the 1960s. Hulme et al. (2001) found a decrease in precipitation exceeding 25% within the last century over some western and eastern parts of the Sahel. Temperature observations show a warming of the African continent in the last 100 years by about 0.5°C. The rates of warming as well as the periods of most rapid warming (1910-1930 and from 1970 onwards) were similar to observed global trends (Houghton et al., 2001). Concentrating on the Volta region, a linear trend analysis was performed by Neumann et al. (2007). In this analysis, linear trends of temperature, precipitation, and discharge time series of Ghana and Burkina Faso were derived (see Section 2.2).

Furthermore, daily means spatially averaged over the complete White Volta basin of the long-term, 40-year (1961-2000) simulations are shown for precipitation, temperature and relative humidity in Figure 5.14. In the precipitation time series the rainy and dry season can be clearly identified. Maximum precipitation amounts occur between July and September, followed by decreasing amounts in October and minimum precipitation between November and March, before the rainy season starts from the South in April or May. Maximal daily temperatures occur at the end of the dry season in March followed by a decrease during the rainy season, a second smaller temperature peak in October/November, and a decrease of daily temperatures until January. Mean daily relative humidity time series approximately follow the course of the precipitation one. The time series of daily means are in good agreement with the climate description of the White Volta Basin in Section 2.2.

In Figure 5.15 the time series of annual sums and daily means, spatially averaged over the complete White Volta basin, of the long-term, 40-year (1961-2000) simulations are shown for the following terrestrial water balance variables: actual evapotranspiration, groundwater recharge, and soil moisture. The time

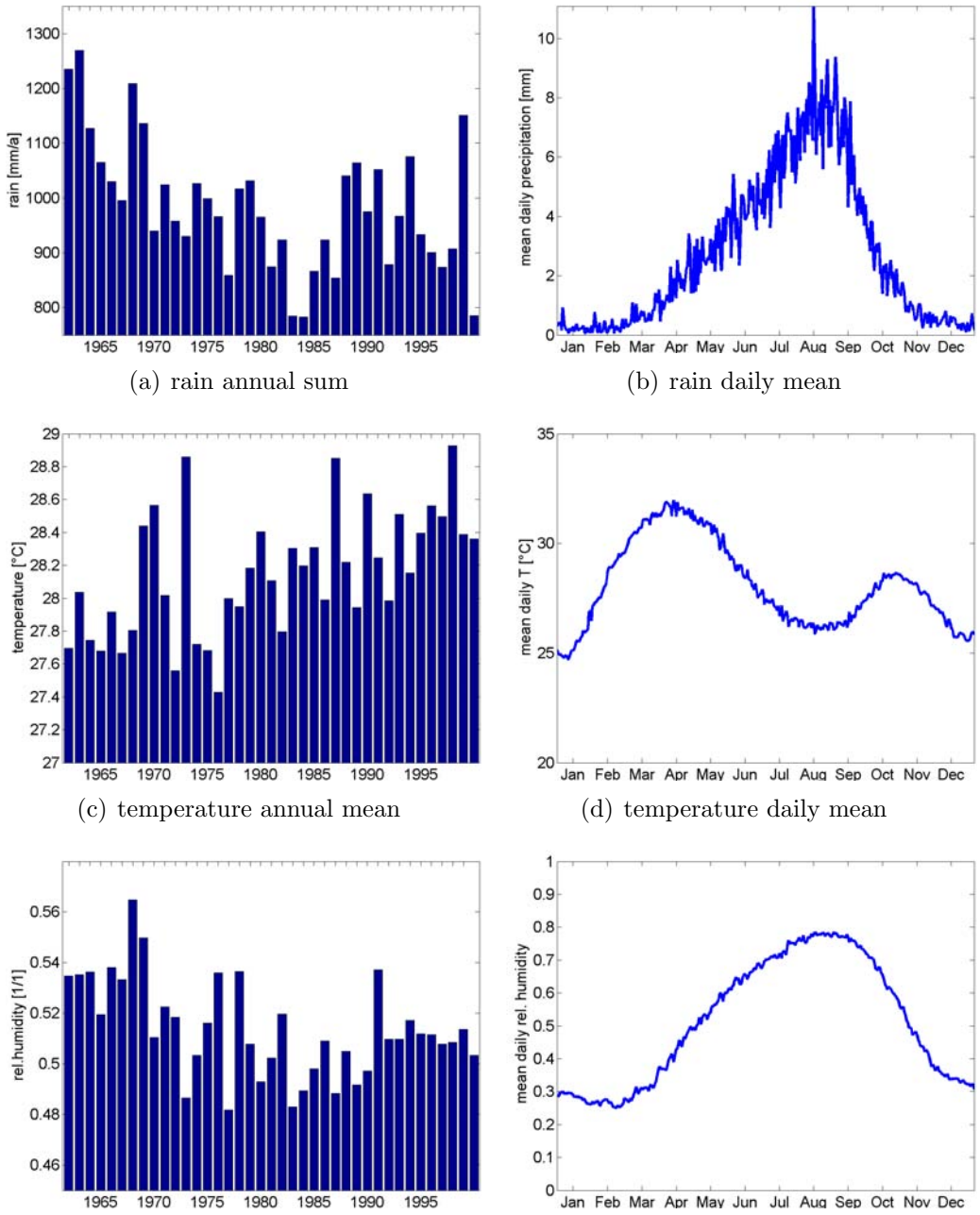

(a) rain annual sum

(b) rain daily mean

(c) temperature annual mean

(d) temperature daily mean

(e) rel. humidity annual mean

(f) rel. humidity daily mean

Figure 5.14: Basin-wide annual sums/means and long-term daily means of rain, temperature, and relative humidity of the long-term (1961-2000) hydrological simulations for the White Volta basin

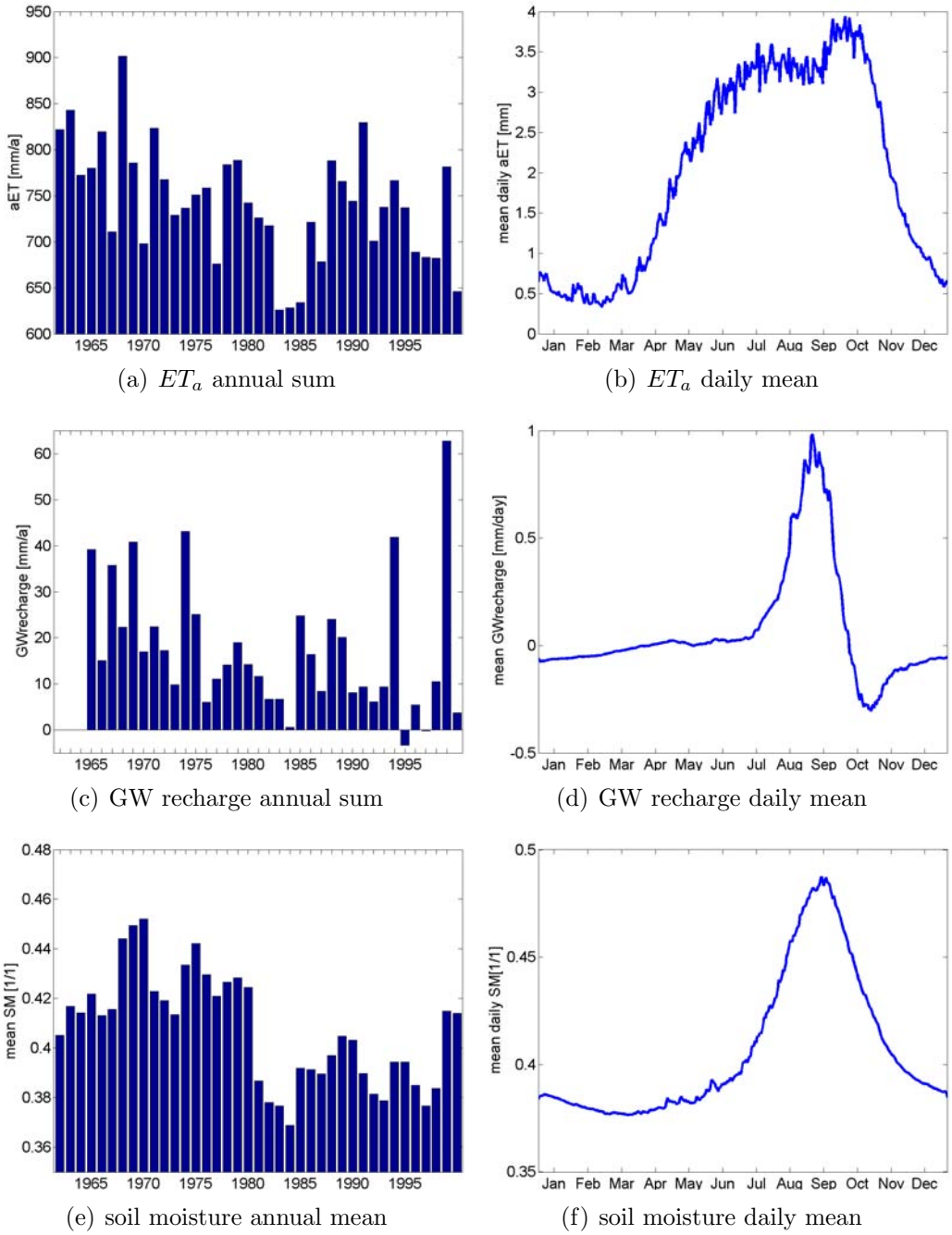

(a) ET_a annual sum (b) ET_a daily mean

(c) GW recharge annual sum (d) GW recharge daily mean

(e) soil moisture annual mean (f) soil moisture daily mean

Figure 5.15: Basin-wide annual sums/means and long-term (1961-2000) daily means of actual evapotranspiration, groundwater recharge, and relative soil moisture of the long-term hydrological simulations for the White Volta basin

series for actual evapotranspiration approximately follows the ones of precipitation, except during the end of the rainy and the beginning of the dry season

(September and October) where high soil moisture values and higher temperatures contribute to higher evapotranspiration values. Groundwater recharge estimations require longer initialization periods in this region. Therefore, the corresponding annual sums in Figure 5.15(b) begin with the year 1965. During the main rainy season, mean daily groundwater recharge values are positive, which means flow direction with gravity. Otherwise they are negative, but with lower magnitudes, which ,in total, leads to positive annual groundwater recharge values, except for 1995. Annual soil moisture means do not respond as fast as e.g. actual evapotranspiration to an increase or decrease of annual precipitation. Therefore, the range of annual soil moisture means is smaller compared to, for example, actual evapotranspiration.

Figure 5.16 shows the time series of annual sums and daily means spatially averaged over the complete White Volta basin over the 40-year (1961-2000) simulations for (a) total runoff and the components (b) direct runoff, (c) interflow, and (d) baseflow. The time series of annual sums approximately follow the one of precipitation with very small total runoff sums in the early 1980s and early 1990s, except for baseflow, which is low but quite constant during the complete time period. The time series of daily mean total and direct runoff, as well as interflow, have similar shapes with different magnitudes. The shape of the interflow time series is smoother compared to the direct runoff one, due to faster response of direct runoff to precipitation events. Baseflow is very low during the complete year with a slight increase during the main rainy season.

The long-term water balance simulations allow the calculation and analysis of the runoff coefficient RC (see Equation 2.1), which determines the percentage of precipitation becoming runoff, and the aridity index dMI, which is defined as

$$dMI = \frac{P}{T + 10} \tag{5.4}$$

where P is the annual precipitation [mm] and T the sum of monthly mean temperatures greater than $0°C$ divided by 12, which is, in this region, the mean annual temperature. This aridity index after DE MARTONNE (1920) is selected to consider the interaction of precipitation and temperature in the hydrological cycle, which is particularly important for semi-arid to sub-humid areas like the White Volta basin. Lower dMI-values indicate higher aridity. Following DE MARTONNE (1920), a dMI below 20 indicates the necessity for irrigation. For dMI-values between 20 and 30 irrigation is often required, but not indispensable. Figure 5.17 shows the aridity index for the long-term water balance simulations. Additionally, the standard deviation of the aridity index for the 15 subcatchments is plotted to illustrate the variability within the White Volta basin. In general, the aridity index between 1961 and 2000 is in the range of 20 and 30, which means irrigation is not essential, but often performed. Minimum aridity indexes are calculated for the early 1980s, with

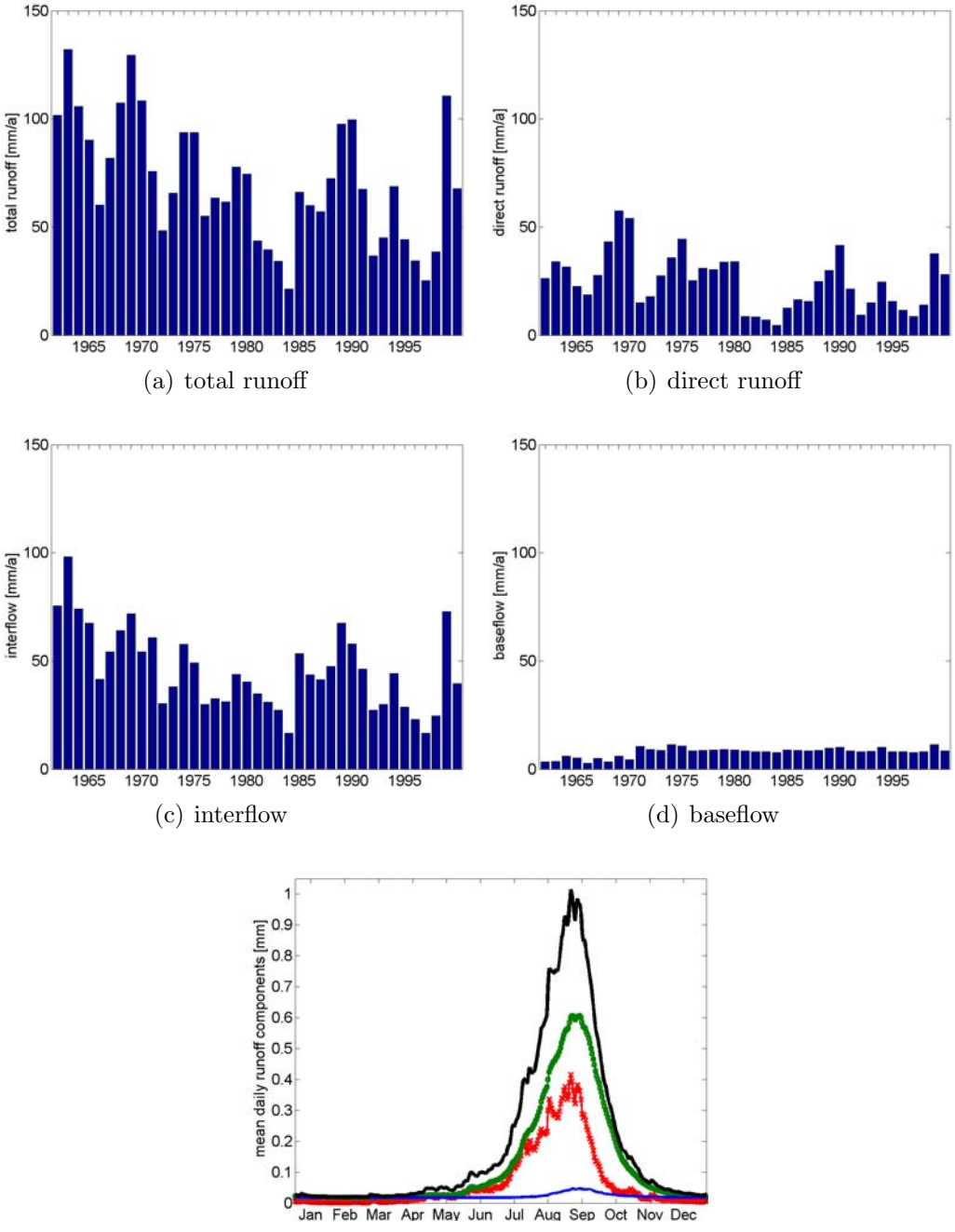

(a) total runoff

(b) direct runoff

(c) interflow

(d) baseflow

(e) runoff components daily mean

Figure 5.16: Basin-wide annual sums and long-term (1961-2000) daily means of total runoff (black), direct runoff (red), interflow (green), and baseflow (blue) of the long-term hydrological simulations for the White Volta basin

values of 20.5 close to the lower boundary and hence indicating the need for irrigation. Considering the standard deviation in the White Volta basin, in particular the subcatchments in the northern part have aridity indexes below 15.

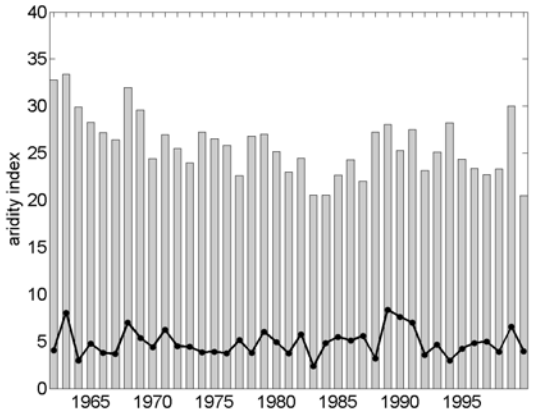

Figure 5.17: Basin-wide mean (bars) and standard deviation (line) of annual aridity index dMI of the long-term (1961-2000) hydrological simulations for the White Volta basin

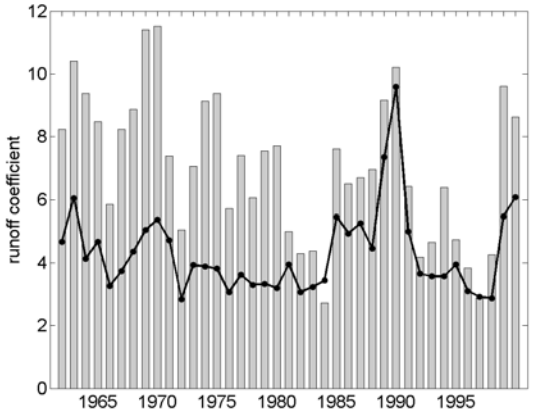

Figure 5.18: Basin-wide mean (bars) and standard deviation (line) of annual runoff coefficients RC of the long-term (1961-2000) hydrological simulations for the White Volta basin

According to the aridity index, the runoff coefficient RC and the standard deviation for the 15 subcatchments is depicted in Figure 5.18. The long-term mean runoff coefficient value for the White Volta basin is approximately 7%, which corresponds well to literature values described in Section 2.3. During the long-term simulations the RC is characterized by a high variability ranging

from 2.7% to 11.5%. Considering the standard deviation in the White Volta basin the variability increases further on subcatchment scale. In general, *RC*s are higher in the southern part, with a long-term mean runoff coefficient of 8.2% for the Ghanaian part, compared to 5.5% for the northern, Burkinabé part of the White Volta basin.

Additionally to long-term time series, the water balance simulations provide spatially distributed estimations of relevant variables, for example of precipitation, actual evapotranspiration or total discharge. In Figure 5.19, spatially distributed annual precipitation fields averaged over the decades 1960s until 1990s are shown to illustrate the spatial development during the long-term simulations. In all four subplots a general gradient of precipitation with lower values in the North and higher values in the South is present. Between the 1960s and 1980s a continuous, basin-wide decrease of annual precipitation occurred, which led to a large water deficit in this region and impacts the terrestrial water balance.

In Figure 5.20, spatially distributed annual actual evapotranspiration fields averaged over the decades 1960s until 1990s are depicted. In addition to the general North-South gradient, the actual evapotranspiration fields are heterogeneous in space due to different characteristics derived from the land use and soil grid influencing the calculation of evapotranspiration. In accordance with the precipitation fields, the comparison of the actual evapotranspiration fields averaged over the decades 1960s until 1990s shows, that the mean annual sums are maximal during the 1960s, followed by a continuously decrease up to the 1980s. During the 1990s a slight increase is simulated in most areas of the White Volta basin.

The spatially distributed annual total runoff fields averaged from the 1960s until the 1990s are shown in Figure 5.21. In general, the total runoff fields are very patchy. During the 1960s until the 1990s total runoff decreases continuously. In some regions in the North-East annual total runoff values of less then 50 mm are simulated. In addition to the spatial distribution of the shown annual fields, for example, the analysis of monthly fields of water balance variables allows investigations on the seasonal development.

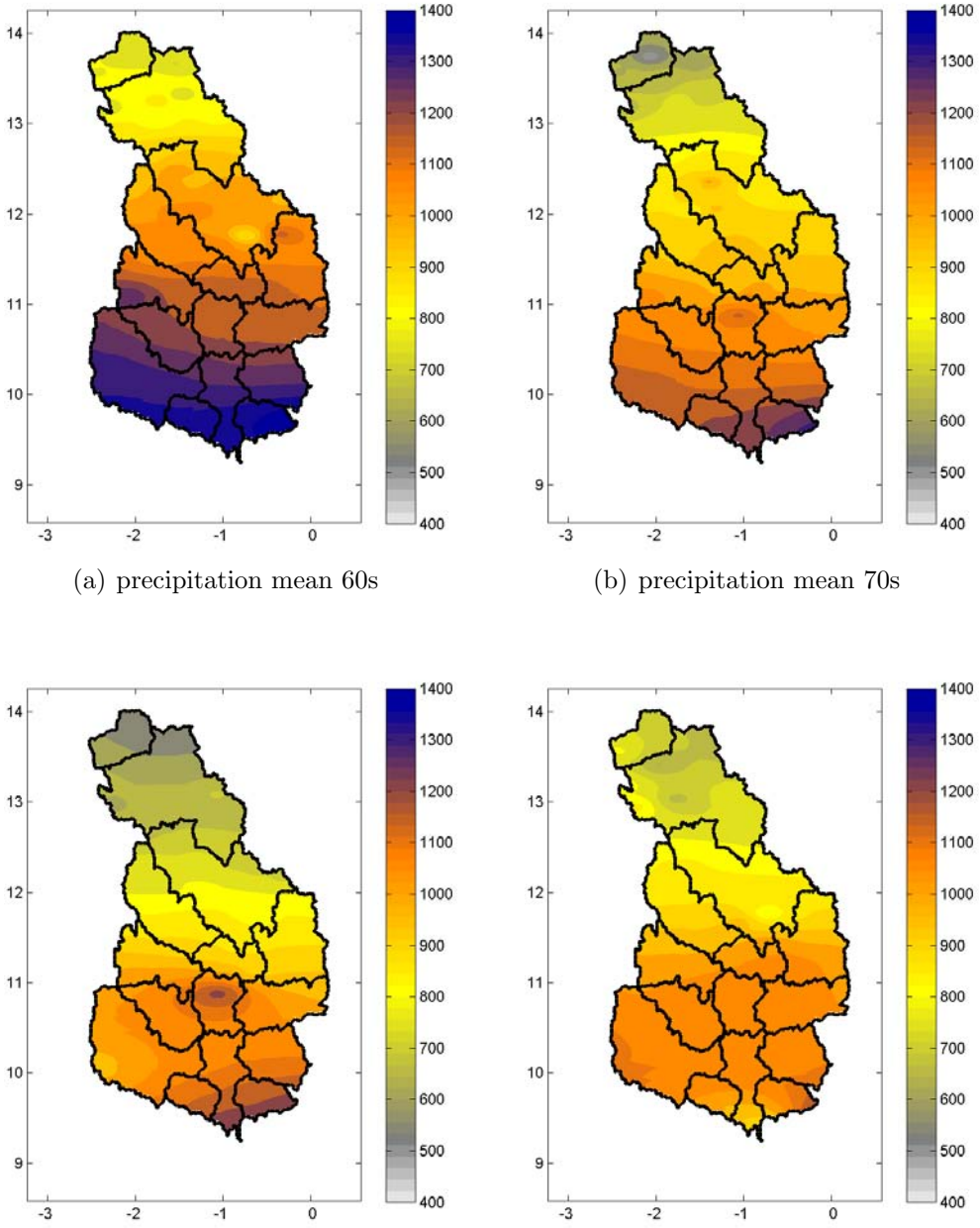

(a) precipitation mean 60s

(b) precipitation mean 70s

(c) precipitation mean 80s

(d) precipitation mean 90s

Figure 5.19: Spatial distribution of mean annual precipitation [mm] for the decades 1961-1970, 1971-1980, 1981-1990, and 1991-2000

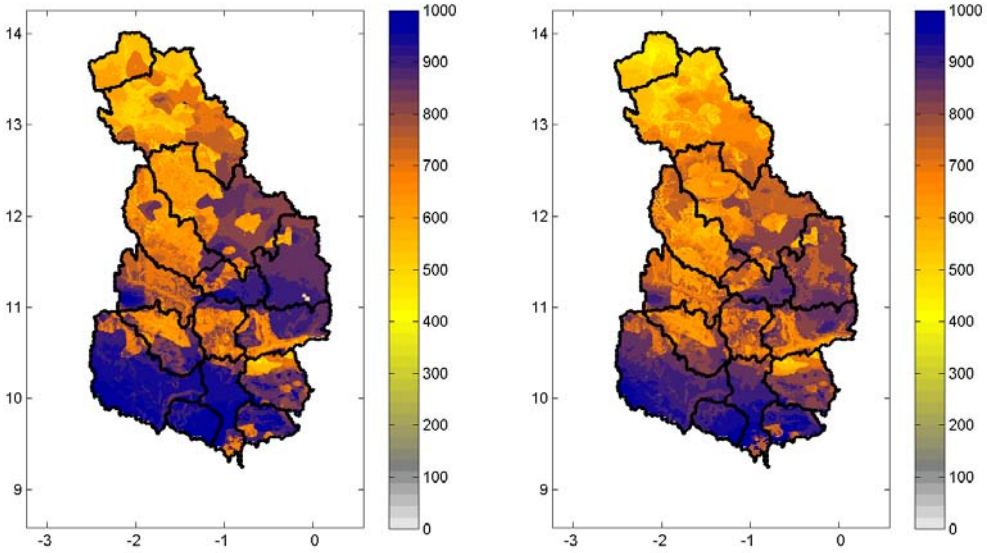

(a) ET_a mean 60s

(b) ET_a mean 70s

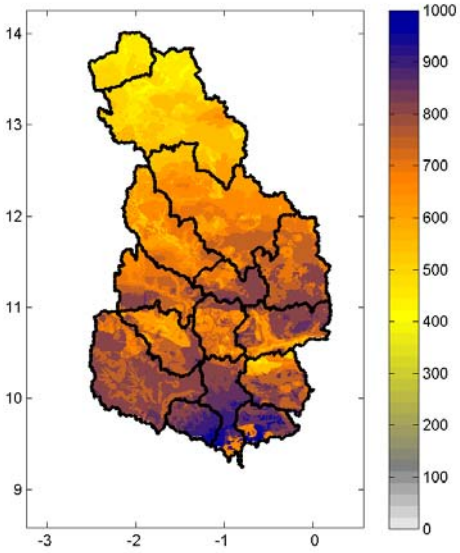

(c) ET_a mean 80s

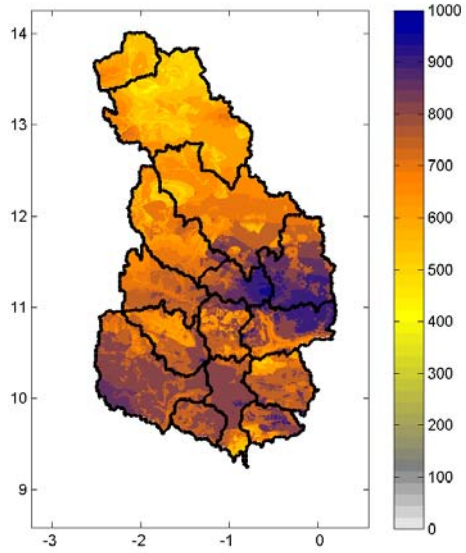

(d) ET_a mean 90s

Figure 5.20: Spatial distribution of mean annual actual evapotranspiration [mm] for the decades 1961-1970, 1971-1980, 1981-1990, and 1991-2000

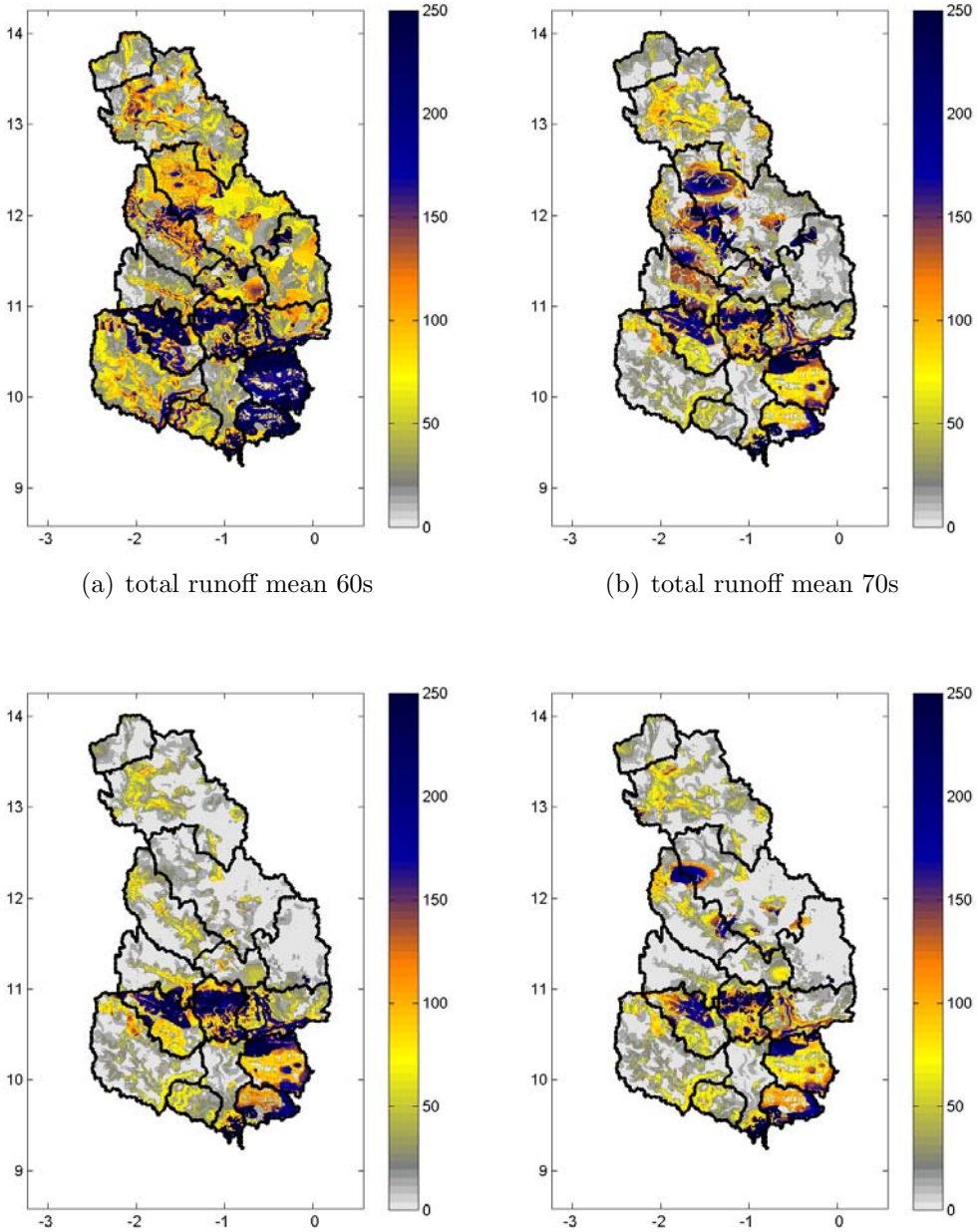

(a) total runoff mean 60s

(b) total runoff mean 70s

(c) total runoff mean 80s

(d) total runoff mean 90s

Figure 5.21: Spatial distribution of mean annual total runoff [mm] for the decades 1961-1970, 1971-1980, 1981-1990, and 1991-2000

5.3 Performance of joint atmospheric-hydrological simulations

As described in Section 3.3, the results of the meteorological simulations are processed to provide the required meteorological input information for hydrological modelling. In this study, *MM5* results for 2004 and 2005 (see Section 5.1) are processed using the developed interface.

For the purpose of comparison and for the investigation of different data sources which are available with different temporal delays, hydrological modelling is additionally performed with *TRMM* data (see Section 4.3 and 5.1.1) and station measurements. Therefore in total three meteorological data sources are investigated which differ, additionally to their time of availability, in the density of the rain gauge network and in the data type:

1. Ground measurements at specific locations (point observations) which require spatial interpolation for hydrological modelling.

2. Results of the meteorological model *MM5*, which provide gridded information with a spatial resolution of 27 x 27 km (domain 2) and 9 x 9 km (domain 3).

3. Remote sensed precipitation data through microwave and visible infrared sensors, which are available as gridded estimates on a 0.25° x 0.25° spatial resolution (*TRMM* product $3B42$).

For the application of the three meteorological data sources, one setup of the hydrological model, calibrated with observation data, was applied first. During this study it turned out that this setup is not optimal for gridded meteorological input data, which are treated as "virtual" stations in the hydrological model and lead to a very dense data network. Furthermore, gridded meteorological input data are available everywhere in the research area, which is usually not the case when applying observation data in particular in ungauged or poorly gauged basins. Therefore, the setup of the hydrological model was adapted for gridded meteorological input data. Applying different setups for each spatial resolution; i.e. for 27 x 27 km (domain 2), 9 x 9 km (domain 3) and 0.25° (*TRMM*) show comparable results. However, they differ significantly from the results if the setup of meteorological point observations is applied. Possible reasons for the comparable results of all gridded input data might be the already quite dense network of the "coarser" grid sizes of domain 2 or *TRMM*, and the availability of meteorological input data everywhere in the basin. Consequently, different setups of the hydrological model are applied. Brath et al. (2004) investigate the influence of the spatial resolution of rainfall data on model calibration by varying size and distribution of the raingauge network.

Bárdossy and Das (2006) conclude that the model using different raingauge networks may need recalibration of model parameters.

In the following sections, results of the hydrological simulations for the three different meteorological input data sources are given. The natural flow regime of the White Volta basin is disturbed by a dam and hydro-power generation in Bagré in the South of Burkina Faso since 1993. Data on water storage and release management is not available. Due to the strong dependency of downstream hydrographs on the management strategies of the Bagré dam, the simulated runoff is replaced with observed values at the next gauging station (Yarugu) to avoid the transmission of errors to the downstream catchments. For this reason, the study focuses on the Ghanaian part of the White Volta catchment.

5.3.1 MM5-WaSiM simulations

Applying *MM5* results as a meteorological data source allows near real time water balance estimations, which are available with a delay of approximately 2 days. As a result of the joint *MM5-WaSiM* simulations, Figure 5.22 depicts the routed discharge time series for 2004 at three gauges where observation data are available: Nasia, a head basin, as well as Pwalugu and Nawuni, the two main gauges along the White Volta in Ghana (see Figure 3.2). The corresponding precipitation time series are given in Appendix A. In Nasia the discharge curves of domain 2 (blue) and domain 3 (green) differ significantly as a result of the differences in the precipitation time series. The measured discharge curve is not well reproduced using meteorological input data from both *MM5* domains. In contrast, the discharge hydrographs of Pwalugu and Nawuni in Figure 5.22(c) and (e) show satisfying and comparable simulation results for both domains. However, differences in the precipitation time series of domain 2 and domain 3 propagate to the discharge hydrographs. Figure 5.23 shows the results of the joint *MM5-WaSiM* simulations for 2005. At all three gauges, routed discharge curves are overestimated for both domains, as result of too high precipitation sums simulated with *MM5*. The scatter plots in Figure 5.4 already indicate this overestimation, which probably occurs in the complete White Volta basin.

This leads, according to the *TRMM* product, to the idea of scaling the *MM5* precipitation results based on a monthly, gridded, global rain gauge product (see Section 5.1.2). The results of joint scaled *MM5-WaSiM* simulation are given in the next paragraph.

5.3.2 Scaled MM5-WaSiM simulations

The scaling with observed, monthly precipitation data leads to a delay of 1 month, comparable to the scaled *TRMM* product, until scaled *MM5* precipitation fields can be applied in hydrological simulations. Figure 5.22 and

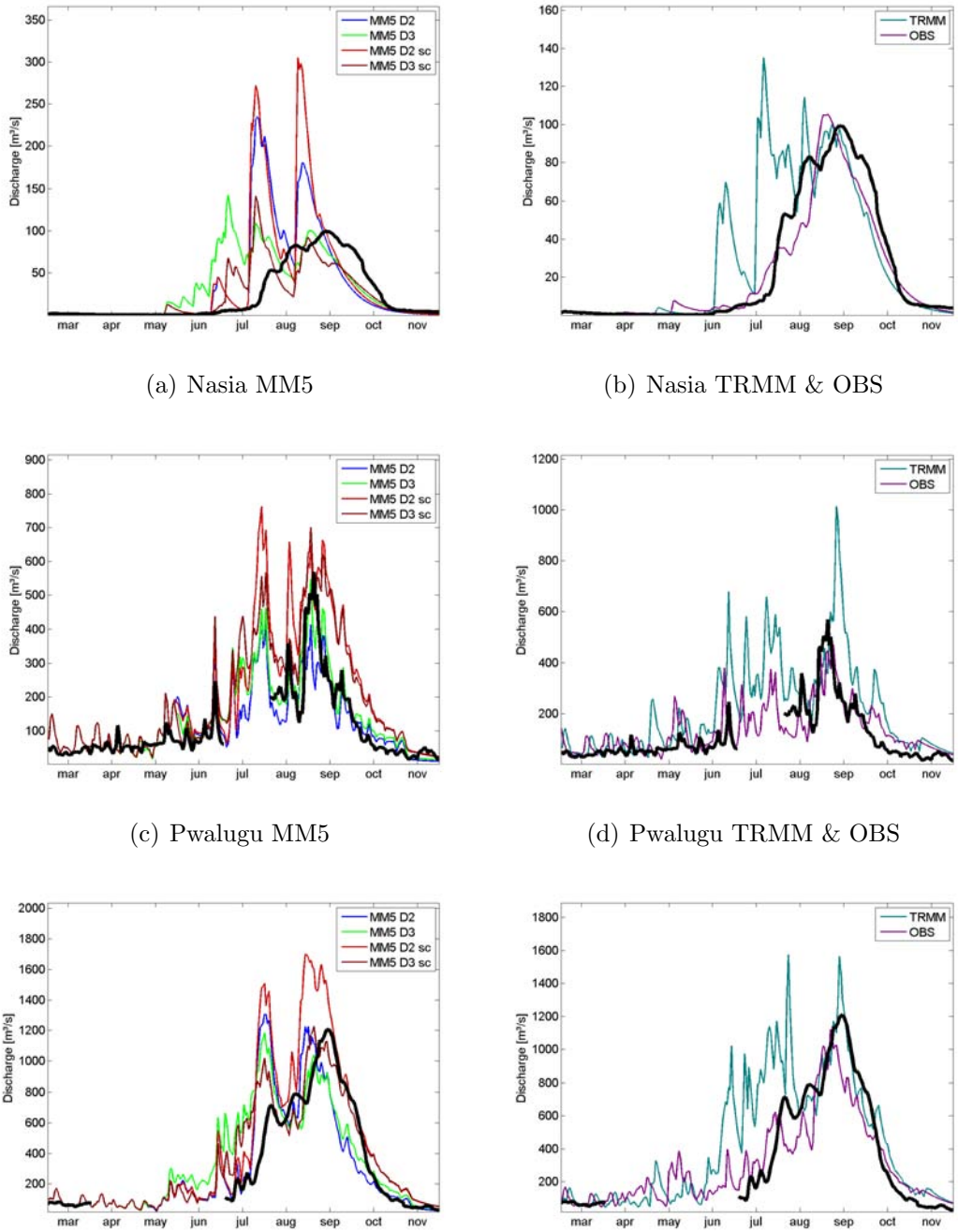

(a) Nasia MM5

(b) Nasia TRMM & OBS

(c) Pwalugu MM5

(d) Pwalugu TRMM & OBS

(e) Nawuni MM5

(f) Nawuni TRMM & OBS

Figure 5.22: Routed vs. measured (black) discharge [m^3/s] for Nasia, Pwalugu, and Nawuni for 2004 using different meteorological data sources: (i) gridded, real time *MM5* results (MM5 D2 and MM5 D3), (ii) gridded, scaled *MM5* results (MM5 D2 sc and MM5 D3 sc), (iii) the gridded, scaled *TRMM* product 3B42, and (iv) station data

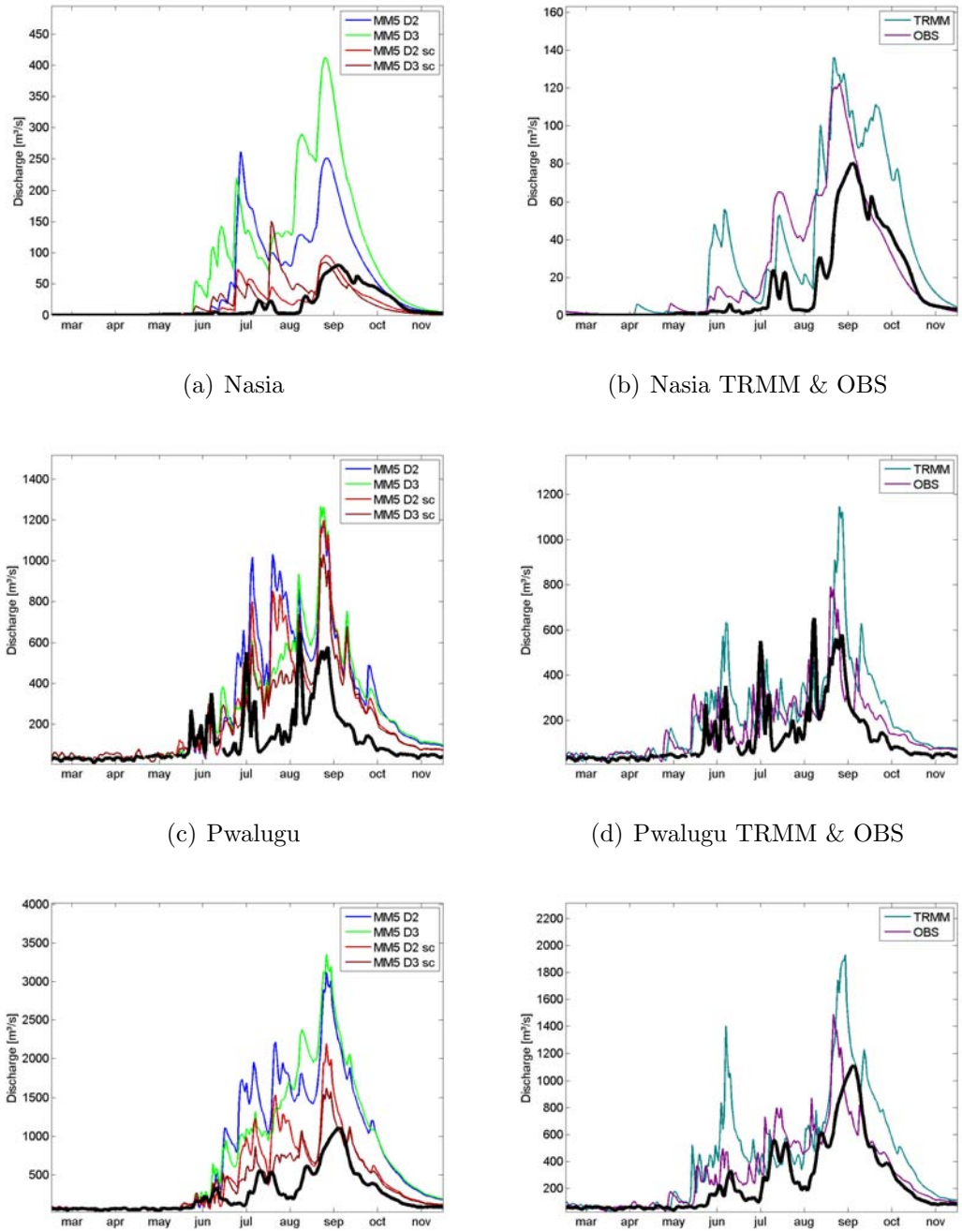

(a) Nasia

(b) Nasia TRMM & OBS

(c) Pwalugu

(d) Pwalugu TRMM & OBS

(e) Nawuni

(f) Nawuni TRMM & OBS

Figure 5.23: Routed vs. measured (black) discharge [m^3/s] for Nasia, Pwalugu, and Nawuni for 2005 using different meteorological data sources: (i) gridded, real time *MM5* results (MM5 D2 and MM5 D3), (ii) gridded, scaled *MM5* results (MM5 D2 sc and MM5 D3 sc), (iii) the gridded, scaled *TRMM* product 3B42, and (iv) station data

Figure 5.23 show additionally the routed discharge time series of the scaled products for domain 2 (bright red) and domain 3 (dark red) for 2004 and 2005, respectively. For 2004, the scaled products do not considerably improve the discharge curves for Nasia. For Pwalugu they lead to higher discharge values during the rainy season. For Nawuni the hydrological simulations with the scaled product of domain 3 improves the simulation quality, in particular in September. For 2005, scaling the *MM5* simulated precipitation leads to a considerable change of the precipitation (see Appendix A) and discharge time series. For 2005, the scaled *MM5* input results in routed discharge hydrographs for all three gauges, which are at least in the same magnitude as the measured ones. However, a slight trend of overestimation is still present.

5.3.3 Scaled TRMM-WaSiM simulations

For this application, the *TRMM* product 3B42 (see Section 4.3) is applied as a data source for precipitation. Hence, other data sources for the remaining, required meteorological variables have to be used. In this study the *MM5* results of domain 2, which have a similar spatial resolution as the *TRMM* product, are used for the remaining meteorological variables. Due to the fact that precipitation is the most important meteorological driving variable for water balance simulations, the data source of the remaining ones has a minor impact on the simulation results. The subplots in the right column in Figure 5.22 and Figure 5.23 show the routed discharge time series in turquoise for 2004 and 2005 respectively using the *TRMM* product 3B42 as the precipitation data source. The corresponding precipitation time series are given in Appendix A. At times, precipitation time series differ significantly from the observation and *MM5*-derived ones for both years. For 2004, the discharge simulation for the head basin Nasia is comparable to the scaled *MM5-WaSiM* simulations, with overestimations in the early phase of the rainy season. For Pwalugu and Nawuni, *TRMM-WaSiM* simulations tend towards overestimating the observed discharges. For 2005, the tendency is similar with comparable performances as the scaled *MM5-WaSiM* simulations.

5.3.4 Station data based WaSiM simulations

Using station data, a delay of one or more years is possible in regions with weak infrastructure and large basins, shared by several countries, like the White Volta basin. In this study, current station data for the Burkinabé part of the basin are still missing. Thus, seven possible stations (see Figure 7.4(a)) in Burkina Faso are selected and filled with *TRMM* data to get a more realistic estimate of the precipitation distribution compared to an extrapolation of measurements from Ghana to the Burkinabé part of the basin. The routed discharge time series of the hydrological simulations driven by station data are shown in purple in the subplots in the right column in Figure 5.22 for 2004 and in Figure 5.23 for

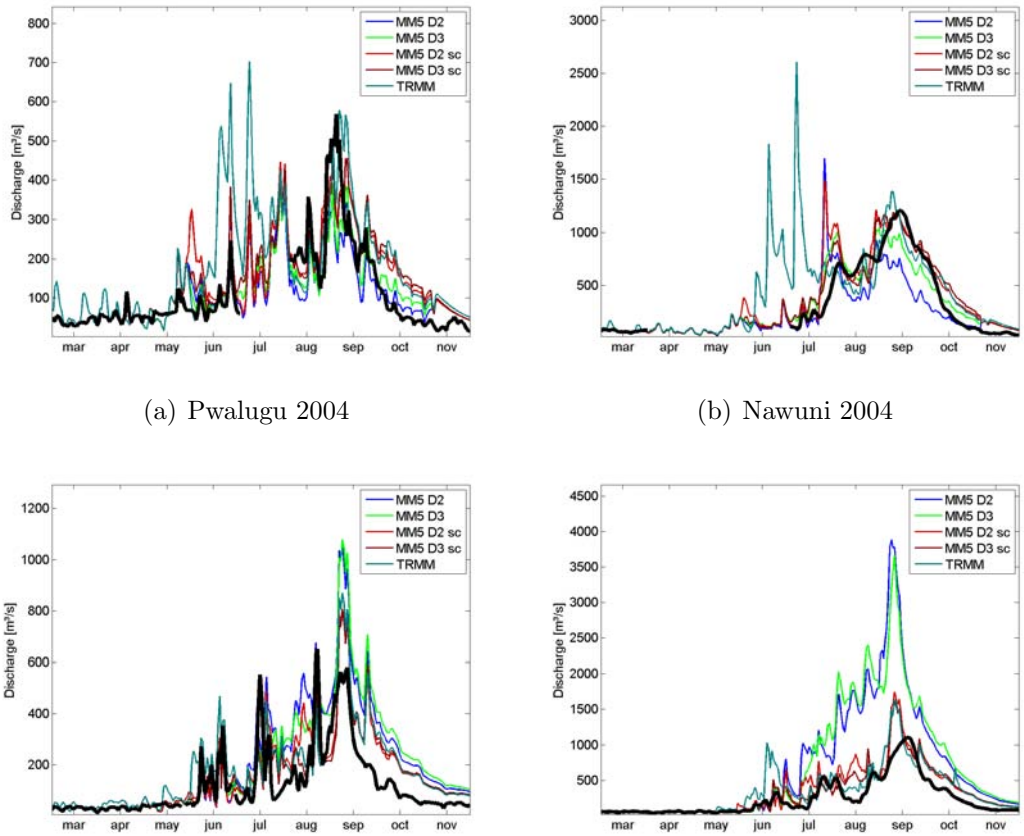

(a) Pwalugu 2004

(b) Nawuni 2004

(c) Pwalugu 2005

(d) Nawuni 2005

Figure 5.24: Routed vs. measured (black) discharge [m^3/s] for Nasia, Pwalugu, and Nawuni for 2004 and 2005 using different meteorological data sources: (i) real time *MM5* results (MM5 D2 and MM5 D3), (ii) scaled *MM5* results (MM5 D2 sc and MM5 D3 sc), and (iii) the scaled *TRMM* product 3B42 applied at observation sites

2005. The corresponding precipitation time series are given in Appendix A. At times, precipitation time series differ significantly from the *TRMM* and *MM5* derived ones for both years. In general, the discharge hydrographs for all three gauges can be simulated fairly well for 2004 and 2005. Compared to 2004 the simulated discharges tend to overestimate the measured ones slightly, which affects Nasia in particular.

5.3.5 WaSiM simulations using MM5/TRMM input data at observation sites

Another possibility of using the *MM5* and *TRMM* results as meteorological input data for hydrological modelling is to interpolate precipitation from the

gridded data sources to the locations of the observation stations, and run the simulations with the observation data setup. The advantage of this application is that no recalibration of the hydrological model is required. However, a lot of information of the available, basin-wide gridded data sources is not considered in the hydrological simulations if only the grid points around the observation stations are taken into account for the interpolation. In this study, the inverse distance weighting method of the four neighbouring grid points for each observation station is applied as interpolation technique. Figure 5.24 shows the routed discharge time series for *MM5-WaSiM* and *TRMM-WaSiM* simulations using *MM5* respectively *TRMM* results at observation stations for 2004 and 2005. For 2004, the simulation results are comparable to the direct application of gridded *MM5* and *TRMM* results. For 2005, the precipitation overestimation of the unscaled *MM5* results also affects the discharge hydrographs. The overestimation is in the same range as with the direct application of gridded, unscaled *MM5* results. The impact of scaling is clearly visible in the precipitation and discharge time series and leads to a satisfying performance of the hydrological simulations with scaled *MM5* and scaled *TRMM* results.

5.3.6 Performance comparison of hydrological modelling using different meteorological data sources

The comparison of the performance of hydrological simulations driven by different meteorological input data sources for 2004 and 2005 is evaluated as follows:

First, for the analysis of the differences between 2004 and 2005 annual precipitation for the shown subcatchments and the entire basin, simulated with *MM5* and *TRMM* results relative to annual precipitations, simulated with observation data, are given in Table 5.9(a). The corresponding results for mean annual routed discharge, which are only available for subcatchments, are shown in Table 5.9(b). Due to missing or incomplete time series, simulation results cannot be compared directly to observations. Thus, hydrological simulation results driven by observation data are chosen as reference with a value of one.

For the hydrological simulations driven with *MM5* results, annual precipitation for 2004 is, in general, underestimated compared to the reference simulations driven by observation data, except for Nasia and Nawuni for domain 3. For 2005, annual precipitation is overestimated by up to 44%. With the scaled *MM5* results, the range of annual precipitation for 2004 and 2005 relative to the reference simulation is between 0.90 and 1.12. These numbers confirm the impact of scaling, which has already been visible in the shown time series. Relative annual precipitation values of scaled *TRMM* results are comparable to the scaled *MM5* ones.

The relative, mean annual routed discharges in Table 5.9(b) indicate, in general, higher values for the simulations driven by *MM5* or *TRMM*. However, they differ in the magnitude. The highest overestimations are simulated with

(a) Precipitation

	2004				2005			
	Nasia	Nawuni	Pwalugu	Mean	Nasia	Nawuni	Pwalugu	Mean
D2	0.86	0.83	0.71	0.53	1.17	1.22	1.31	0.98
D3	1.04	1.04	0.92	0.71	1.44	1.29	1.42	1.03
D2 sc.	1.05	0.99	1.12	0.92	0.99	0.97	1.12	1.01
D3 sc.	1.05	0.99	1.11	0.90	0.98	0.96	1.11	0.99
TRMM	1.05	1.04	1.10	0.95	1.04	0.86	1.15	0.98
Obs	1.00	1.00	1.00	1.00	1.00	1.00	1.00	1.00

(b) Routed discharge

	2004			2005		
	Nasia	Nawuni	Pwalugu	Nasia	Nawuni	Pwalugu
D2	1.60	1.01	0.92	2.20	2.33	1.76
D3	1.52	1.12	1.07	3.37	2.33	1.63
D2 sc.	1.79	1.40	1.48	0.73	1.36	1.49
D3 sc.	1.09	1.15	1.40	0.84	1.14	1.32
TRMM	1.23	1.57	1.88	1.31	1.32	1.30
Obs	1.00	1.00	1.00	1.00	1.00	1.00

Table 5.9: Annual precipitation and routed discharge sums using (i) real time *MM5* results (D2 and D3), (ii) scaled *MM5* results (D2 sc. and D3 sc.), and (iii) the scaled *TRMM* product as meteorological input relative to the simulation result using (iv) observation data (Obs) for 2004 and 2005

the unscaled *MM5* results for 2005, which also appear in the runoff time series in Figure 5.23. Therefore, the scaling of *MM5* results leads to a distinctive decrease of mean annual routed discharge for 2005. For 2004, positive and negative changes occur due to the scaling of *MM5* results. Furthermore, Table 5.9 clearly shows a nonlinear and subcatchment specific relationship between precipitation and runoff.

Second, Nash-Sutcliffe model efficiencies, NSE, are calculated for the performance comparison of the hydrological simulations driven by the different meteorological input data sources. In Table 5.10, NSE values for the logarithms of the runoff values, due to the objective of simulating the entire discharge hydrograph without special emphasis on peak flows, are given for all applied meteorological input data sources. For each station and for each year best $logNSE$ values of all performed hydrological simulations are highlighted. In general, $logNSE$ values for 2004 are better than the ones for 2005. The scaling leads, except for the head basin Nasia, to reasonable results for 2005. For 2004, scaling affects the model's performance positively (Nasia) and negatively (Pwalugu). $logNSE$ values for hydrological simulations driven by *TRMM* data are similar or worse than the ones with scaled *MM5* results for both years and the unscaled *MM5* results for 2004. The best $logNSE$ values for

(a) MM5

	2004			2005		
	Nasia	Nawuni	Pwalugu	Nasia	Nawuni	Pwalugu
D2	0.53	0.78	0.52	-0.65	-0.15	-0.09
D3	0.27	0.71	**0.62**	-1.24	-0.07	0.06
D2 sc.	0.63	0.77	0.39	0.16	0.53	0.22
D3 sc.	0.58	0.75	0.47	-0.30	0.72	0.40

(b) TRMM and Observations

	2004			2005		
	Nasia	Nawuni	Pwalugu	Nasia	Nawuni	Pwalugu
TRMM	0.55	0.62	0.13	0.17	0.47	0.35
Obs	**0.68**	**0.80**	0.46	**0.32**	**0.75**	**0.56**

(c) MM5/TRMM at Observations

	2004			2005		
	Nasia	Nawuni	Pwalugu	Nasia	Nawuni	Pwalugu
D2 at Obs	0.79	0.74	0.54	-0.78	0.15	0.34
D3 at Obs	0.81	0.80	0.53	-0.63	0.14	0.31
D2 sc. at Obs	0.80	0.77	0.34	0.35	0.72	0.56
D3 sc. at Obs	0.80	0.74	0.35	0.30	0.80	0.59
TRMM at Obs	0.57	0.54	0.15	0.14	0.71	0.51

Table 5.10: Nash-Sutcliffe efficiencies, logNSE, of the hydrological modelling results using different meteorological input for 2004 and 2005: (a) real time *MM5* (D2 and D3) and scaled *MM5* results (D2 sc. and D3 sc.), (b) scaled *TRMM* product and observations, (c) all gridded meteorological data sources at observation sites

all simulations listed in Table 5.10(a) and (b) are obtained with meteorological observation data. Table 5.10(c) depicts $logNSE$ values of hydrological simulations where *MM5* results or *TRMM* data are interpolated for each location of the observation stations and hydrological simulations are performed with the station data setup. Applying this method leads to good model performances; in the majority to the best ones of all performed hydrological simulations, although a lot of information of the basin-wide, available, gridded data sources is not considered in these hydrological simulations.

The performance comparison of hydrological modelling results using different meteorological data sources shows, that the estimation and representation of the high spatial and temporal distribution of precipitation is crucial for the hydrological simulation results. For example, according to Beven (2001) the estimation of precipitation is very important in rainfall-runoff modeling since no model, however well founded in physical theory or empirically justified by past performance, will be able to produce accurate hydrograph predictions if the in-

puts to the model do not characterize the precipitation inputs. This implicates to correct known precipitation biases before the application in hydrological simulations.

5.4 Summary

In this chapter hydrological simulations driven by different meteorological input data sources and for different time periods are performed. Current and near real time hydrological simulations for the White Volta basin require meteorological modelling results. The performance of the *MM5* simulations is good and comparable to the performance of the scaled *TRMM* product 3B42, which is available with one month delay. The performance is further improved by scaling the *MM5* results with gridded observations from *GPCC*.

The hydrological model *WaSiM* is calibrated and validated with historical observation data. The performance is good, considering the limited data availability of meteorological data and the coarse resolution of soil and land use data. With the historical data sets, long-term (1961-2000) water balance simulations are performed, which provide long-term information on the temporal and spatial distribution of water balance variables in the White Volta basin.

Near real time water balance estimations require joint atmospheric- hydrological simulations. The joint *MM5-WaSiM* results in expost hindcast mode show a good performance for 2004 and a weaker one for 2005. This is due to precipitation overestimations. Scaled *MM5* results improve the simulation results considerably for 2005. The performance of the hydrological simulations using the scaled *TRMM* product 3B42 are good. However, the performance of hydrological simulations driven by *TRMM* data is lower compared to the simulations with real time and scaled *MM5* output for 2004 and scaled *MM5* output for 2005. The use of station data as the meteorological data source leads to good and usually best model efficiencies. In the majority of cases, the performances of hydrological simulations using *MM5* and *TRMM* results at the observation stations outperform the previously applied simulation results, although a lot of information from the gridded data sources is not considered. In general, the performance comparison of hydrological modelling results using different meteorological data sources shows, that the estimation and representation of the high spatial and temporal distribution of precipitation is crucial for the hydrological simulation results.

In this chapter, validation of hydrological modelling driven by the different meteorological input data sources, is based on the comparison to available, observed discharges. The application, and the potential of joint atmospheric-hydrological simulations, will be discussed in detail in Chapter 8.

6 Assimilation of satellite derived land surface properties

6.1 Introduction

A major problem in hydrology is the lack of adequate data to quantitatively describe hydrological processes accurately. For this purpose, additionally to meteorological input discussed in the previous chapter, land surface properties are required. In general, remote sensing technology helps answer hydrological questions as follows (Schultz, 1988):

- It produces areal measurements in place of point measurements.
- All information is collected and stored at one place.
- It offers high resolution in space and/or time.
- Data are available in digital form.
- Data acquisition does not interfere with data observation.
- Data can be gathered for remote areas that are otherwise inaccessible.
- Once the remote sensing networks are installed, data measurement is relatively inexpensive.

According to Singh (1995), remote sensing and satellite data can be used for watershed modelling. This data are useful, especially when data collection sites and the cost-effectiveness of data collection are important on the one hand, and increasing requirement for data on the other hand. For the White Volta basin, or in general for basins with a weak infrastructure and few or no observation data, remote sensing is a valuable data source and satisfies several data requirements in hydrological modelling. A further important point is the time of data availability. This depends on the product but, in general, remote sensing data are transmitted faster compared to data loggers with offline data transfer, which require data collection on site and partial digitalization before they become available for modelling purposes.

Different kinds of remote sensing data are used in hydrology. According to Singh (1995), these can be summarized in two ways: First, satellite data

can be used to better define soils and land covers over a watershed, which are needed to determine infiltration, evapotranspiration and runoff. Second, remote sensing measures data over a space rather than at a point, and can, therefore, be used to correct errors in input data based on point measurements. Furthermore, remote sensing data can be used to estimate evapotranspiration and soil moisture fields using thermal infrared images.

In this study, remote sensing data is used for a better description of land surface parameters in hydrological modelling. Thus, satellite data are not used to better define soils and land cover, but rather to describe land surface properties over a watershed. Albedo and the leaf area index (LAI) are essential input data for distributed hydrological modelling. Both variables have an impact on the calculation of potential evapotranspiration in hydrological modelling, which is described in the following section.

6.2 Potential evapotranspiration after Penman-Monteith

The following section is mainly based on Schulla and Jasper (2000). For the calculation of potential evapotranspiration with *WaSiM*, the approach after Penman-Monteith (Monteith, 1975; Brutsaert, 1982) is used:

$$\lambda E = \frac{3.6 \cdot \frac{\Delta}{\gamma_p}(\boldsymbol{R_N} - G) + \frac{\rho \cdot c_p}{\gamma_p \cdot r_a}(e_s - e) \cdot t_i}{\frac{\Delta}{\gamma_p} + 1 + \frac{\boldsymbol{r_s}}{r_a}} \tag{6.1}$$

with

	λ	$[kJ/kg]$	latent vaporization heat: $\lambda = 2500.8 - 2.372 \cdot T[^\circ C]$
	E	$[mm/m^2]$	latent heat flux: $[mm/m^2] \equiv [kg/m^2]$
	Δ	$[hPa/K]$	tangent of saturated vapour pressure curve $\Delta = \frac{\partial e_s}{\partial T}$
	$\boldsymbol{R_N}$	$\boldsymbol{[Wh/m^2]}$	**net radiation**
	G	$[Wh/m^2]$	soil heat flux, here: $0.1 \cdot R_N$
	ρ	$[kg/m^3]$	density of dry air
	c_p	$[kJ/(kg \cdot K)]$	specific heat capacity of dry air at constant pressure: $c_p = 1.005$
	e_s	$[hPa]$	saturation vapour pressure at temperature T
	e	$[hPa]$	actual vapour pressure (observed)
	t_i	$[-]$	number of seconds within a time step
	γ_p	$[hPa/K]$	psychometric constant
	$\boldsymbol{r_s}$	$\boldsymbol{[s/m]}$	**bulk-surface resistance**
	r_a	$[s/m]$	bulk-aerodynamic resistance

Equation 6.1 has units of energy flux, i.e. the flux of latent heat in $[kJ/m^2]$. The factor of 3.6 is the result of the conversion of net radiation from $[Wh/m^2]$ to $[kJ/m^2]$. The potential evaporation approach after Penman-Monteith is affected by surface albedo and LAI through the calculation of net radiation and bulk-surface resistance respectively (see bold variables in Equation 6.1). The net radiation R_N is defined as

$$R_N = (1 - \boldsymbol{\alpha}) \cdot RG - R_L \tag{6.2}$$

with	R_N	$[Wh/m^2]$	net radiation
	$\boldsymbol{\alpha}$	$[-]$	**surface albedo**
	RG	$[Wh/m^2]$	global radiation: $RG = R_{sun} + R_{sky}$ with shortwave direct R_{sun} and diffuse R_{sky} radiation
	R_L	$[Wh/m^2]$	longwave radiation: $R_L = R_{out} - R_{in}$

Thus, surface albedo $\boldsymbol{\alpha}$ is defined as the reflectance of incident energy by the surface integrated over the visible wavelengths (Dingman, 2002). Surface albedo values are determined by surface reflectance properties, which vary for different forms of surface materials and wetness. Considering Equation 6.1 and Equation 6.2, increasing surface albedo values lead to decreasing net radiation R_N and latent heat flux λE.

The surface resistances r_s are estimated differently for day and night. For the bright day r_s is defined as:

$$\frac{1}{r_s} = \frac{(1 - A)}{r_{sc}} + \frac{A}{r_{ss}} \tag{6.3}$$

with	r_s	$[s/m]$	minimum surface resistance
	r_{sc}	$[s/m]$	r_s of plants if fully supplied with water
	r_{ss}	$[s/m]$	surface resistance for bare soil: ≈ 150
	$1 - A$	[-]	evaporation effective vegetation coverage $A = f^{\boldsymbol{LAI}}$ with $f \approx 0.6...0.7$

At night time the following relation is valid:

$$\frac{1}{r_s} = \frac{\boldsymbol{LAI}}{2500} + \frac{1}{r_{ss}} \tag{6.4}$$

The $\boldsymbol{LAI}$ $[\mathrm{m}^2/\mathrm{m}^2]$ is defined as the relative size of a single "big leaf" which represents a reasonable uniform vegetated surface whose total conductance of water vapour is proportional to the sum of the conductances of millions of individual leafs. The variable f in Equation 6.3 is a shelter factor that accounts for the fact that some leafs are sheltered from the sun and wind and

thus transpire at lower rates (DINGMAN, 2002). In Figure 6.1, the relationship of minimum surface resistances and LAI is illustrated for day and night. Reciprocal values of minimum surface resistance at night increase slightly with increasing LAI values. On a bright day reciprocal values of minimum surface resistance for bare soil decrease with increasing LAI values, whereas the values of plants increase. Due to the fact that the impact of plants on the reciprocal values of minimum surface resistance is larger compared to bare soils, in total an increase of LAI values leads to an increase of reciprocal values of minimum surface resistance on a bright day. Considering Equation 6.1, the flux of latent heat λE is proportional to the reciprocal value of minimum surface resistance r_s. Thus, the impact of LAI is comparable to the results in Figure 6.1, which show that an increase of LAI values leads to an increase of latent heat flux on a bright day and by night.

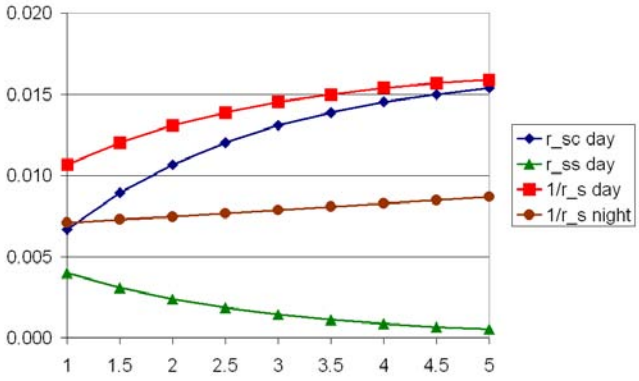

Figure 6.1: Relationship between LAI and reciprocal values of minimum surface resistances of plants (blue diamonds) and bare soil (green triangles) on a bright day, and reciprocal values of total minimum surface resistances on a bright day (red squares) and by night (brown circles)

6.3 Assimilation of satellite derived land surface properties in WaSiM

In *WaSiM*, land surface properties are usually taken from standard literature values and incorporated into hydrological modelling through tables depending on the land use. For surface albedo, only one value per land use type can be defined. For the LAI and other vegetation parameters; e.g. root depth, the intra-annual phenological development is considered by introducing four seasons. For the White Volta basin only two main seasons can be distinguished, thus the number of seasons is reduced to two (see Section 3.2.3).

Due to the fact that land surface properties are incorporated into hydrological modelling through land use, the spatial distribution of the land use grid with

static land surface properties has a high influence on the modelling result. Thus, values derived from standard literature can be imprecise for specific areas. This impreciseness is again more pronounced in developing countries, because the land use grid is less accurate and less field measurements of land surface properties exist.

On the other hand, space-borne remote sensing systems such as MODerate resolution Imaging Spectroradiometer (*MODIS*) acquire full global coverage within 1 to 2 days. A large suite of land surface properties is made available free of charge as composites of daily, 8-day or 16-day periods with a spatial resolution of 1000 m or less. In this study, the *MODIS* products of the Leaf Area Index (*LAI*, MOD15A2) and albedo (MOD43B3) are applied. According to Talagrand (1997) who defined data assimilation as "using all the available information, to determine as accurately as possible the state of the atmospheric (oceanic) flow", the import of satellite-derived land surface properties into the hydrological model is defined here as assimilation, because these data are available with a high resolution in space and time, and they provide estimations of land surface properties depending on observed reflectance.

In this study, the assimilation of satellite-derived land surface properties into the hydrological model is performed on a monthly scale. This time scale is selected as a trade-off between the representation of the annual course of land surface properties, and minimizing the number of invalid pixels due to clouds, by averaging two or four composites for surface albedo and *LAI*, respectively.

The surface albedo grid is defined as one of two variable grids in *WaSiM*, which can be either imported as a regular grid or derived from land use. Thus, the import of satellite-derived albedo grids can be performed without changes in the *WaSiM* code. Hydrological simulations are performed for each month and attached.

The *LAI* grid is created internally in *WaSiM*, thus an import of *LAI* grids is not possible with the control file, but it requires modifications in the *WaSiM* code. First, monthly *LAI* grids are imported as additional standard grids, defined in the *WaSiM* control file. Second, the generation of the *LAI* grids in the *WaSiM* code is replaced by the imported ones as follows: In *WaSiM*, *LAI* grids are generated on a daily basis. Usually, the tabulated, land use specific *LAI* values for the different seasons are linearly interpolated between the defined seasonal nodes for each grid point to consider the phenological inter-annual development. In the case of imported *LAI* grids, linear interpolation between the grids is performed for the generation of daily values for each grid point. In this study, where satellite-derived, monthly *LAI* grids are imported, daily values are interpolated between twelve nodes, each defined in the middle of a month. To control the import and linear interpolation of the *LAI* grids, the daily value for a specific point within the basin is recorded in the protocol of the simulation run.

6.4 MODIS-Products for the White Volta basin

6.4.1 MODIS instrument

As already mentioned in the previous section, the *MODIS* products of the Leaf Area Index (*LAI*, MOD15A2) and albedo (MOD43B3) are applied in this study. The MODerate resolution Imaging Spectroradiometer (*MODIS*) instrument launched onboard Terra (EOS-AM1) and Aqua (EOS-PM1) in 2000 and 2002, respectively, is a part of NASA's Earth Observing Systems (EOS) (Justice et al., 2002). A near-polar sun synchronous orbit at 705 km and a swath of 2300 km allow global coverage within one to two days. Each instrument has 36 spectral bands ranging from the visible to the thermal infrared with near-nadir spatial resolutions of 250, 500, and 1000 meters (Guentner et al., 2002; Wolfe, 2002). To investigate terrestrial ecological processes, the *MODIS* Land (MODLand) science team offers a wide range of value-added products based on *MODIS* calibrated radiances (Justice et al., 1998).

This study employs 8-day products of the *LAI* (MOD15A2) and 16-day standardized albedo composites (MOD43B3) of *MODIS* collection 4. The *MODIS* products are preprocessed at the "Remote Sensing Unit" at the Institute for Geography, University of Wuerzburg, which are project partners in the *GLOWA*-Volta project. The preprocessing, based on Wagner et al. (2007), is shortly described in the following two sections.

6.4.2 MODIS LAI and albedo for the White Volta basin

The *LAI* is defined as the total one-sided leaf area per unit ground surface (Privette et al., 2002). The standard procedure uses look-up-tables of simulated values generated by radiation transfer models (Knyazikhin et al., 1998). For collection 4, processing is separated into six biome-classes representing the most dominant vegetation types on a global scale because the retrieval of the *LAI* from spectral radiances strongly depends on leaf properties and vegetation structure (Myneni et al., 1997). Even though designed to include the first seven *MODIS* channels ranging from the visible blue to the short wave infrared (Knyazikin et al., 1998), current collection 4 data only consider red and near infrared wavelengths, due to several difficulties, such as noise in the blue channel caused by atmospheric influences. If the standard routine fails because of insufficient cloud-free observations, a back-up algorithm estimates *LAI* utilizing known empirical regressions between the Normalized Difference Vegetation Index (*NDVI*) and *LAI* (Myneni et al., 2002).

The MOD43B3 product belongs to the group of Bidirectional Reflectance Distribution Function (BRDF)/albedo products and contains black-sky (directional hemispherical) and white-sky (bi-hemispherical) albedo for the first seven *MODIS* channels (Schaaf et al., 2002). A constant situation of the earth's surface is assumed for the 16-day compositing period, and values are adjusted to

local solar-noon angles. The so-called RossThickLiSparse-Reciprocal model, a linear kernel function, is used for the derivation of single band albedos (Lucht et al., 2000). In addition, a broadband albedo from 0.3 μm to 4.0 μm is computed by integrating narrow band albedos (Liang, 2000). This study employs broadband white-sky albedo composites. MOD15A2 and MOD43B3 products are distributed as gridded 1 km spatial resolution data sets in the Sinusoidal projection and are reprojected to *UTM* zone 30 N. The unique concept of quality assurance and *MODIS* product validation (Roy et al., 2002) allowed the generation of science-quality time series.

6.4.3 MODIS time series generation

All *MODIS* products comprise additional so-called Quality Assurance Science Data Set (QA-SDS) for error estimation, atmospheric inferences, algorithms, or important surface characteristics (Roy et al., 2002). *MODIS* quality layers indicate crucial information such as cloud coverage, which is not reflected in the actual data set (Colditz et al., 2006). Besides a so-called mandatory flag, a general quality indicator available for all products, additional product-specific quality assurance flags specify the usability of each data set. The QA-SDS of the MOD15 product indicates potential cloud coverage, the algorithm used for *LAI* estimation, and possible detector failures. An additional QA-SDS provides important surface state information, which is generated by upstream data production (level 2 and 3) including a land/ water mask, more specific cloud information including cloud shadow, and aerosol retrieval (Myneni et al., 2002). Similarly, detailed quality estimators are contained in the albedo product, where the first part focuses on general issues such as mean solar angle, land/ water, or snow, and the latter part on band specific issues (Schaaf et al., 2002). The Time Series Generator (*TiSeG*, Colditz et al., 2007) is used to analyze the QA-SDS of gridded *MODIS* products (Level 2G, 3, and 4). The interactive software computes and visualizes the data availability according to user-defined quality specifications. Two critical indices, the number of invalid pixels and the maximum gap length, are computed and displayed spatially and temporally. The number of invalid pixels is a general indication of the data availability. The maximum gap length computes the longest period of invalid data according to user-defined quality settings. Next, pixels indicated as invalid data can be either masked or interpolated with spatial or temporal approaches. A thorough discussion of *TiSeG*, its functionalities, design, and performance is provided in Colditz et al. (2007).

As an example, *LAI* time series processing is shown. The *LAI* time series generation with *TiSeG* involves a quality analysis followed by a linear temporal interpolation of all pixels which do not have good or acceptable quality. In total, the selected settings result in 70% of pixels beeing acceptable for interpolation. All pixels belonging to an internal mask of water, urban, and non-vegetated

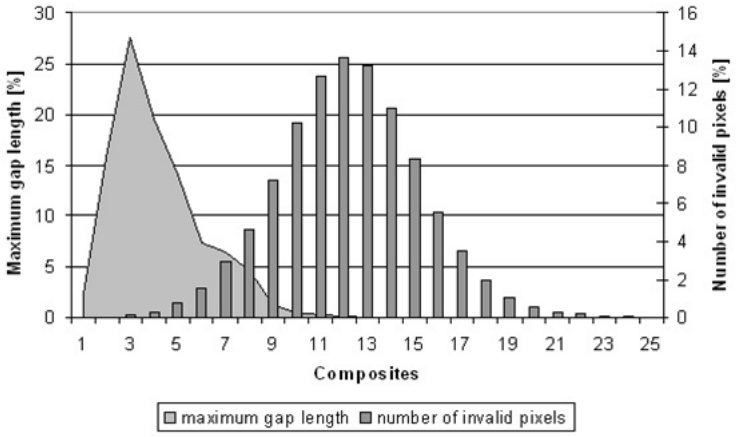

Figure 6.2: Histogram of maximum gap length (bright filled area) and number of invalid pixels (dark columns) for *LAI* time series

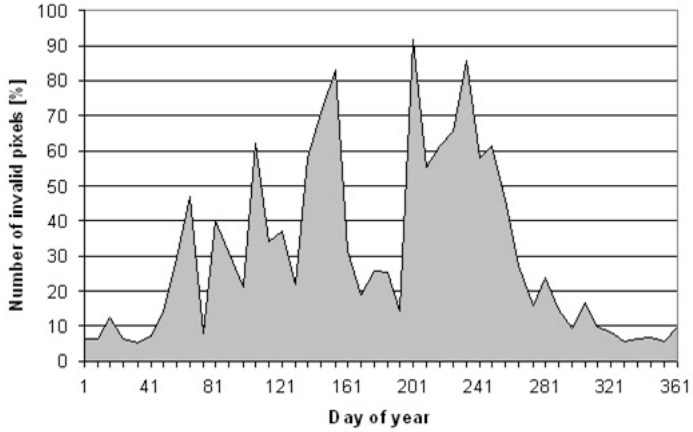

Figure 6.3: Temporal plot of the number of invalid *LAI* pixels in percent

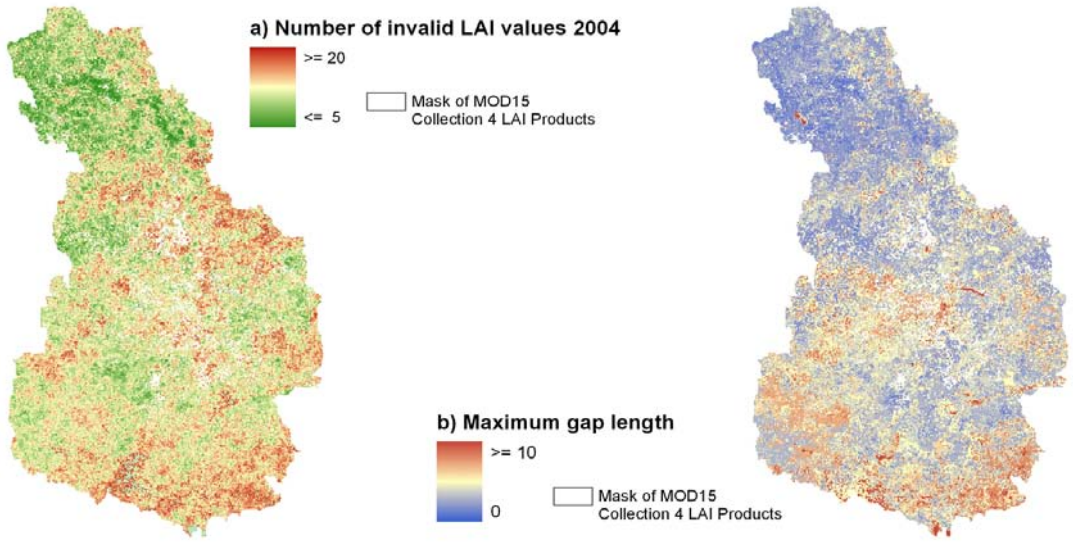

Figure 6.4: Spatial quality analysis with *TiSeG*, (a) number of invalid *LAI* values, (b) maximum gap length

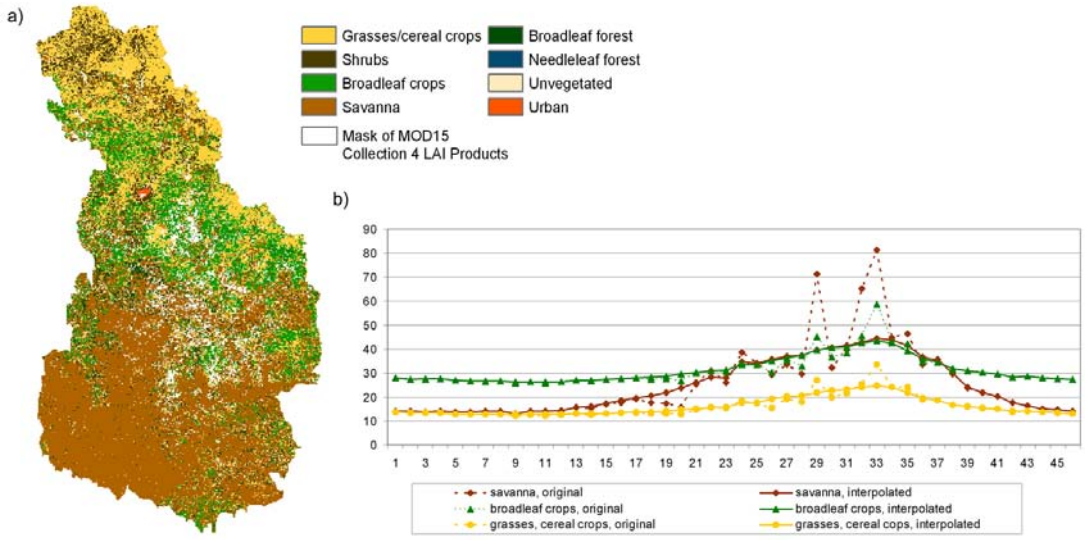

Figure 6.5: The biome map of the White Volta basin (a) and original (dashed lines) and *TiSeG* corrected (solid lines) average *LAI* (multiplied by factor 10) plots (b) for dominating biomes savannah, broadleaf crops, and grassland/cereal crops

pixels are excluded from *LAI* processing. For a single pixel the respective time series contains between 0 and 25 invalid values (Figure 6.2). Except for better conditions in the northernmost portion, the spatial distribution of invalid pixels is nearly homogeneous throughout the White Volta catchment (Figure 6.4(a)). The temporal analysis reveals that most invalid pixels occurr in the wet season between March and September (Figure 6.3). The latter shows the seasonality with a long-lasting rainy period and substantial cloud coverage throughout the summer. The frequent drops in the graph however, indicate that the resulting data gaps are comparatively short. The maximum gap to be interpolated is lower than eight composites for more than 85% of the entire catchment (Figure 6.2) and the spatial view depicts a decreasing trend of the maximum gap towards less cloudy conditions in the northern area (Figure 6.4(b)). For the dominating biomes, savannahs in the South as well as grassland/cereal crops and broadleaf crops in the northern part of the catchment (Figure 6.5(a)), the average *LAI* time series are depicted in Figure 6.5(b). Changes resulting from temporal interpolation with respect to original data are highlighted. The dashed lines representing the original data clearly show inaccuracies which are excluded with the quality analysis using *TiSeG* (solid lines). Outliers in the late wet season are eliminated. The interpolated *LAI* profiles represent the expected phenological development starting to increase with the beginning of the wet season.

6.5 Relationship between albedo, LAI and precipitation

In the following section the relationship between albedo, *LAI* and precipitation for the White Volta basin is given, which is described for the sahel zone in Govaerts and Lattanzio (2007). Due to the climate and atmospheric dynamics in West Africa, which are described in Section 2.2, around 80% of annual precipitation falls between July and September, which induces fast vegetation growth. The following dry season produces a rapid drying of the vegetation. These successive vegetation growth and senescence phases are resposible for vegetation physiological modifications that result in changes of the spectral signature and brightness of land surfaces, thereby affecting the surface albedo. As bare soils tends to be brighter than vegetation, an increase in vegetation cover generally translates into a decrease in surface albedo (Pinty et al., 2000).

This relationship between precipitation, vegetation, and surface albedo seasonal cycles over the White Volta is shown in Figure 6.6. It can be seen that the precipitation seasonal cycle (blue) affects both the surface albedo (green) and vegetation (red). Increased precipitation amounts from June to September determine the surface albedo decrease and the *LAI* increase observed from July to September. Both variables respond approximately with one month delay on

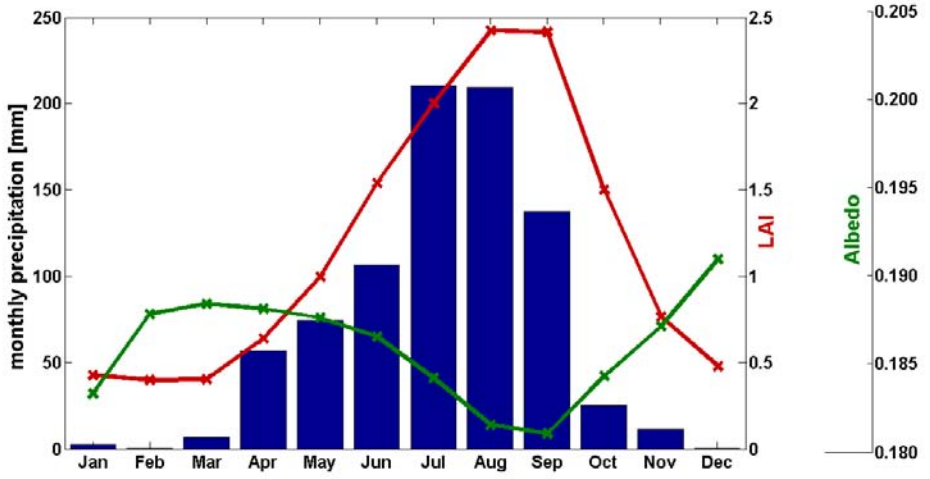

Figure 6.6: Seasonal cycle of monthly mean precipitation [mm/month], leaf area index *LAI* (red) and surface albedo (green) averaged over the White Volta basin for 2004

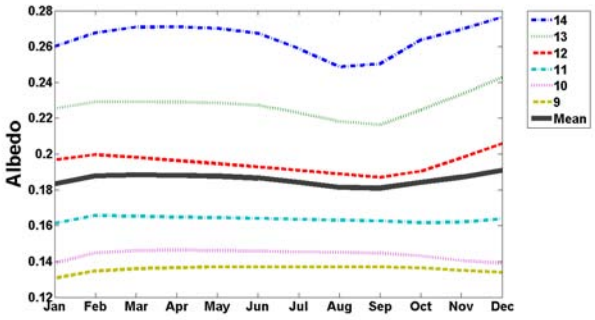

(a) albedo

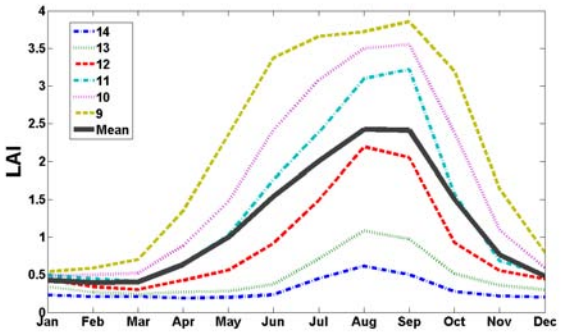

(b) leaf area index

Figure 6.7: Latitudinal profile of the seasonal cycle of monthly mean (a) surface albedo and (b) leaf area index *LAI* over the White Volta basin for 2004

changes in precipitation, which can also be seen at the end of the rainy season with a delayed decrease or increase of *LAI* and albedo values respectively. Figure 6.7 shows the latitudinal profile, with one degree resolution, of the seasonal cycle of monthly mean surface albedo and leaf area index *LAI* over the White Volta basin for 2004. For both variables, a large latitudinal dependency exists. For surface albedo this latitudinal dependency is more pronounced than the seasonal cycle. Highest surface albedo values are measured in the North in less vegetated region, which also show dynamics in the seasonal cycle. For latitudes 9° to 11°, albedo is almost constant for the entire year. For the *LAI*, highest values and dynamics are measured in the South which decrease continuously with increasing latitude. The seasonal cycle is more pronounced compared to the one of surface albedo.

6.6 Impact of satellite derived land surface properties on hydrological simulations

The preprocessed, disseminated *MODIS* data have to be processed further for the application in the hydrological model. *MODIS* data are stored in tiles of 10° by 10° using the integerized sinusoidal grid projection. The White Volta basin is located in four tiles. Thus, these four tiles have to be merged before the area of the White Volta basin is clipped. Afterwards, a resampling method is required to convert the *MODIS* data to the grid size of the hydrological simulations. In this study, *MODIS* data with a spatial resolution of 926.6 m are interpolated to 1000 m using the nearest neighbour method. Thus, gridded *MODIS* data with a spatial resolution of 1 km and a temporal one of 8-days for *LAI* and 16-days for albedo are available for hydrological simulations. As already mentioned in Section 6.3, the *MODIS* albedo and *LAI* time series are aggregated to monthly means for the hydrological simulations. Comparisons between standard literature tabulated and *MODIS* values are presented in the following sections.

6.6.1 Albedo comparison

In *WaSiM* the albedo is time-invariant which results in one value per land use class, which are taken from Grell et al. (1995). Figure 6.8 shows a comparisons between standard literature tabulated and *MODIS* quarterly values, averaged from monthly ones, for 2004. Figure 6.8 shows a North-South gradient of the albedo values in all subplots. For the *MODIS* albedo grids the gradients are larger and also more heterogeneous in the spatial dimension. During the rainy season (Jul-Sep), the *MODIS* albedo grid is more homogeneous compared to the rest of the year. However, all seasonal aggregations depict similar spatial patterns of *MODIS* albedo which shows the stability of the parameter confirming the time-invariance of the albedo assumed in *WaSiM*. For 2005

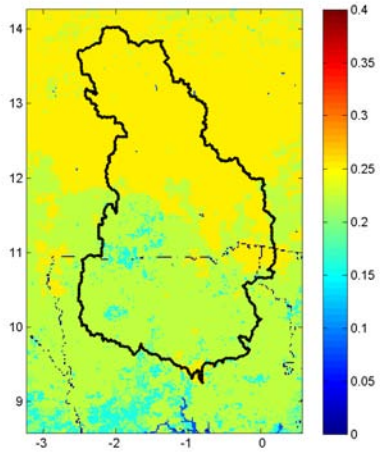

(a)

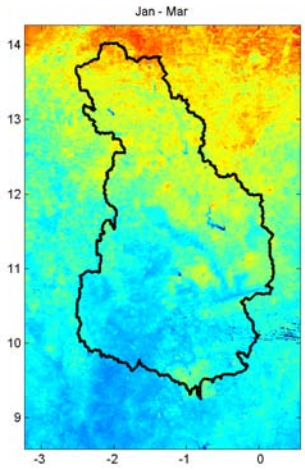

(b) MODIS: Jan-Mar

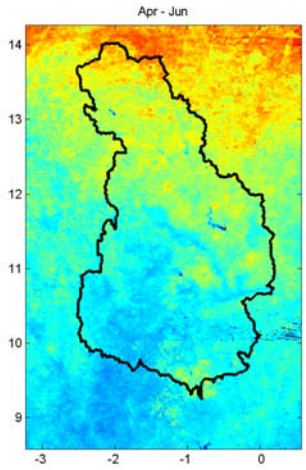

(c) MODIS: Apr-Jun

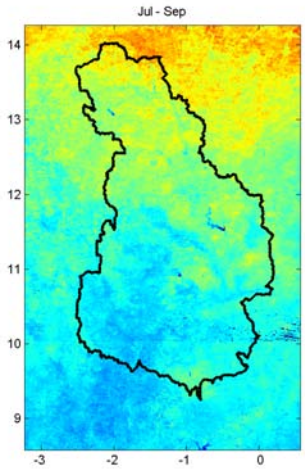

(d) MODIS: Jul-Sep

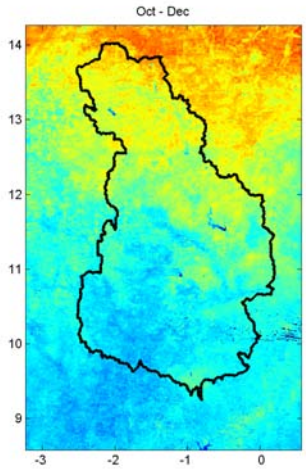

(e) MODIS: Oct-Dec

Figure 6.8: Albedo grid of the White Volta basin using (a) static tabulated values and (b)-(e) dynamic *MODIS* estimates averaged to 3-month means for 2004

(see Figure A.3 in Appendix A), the spatial distribution and absolute values are in general comparable to the results of 2004, but the more homogeneous field with lower values during the rainy season (Jul-Sep) is less pronounced.

Overall, *MODIS* albedo values are slightly lower compared to standard literature ones. The benefit of using *MODIS* data obviously results from the increased level of detail in the spatial dimension.

6.6.2 LAI comparison

Figure 6.9 shows a comparison between standard literature tabulated- and *MODIS* values for 2004, where monthly *MODIS* data are averaged to quarterly means. For the *LAI*, two seasons are defined for the hydrological simulations with tabulated land surface parameter values (Fensholt et al., 2004; Asner et al., 2003): a dry season between November and April with *LAI* values of mostly 0.5 in the northern and 1.5 in the southern part of the catchment and a rainy season between May and October with corresponding *LAI* values of 1.5 and 2.5 (see Figure 6.9(a)-(b)). The 3-monthly averaged *LAI* values of *MODIS* (Figure 6.9(c) to (f)) are relatively constant at about 0.5 between January and March. The *LAI* values start to increase according to the expected phenological development, beginning with the rainy season starting from the South (see also Figure 6.5). During the rainy season, between July and September, the *LAI* values reach their maxima. With the beginning of the dry season between October and December the *LAI* values decrease from the North. For 2005 (see Figure A.4 in Appendix A), the temporal development and spatial distribution are in general comparable to the results of 2004. However, some differences occur. The increase of *LAI* values from April to June is less pronounced and also the *LAI* maxima between July and September are slightly lower.

The temporal development of the *LAI* values is more distinctive in the southern and central part of the White Volta basin. The comparison of static literature values and dynamic *MODIS* estimates for *LAI* shows that the temporal development of *LAI* values is not sufficiently represented by two seasons with static values. In comparison to *MODIS LAI*, the tabulated values overestimate the *LAI* during the dry season and underestimate it during the rainy season in the southern part of the catchment.

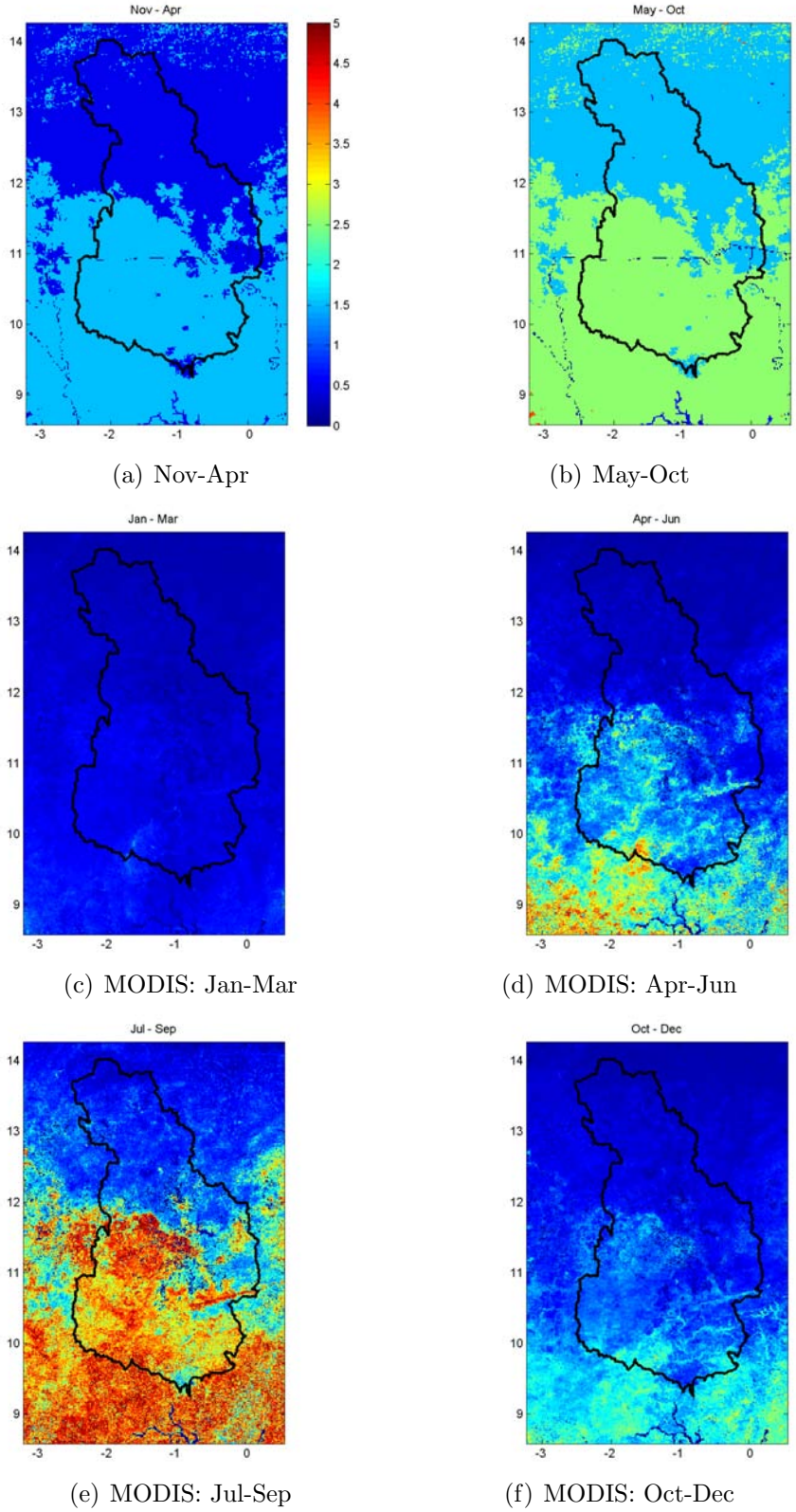

(a) Nov-Apr (b) May-Oct

(c) MODIS: Jan-Mar (d) MODIS: Apr-Jun

(e) MODIS: Jul-Sep (f) MODIS: Oct-Dec

Figure 6.9: *LAI* grid of the White Volta basin using (a)-(b) static tabulated values and (c)-(f) dynamic *MODIS* estimates averaged to 3-month means for 2004

6.6.3 Impact of MODIS albedo and LAI on water balance estimation

The results of the hydrological simulations, driven by static and dynamic albedo and *LAI MODIS* estimates, are discussed in this section.

Impact of MODIS albedo and LAI on daily time series

First, time series and the sum of differences with respect to static tabulated values of daily potential and actual evapotranspiration, as well as total discharge, for the White Volta basin for 2004 and 2005 using (i) static tabulated values for albedo and *LAI*, (ii) dynamic *MODIS* estimates for albedo and static tabulated values for *LAI*, (iii) static tabulated values for albedo and dynamic *MODIS* estimates for *LAI*, and (iv) dynamic *MODIS* estimates for albedo and *LAI* are investigated in Figure 6.10 to Figure 6.12.

For potential evapotranspiration (see Figure 6.10), the time series of all applied combinations are similar, except during the dry season, between November and March and at the end of the year, when slightly higher values are calculated using nothing or only albedo from *MODIS* estimates. The sum curves of daily differences show that, using dynamic *MODIS* estimates for albedo and static tabulated values for *LAI* (green), leads to slightly higher values during the complete year, whereas *MODIS* estimates for *LAI* (red) are lower during the dry and equal to slightly higher during the rainy season. These results agree well with the theoretical impact of albedo and *LAI* on the calculation of potential evapotranspiration after Penman-Monteith (see Section 6.1) and the differences of albedo and *LAI* grids using static tabulated or dynamic *MODIS* values. For albedo, the overall *MODIS* values are slightly lower compared to standard literature ones, which leads to slightly higher potential evapotranspiration rates, and thus a positive sum of differences values. For the *LAI*, *MODIS* values are, compared to tabulated ones, lower during the dry season and higher during the rainy season in the southern part of the catchment. For the calculation of potential evapotranspiration, these differences lead to slightly lower values during the dry and higher ones during the rainy season using *MODIS LAI* estimates. This is depicted in the sum of differences curve for *MODIS LAI*. Using *MODIS* estimates for both, albedo and *LAI*, results in a sum of differences curve showing the dynamic of the *MODIS LAI* curve and the impact of positive changes applying *MODIS* albedo. The temporal development of the sum of differences curves is similar for both years, but the interannual variations of albedo and *LAI*, discussed in Section 6.6.1 and Section 6.6.2, impact mainly the magnitude.

For actual evapotranspiration (see Figure 6.11), the time series of all applied combinations are similar. The sum curve of daily differences for albedo increases continuously until the end of the rainy season, according to the results

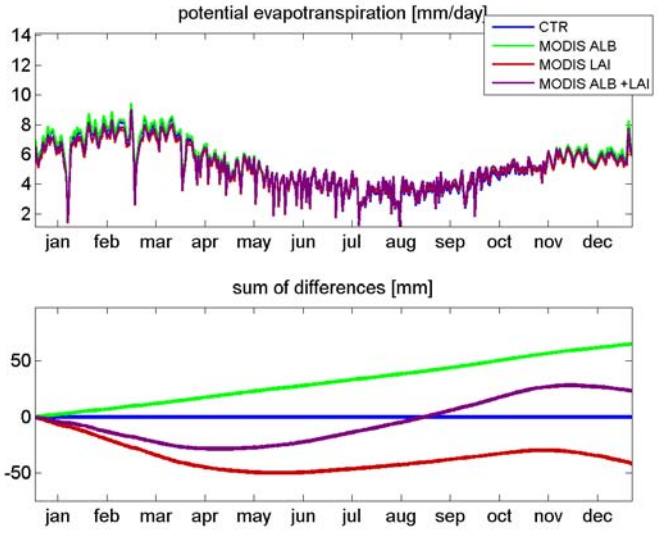

(a) 2004

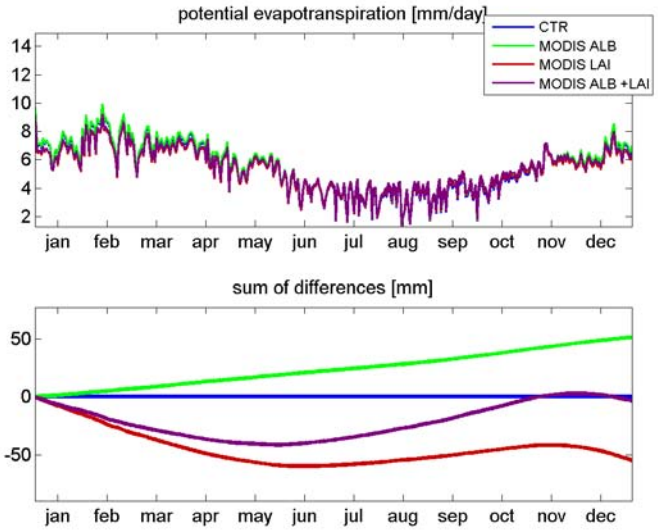

(b) 2005

Figure 6.10: Daily potential evapotranspiration [mm]: time series and sum of differences with respect to static tabulated values for the White Volta basin for 2004 and 2005, using static values for albedo and *LAI* (blue), *MODIS* values for albedo and static ones for *LAI* (green), static values for albedo and *MODIS* ones for *LAI* (red), and *MODIS* values for albedo and *LAI* (purple)

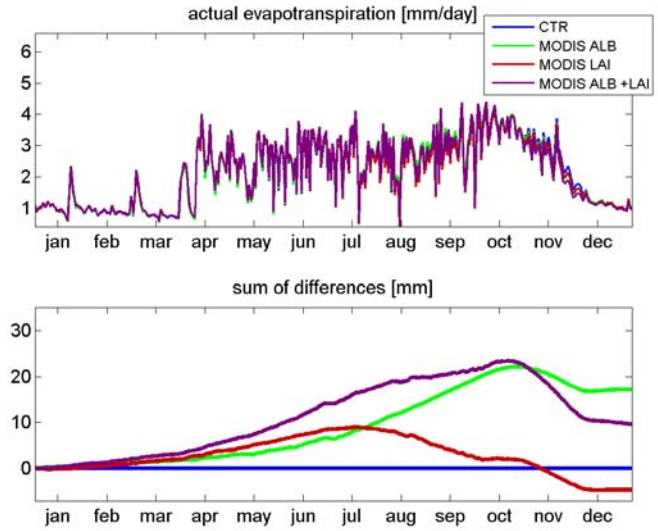

(a) 2004

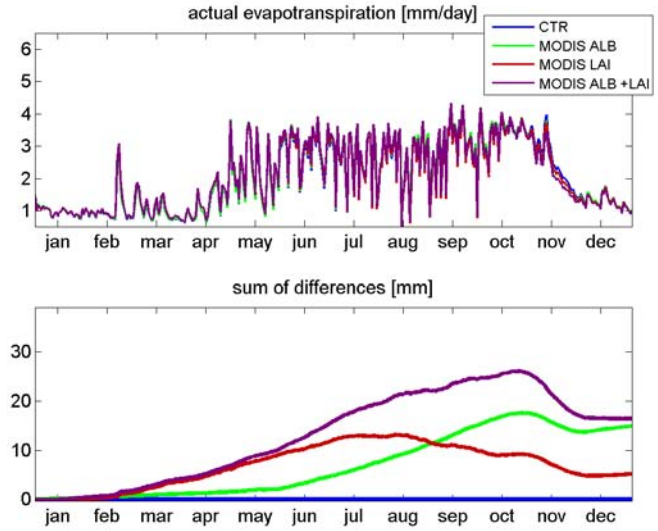

(b) 2005

Figure 6.11: Daily actual evapotranspiration [mm]: time series and sum of differences with respect to static tabulated values for the White Volta basin for 2004 and 2005, using static values for albedo and *LAI* (blue), *MODIS* values for albedo and static ones for *LAI* (green), static values for albedo and *MODIS* ones for *LAI* (red), and *MODIS* values for albedo and *LAI* (purple)

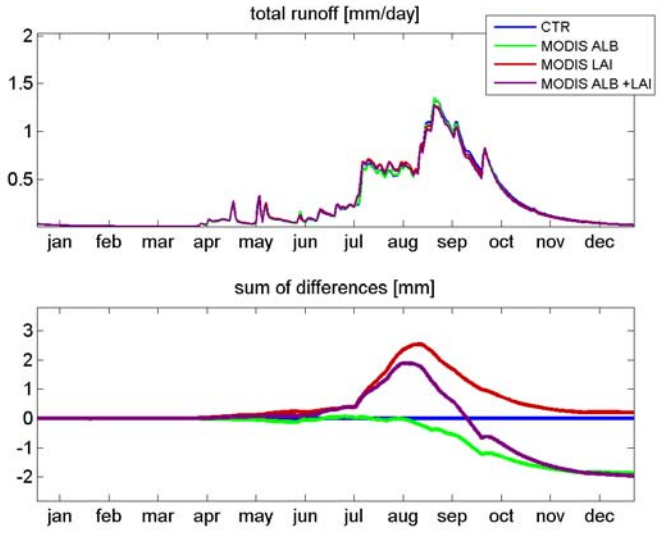

(a) 2004

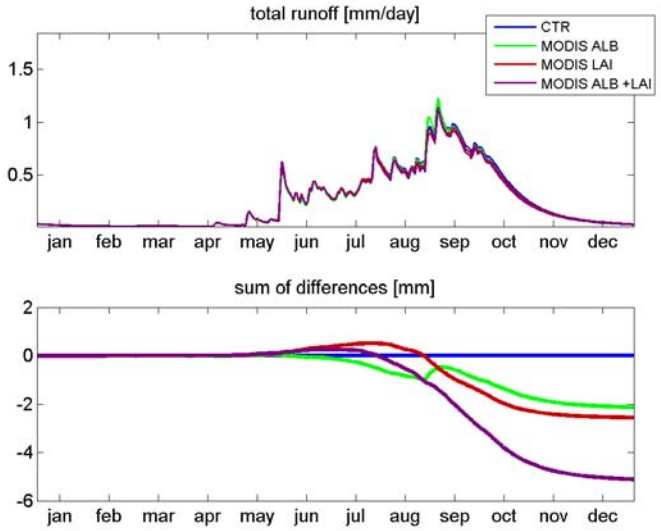

(b) 2005

Figure 6.12: Daily total runoff [mm]: time series and sum of differences with respect to static tabulated values for the White Volta basin for 2004 and 2005, using static values for albedo and *LAI* (blue), *MODIS* values for albedo and static ones for *LAI* (green), static values for albedo and *MODIS* ones for *LAI* (red), and *MODIS* values for albedo and *LAI* (purple)

of potential evapotranspiration. For *LAI*, higher actual evapotranspiration values are calculated until July using *MODIS* estimates. The annual sum of daily differences is slightly negative for 2004 and positive for 2005. In contrast to potential evapotranspiration, daily actual evapotranspiration values are higher compared to static, tabulated ones during the dry season. This is due to a higher soil water content in the simulations with *LAI* from *MODIS* estimates, which are not shown here. Using *MODIS* estimates for both, albedo and *LAI*, higher actual evapotranspiration values are calculated compared to static, tabulated ones until the end of the rainy season, and lead to a positive annual sum of daily differences. The interannual variations of albedo and *LAI* impact mainly the magnitude of the sum of differences for actual evapotranspiration, which leads for the *LAI* in total to negative (2004) and positive (2005) annual sum of daily differences.

For total runoff (see Figure 6.12) the time series of all applied combinations are again very similar. The range of the sum curves of daily differences is narrow. Generally, *MODIS* estimates for *LAI* lead to minimally higher values of total runoff from June to August. For the rest of the rainy season differences are slightly negative. The same applies using *MODIS* estimates for albedo. Thus, using *MODIS* estimates for both, albedo and *LAI*, in total the annual sum of daily differences is negative. For total runoff, the interannual variations of albedo and *LAI* impact both the temporal development and magnitude of the sum of differences.

Impact of MODIS albedo and LAI on annual spatial distribution

Additionally to the time series, the impact of dynamic estimates of albedo and *LAI* on the spatial distribution of water balance variables in the White Volta basin is investigated.

First, the spatial distribution of annual potential evapotranspiration is shown for 2004 (see Figure 6.13) and for 2005 (see Figure 6.14) using (i) static tabulated values for both variables, (ii) dynamic *MODIS* estimates for albedo and static tabulated values for *LAI*, (iii) static tabulated values for albedo and dynamic *MODIS* estimates for *LAI*, and (iv) dynamic *MODIS* estimates for albedo and *LAI*. The impact of the applied data sources for albedo and *LAI* on the spatial distribution of annual potential evapotranspiration is clearly visible. The use of dynamic *MODIS* estimates for albedo increases the spatial variability in the northern part of the White Volta basin compared to the simulation results using static tabulated values for both variables. In contrast, dynamic *MODIS* estimates for *LAI* impact annual potential evapotranspiration mainly in the central and southern part of the White Volta basin. The use of dynamic *MODIS* estimates for albedo and *LAI* leads to a superposition of both described impacts.

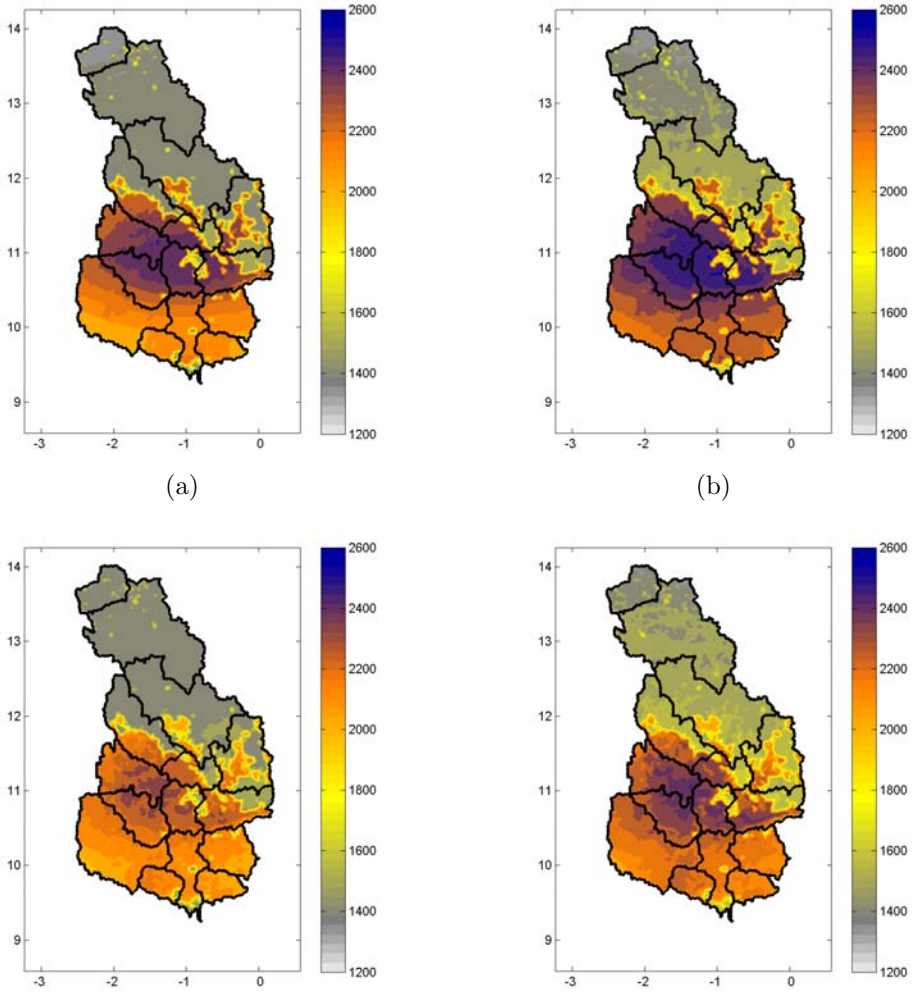

Figure 6.13: Annual potential evapotranspiration [mm] for the White Volta basin for 2004 using (a) static tabulated values for albedo and *LAI*, (b) dynamic *MODIS* estimates for albedo and static tabulated values for *LAI*, (c) static tabulated values for albedo and dynamic *MODIS* estimates for *LAI*, and (d) dynamic *MODIS* estimates for albedo and *LAI*

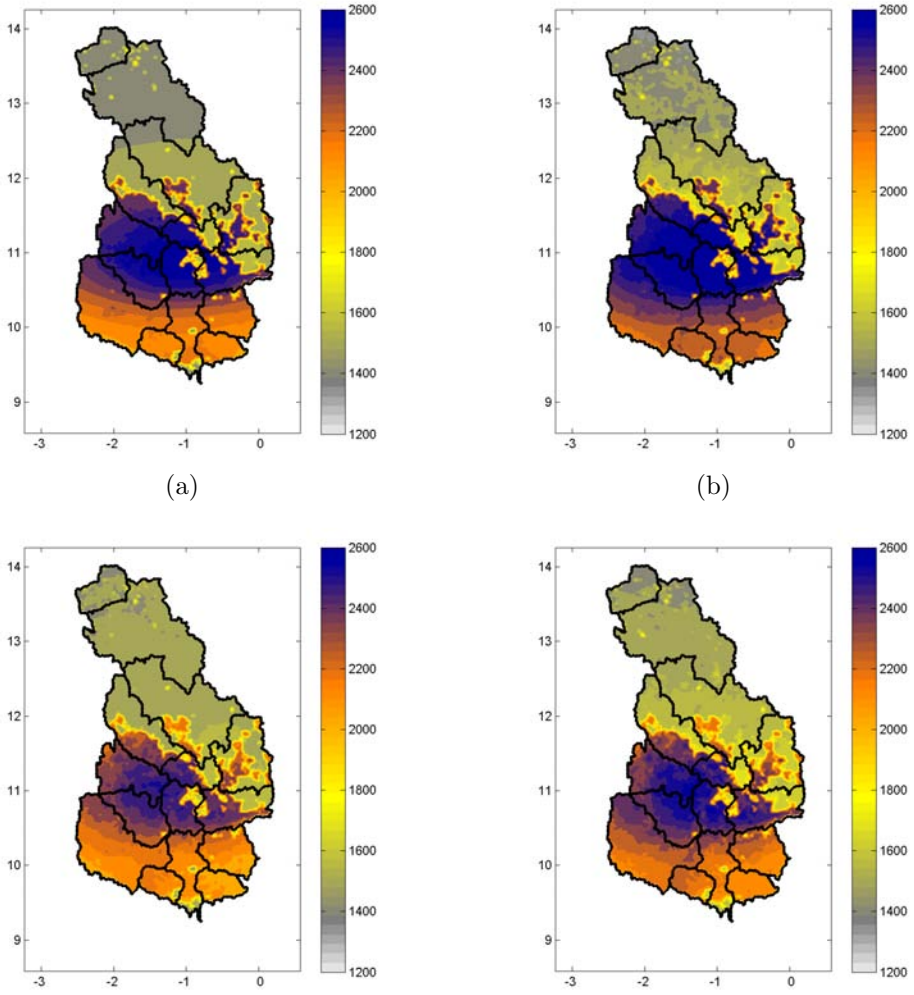

Figure 6.14: Annual potential evapotranspiration [mm] for the White Volta basin for 2005 using (a) static tabulated values for albedo and *LAI*, (b) dynamic *MODIS* estimates for albedo and static tabulated values for *LAI*, (c) static tabulated values for albedo and dynamic *MODIS* estimates for *LAI*, and (d) dynamic *MODIS* estimates for albedo and *LAI*

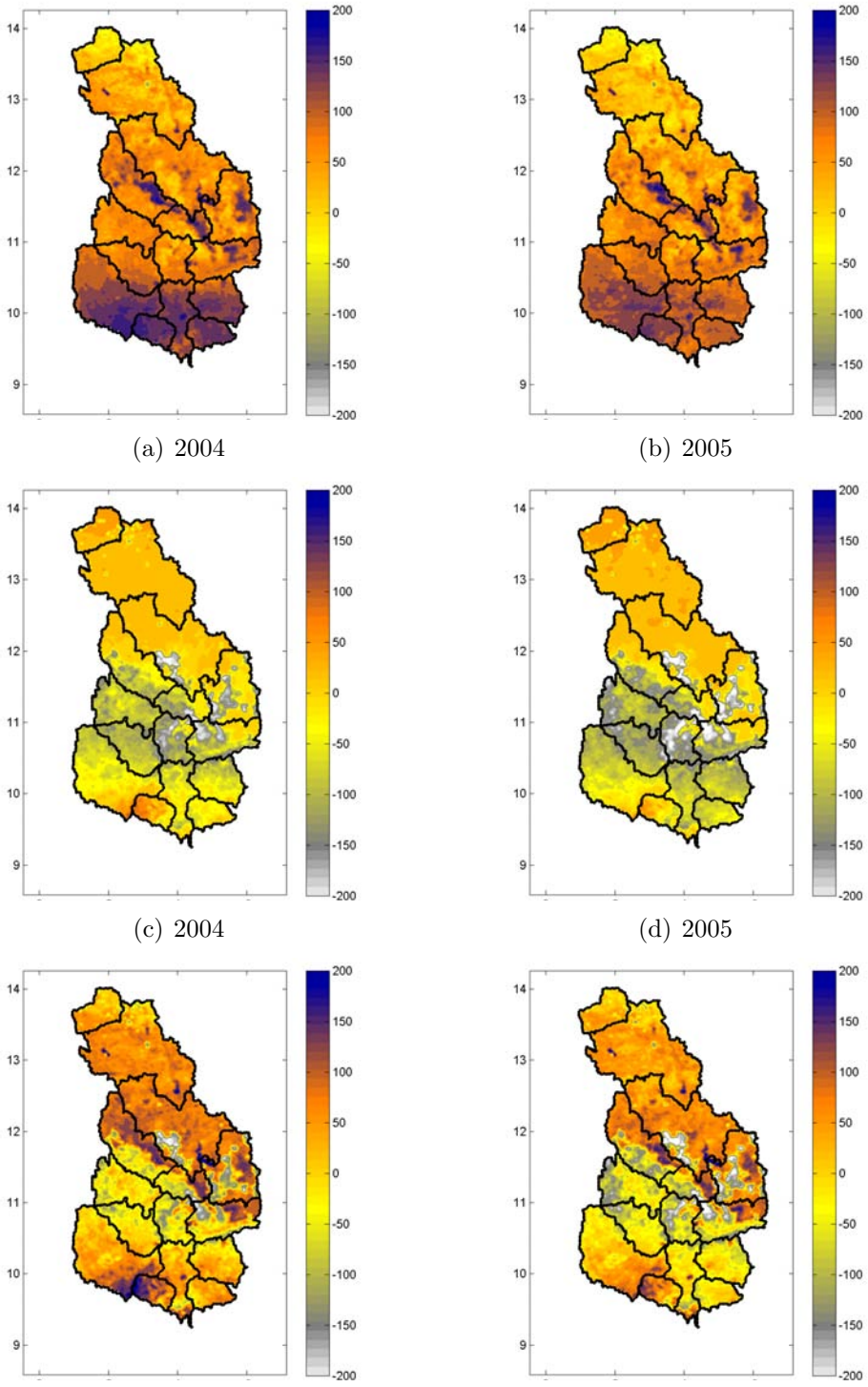

(a) 2004 (b) 2005

(c) 2004 (d) 2005

(e) 2004 (f) 2005

Figure 6.15: Differences of annual potential evapotranspiration [mm] with respect to static tabulated values for albedo and *LAI* for the White Volta basin for 2004 and 2005 between dynamic *MODIS* estimates for albedo and static tabulated values for *LAI* (see (a) and (b)), static tabulated values for albedo and dynamic *MODIS* estimates for *LAI* (see (c) and (d)), and dynamic *MODIS* estimates for albedo and *LAI* (see (e) and (f))

The calculation of differences between annual potential evapotranspiration using dynamic *MODIS* estimates for albedo, and/or *LAI* and static tabulated values for both variables, shows the impact in detail (see Figure 6.15). Additionally to the increased spatial variability in the northern part of the White Volta basin, *MODIS* albedo increases annual potential evapotranspiration in the South of the basin. The impact of *MODIS LAI* occurs mainly in the southern and central part of the basin and is predominantly negative. Using *MODIS* estimates for both parameters, the differences of potential evapotranspiration are very heterogeneous in space with positive and negative differences in almost all subcatchments. Although the spatial distribution of the differences of potential evapotranspiration is comparable for 2004 and 2005, the impact of interannual variations of albedo and *LAI* is clearly visible.

Figure 6.16 shows differences of annual actual evapotranspiration using dynamic *MODIS* estimates for albedo and/or *LAI* with respect to static tabulated values for both variables for 2004 and 2005. Using *MODIS* estimates for albedo leads to heterogeneous and, in total, slightly positive differences of actual evapotranspiration. The impact of *MODIS LAI* is predominantly positive in the northern and negative in the central and southern part of the White Volta basin. Thus, positive differences in the northern, and negative ones in the southern part, are simulated using dynamic *MODIS* estimates for both, albedo and *LAI*. Despite similar differences with respect to static tabulated values, the impact of interannual variations of albedo and *LAI* on the spatial distribution of actual evapotranspiration is again clearly visible.

Compared to static, tabulated values, dynamic *MODIS* estimates for albedo and/or *LAI* also have an impact on the spatial distribution of total annual runoff (see Figure 6.17), which is predominantly negative in the southern and central and positive in the northern part of the White Volta basin. Additionally, the positive difference in the northernmost subcatchment using *MODIS* estimates for *LAI* for 2004 is conspicuous. It cannot be completely explained with the results of the previous figures, where higher values are also simulated in this region. Furthermore, the land use and, in this case, in particular the soil texture discretization (see Figure 3.3), impact the spatial distribution of these results. Further possibilities are that *WaSiM* is not calibrated sufficiently for this northernmost subcatchment due to missing observation data and that the initialization period is too short for this dry region, which may explain that this impact does not occur in 2005. Besides, smaller differences on the spatial distribution of total annual runoff occur due to interannual variations of albedo and *LAI*.

Statistical analysis of the impact of MODIS albedo and LAI

For the shown variables, potential and actual evapotranspiration, and total runoff basin-wide mean and standard deviation of absolute values, and *RMSE*

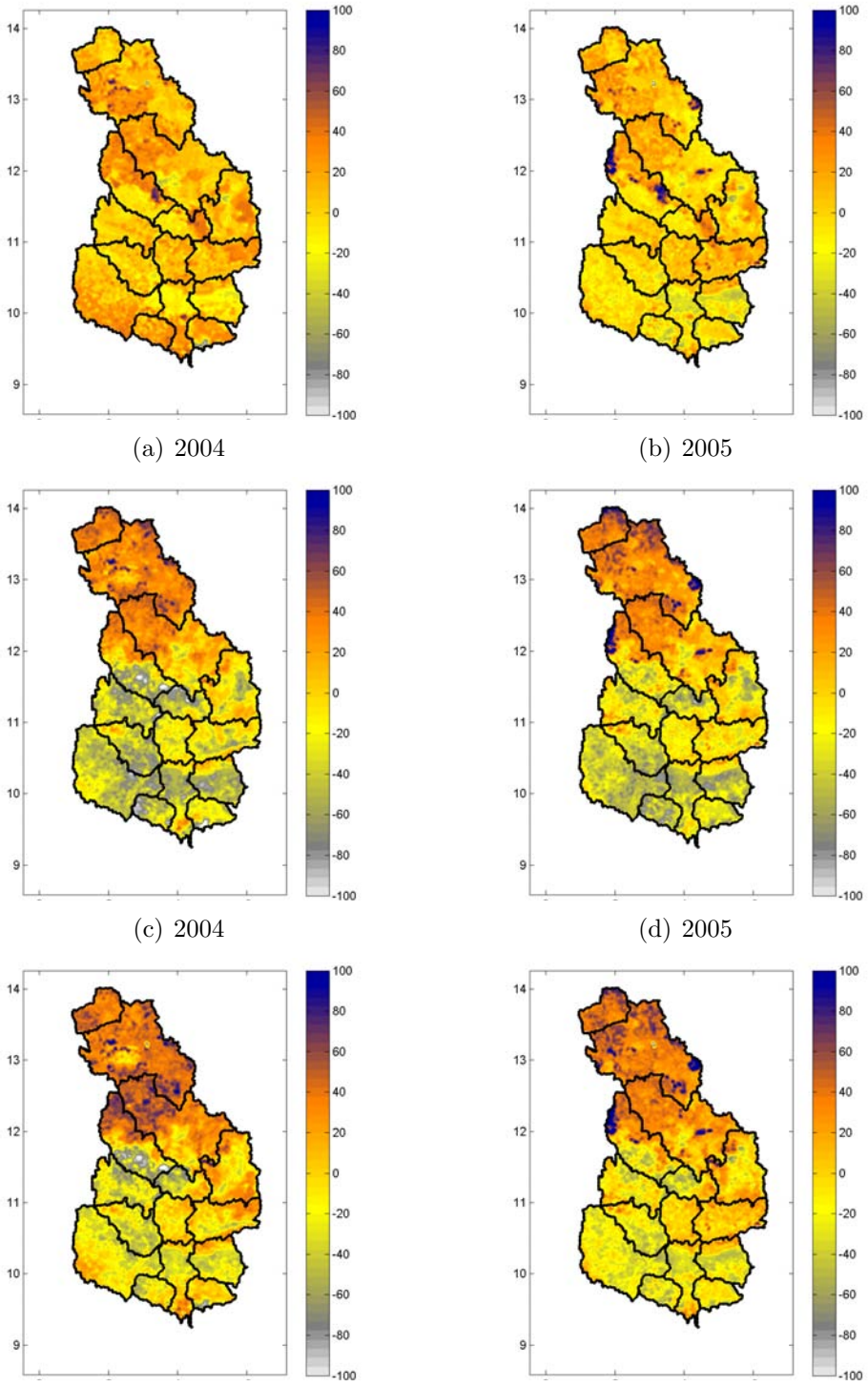

(a) 2004 (b) 2005

(c) 2004 (d) 2005

(e) 2004 (f) 2005

Figure 6.16: Differences of annual actual evapotranspiration [mm] with respect to static tabulated values for albedo and *LAI* for the White Volta basin for 2004 and 2005 between dynamic *MODIS* estimates for albedo and static tabulated values for *LAI* (see (a) and (b)), static tabulated values for albedo and dynamic *MODIS* estimates for *LAI* (see (c) and (d)), and dynamic *MODIS* estimates for albedo and *LAI* (see (e) and (f))

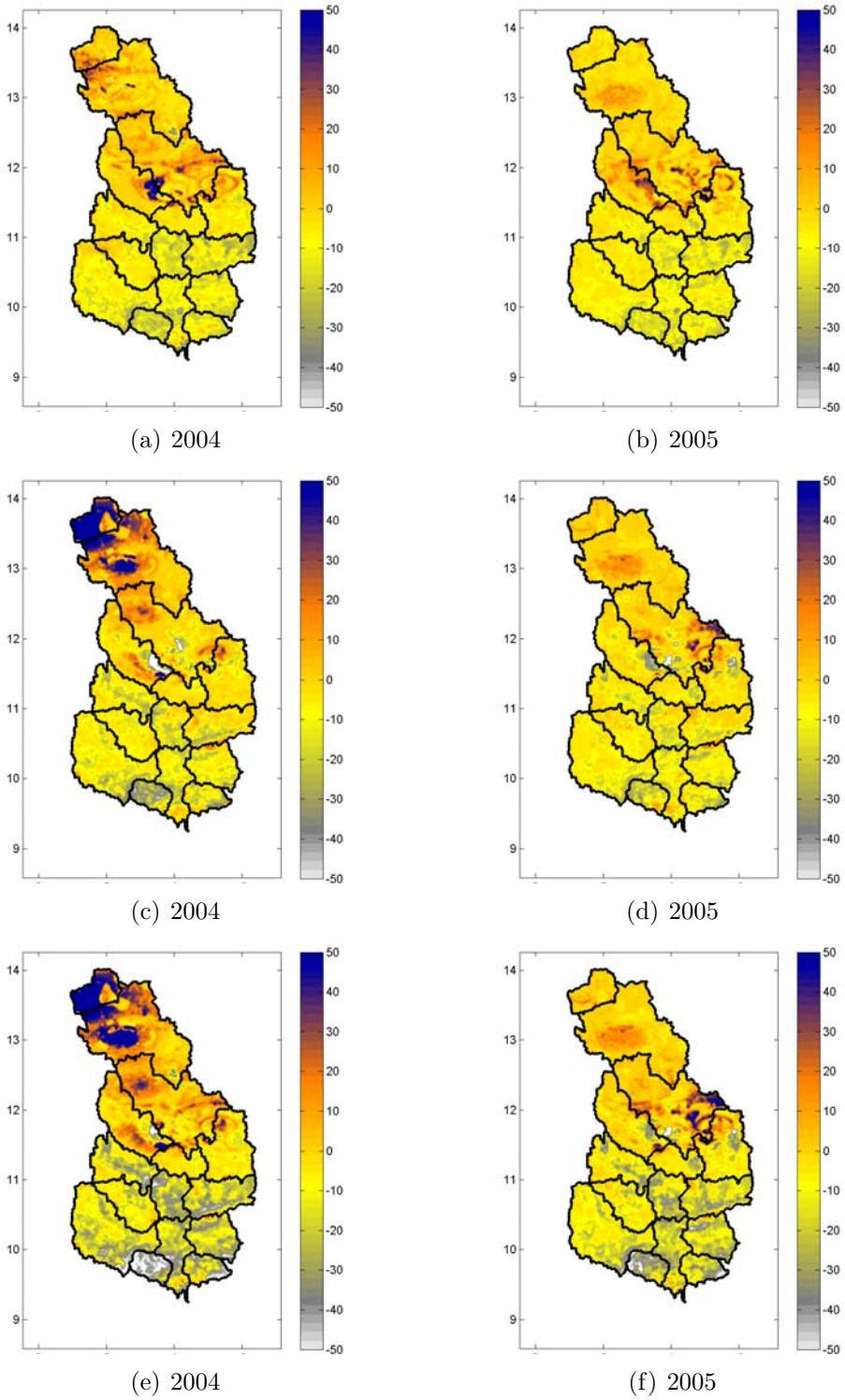

(a) 2004 (b) 2005

(c) 2004 (d) 2005

(e) 2004 (f) 2005

Figure 6.17: Differences of annual total runoff [mm] with respect to static tabulated values for albedo and *LAI* for the White Volta basin for 2004 and 2005 between dynamic *MODIS* estimates for albedo and static tabulated values for *LAI* (see (a) and (b)), static tabulated values for albedo and dynamic *MODIS* estimates for *LAI* (see (c) and (d)), and dynamic *MODIS* estimates for albedo and *LAI* (see (e) and (f))

results with respect to static tabulated values for albedo and *LAI* are listed for 2004 and 2005 in Table 6.1(a) and (b). The means in Table 6.1(a) agree well with the sum of daily differences in Figure 6.10 to Figure 6.12. The percentage change of mean annual sums using dynamic *MODIS* estimates for albedo and *LAI*, compared to static tabulated values, amounts to plus 2% for potential, and plus 1% for actual evapotranspiration, and minus 1% for total runoff for 2004. For 2005, the percentage changes are minus 0.2% for potential and plus 1% for actual evapotranspiration, and minus 5% for total runoff. The differences in total runoff are mainly due to the high values in the northernmost subcatchment for 2004. Furthermore, despite higher mean annual potential evapotranspiration, the actual evapotranspiration is slightly lower for 2005 and the ratio of total discharge and actual evapotranspiration varies. Considering the standard deviation, the impact is more pronounced. Dynamic *MODIS* estimates for *LAI* decrease the standard deviation values for all three variables. The percentage change of the standard deviation of annual sums using dynamic *MODIS* estimates for albedo and *LAI* compared to static tabulated values amounts to minus 11% for potential and minus 12% for actual evapotranspiration, and minus 10% for total runoff for 2004. The corresponding values for 2005 are in the same range with minus 12% for potential and minus 11% for actual evapotranspiration, and minus 7% for total runoff. The *RMSE* values in Table 6.1(b) confirm the results with absolute values. The tendency of the *RMSE* values is similar for 2004 and 2005, except for potential evapotranspiration using *MODIS* estimates for albedo or *LAI*. For total runoff, *RMSE* values are highest using dynamic *MODIS* estimates for both variables.

In Table 6.1(c), standard deviation values within the subcatchments are given as a measure of the spatial variability within and between the subcatchments. For all three variables, *MODIS* estimates for albedo and *LAI* lead to a decrease of mean and standard deviation values. This means, that, in this study, the use of dynamic *MODIS* estimates leads to a decrease of spatial variability of evapotranspiration and total runoff on subcatchment scale, despite the higher spatial variability and the seasonal development of the *MODIS* albedo and *LAI* fields.

(a) annual sums

	Method	ET_p [mm]		ET_a [mm]		total Q [mm]	
		mean	std	mean	std	mean	std
2	Tabulated	1879.00	421.87	770.08	119.17	80.76	79.55
0	MODIS ALB	1961.20	436.17	784.75	116.37	79.31	75.43
0	MODIS LAI	1850.60	371.51	763.01	100.80	81.34	74.39
4	MODIS ALB & LAI	1915.70	375.35	779.15	104.66	79.56	71.40
2	Tabulated	1965.70	467.08	733.76	120.59	85.35	75.12
0	MODIS ALB	2035.30	485.88	740.73	112.11	83.49	72.05
0	MODIS LAI	1926.10	399.56	738.94	105.02	82.94	72.76
5	MODIS ALB & LAI	1962.40	409.66	743.88	107.27	80.60	70.21

(b) RMSE

	Method	ET_p [mm]		ET_a [mm]		total Q [mm]	
		mean	std	mean	std	mean	std
2	Tabulated	0.00	0.00	0.00	0.00	0.00	0.00
0	MODIS ALB	95.12	45.97	29.63	21.52	14.43	12.49
0	MODIS LAI	71.94	50.89	45.16	28.03	21.16	18.83
4	MODIS ALB & LAI	87.19	49.22	43.39	26.18	28.01	22.98
2	Tabulated	0.00	0.00	0.00	0.00	0.00	0.00
0	MODIS ALB	83.89	44.60	31.91	27.70	11.34	10.03
0	MODIS LAI	87.53	58.70	44.80	31.60	13.92	12.86
5	MODIS ALB & LAI	86.86	54.61	42.74	30.60	18.48	15.50

(c) standard deviation within subcatchments

	Method	ET_p [mm]		ET_a [mm]		total Q [mm]	
		mean	std	mean	std	mean	std
2	Tabulated	214.15	146.64	83.46	23.14	66.00	27.72
0	MODIS ALB	204.06	137.37	79.36	22.57	64.80	25.88
0	MODIS LAI	183.72	127.65	79.17	17.47	62.85	27.63
4	MODIS ALB & LAI	173.26	115.66	79.92	18.05	61.58	26.12
2	Tabulated	238.51	161.72	87.47	23.58	60.23	25.47
0	MODIS ALB	232.61	154.06	82.00	23.77	58.83	24.58
0	MODIS LAI	200.86	136.52	82.34	20.28	58.28	26.05
5	MODIS ALB & LAI	193.37	126.16	82.38	21.70	57.16	25.38

Table 6.1: Statistics of absolute values (a), *RMSE* results (b) with respect to static tabulated values for albedo and *LAI*, and (c) standard deviation within subcatchments of annual potential and actual evapotranspiration, and total discharge [mm] for the White Volta basin for 2004 using (i) static values for both variables, (ii) *MODIS* values for albedo and static ones for *LAI*, (iii) static values for albedo and *MODIS* ones for *LAI*, and (iv) *MODIS* estimates for albedo and *LAI*

6.7 Summary

In this chapter, the impact of satellite derived land surface properties on hydrological simulations is investigated. The *MODIS* products for albedo and leaf area index *LAI* are assimilated into the hydrological model. Both variables have an impact on potential evapotranspiration, which is calculated using the Penman-Monteith approach. The comparison between static tabulated values from standard literature and dynamic *MODIS* estimates shows, for albedo, a comparable spatial distribution within the White Volta basin with slightly lower *MODIS* derived values. However, *MODIS* provides an increased level of detail in the spatial dimension. For the *LAI*, the temporal development is not sufficiently represented by two seasons with static tabulated values. In comparison to *MODIS LAI*, the tabulated values overestimate the *LAI* during the dry season and underestimate it during the rainy season in the southern part of the catchment.

The impact of *MODIS* estimates of albedo and *LAI* on daily time series of potential, and actual evapotranspiration, as well as total discharge, is minor. However, the sum curves of daily differences with respect to static tabulated values show occurring differences. For potential evapotranspiration, dynamic *MODIS* estimates for albedo lead to slightly higher values throughout the whole year, whereas *MODIS* estimates for *LAI* are lower during the dry and equal to slightly higher during the rainy season. These results agree well with the theoretical impact of albedo and *LAI* on the calculation of potential evapotranspiration and the differences of albedo and *LAI* grids using static tabulated or dynamic *MODIS* values. The comparison between the simulation results for 2004 and 2005 shows, that for all water balance variables the temporal development of the sum of differences curves using static tabulated or dynamic *MODIS* estimates for albedo and *LAI* is similar for both years. However, the interannual variations of *MODIS* albedo and *LAI* impact mainly the magnitude of differences.

The impact of dynamic estimates of albedo and *LAI* on the spatial distribution of water balance variables in the White Volta basin is clearly visible. The calculated differences of water balance variables, using *MODIS* estimates or static tabulated values, are very heterogeneous in space with positive and negative signs in almost all subcatchments. Overall, the use of dynamic *MODIS* estimates leads to slightly higher evapotranspiration and runoff values in the North and lower ones in the South of the White Volta basin. In total, the percentage change of mean annual sums using dynamic *MODIS* estimates, compared to static tabulated values, amounts to 0% to plus 2% for potential, and plus 1% for actual evapotranspiration, and minus 5% to minus 1% for total runoff in 2004 and 2005. Furthermore, the use of dynamic *MODIS* estimates decreases standard deviation values of evapotranspiration and total runoff on sub- and catchment scale compared to tabulated static ones for albedo and

LAI. Despite similar differences with respect to static tabulated values, the impact of interannual variations of *MODIS* estimates for albedo and *LAI* on the spatial distribution of all water balance variables is clearly visible.

7 Propagation of precipitation uncertainties in water balance estimations

Scientifically sound decisions in sustainable water management are usually based on hydrological modelling, which requires meteorological driving information. In contrast to the joint atmospheric-hydrological simulations in Section 5.3, station data are used as meteorological input in the traditional and usual application. Consequently, these point measurements have to be converted to areal information using various interpolation techniques, e.g. geostatistical methods like inverse distance weighting or kriging. The selection of an appropriate method depends on a number of factors, including the time available, the density of the gauge network, and the spatial variability of the meteorological parameter. In general, in regions with a weak infrastructure usually only a sparse density of gauges and a variable length of periods containing large data gaps is available. Consequently, the areal estimations are afflicted with larger uncertainties. This problem arises particularly for discontinuous and spatially highly variable parameters, such as precipitation. Precipitation, however, is the basic component of the water balance. Therefore, the areal estimation of precipitation is a major task in hydrological simulations. In this study, the geostatistical interpolation techniques of inverse distance weighting and kriging as well as turning band simulations are applied for the areal estimation of precipitation, and their impacts on hydrological simulations are investigated in a region with only little hydro-meteorological information.

7.1 Geostatistical interpolation techniques

For the spatial interpolation of point measurements to areal information, a weighted combination of measurements in the surrounding area are usually calculated for each grid point (see Equation 7.1). The sum of weights equals one and for each grid point each measurement has a specific weight, which determines the portion of each measurement on the interpolation value. There are different methods to determine the weights. The applied methods in this study are described in the following sections.

7.1.1 Inverse distance weighting

A simple technique to determine the weights is an inverse distance weighting (IDW) of gauge values for each grid point. Weights are calculated depending on the distances between the location requiring an estimate and the location of the observations. The interpolated value $Z^*(u_0)$ at location u_0 is calculated by:

$$Z^*(u_0) = \sum_{i=1}^{N} \lambda_i \cdot Z(u_i) \tag{7.1}$$

where λ_i is the weight of the value $Z(u_i)$ observed at station i. The sum of weights λ_i equals one, and each weight λ_i is calculated as the weighted, reciprocal distance between station u_i and location u_0. N stands for the number of observations in the surrounding area of u_0 defined by a maximal distance.

7.1.2 Ordinary kriging

Kriging is a geostatistical method that uses the variogram of the precipitation field (i.e. the variance between pairs of points that lie different distances apart) to estimate interpolated values. With the variogram, kriging incorporates the spatial structure of the variable in the estimation. Kriging calculates the "best" estimate of the values ($BLUE$: Best Linear Unbiased Estimator), taking into account the layout of the observation network relative to the interpolation grid. The application of the kriging method assumes second order stationarity of the random function $Z(u)$. The assumption of second order stationarity consists of two conditions (Bárdossy, 2003):

- The expected value of the random function $Z(u)$ is constant all over the domain D:
  $E[Z(u)] = m$ for all $u \in D$.
- The covariance of two random variables corresponding to two locations depends only on the vector h separating these two points:
  $E[(Z(u+h) - m)(Z(u) - m)] = C(h)$ for any $u, u+h \in D$.

$C(h)$ is called covariance function. The resulting, in this study precipitation field is optimal in the sense of identifying gauge weightings to minimize the estimation error (Robinson, 2005). The reliability of the results is calculated as kriging error (estimation variance) for each grid point (e.g. Schafmeister, 1999).

Kriging requires an experimental variogram analysis for the estimation of the spatial variability of the variable. The experimental variogram is defined as

$$\gamma(h) = \frac{1}{2N(h)} \sum_{i=1}^{N(h)} [Z(u_i) - Z(u_i + h)]^2 \tag{7.2}$$

In general, the experimental variogram is fitted with a theoretical function which allows the analytical estimation of the variogram for any distance h. Therefore, several theoretical variograms are available. In this study, the nugget, spherical and exponential variogram are used as theoretical variograms. These types belong to the most frequently used theoretical variograms. The nugget model is usually combined with another variogram to describe the microscale variation in the vicinity of its origin (Cressie, 1991). Therefore, combinations of nugget and spherical model and of nugget and exponential model are applied in this study. These combinations are described by their nugget c_0, their sill c_s and c_e, respectively, and their range a_s and a_e, respectively. The first combination of the nugget and spherical variogram is given by:

$$\gamma(h) = c_0 + \begin{cases} c_s \cdot (\frac{3}{2}\frac{h}{a_s} - \frac{1}{2}\frac{h^3}{a_s^3}) & if\ h \leq a_s \\ c_s & otherwise \end{cases} \tag{7.3}$$

The second combination of the nugget and exponential variogram is given by:

$$\gamma(h) = c_0 + c_e \left\{ 1 - exp(-\frac{h}{a_e}) \right\} \tag{7.4}$$

The relationship between the variogram $\gamma(h)$ and the covariance function $C(h)$ from the second order stationarity assumption is:

$$\gamma(h) = C(0) - C(h) \qquad with \qquad C(0) = Var[Z(u)] \tag{7.5}$$

With the results of the variogram analysis, precipitation values at unsampled locations $Z^*(u_0)$ can be estimated using ordinary kriging OK (see e.g. Schafmeister, 1999; Kitanidis, 1997). OK applies weighted linear combinations of N neighbouring observations $Z(u_i)$ for the estimation at unsampled locations (see Equation 7.1). λ_i are now called kriging weights. Estimation of the kriging weights in OK meets the following specifications:

1. Unbiasedness: on average the estimation error must be zero. Implying stationarity, which means $E[Z(u_i)] = m$ and $Z(u_0) = m$, that is

$$\begin{aligned} E[Z^*(u_0) - Z(u_0)] &= E[\sum_{i=1}^{N} \lambda_i \cdot Z(u_i) - Z(u_0)] \\ &= \sum_{i=1}^{N} \lambda_i m - m = m \sum_{i=1}^{N} (\lambda_i - 1) = 0 \end{aligned} \tag{7.6}$$

   For the estimator to be unbiased for any value of the mean m, it is required that the sum of λ_i is equal 1.

2. Minimum variance: the mean square estimation error must be minimum, i.e.

   $E[Z^*(u_0) - Z(u_0)]^2$ is minimal.

By means of variograms $\gamma(h)$ specification 2 gets the form:

$$\begin{aligned} E[Z^*(u_0) - Z(u_0)]^2 &= Var(Z^*(u_0) - Z(u_0)) \\ &= 2 \cdot \sum_{i=1}^{N} \lambda_i \gamma(u_i - u_0) - \sum_{i=1}^{N} \sum_{j=1}^{N} \lambda_i \lambda_j \gamma(u_i - u_j) \end{aligned} \tag{7.7}$$

This is a constrained optimization problem where values of $\lambda_1, ..., \lambda_N$ have to be selected that minimize Equation 7.7 while satisfying the constraint that the sum of λ_i has to be equal 1. With the introduction of a Lagrange multiplier μ, the necessary conditions for the minimization are given by the linear kriging system of $N + 1$ equations with $N + 1$ unknowns:

$$\begin{aligned} \sum_{j=1}^{N} \lambda_j \gamma(u_i - u_j) + \mu &= \gamma(u_i - u_0), \qquad i = 1, 2, ..., N \\ \sum_{j=1}^{N} \lambda_j &= 1 \end{aligned} \tag{7.8}$$

7.1.3 External drift kriging

Apart from *OK* described above, external drift kriging *EDK* (Ahmed and de Marsily, 1987) is applied, where expert knowledge is incorporated in the system as external drift. Here, it is supposed that an additional variable $Y(u)$ exists that is linearly related to $Z(u)$. The estimator thus depends on the additional variable $Y(u)$. Therefore, $Y(u)$ has to be available at a high spatial resolution, preferably as a regular grid. Applying *EDK* the intrinsic hypothesis that $E[Z(u_i)] = m$ and $Z(u_0) = m$ are constant within the domain research area, is not required anymore. Instead, the expected value of $E[Z(u)]$ is linearly related to one or more additional variables $Y(u)$. For one additional variable the expected value $E[Z(u)] = a_0 + a_1 \cdot Y(u)$, where a_0 and a_1 need not to be known explicitly (Brommundt and Bárdossy, 2007). The linear kriging

system with one external drift is:

$$\begin{aligned} \sum_{j=1}^{N} \lambda_j \gamma(u_i - u_j) + \mu_0 + \mu_1 \cdot Y(u_j) &= \gamma(u_i - u_0), \qquad i = 1, 2, ..., N \\ \sum_{j=1}^{N} \lambda_j &= 1 \\ \sum_{j=1}^{N} \lambda_j \cdot Y(u_j) &= Y(u_0) \end{aligned} \tag{7.9}$$

In this study, the following variables, which are related to the precipitation distribution in the Volta basin, are investigated as external drifts. The spatial distribution of the applied external drifts are illustrated in Figure 7.7 and Figure 7.8 on the left side:

- **Digital elevation model:** For the spatial interpolation of precipitation, topographic information is often used as external drift due to the relationship between elevation and spatial precipitation structure (e.g. Brommundt and Bárdossy, 2007). As the Volta, and especially the White Volta basin, is very flat and precipitation accumulation is not dominated by topography, further external drifts are investigated.

- **Distance to sea information:** In the Volta basin the general spatial distribution of precipitation is characterized by a strong North-South gradient and thus the isolines continue parallel to the coastline of the Gulf of Guinea. This partition is also in accordance with the annual cycle of the *ITCZ* (see Section 2.2).

- **Long-term mean annual and monthly rainfall:** In addition to the strong North-South gradient, a West-East gradient is present in the spatial distribution of precipitation, especially along the coast, which is not considered using the distance to sea information as external drift. Therefore, long-term mean precipitation data (1961-1999) of 29 stations in Burkina Faso and Ghana are spatially interpolated on a monthly and annual scale using *OK* and *EDK* with distance to sea information as external drift. The mean annual precipitation fields interpolated with *OK* and *EDK* are shown in Figure 7.8(a) and (c). In comparison to the distance to sea plot, the isolines of mean annual precipitation are not parallel along the coast. There is a maximum in the South-West of Ghana and a local minimum with low annual rainfall accumulation along the coast of Ghana and Togo, which is known in literature as Togo gap. Using distance to sea information as external drift, the long-term mean annual precipitation isolines are more parallel to the coastline compared to the

OK results. The patterns and values of the precipitation interpolation by *EDK* are in good agreement with the results of Orstom (1996). The *EDK* result shows more realistic patterns in areas with a patchy and low dense meteorological observation network, particularly in Burkina Faso.

- **Leaf area index (*LAI*):** The background to using a biological parameter as external drift is the dependency of plant growth on precipitation (see Figure 6.6). This dependency is given in particular in semi-arid regions with distinctive dry and rainy seasons. As described in Chapter 6, *MODIS* provides *LAI* information as 8-day composites with a spatial resolution of 1 km. For *EDK*, this *LAI* information is used first as annual mean and second as positive differences between the current and past 8-day composite. Due to the fact that the *LAI* data are from the same time period as the time period of interest, the temporal development of the generated *LAI* is a consequence of the available precipitation. In addition to the positive differences of the current, the positive differences of the future minus the current composite are also used as external drift, to consider a certain delay of one composite (lag 1) between precipitation and plant growth.

  However, the use of *LAI* as external drift for precipitation interpolation contains some limitations. Although plant growth depends strongly on precipitation, further components have an impact on the phenological development, e.g. the soil type and anthropogenic activities like irrigation and fertilization.

7.2 Turning band simulations

In addition to spatial interpolation methods, geostatistical simulations are performed for areal precipitation. Geostatistical simulations generate equally probable realizations with prescribed variability. The simulation is said to be "conditional" if the resulting realizations honour observed data at their locations. Simulations differ from kriging or any spatial interpolation methods as follows: The goal of interpolation algorithms is to provide the "best", hence, unique, local estimate of the variable. In simulations, reproduction of global features and statistics take precedence over local accuracy (Deutsch and Journel, 1998). Geostatistical simulations reproduce the variability of the regionalized variable, which means that the variograms of the measured and simulated values coincide. Therefore, both sets of values have the same spatial and/or temporal variability (Ezzedine, 2005). In contrast to simulations, kriging and most interpolation techniques deliver idealized smooth results with lower variabilities compared to the variability of observations. This is due to the minimum estimation variance which is used as optimization criterion and necessarily yields less variable estimators (Bárdossy, 2003). Therefore, geostatistical simula-

tion methods are applied if not the best but the range is the main objective of the investigation. In this study, possible ranges of terrestrial water balance variables are investigated which are an important additional information for e.g. decisions in water resources management. Furthermore, the variability of precipitation, which is one of the most important input variables for hydrological modelling, has a considerable impact on hydrological model's predictive uncertainty (Zehe et al., 2005). Therefore, geostatistical simulations usually conditioned on observations preserve typical fluctuation patterns (Mantoglou and Wilson, 1982). For geostatistical simulations the turning band method is chosen.

7.2.1 Turning band method

The following brief description of turning band simulations is mainly based on Bárdossy (2003) and Ezzedine (2005). The turning band method was developed by Matheron (1973) and mostly applied in geological mining problems. It provides unconditional realizations of a standard Gaussian field $Z(x)$ with a given covariance $C_Z(h)$. Unconditional simulation means that observation data are not used directly, but influence the simulation results only through the variogram. The turning band method involves the simulation of isotropic random fields in two- or higher-dimensional spaces by using a sequence of one-dimensional processes along lines crossing the space. Thereby sets of one-dimensional simulations are merged to one multi-dimensional set, while preserving the statistical properties of the random field. One-dimensional simulations are performed for different possible directions "turning" around a centre point (see Figure 7.1). Depending on the variogram, different covariance structures have to be used for the one dimensional simulations (Bárdossy, 2003). Afterwards, at each point of the two-dimensional field, a weighted sum of the corresponding values of the line processes is assigned.

Suppose that for a set of lines $l = 1, ..., L$ all going through the origin of the coordinate system and having a direction given by the unit vector u_i, random functions with zero mean and $C_1(r)$ covariance functions are simulated independently. Let $Z_l(x)$ for $l = 1, ..., L$ be these functions. Then for a point x the random function $Z(x)$ can be defined as:

$$Z(x) = \frac{1}{\sqrt{L}} \sum_{l=1}^{L} Z_l(\langle x, u_i \rangle) \tag{7.10}$$

where $\langle ., . \rangle$ denotes the scalar product of the vectors. For two-dimensional isotropic processes, selecting $h = (r, 0)$ and introducing polar coordinates gives the following relation between the one and two-dimensional covariance functions $C_1(r)$ and $C_2(r)$:

$$C_2(r) = \frac{2}{\pi} \int_0^r \frac{C_1(\tau)}{\sqrt{r^2 - \tau^2}} d\tau$$

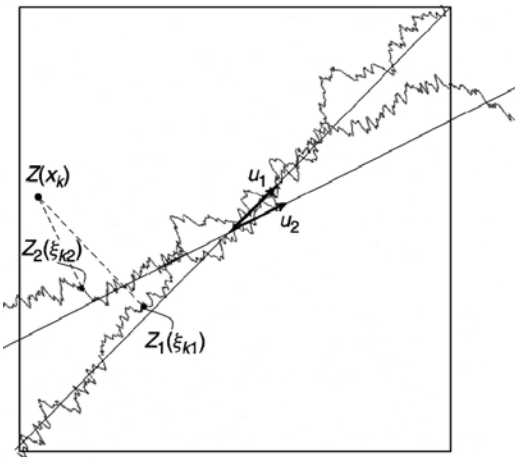

Figure 7.1: Illustration of the turning band method (from: Ezzedine, 2005)

with $\tau = r \cos \varphi$.

The advantage of the turning band method is that it is nearly independent of the number of points. Moreover, the algorithm is fast because it achieves two or three-dimensional simulations through a series of one-dimensional simulations (Deutsch and Journel, 1998). A disadvantage is that measurement data are not used directly, only through the variogram, in unconditional simulations (Bárdossy, 2003). In contrast to the interpolation methods, turning band simulations preserve the statistics of the real random field.

7.2.2 Conditional simulations

With some modifications the results of unconditional simulations can be transferred to conditional simulations. Thereby, the knowledge of the value of a selected parameter at a given point restricts the possible values in a neighbourhood. Those realizations are especially interesting where the simulated values equal the measured values at the observation points. Thus, unconditional random fields can be made conditional with a simple double kriging, which is defined as follows (Bárdossy, 2003):

$$Z_C(x) = Z^*(x) + (Z_S(x) - Z_S^*(x)) \tag{7.11}$$

where: $Z_C(x)$ is the conditionally simulated value at point x
$Z^*(x)$ is the kriging estimator of Z at x based on measurements
$Z_S(x)$ is the unconditionally simulated value at point x
$Z_S^*(x)$ is the kriging estimator of Z_S at point x based on the unconditionally simulated values at the measurement points

Because of the exactness property of kriging, it is essential for measurement points x_i, that

$$\begin{aligned} Z^*(x_i) &= Z(x_i) \\ Z_S^*(x_i) &= Z_S(x_i) \end{aligned} \tag{7.12}$$

Thus by definition

$$Z_C(x_i) = Z(x_i) \tag{7.13}$$

This means that the above modification of the unconditional simulation reproduces the measured values at the observation points. The conditioning of the unconditional simulation does not influence the variability, thus $Z_C(x)$ and $Z_S(x)$ have the same variogram.

7.2.3 Normal score transformation

Due to the fact that daily precipitation data are usually not Gaussian distributed, a data transformation is required before the application of turning band simulations. Applying daily precipitation data, observations with zero precipitation are the critical values. Therefore, daily precipitation data are "Gaussianized" using normal score transformation. This requires the following steps:

1. Statistical parameters *mean* and *std* of observation data are calculated for each time step.
2. Transformation to standard normal distribution. In the process, for all observations with zero precipitation a random number is drawn, which fills the Gaussian curve left of this limit.
3. Calculation of the experimental and theoretical variograms of the normal score transformed variable.
4. After the turning band simulations, the results are transformed back to the original scale.

In the following section, the introduced geostatistical interpolation methods and turning band simulations are applied for the total areas of Burkina Faso and Ghana, which enclose the complete White Volta basin. Due to the locations of the 22 observation stations (see Figure 4.1), spatial interpolations and simulations for the total area of Ghana are reasonable. Due to missing data for Burkina Faso, seven additional existing meteorological stations in Burkina Faso are selected and filled with *TRMM* data for this study. The locations of these stations are marked with an asterixs in Figure 7.4(a). In the following, all 29 stations are considered as observation data. The investigation period is

2004. In addition, the extension of the investigation area to the total areas of Burkina Faso and Ghana allows a better investigation along the boundaries of the White Volta basin, and extends the availability of gridded precipitation estimations, which is an important input data source for further studies in the *GLOWA*-Volta project.

7.3 Areal precipitation results

The introduced geostatistical interpolation methods and turning band simulations are applied on a daily basis for 2004. One special problem for geostatistical interpolation of whole time series is the effective and reliable estimation of variograms for each time step (Haberlandt, 2007). Therefore, an experimental variogram analysis for the estimation of the spatial variability of the variable is required.

7.3.1 Variogram analysis

For practical reasons, the experimental variogram is usually calculated in distance classes. In this study, a class width of 10 km is chosen. Furthermore, a monotonization of class values is performed for each day. Figure 7.2(a) shows the experimental variogram of the summed daily experimental variograms before and after monotonization, which leads to a stepwise increasing shape of the experimental variogram.

For the integration of the experimental variogram into kriging methods or turning band simulations, theoretical variograms are fitted to the experimental variogram, which allow analytical estimations of the variograms for any distance h. In this study, the experimental variogram is fitted with two combinations of theoretical variograms: first, the nugget- and spherical model, and second the nugget- and exponential model (see Section 7.1.3) to determine the sills c and ranges a of the theoretical variograms. For the summed daily experimental variograms, Figure 7.2(b) and (c) show the fitted theoretical variograms with and without nugget at the origin. The experimental variogram in Figure 7.2(a) indicates the "microvariability" of this data set. Microvariability is defined as variability at a smaller scale than the separation distance between the closest measurement points (Kitanidis, 1997), which are rain gauges in this study. In Figure 7.3, the maximal available distance pairs for the experimental variogram analysis are given per class width. In general, only the first 30 or less classes are considered in the analysis, which is sufficient for the calculation of the sill and range of the model. The shortest available distance between two rain gauges in this study is 14.5 km. Therefore, the number of distance pairs in the first class between 0 and 10 km is zero, which results in a variogram value of 0 and leads to differences around the origin. Without considering the first class value, the results from a combination of nugget and spherical or exponential model

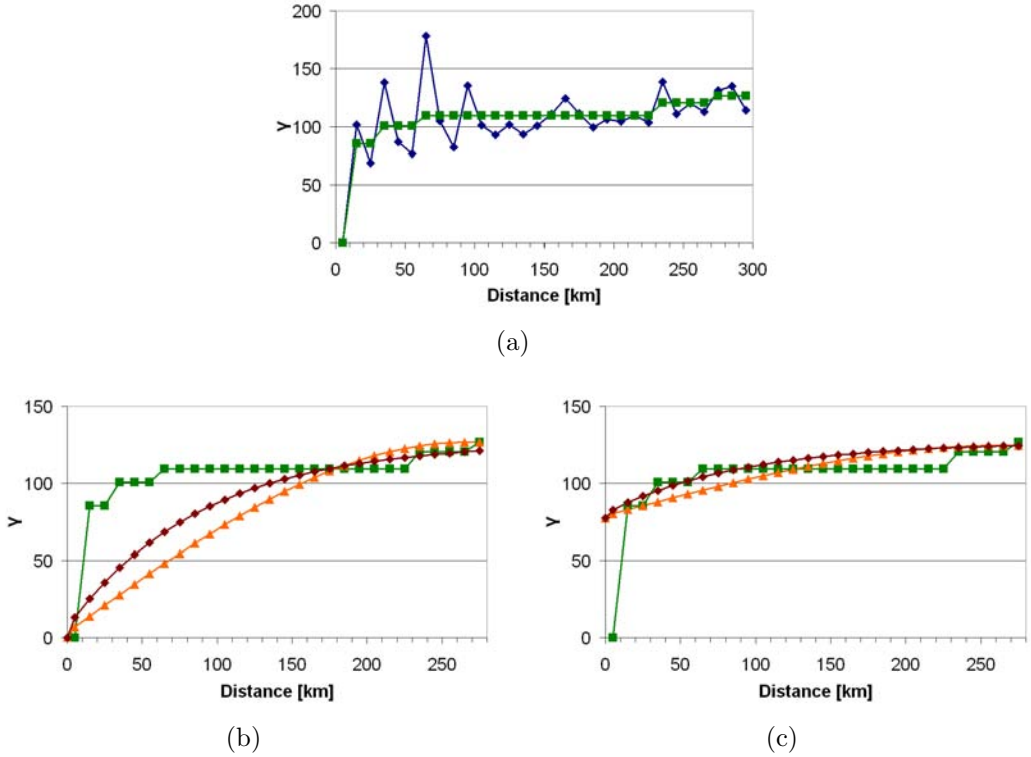

Figure 7.2: Results of variogram analysis: (a) Experimental variogram (γ values $[mm]^2$) of summed daily experimental variograms before (blue diamonds) and after (green squares) monotonization, (b) fitted theoretical spherical (orange triangles) and exponential (brown squares) variograms without nugget model, and (c) fitted theoretical spherical (orange triangles) and exponential (brown squares) variograms with nugget model

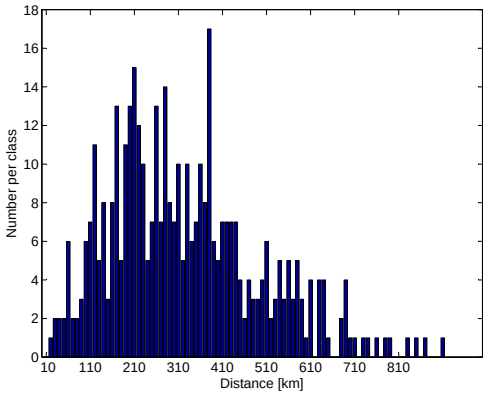

Figure 7.3: Histogram of maximal available, classified (10 km width) distance pairs of the 29 rain gauges for 2004

as theoretical variogram perform better.

The experimental variogram analysis and fitting of theoretical variograms are performed for each day. These results are a prerequisite for the spatial interpolation using kriging methods or turning band simulations, which are discussed in the following sections.

7.3.2 Areal precipitation fields

The interpolation methods described in Section 7.1.1 and Section 7.1.2 are applied to calculate daily precipitation fields for 2004. To account for the strong latitudinal dependency of the spatial precipitation distribution in West Africa, an anisotropy factor of 0.5 is applied to increase the influence of stations in longitudinal direction, compared to the ones in latitudinal direction, for each gridpoint. Due to the fact that for the calibration and validation of *WaSiM* the *IDW* method was applied for interpolation (Wagner et al., 2006), *IDW* and Thiessen polygons, as a special case of *IDW*, are applied as "standard" interpolation techniques for the comparison with kriging and turning bands results. First, the spatial distribution of annual precipitation will be discussed. Second, cross validation results will be compared applying several performance indices.

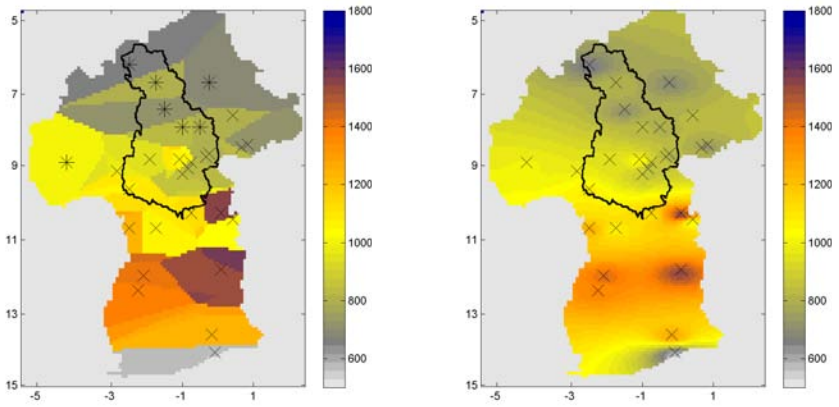

(a) Thiessen (b) IDW

Figure 7.4: Annual precipitation [mm] for 2004 using Thiessen polygons and *IDW* as interpolation methods

The spatial distribution of annual precipitation, applying the interpolation methods Thiessen polygon and *IDW* are given in Figure 7.4. The edges around each Thiessen polygon are not sharp because this figure shows the aggregated annual precipitation as the sum of 366 daily precipitation fields, which are interpolated with different numbers of observation data depending on the availability. The annual precipitation field calculated by Thiessen polygons has a minimum along the shore in Ghana. This is equal to the observations made at

the station Accra. Further differences between the annual precipitation fields calculated by Thiessen polygons and *IDW* are the two maxima in the East of Ghana, which are more pronounced using Thiessen, and the results in the North of Burkina Faso.

Ordinary kriging

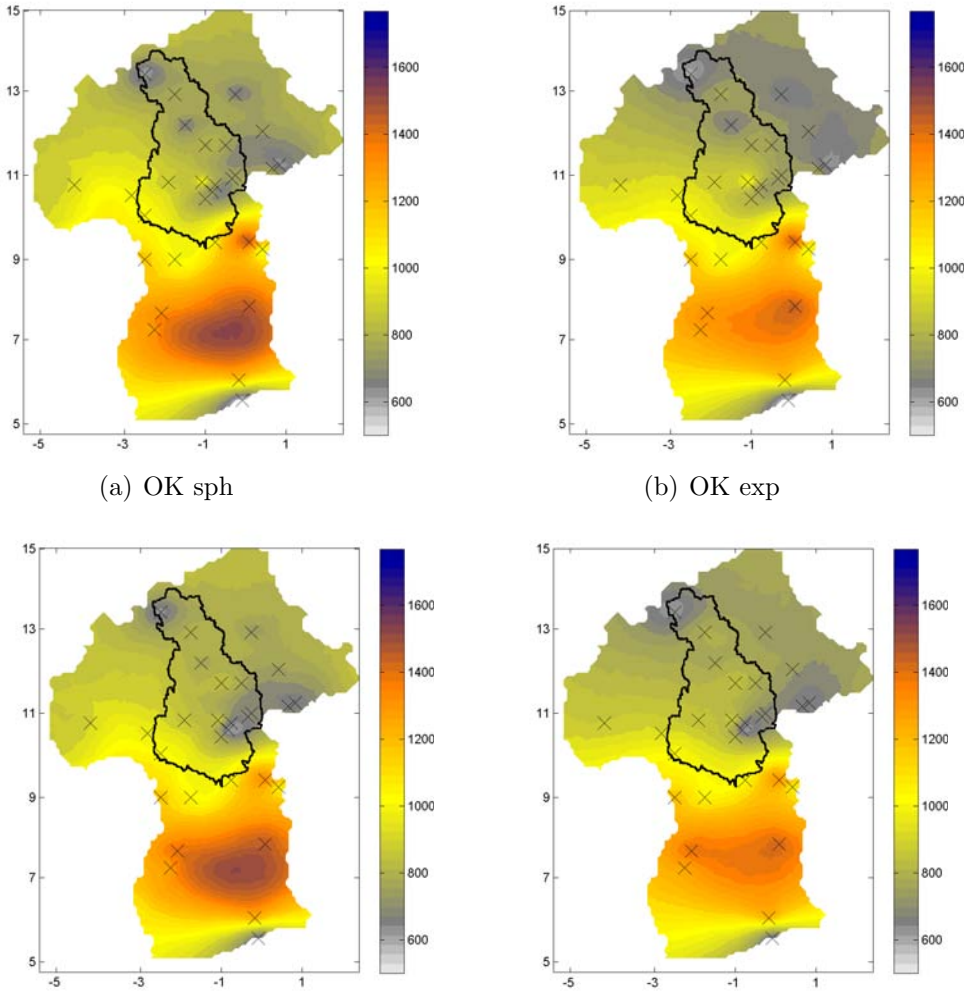

(a) OK sph (b) OK exp

(c) OK nug+sph (d) OK nug+exp

Figure 7.5: Annual precipitation [mm] for 2004 using ordinary kriging (*OK*) with different theoretical variogram combinations: (a) spherical, (b) exponential, (c) nugget and spherical, and (d) nugget and exponential model

In Figure 7.5, annual precipitation fields using *OK*, with different theoretical variograms and combinations described in Section 7.1.2, are shown. The main differences when applying a spherical or exponential variogram model occur mainly at regions with little or no observations; North of Burkina Faso and a part of central Ghana around longitude -1° and latitude 7°. Applying the

spherical variogram, the maximum in the region in central Ghana is higher than the closest observation value in the North-East, but it can be explained when considering further neighbouring stations in the South and West. For every day, the interpolated time series of the grid point with maximum annual precipitation is always lower or equal than one of the neighbouring stations. This means that the high annual precipitation amounts in this region are a consequence of the interpolation of observation data with different precipitation patterns. Applying the exponential variogram, the range which separates the correlated and uncorrelated random variables is larger. This is because, in theory, there is no defined distance for the range (see Equation 7.5), but random variables outside of an effective range of $3 \cdot a$ can be considered as independent. Therefore, more observation stations are considered in the interpolation and the high annual precipitation amounts in this region diminish.

Compared to the differences when applying a spherical and exponential variogram model, the effects on the shape when adding a nugget model c_0 to each model are minor, but larger in the total values of the spatial distribution of annual precipitation.

Estimation variance

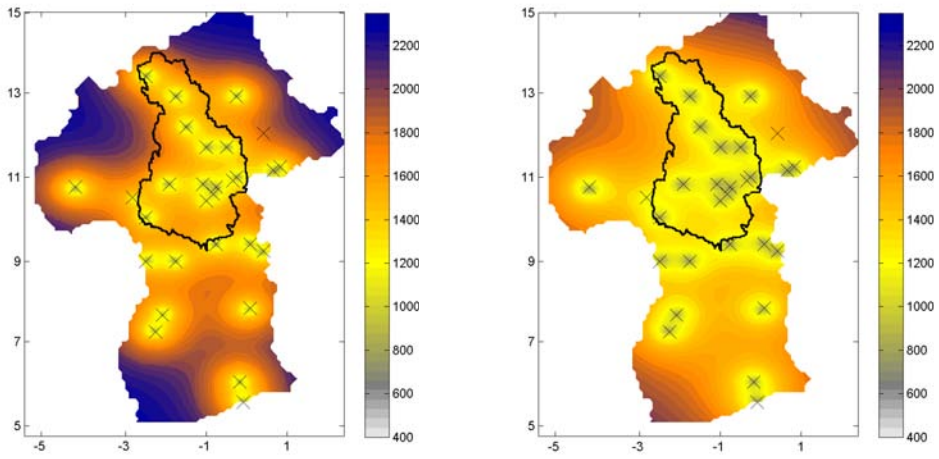

(a) $\sqrt{\sigma^2}$ OK nug+sph (b) $\sqrt{\sigma^2}$ OK nug+exp

Figure 7.6: *OK* estimation variances (square root) [mm] applying theoretical variogram combinations nugget plus spherical (a) or exponential (b) model for 2004

Kriging provides, in addition to the areal information of the regionalized variable for each grid point and for each time step a kriging error; the estimation variance σ^2 (see Section 7.1.2). With the help of estimation variance the reliability of the results is calculated under consideration of the layout of the observation network relative to the interpolation grid (Schafmeister, 1999). In Figure 7.6, the square root of the estimation variances calculated using *OK*

with the theoretical variogram combinations nugget plus spherical or exponential model are shown. In both figures, the errors are small in the area around the observations. At the boundaries of the research area, estimation variances are maximal, especially in the South-West corner of Ghana and in the North and West of Burkina Faso. This is due to missing observation data in these regions and their surrounding areas. The *TRMM* stations in Burkina Faso are selected with respect to the hydrological modelling of the White Volta basin. Therefore, the high estimation variances in the mentioned regions in Burkina Faso and Ghana are not relevant for the water balance simulations in the White Volta basin. The annual estimation variances applying different theoretical variogram combinations differ in their magnitude, but the shapes of the spatial distributions look similar. The reason for the higher values when applying the spherical model is the smaller range compared to the exponential model.

The estimation variance results provide important information for the evaluation of (i) the precipitation interpolations and (ii) the water balance simulations. Herewith the reliability of the simulations with respect to the regionalized variable can be estimated for each grid point, which further allows the assessment of confidence intervals. The identification of regions with higher estimation variances may also support stakeholders and authorities in the selection of new locations for observation stations.

External drift kriging

In the following, the results of the investigation of several external drifts, which have been described in Section 7.1.3, are presented for the theoretical variogram model, combining the nugget and exponential model. For the performance comparison with cross validation in Section 7.3.3, all possibilities are considered. Compared to the *OK* results, *EDK* increases spatial variability of the precipitation fields based on the external drift. Applying e.g. the elevation model as external drift, the annual precipitation field follows the valleys and mountain ridges (see Figure 7.7(a) and (b)). Distance to sea information as external knowledge stretches the kriging results further in longitudinal direction parallel to the coastline (see Figure 7.7(c) and (d)).

The application of non-gridded information as external drift, e.g. observation data, first requires the spatial interpolation of point information. In this study, the long-term (1961-1999) annual precipitation means of 29 stations in Burkina Faso and Ghana are interpolated using *OK* and *EDK* with distance to sea information as external drift to provide gridded long-term mean precipitation fields on a monthly and annual scale. In Figure 7.8(a), the *EDK* result of the long-term annual precipitation mean is shown. The impact of this external drift on the annual precipitation field for 2004 is depicted in Figure 7.8(b). The main difference between applying long-term mean precipitation fields as external drifts and the interpolation results discussed so far occurs along the coastline with the maximum in the South-West of Ghana. Furthermore, an increase

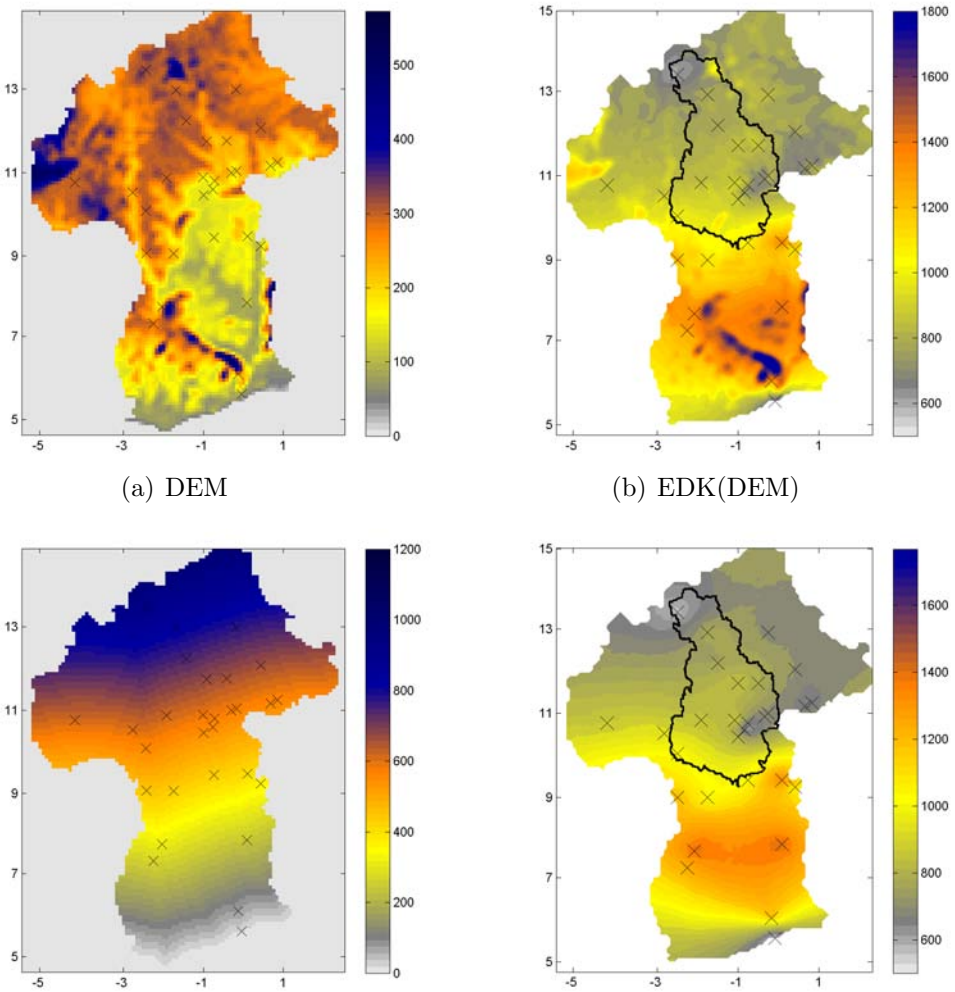

(a) DEM (b) EDK(DEM)

(c) Distance to coast (d) EDK(Distance)

Figure 7.7: External drift kriging (*EDK*) results for 2004: impact of the external drifts (a) digital elevation model [m] and (c) distance to the coastline [km] on the spatial distributions of annual precipitation [mm] (b) and (d) respectively

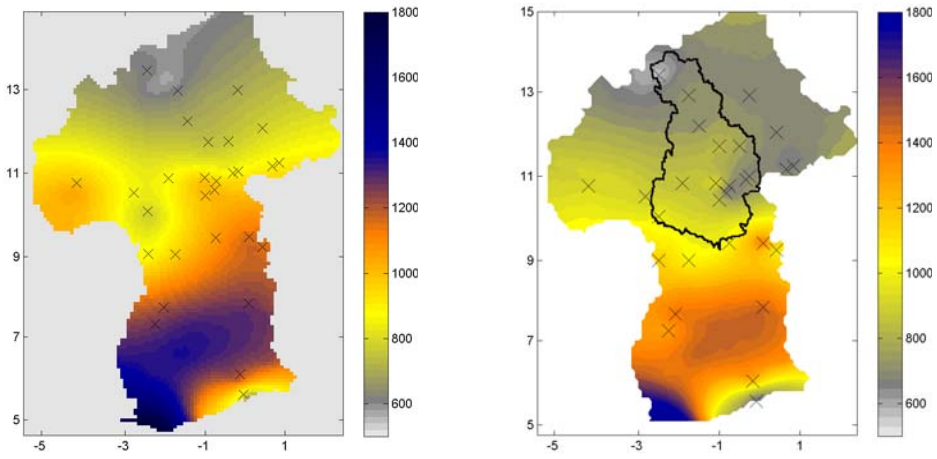

(a) Rain (40a) (b) EDK(Rain 40a)

Figure 7.8: External drift kriging (*EDK*) result for 2004: impact of the external drift (a) long-term (40 years) annual precipitation [mm] mean on (b) the spatial distribution of annual precipitation [mm]

of annual precipitation in a region around longitude -1° and latitude 7° is calculated applying long-term mean precipitation as external drift. Compared to the *OK* results (see Figure 7.5), the higher annual precipitation amounts in this region occur mainly due to the external drift and not due to the applied theoretical variogram. In the Burkinabè part the results are comparable to the other kriging ones.

As described in Section 7.1.3, the *LAI* is applied as external drift in two ways: as annual mean and as positive differences between the current and past 8-day composites of 2004. It is worth mentioning that the mean annual *LAI* in Figure 7.9(a) represents the agroecological zones (see Figure 2.3) well. The highest mean *LAI* values occur in the tropical rain forest in the South-West of Ghana. The coastal savannah along the shoreline East of the tropical rain forest with lower mean *LAI* values can be clearly distinguished. North of the tropical rain forest, the mean *LAI* decreases continuously with increasing latitudes and is in good agreement with the agroecological zones Guinea and Sudan savannah and the Sahel zone. Furthermore, Lake Volta with zero *LAI*, and lower *LAI*'s around cities like Accra, Kumasi and Ouagadougou, in comparison to their surrounding area can be clearly distinguished. The annual precipitation field applying the mean *LAI* for 2004 as external drift is given in Figure 7.9(b). The main differences to, e.g the *OK* results, occur in the tropical rain forest region and West of Lake Volta. In Burkina Faso the spatial distribution is comparable, but more patchy.

To consider the temporal development of the *LAI* as a consequence of precipitation, positive differences between the current and past 8-day composite,

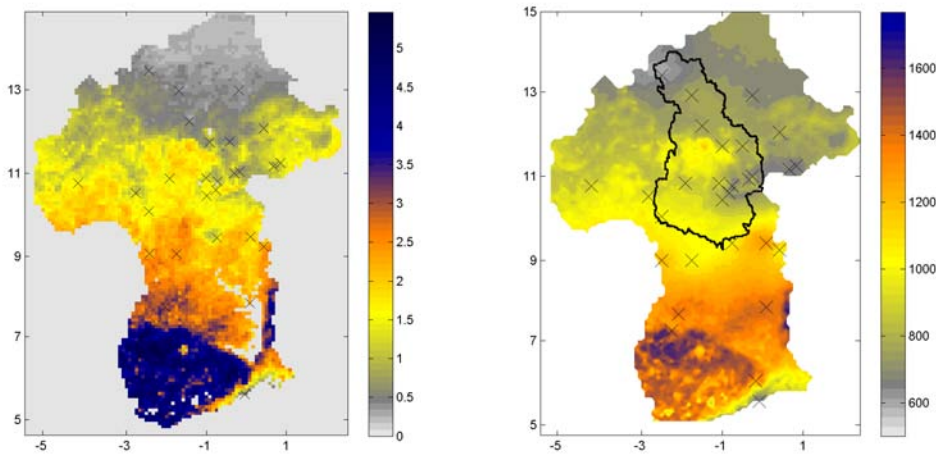

(a) LAI mean (b) EDK(LAI mean)

Figure 7.9: External drift kriging (*EDK*) result for 2004: impact of the external drift (a) mean *LAI* for 2004 on (b) the spatial distribution of annual precipitation [mm]

which represent the *LAI* growth per composite, are applied as further external drift. Due to the fact that (i) the *LAI* and precipitation data are both from 2004 and (ii) precipitation is the limiting factor of plant growth in this region, the relation between precipitation and *LAI* is given. However, it has to be mentioned that this external drift cannot be applied for the complete year, because at the end of the rainy season and during the dry season there are no positive changes of *LAI* and therefore the external drift is not defined. This external drift works best for the first half of the rainy season. During this period, it is a very effective and valuable additional information, especially for precipitation interpolation on a regional scale. In Figure 7.10, the application of *LAI* growth per composite is given exemplarily for July 09, 2004. For this date, the positive development of *LAI* 8-day composites between July 03 and July 10 (lag 0), and the one composite delayed positive *LAI* development between July 11 and July 18 (lag 1) are given in Figure 7.10(a) and (c). The white patches are non positive changes of *LAI* and are therefore not defined. The main differences between Figure 7.10(a) and (c) occur in the centre of the White Volta basin, where, in the period of July 03 to July 10, the *LAI* increase is maximal and, during the following 8-day composites, the *LAI* values do not increase further. Therefore, in accordance to external drifts, higher precipitation amounts are calculated applying the "lag 0" positive *LAI* changes in the centre of the White Volta basin. Particularly in Burkina Faso, patches with higher precipitation amounts are interpolated according to the external drifts of positive *LAI* changes. In the surroundings of maximal precipitation in the South-West both interpolations provide comparable results.

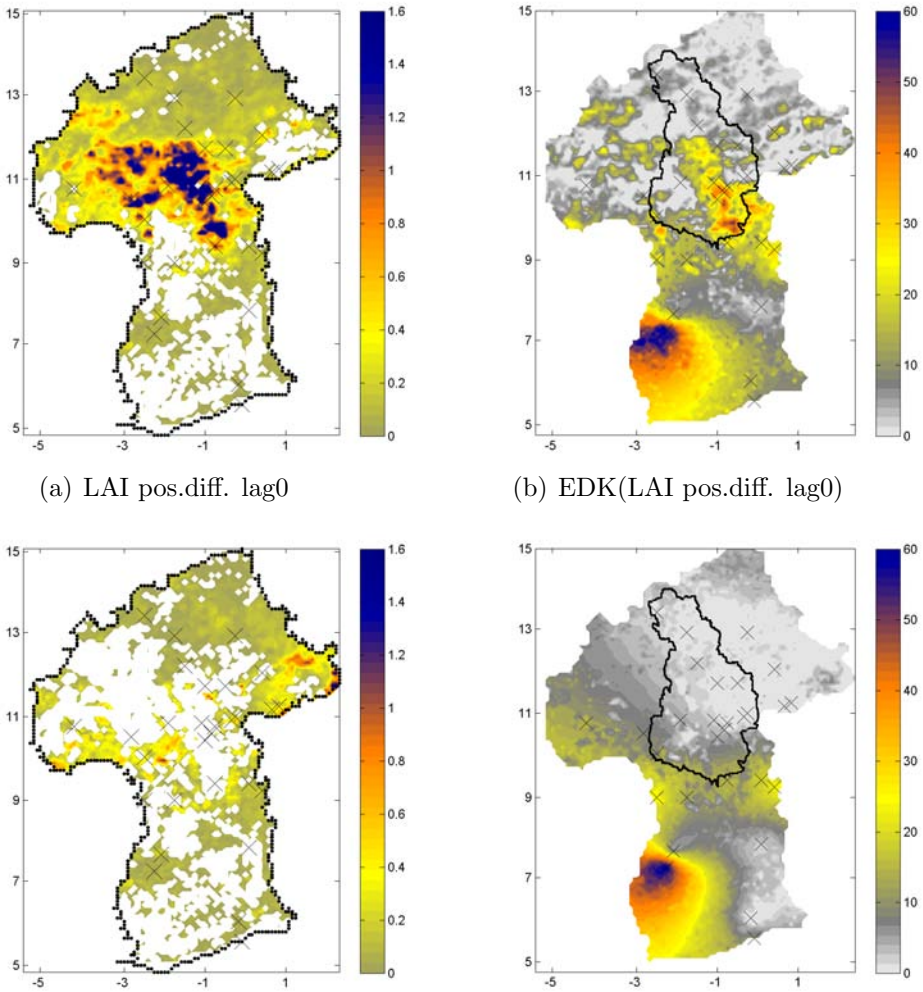

(a) LAI pos.diff. lag0

(b) EDK(LAI pos.diff. lag0)

(c) LAI pos.diff. lag1

(d) EDK(LAI pos.diff. lag1)

Figure 7.10: External drift kriging (*EDK*) result for July 09, 2004: impact of the external drift positive differences of *LAI* values between (a) July 03 to July 10 (lag0) respectively (c) July 11 to July 18 (lag1) on the spatial distribution of precipitation [mm]

This example, with positive differences of *LAI* 8-day composites, shows the potential of applying highly spatial and temporal resoluted remote sensing information which are related to the regionalized variable. Remote sensing data may provide important additional information, especially for short-term and small scale interpolations.

In summary, the areal annual precipitation fields have shown that the application of external drifts, which is related to the regionalized variable, supports the spatial interpolation of point measurements. The long-term mean precipitation field provides important additional information, e.g precipitation maximum in the South-West of Ghana, for the spatial interpolation of precipitation observations. Especially in regions with a weak infrastructure, where meteorological data are not available with a sufficient spatial resolution, adequate external drifts may support the spatial interpolations of coarse-resolution meteorological point observations and hereby may help to decrease interpolation uncertainties.

7.3.3 Cross validation results

Cross validation is applied for all described spatial interpolation methods, to compare the performances.Therefore, rainfall is estimated successively for each sampled location using the known neighbours, but always discarding the observed value for the specific target location (Isaaks and Srivastava, 1989). The observed values $z(u)$ are then compared with the interpolated ones $z^*(u)$ using the following performance measures (Haberlandt, 2007):

1. Bias:
$$Bias = \frac{1}{n} \cdot \sum_{i=1}^{N} [z^*(u_i) - z(u_i)] \tag{7.14}$$

2. Root mean square error *RMSE*:
$$RMSE = \sqrt{\frac{1}{n} \cdot \sum_{i=1}^{N} [z^*(u_i) - z(u_i)]^2} \tag{7.15}$$

3. *RMSE* normalised with the observed average $\overline{z}$
$$n.RMSE = \frac{RMSE}{\overline{z}} \tag{7.16}$$

4. Coefficients of determination R^2 (see Equation 5.1), defined as square of Pearson correlation coefficient between $z^*(u)$ and $z(u)$.

5. Ratio of the variance of estimated values to the observed values:

$$RVar = \frac{VAR[z^*(u)]}{VAR[z(u)]} \tag{7.17}$$

RVar assesses the ability of the interpolation method to preserve the observed variance. This is an important performance measure because interpolation usually leads to a smoothing of the observations (Haberlandt, 2007).

Comparison of performance indices

Daily cross validation products are first accumulated for 2004 and then annual performance indices are calculated. These are listed in Table 7.1 to Table 7.3.

Method	Vario	Bias	RMSE	n.RMSE	R^2	RVar
Thiessen	-	-21.5	329.3	0.343	0.321	1.085
IDW	-	-126.3	284.9	0.302	0.493	0.719
OK	exp	21.5	243.0	0.257	0.558	0.777
OK	sph	37.9	255.0	0.270	0.527	0.807
OK	nug, exp	25.5	245.5	0.260	0.565	0.844
OK	nug, sph	35.8	255.1	0.270	0.534	0.844
EDK dem	exp	53.9	255.6	0.271	0.552	0.880
EDK dem	sph	60.7	268.4	0.284	0.509	0.879
EDK dem	nug, exp	48.6	255.0	0.270	0.560	0.926
EDK dem	nug, sph	51.7	266.4	0.282	0.512	0.892
EDK dist	exp	27.6	284.6	0.302	0.439	0.935
EDK dist	sph	33.3	306.9	0.325	0.373	1.009
EDK dist	nug, exp	22.0	282.5	0.299	0.458	0.980
EDK dist	nug, sph	24.3	302.9	0.321	0.390	1.023

Table 7.1: Cross validation results for the spatial interpolation of precipitation for 2004 using the following methods: Thiessen polygons, inverse distance weighting (*IDW*), ordinary kriging (*OK*) and external drift kriging (*EDK*), with digital elevation model (EDK dem) and distance to the coastline (EDK dist) as external drifts

Considering normalised root mean square error (*n.RMSE*), kriging interpolation results in Table 7.1 outperform the Thiessen polygon and *IDW* methods, expect for *EDK* with distance to coastline information and the spherical variogram model. Best results with lowest *n.RMSE* and highest R^2 in Table 7.1 are obtained with *OK* and the exponential variogram model. Applying external drifts increases the fraction of variance *RVar*. In particular with distance to coastline information, values close to one are reached.

In Table 7.2, cross validation results applying long-term mean annual and monthly precipitation data are summarized. The adding of distance to sea

information as external drift for the interpolation of long-term observations improves the interpolation results with lower *n.RMSE* and higher R^2 values. *EDK* with long-term mean monthly precipitation information decreases the *n.RMSE* further, but also lowers R^2 and *RVar* values. One possible reason for the decrease in variance are quite homogeneous monthly precipitation fields during the dry season. Compared to the *OK* results in Table 7.1, *EDK* with long-term mean monthly or annual precipitation information leads, in general, to decreasing *n.RMSE* and increasing R^2 and *RVar* values. In particular with the mean annual precipitation, *RVar* is close to one and thus preserves the observed variability.

In Table 7.3, cross validation results applying *LAI* information as external drift, are listed. First, mean *LAI* for 2004 is applied as external drift. Compared to the other kriging results, mean *LAI* does not improve the interpolation results. The cross validation results applying positive differences of *LAI* 8-day composites cannot be compared directly to the previous annual results, because *EDK* is only applied if positive *LAI* differences exists. The performance of both options is comparable. However, *RVar* values are slightly higher considering a lag of one *LAI* composite.

Summarizing the cross validation results, the kriging methods outperform the *IDW* interpolation. Considering external drifts increases the *RVar* values close to one, which means that the observed variability is preserved using *EDK*.

Method	**Vario**	**Bias**	**RMSE**	**n.RMSE**	$\boldsymbol{R^2}$	**RVar**
EDK a. rain OK	exp	62.4	253.9	0.269	0.589	0.996
EDK a. rain OK	sph	71.0	241.8	0.256	0.631	0.957
EDK a. rain OK	nug, exp	58.6	254.5	0.270	0.604	1.094
EDK a. rain OK	nug, sph	63.7	238.6	0.253	0.644	1.007
EDK a. rain EDK	exp	60.8	251.8	0.267	0.597	1.006
EDK a. rain EDK	sph	63.3	230.9	0.245	0.664	0.989
EDK a. rain EDK	nug, exp	57.2	252.4	0.268	0.611	1.101
EDK a. rain EDK	nug, sph	56.2	227.7	0.241	0.676	1.033
EDK m. rain EDK	exp	50.4	234.7	0.252	0.589	0.878
EDK m. rain EDK	sph	57.4	238.0	0.255	0.588	0.902
EDK m. rain EDK	nug, exp	45.6	232.9	0.250	0.601	0.920
EDK m. rain EDK	nug, sph	50.69	240.662	0.258	0.587	0.972

Table 7.2: Cross validation results for the spatial interpolation of precipitation for 2004 using external drift kriging (*EDK*) with long-term mean annual and monthly rainfall (EDK a. rain and EDK m. rain) as external drifts

Method	Vario	Bias	RMSE	n.RMSE	R^2	RVar
EDK mean LAI	exp	84.2	310.9	0.329	0.449	1.194
EDK mean LAI	sph	73.2	268.7	0.285	0.552	1.018
EDK mean LAI	nug, exp	60.6	277.4	0.294	0.529	1.102
EDK mean LAI	nug, sph	53.3	248.7	0.264	0.598	0.986
EDK delta LAI	exp	49.1	161.5	0.221	0.735	0.880
EDK delta LAI	sph	46.9	161.7	0.221	0.739	0.944
EDK delta LAI	nug, exp	37.8	152.3	0.208	0.755	0.8673
EDK delta LAI	nug, sph	36.3	154.9	0.212	0.751	0.923
EDK delta LAI lag1	exp	44.5	176.4	0.248	0.735	0.917
EDK delta LAI lag1	sph	43.5	174.1	0.245	0.749	0.980
EDK delta LAI lag1	nug, exp	38.7	173.7	0.244	0.738	0.907
EDK delta LAI lag1	nug, sph	37.0	172.2	0.242	0.745	0.943

Table 7.3: Cross validation results for the spatial interpolation of precipitation for 2004 using external drift kriging (*EDK*) with mean leaf area index for 2004 (EDK mean LAI), and positive differences of LAI 8-day composites for July 09, 2004 without (EDK delta LAI) and with a lag of one composite (EDK delta LAI lag1)

7.3.4 Turning bands results

As described in Section 7.2, daily precipitation data have to be normal score transformed before applying turning band simulations. Herewith, original observations with zero precipitation are transformed by random numbers, filling the Gaussian curve left of zero. According to the kriging interpolations, seven meteorological stations with *TRMM* data are added as input data for the Burkinabè part of the research area. As a consequence of this transformation, the experimental and theoretical variograms have to be recalculated. In addition,the number of bands has to be defined to start the turning band simulations. In this study, 24 bands are selected which is within the range (between 18 and 36) required for two-dimensional problems (BÁRDOSSY, 2006). For each (daily) time step a random number between 1 and 101 is drawn which defines how many simulations are performed for this specific day. Thus, for each time series and for each day, random numbers of simulations are performed which can be arbitrarily combined for the following analysis. For this study this means that annual time series with random numbers of simulations per day are performed. Finally, the results of the turning bands simulations have to be transformed back and negative simulated values have to be replaced by zero.

In Figure 7.11, the annual precipitation for 2004, calculated with two different combinations of daily turning band simulations, are shown exemplarily. Furthermore, mean and standard deviation of all turning band simulations for annual precipitation at each grid point are depicted in Figure 7.12. The

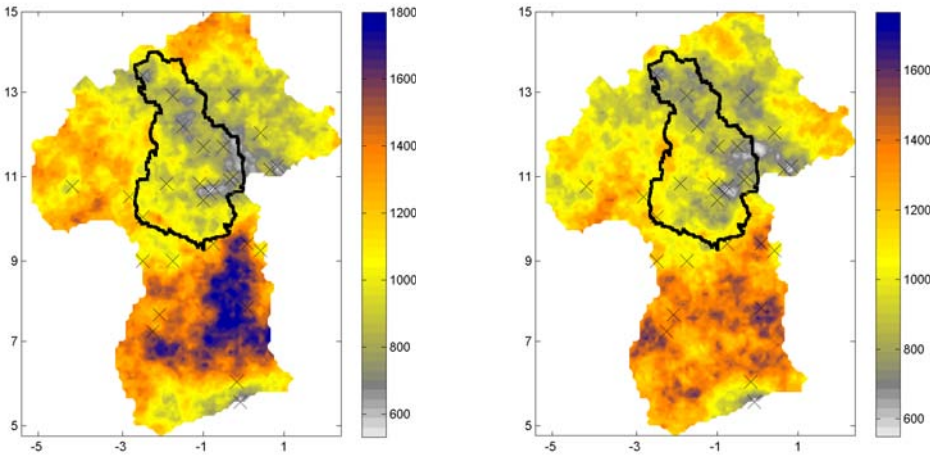

(a) (b)

Figure 7.11: Two examples of turning band simulations showing annual precipitation for 2004 [mm]

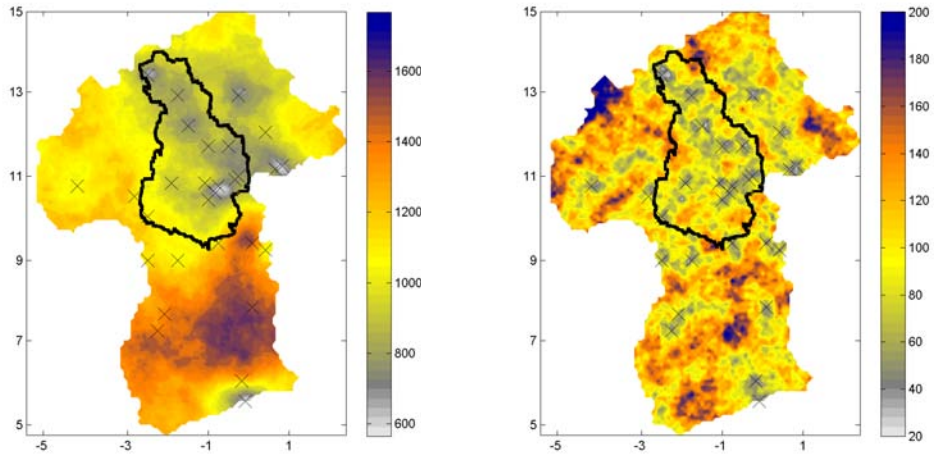

(a) mean (b) standard deviation

Figure 7.12: Mean and standard deviation of all turning band simulations for annual precipitation for 2004 [mm]

patterns of the mean precipitation field are comparable to the *OK* results in Figure 7.5. This is expected, due to the fact that the same input data source, despite the transformation, is used. Furthermore, averaging leads to a smoothing effect of the differences between the turning band simulations. In comparison to the *OK* results, the spatial variability of annual precipitation is increased when applying turning band simulations. This difference is even more pronounced when comparing *OK* and single turning band simulation results. Here the smoothing effect through averaging does not occur. Hence, the turning band simulations increase the spatial variability of the precipitation fields. The standard deviation plot in Figure 7.12(b) is shown as measure of differences between the single turning band simulations. The main differences occur in regions with little or no observations, in particular in the North-West of Burkina Faso, in central Ghana around longitude -1° and latitude 7°, and in the South-West of Ghana. Despite the patchy figures and differences in weak and ungauged regions, the latitudinal dependency of annual precipitation is still distinguishable.

7.4 Impact of areal precipitation estimations on hydrological modelling

The impact of the differences of areal precipitation fields, due to the selected spatial interpolation methods described in the previous sections on the spatial and temporal changes of water balance variables, is investigated for the White Volta basin, which is only a section of the total area of Ghana and Burkina Faso discussed so far in this chapter. The location of the White Volta basin indicates that the differences along the shore are not relevant for the hydrological investigations. Hydrological modelling results of the applied, different spatial interpolation methods are described in the following sections.

7.4.1 Impact on discharge time series

First, routed discharge time series are given for Nawuni, the outlet of the entire White Volta basin. Figure 7.13 shows the results using Thiessen polygons (blue) or *IDW* (green) as spatial interpolation method for precipitation. Compared to the performance of the hydrological simulations using *IDW*, the Thiessen polygon method leads to higher peaks as well as larger total volumes of discharge.

Hydrological modelling results using *OK* as spatial interpolation method are shown in Figure 7.14. The impact of the applied theoretical variograms on the daily time series of routed discharge is small. Differences occur depending on the use of a nugget model or not. The simulations without nugget effect (blue and red lines) lead to slightly higher discharge values.

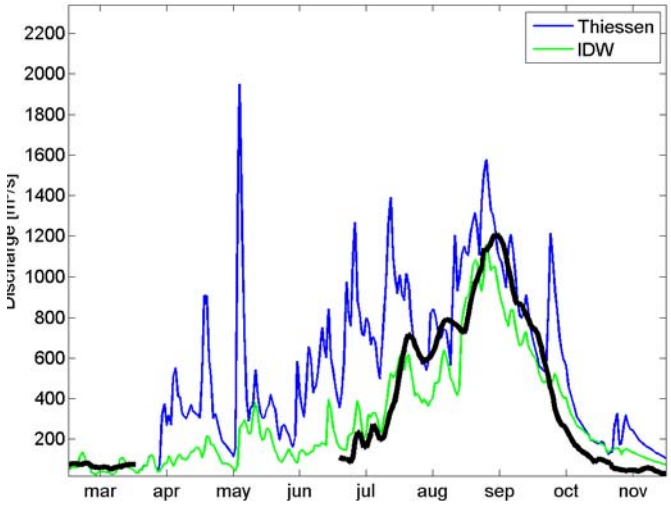

(a) Nawuni

Figure 7.13: Routed vs. measured discharge [m^3/s] for Nawuni (2004) using Thiessen polygons (blue) or inverse distance weighting (green) as spatial interpolation method for precipitation

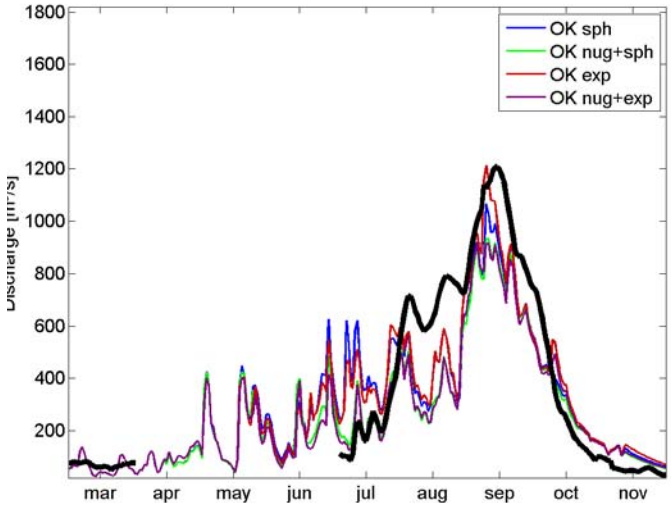

(a) Nawuni

Figure 7.14: Routed vs. measured discharge [m^3/s] for Nawuni (2004) using ordinary kriging with different theoretical variogram models as spatial interpolation method for precipitation: spherical (blue), nugget plus spherical (green), exponential (red) and nugget plus exponential (purple)

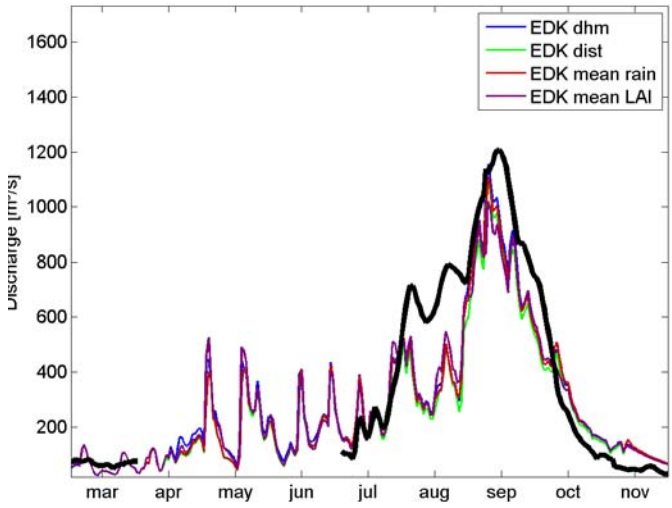

(a) Nawuni

Figure 7.15: Routed vs. measured discharge [m^3/s] for Nawuni (2004) using external drift kriging with the digital elevation model (blue), distance to coast (green), long-term mean annual precipitation grid (red), and mean annual leaf area index (purple) as external drifts, and the nugget plus exponential (exp) variogram model

Like for the simulation results using *OK* as interpolation method, the impact of the applied theoretical variograms on the daily discharge time series is small using *EDK* with the different external drifts. Therefore, Figure 7.15 shows only simulation results using a combination of nugget and exponential model as the theoretical variogram. For the spatial interpolation of precipitation *EDK* is applied with (i) digital elevation model, (ii) distance to coast, (iii) mean annual precipitation grid interpolated with *EDK* using the distance to the coastline information, and (iv) mean annual leaf area index (*LAI*) as external drifts. Figure 7.15 depicts minor impacts of all applied external drifts on the discharge.

The results show that the impact of the external drift on the discharge time series is small. This also applies for the other subcatchments. The general characteristics of the time series are comparable. Some differences occur whether a nugget model is considered or not. The nugget model describes the microscale variation in the vicinity of its origin. Thus, without a nugget model the microscale variation has a larger sphere of influence which impacts the spatial interpolation. This may be a reason for the occurrence of small differences.

7.4.2 Impact on spatial distribution of water balance variables

In this section, the impact of the spatial interpolation method for precipitation on the spatial distribution of water balance variables is investigated. Although the results in the previous Section 7.4.1 have shown a minor impact on aggregated variables and corresponding time series (routed discharge), an impact on the spatial distribution of water balances variables may occur.

For the purpose of comparison, absolute and *RMSE* values, compared to the reference *IDW* result, are calculated for each interpolation method. Due to the fact that the different simulation results are not compared to observation data but to one specific simulation result, the *RMSE* values in the following tables do not express errors, but differences compared to the reference simulation.

Basin wide mean and standard deviation of absolute and *RMSE* values are listed for three important variables of the terrestrial water balance: precipitation, actual evapotranspiration, and total runoff (Table 7.5 and Table 7.6) for all applied spatial interpolation methods. The comparison of absolute values in Table 7.5 for the applied spatial interpolation methods shows that annual precipitation calculated with *IDW* is maximal. Annual actual evapotranspiration values are in the same range for all applied methods, but differ in accordance to precipitation differences. For total discharge, mean annual results are ambiguous. For the standard deviation of these two variables, higher values are calculated (i) with the exponential in contrast to the spherical variogram, and (ii) without the consideration of an additional nugget model. For total discharge, the differences using a nugget model in the variogram analysis are larger compared to the other variables for both the mean and standard deviation.

The calculation of the coefficient of variation *CV*, which is defined as

$$CV = 100 \cdot \frac{std}{mean} \tag{7.18}$$

leads to the following summarized results:

	rain	$\boldsymbol{ET_a}$	**total Q**
IDW	12.4	16.4	98.9
OK	10.7 - 12.4	15.8 - 16.9	84.6 - 102.1
EDK	11.2 - 14.3	15.8 - 17.4	83.9 - 96.6

Table 7.4: Range of coefficient of variations *CV* for annual precipitation, actual evapotranspiration and total runoff using *IDW*, *OK*, and *EDK* for the spatial interpolation of precipitation

The results in Table 7.4 show that relative small changes in the precipitation distribution may lead to large differences in total runoff. Considering only the

applied kriging methods, all applied external drifts result in higher *CV* values compared to *OK* for annual precipitation. With respect to the variogram model, higher *CV* values are calculated for precipitation and actual evapotranspiration (i) with exponential, in contrast to spherical, variograms, and (ii) without the consideration of an additional nugget model, according to the standard deviation results. For total discharge it is vice versa. Overall, the mean *CV* value for all applied *EDK* methods, compared to *OK*, is slightly larger for precipitation and evapotranspiration and lower for total discharge.

The comparison of *RMSE* in Table 7.6 shows the maximal value for total runoff using Thiessen polygon, which confirms the large differences in the discharge time series in Figure 7.13. For all three variables (i) spherical, in contrast to exponential, variograms, and (ii) the use of an additional nugget model lead to higher *RMSE* values. These results seem to be contrary to the ones in Table 7.5, where for the standard deviation highest absolute values are calculated using the exponential model without nugget. Due to the definition of *RMSE* in this section, the differences between kriging and *IDW* interpolations determine the results in Table 7.5. Thereby the decreasing influence with increasing distance of the *IDW* method is more comparable to a variogram without nugget model in contrast to a combination with nugget model, where microvariability determines a large part of the total variability already around the origin (see Figure 7.2). There is no clear trend for the mean and standard deviation of *RMSE* values for all three variables between *OK* and *EDK*. Calculated *CV* values for the *RMSE* results show that the mean *CV* value for all applied *EDK* methods, compared to *OK*, is larger for all three variables.

Method	Vario	rain [mm]		ET_a [mm]		total Q [mm]	
		mean	std	mean	std	mean	std
Thiessen		863.44	146.93	738.30	137.59	165.26	111.12
IDW		873.80	107.94	761.85	124.65	80.24	79.40
OK	exp	816.99	101.39	744.73	126.26	87.62	74.15
OK	sph	825.65	95.84	749.43	120.91	80.10	72.27
OK	nug, exp	823.82	87.76	755.69	121.92	62.27	62.33
OK	nug, sph	827.30	88.81	755.39	119.52	62.76	64.06
EDK dem	exp	844.86	110.76	762.76	127.73	90.69	77.91
EDK dem	sph	845.08	104.32	762.35	122.60	84.67	76.16
EDK dem	nug, exp	841.65	95.63	766.18	124.46	73.61	67.79
EDK dem	nug, sph	840.03	94.36	764.19	120.82	70.77	68.35
EDK dist	exp	817.23	105.37	745.68	127.71	87.88	74.45
EDK dist	sph	819.28	101.46	748.92	124.17	68.90	61.63
EDK dist	nug, exp	812.10	94.89	745.93	124.14	83.32	73.48
EDK dist	nug, sph	811.67	96.02	747.50	122.22	68.01	63.24
EDK rain OK	exp	822.10	104.19	748.09	126.56	90.10	75.83
EDK rain OK	sph	828.63	100.82	750.32	122.17	86.78	76.68
EDK rain OK	nug, exp	811.45	96.41	747.96	123.60	73.51	65.42
EDK rain OK	nug, sph	813.48	92.76	746.03	120.51	75.26	67.97
EDK rain EDK	exp	820.22	104.92	747.10	126.58	89.86	75.39
EDK rain EDK	sph	820.44	101.78	746.08	122.77	86.81	75.80
EDK rain EDK	nug, exp	811.96	95.98	748.22	123.57	73.77	65.52
EDK rain EDK	nug, sph	812.80	95.76	746.73	121.00	73.95	66.81
EDK mean LAI	exp	860.58	123.08	775.64	135.01	85.57	76.90
EDK mean LAI	sph	862.97	116.52	774.08	130.79	82.52	75.41
EDK mean LAI	nug, exp	853.73	117.97	776.30	133.16	68.36	63.85
EDK mean LAI	nug, sph	855.21	116.37	774.97	130.47	68.22	65.09

Table 7.5: Mean and standard deviation of basin-wide annual precipitation, actual evapotranspiration, and total runoff [mm] for 2004 applying the following spatial interpolation methods for precipitation: Thiessen polygons, inverse square distance weighting (IDW), ordinary kriging (OK) and external drift kriging (EDK) with digitial elevation model (EDK dem), distance to the coastline (EDK dist), long-term mean annual precipitation (EDK rain), and mean leaf area index LAI for 2004 as external drifts

Method	Variogram	rain [mm]		ET_a [mm]		total Q [mm]	
		mean	std	mean	std	mean	std
Thiessen		69.87	52.75	59.85	43.15	113.36	78.35
IDW		0.00	0.00	0.00	0.00	0.00	0.00
OK	exp	60.82	22.09	28.58	20.43	31.25	22.82
OK	sph	66.88	42.34	35.00	24.28	31.58	22.32
OK	nug, exp	73.04	48.05	37.38	27.16	39.65	31.74
OK	nug, sph	82.09	53.34	44.66	29.52	40.66	33.57
EDK dem	exp	57.54	36.82	34.32	28.54	28.35	20.53
EDK dem	sph	65.09	44.93	38.57	30.92	29.53	21.36
EDK dem	nug, exp	64.53	42.28	38.58	31.99	32.61	26.18
EDK dem	nug, sph	72.58	49.43	43.13	33.33	34.98	28.95
EDK dist	exp	59.85	19.71	28.69	21.56	32.04	23.87
EDK dist	sph	65.94	38.10	34.06	25.22	36.92	29.54
EDK dist	nug, exp	76.89	42.58	33.23	23.21	31.95	22.62
EDK dist	nug, sph	80.50	50.38	37.96	27.52	38.53	31.51
EDK rain OK	exp	56.24	21.33	28.65	21.56	30.68	23.20
EDK rain OK	sph	61.92	36.43	33.39	23.21	31.70	22.90
EDK rain OK	nug, exp	72.11	35.61	30.86	22.13	32.51	25.48
EDK rain OK	nug, sph	77.46	46.92	38.04	26.23	35.65	28.35
EDK rain EDK	exp	57.51	20.48	28.68	21.38	30.74	23.26
EDK rain EDK	sph	63.61	33.54	33.66	23.12	31.30	22.87
EDK rain EDK	nug, exp	71.04	34.19	30.97	22.24	32.40	25.38
EDK rain EDK	nug, sph	74.37	42.98	35.54	25.16	34.64	27.65
EDK mean LAI	exp	66.30	45.06	52.75	47.66	29.65	22.40
EDK mean LAI	sph	68.09	49.39	52.06	43.80	31.52	23.57
EDK mean LAI	nug, exp	79.21	52.81	56.59	50.00	36.68	29.51
EDK mean LAI	nug, sph	81.48	59.13	56.93	48.23	38.48	31.45

Table 7.6: Mean and standard deviation of basin-wide annual *RMSE* results with respect to the *IDW* method for precipitation, actual evapotranspiration, and total runoff [mm] for 2004 applying the following spatial interpolation methods for precipitation: Thiessen polygons, inverse square distance weighting (*IDW*), ordinary kriging (*OK*) and external drift kriging (*EDK*) with digitial elevation model (EDK dem), distance to the coastline (EDK dist), long-term mean annual precipitation (EDK rain), and mean leaf area index *LAI* for 2004 as external drifts

In addition to the above shown tables, the spatial distribution of the applied external drifts, and the differences of the simulated annual precipitation, actual evapotranspiration, and total runoff resulting from the *EDK* and *IDW* interpolations for areal precipitation are shown in Figure 7.16 to Figure 7.18. The differences for each grid point are defined as the results of the hydrological simulations using a kriging method minus the ones using *IDW* for the calculation of areal precipitation.

Figure 7.16 depicts simulation results using the digital elevation model as external drift. The impact of the digital elevation model on the spatial distribution of annual precipitation is reflected in the spatial distribution of annual actual evapotranspiration and total runoff, despite the large heterogeneities with positive and negative differences in almost all subcatchments. Compared to the total runoff differences, the impact of the external drift is more pronounced in the spatial distribution of actual evapotranspiration. The differences compensate each other on the total catchment scale to 2.3 mm for annual actual evapotranspiration and to -3.7 mm for annual total runoff for the year 2004.

Figure 7.17 shows the results of the hydrological simulation using the mean *LAI* as external drift. The mean *LAI* is maximal in the South-West part of the White Volta basin, which impacts particularly the precipitation interpolation between latitude 11° and 12° and hence the spatial distribution of annual actual evapotranspiration and total runoff. These differences compensate each other on the total catchment scale to 3.6 mm for annual actual evapotranspiration and to -5.4 mm for annual total runoff for the year 2004.

Compared to the previous simulation results, the impact of mean annual precipitation as external drift on hydrological simulation results is less pronounced for all three variables (see Figure 7.18). One reason may be the relatively smooth shape of the external drift, which is due to the required spatial interpolation of observation data to get the gridded mean annual precipitation field. On the catchment scale, the annual differences of -1.3 mm for actual evapotranspiration and -4.0 mm for total runoff are calculated.

In addition to the areal estimation of the regionalized variable, kriging provides a spatially distributed estimation variance, which is shown as square root in Figure 7.19 for the White Volta basin, applying *EDK* with digital elevation model (a) and mean annual precipitation (b) as external drifts. With the estimation variance as a measure of the reliability of the spatially interpolated precipitation field, the reliability of the hydrological simulations, due to uncertainties in the areal precipitation interpolation, can be estimated. The errors are small and situated circularly around the observations, and maximally along the boundaries of the White Volta basin in the North, West and South, due to missing observation data.

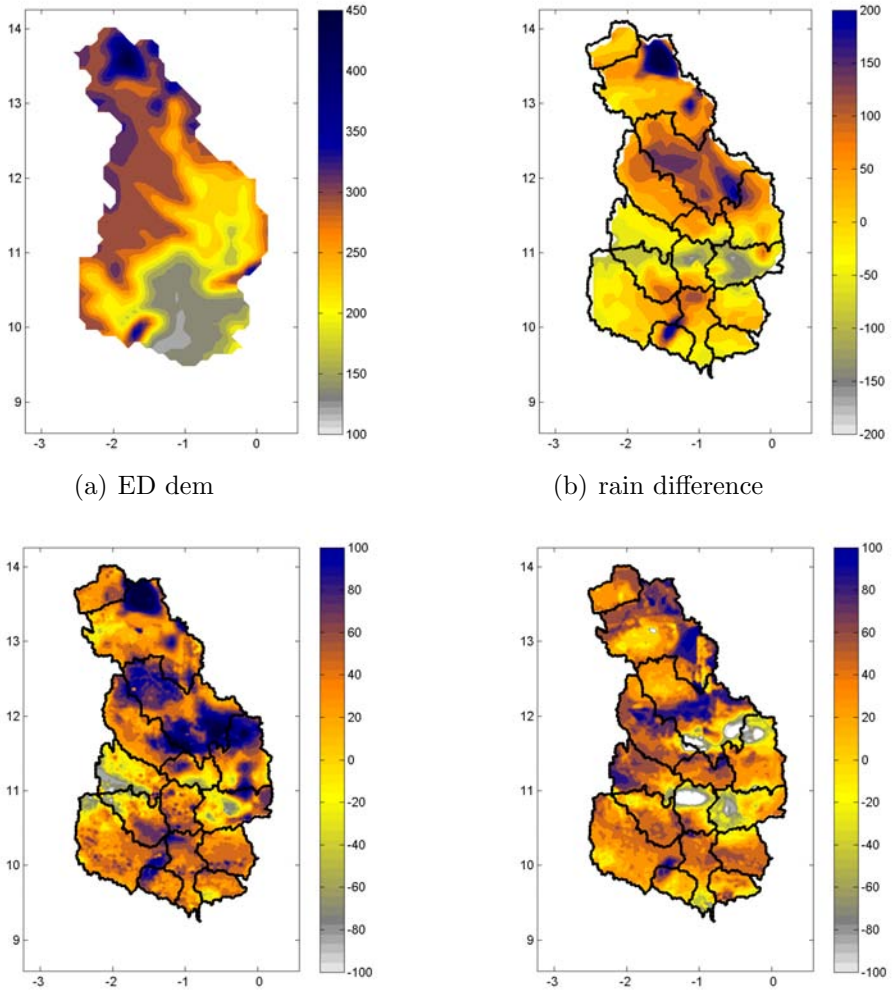

(a) ED dem

(b) rain difference

(c) ET_a difference

(d) total runoff difference

Figure 7.16: Spatial distribution of (a) the external drift digital elevation model, the differences in the interpolated annual precipitation (b), simulated actual evapotranspiration (c), and total discharge (d) [mm] resulting from the applied interpolation methods *EDK* and *IDW* for areal precipitation

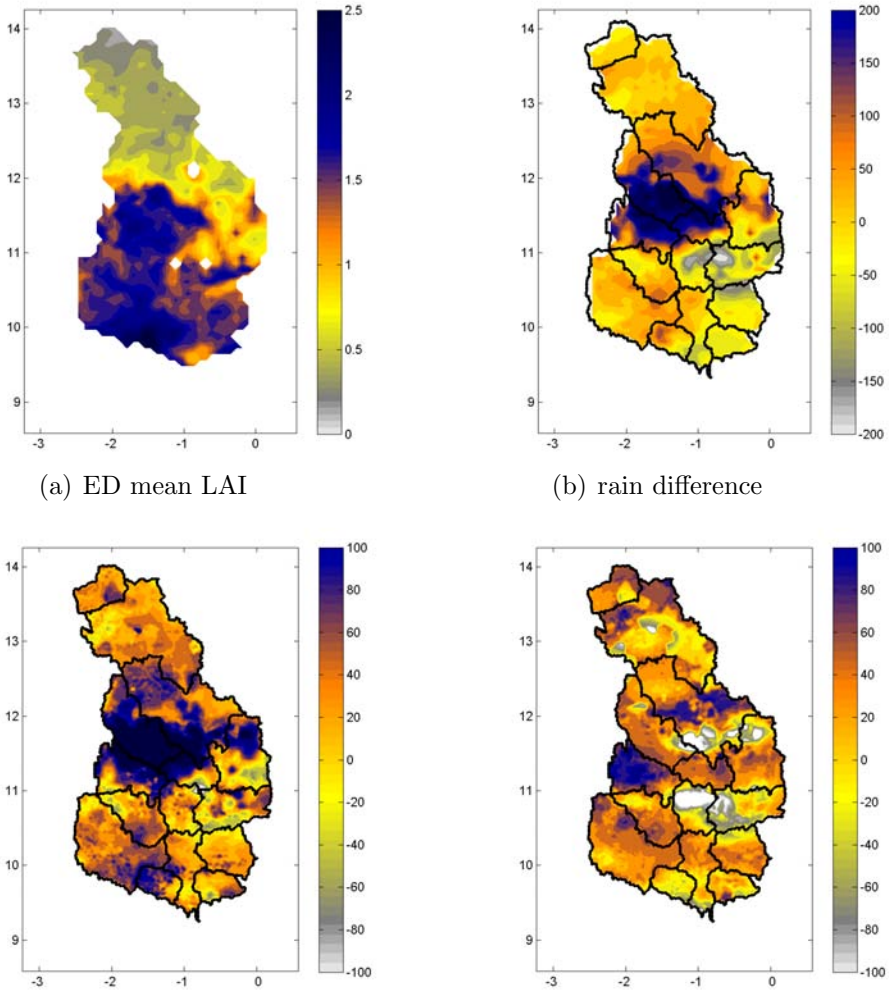

(a) ED mean LAI

(b) rain difference

(c) ET_a difference

(d) total runoff difference

Figure 7.17: Spatial distribution of (a) the external drift mean annual *LAI* for 2004, the differences of the interpolated annual precipitation (b), simulated actual evapotranspiration (c), and total discharge (d) [mm] resulting from the applied interpolation methods *EDK* and *IDW* for areal precipitation

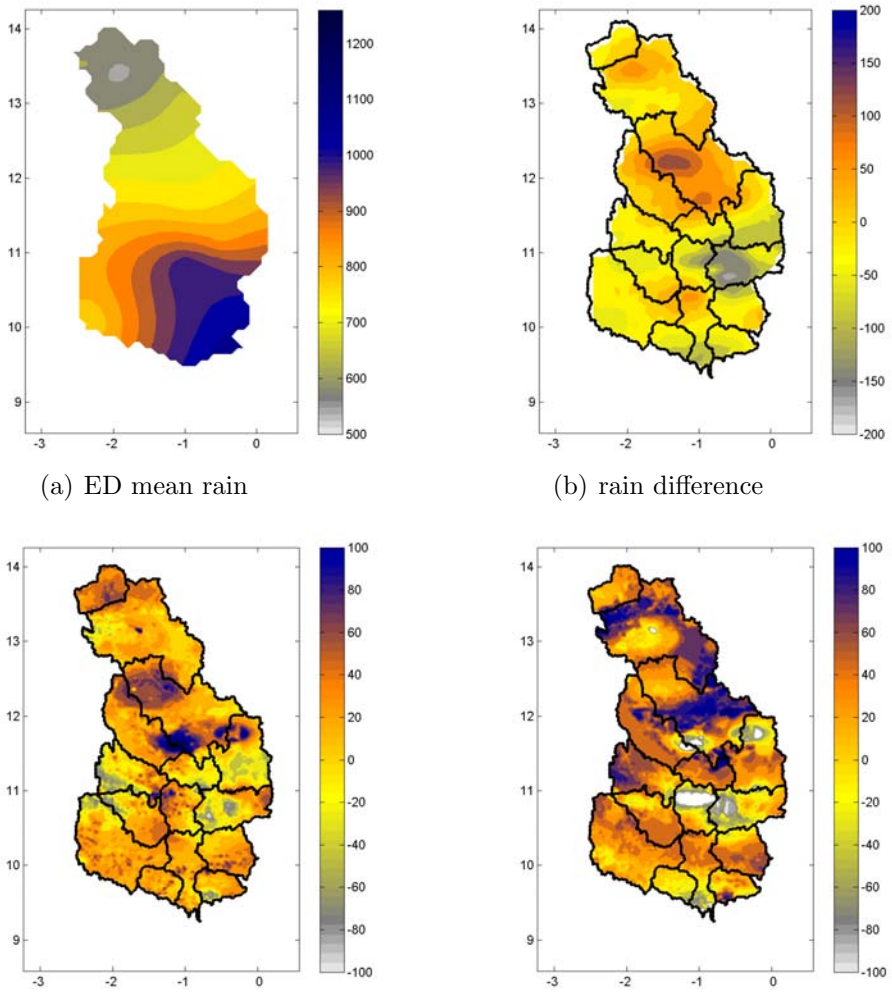

(a) ED mean rain

(b) rain difference

(c) ET_a difference

(d) total runoff difference

Figure 7.18: Spatial distribution of (a) the external drift long-term mean annual precipitation, the differences of the interpolated annual precipitation (b), simulated actual evapotranspiration (c), and total discharge (d) [mm] resulting from the applied interpolation methods *EDK* and *IDW* for areal precipitation

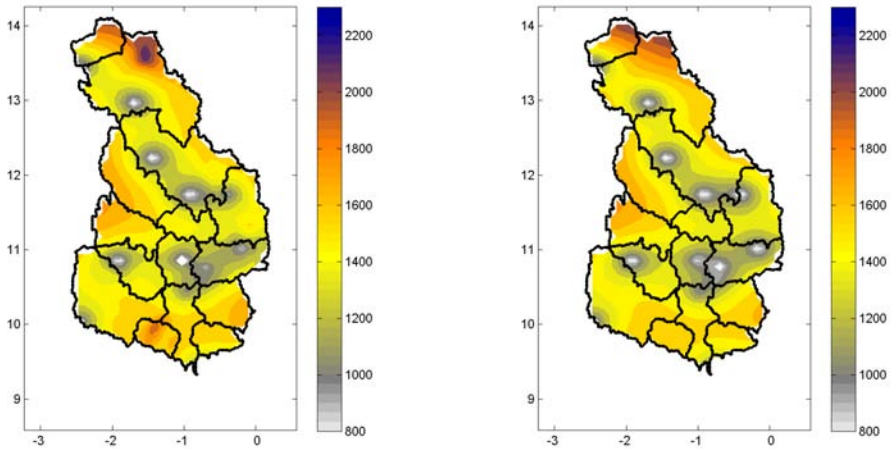

(a) $\sqrt{\sigma^2}$ EDK dem (b) $\sqrt{\sigma^2}$ EDK mean rain

Figure 7.19: External drift kriging estimation variances using (a) digital elevation model and (b) mean annual precipitation as external drift for 2004

In summary, the results show that the selected kriging method produces small differences for spatially aggregated variables. The corresponding time series of e.g. routed discharge do not differ significantly. The selected kriging method affects the spatial distribution of water balance variables. For absolute values, the use of external drifts leads to increasing standard deviation and *CV* values for precipitation compared to *OK*. *RMSE* values, defined as differences between kriging and *IDW* results, are higher when considering an additional nugget model in the variogram analysis. The spatial distribution of annual differences of water balance variables, calculated as differences between hydrological simulations using a selected kriging method and *IDW* as interpolation method, show large heterogeneities with basin-wide positive and negative signs. Despite the large heterogeneity the impact of the external drift can be detected in the corresponding spatial distributions.

7.5 Impact of turning band simulations for precipitation on hydrological modelling

The results of the turning band simulations (see Section 7.3.4) are applied as precipitation input to investigate the impact of uncertainties on hydrological modelling results, due to spatial interpolation or simulation of station data. Therefore, different randomly selected daily turning band results are connected to time series, which then allow scenario simulations for the estimation of uncertainties in water balance estimations due to uncertainties resulting from the precipitation input. This means that for this investigation not single hydrological simulations, but the entirety of simulations driven with randomly selected time series of daily turning band results, are relevant. Thus, these simulations provide ranges of the temporal development and spatial distribution of water balance variables due to uncertainties from the spatial interpolation of precipitation measurements.

First, basin-wide mean and standard deviation of absolute and *RMSE* values are listed for precipitation, actual evapotranspiration, and total runoff (Table 7.7 and Table 7.8). *RMSE* is again defined as the difference between the applied interpolation/simulation method compared to the *IDW* result. In both tables, the results of the previous interpolations are added for the purpose of comparison.

Method	**Vario**	**rain [mm]**		**ET_a [mm]**		**total Q [mm]**	
		mean	**std**	**mean**	**std**	**mean**	**std**
Thiessen		863.44	146.93	738.30	137.59	165.26	111.12
IDW		873.80	107.94	761.85	124.65	80.24	79.40
OK	mean	823.44	93.45	751.31	122.15	73.18	68.20
OK	min	816.99	87.76	744.73	119.52	62.27	62.33
OK	max	827.30	101.39	755.69	126.26	87.62	74.15
EDK	mean	830.27	103.47	756.25	125.50	79.13	70.68
EDK	min	811.45	92.76	745.68	120.51	68.01	61.63
EDK	max	862.97	123.08	776.30	135.01	90.69	77.91
TB	mean	920.64	138.38	778.05	130.69	136.60	98.21
TB	min	898.53	125.14	765.01	124.98	121.64	84.47
TB	max	949.74	161.05	788.79	138.78	150.57	115.13

Table 7.7: Annual sums for 2004 using the spatial interpolation methods Thiessen polygons, inverse distance weighting (*IDW*), ordinary (*OK*) and external drift kriging (*EDK*), and turning band simulations (*TB*)

Table 7.7 shows the annual precipitation results for 2004 using the applied interpolation methods and turning band simulations. Annual precipitation

Method	Vario	rain [mm]		ET_a [mm]		total Q [mm]	
		mean	std	mean	std	mean	std
Thiessen		69.87	52.75	59.85	43.15	113.36	78.35
IDW		0.00	0.00	0.00	0.00	0.00	0.00
OK	mean	70.70	41.46	36.40	25.35	35.79	27.61
OK	min	60.82	22.09	28.58	20.43	31.25	22.32
OK	max	82.09	53.34	44.66	29.52	40.66	33.57
EDK	mean	68.61	40.10	38.33	29.85	33.04	25.53
EDK	min	56.24	19.71	28.65	21.38	28.35	20.53
EDK	max	81.48	59.13	56.93	50.00	38.53	31.51
TB	mean	135.69	89.34	70.39	47.58	86.43	58.94
TB	min	117.74	82.13	60.42	39.59	68.34	45.53
TB	max	160.84	103.80	83.09	54.91	109.63	80.79

Table 7.8: *RMSE* results with respect to the *IDW* interpolation of annual sums for 2004 using the interpolation methods Thiessen polygons, inverse distance weighting (*IDW*), ordinary kriging (*OK*) and external drift kriging (*EDK*), and turning band simulations (*TB*).

results of the turning band simulations are higher compared to the other methods. This is a consequence of the non-linear Gaussian transformation within the normal score transformation (see Section 7.2). Hence, mean and standard deviation of actual evapotranspiration and total runoff are also higher than for the other methods (Table 7.7).

It is worth mentioning that the standard deviation values are higher for the turning band simulations, except for the Thiessen polygons, which are excluded in the following analysis. The calculation of coefficients of determination *CV* confirms the increase of spatial variability of the considered variable with the turning band simulations. In Table 7.9, mean *CV* values for precipitation, actual evapotranspiration, and total runoff of the turning band simulations are added to the results of Table 7.4. Considering all interpolation methods, an

	rain	ET_a	total Q
IDW	12.4	16.4	98.9
OK	11.4	16.3	94.3
EDK	12.5	16.6	89.6
TB's	**15.0**	**16.8**	**71.9**

Table 7.9: Mean coefficient of variations *CV* for annual precipitation, actual evapotranspiration and total runoff using *IDW*, *OK*, *EDK*, and turning band simualtion (*TB's*) for the spatial interpolation/simulation of daily areal precipitation

increase of the spatial variability of the precipitation grid leads, in general, to (i) an increase of spatial variability for actual evapotranspiration and (ii) a decrease of variability for total discharge. Another reason for the small CV values for turning band simulations are the high means, which again demonstrate that small changes in precipitation may cause large changes in runoff. The $RMSE$ values in Table 7.8 confirm the results with absolute values, in particular the increase of standard deviation values using turning band simulations.

Second, to investigate the impact of turning band simulations on the spatial distribution in detail, the standard deviation of all hydrological simulations, using all turning band results for each grid point, are depicted for annual precipitation, actual evapotranspiration, and total runoff in Figure 7.20. Figure 7.20(a) shows the highest standard deviation values and thus large uncertainties along the boundaries of the White Volta basin. Furthermore, large uncertainties partly occur in the Southern part, in particular in the South-East, where the subcatchment Nasia is located. The spatial distribution of standard deviation values for actual evapotranspiration in Figure 7.20(b) is very patchy. The absolute values are smaller compared to the ones for precipitation. The propagation of uncertainties in the precipitation estimation is clearly visible. The same applies for total runoff in Figure 7.20(c). Simulation results for the subcatchments in the South-East of the White Volta basin are afflicted with larger uncertainties.

Third, the impact on the temporal development of water balance variables applying turning band simulations is investigated. In Figure 7.21, time series of the spatially averaged daily range and mean value for precipitation, actual evapotranspiration, and total runoff for 2004 using turning band simulations as precipitation input is shown. Figure 7.21(a) shows that the range of possible daily precipitation amounts is large. The impact of these differences is clearly visible in the time series of actual evapotranspiration and in particular in that of total runoff. For example, total runoff values vary between 1 and 2 mm/day during the peak in September.

The routed discharge results, using turning band simulations as meteorological input data source, are depicted in Figure 7.22 for the gauges Nasia, Pwalugu, and Nawuni. The time series for the head basin Nasia demonstrate that the mean routed discharge of all hydrological modelling results using turning band simulations overestimate the observed discharges, but the measurements are in general within the range of all modelling results. The band of possible modelling results is wide, which corresponds to the results of the spatial distribution, with large uncertainties for the subcatchments in the South-East for precipitation and total runoff. Compared to the head basin Nasia, the impact of turning band simulations as meteorological input data source is less pronounced for the two main stations along the White Volta; Pwalugu and Nawuni. Observed discharges are mainly within the range of all modelling results, except at the

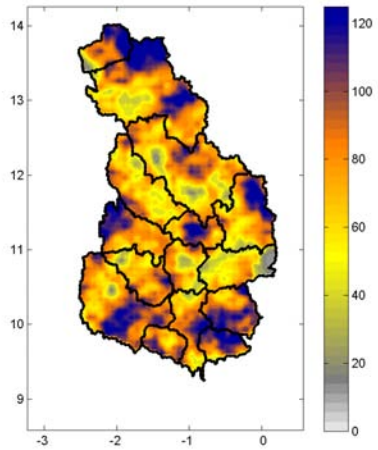

(a) rain

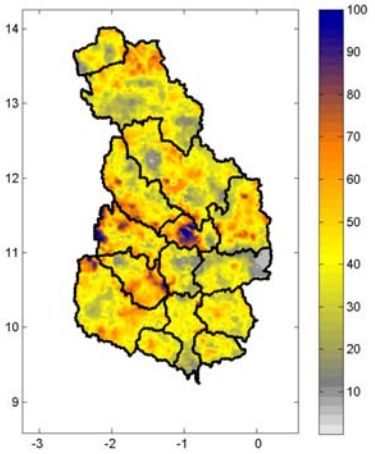

(b) actual evapotranspiration

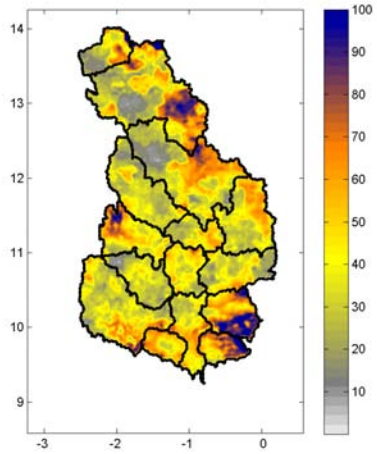

(c) total runoff

Figure 7.20: Spatial distribution of standard deviation of all hydrological simulations using all turning band results for annual precipitation (a), actual evapotranspiration (b), and total runoff (c) [mm] for 2004

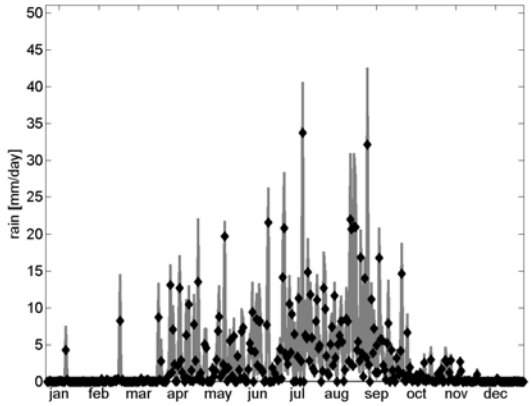

(a) precipitation

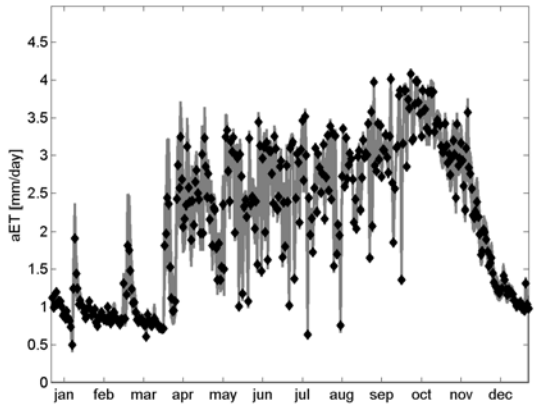

(b) actual evapotranspiration

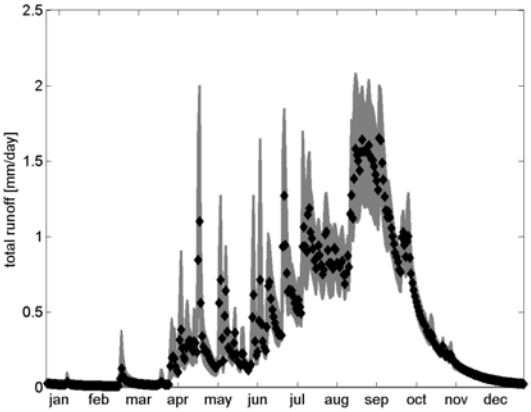

(c) total runoff

Figure 7.21: Time series of the spatially averaged daily range (grey) and mean value (black) for precipitation (a), actual evapotranspiration (b), and total runoff (c) for 2004 using turning band simulations as precipitation input

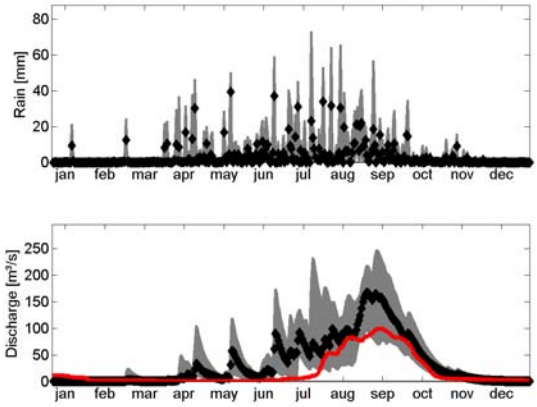

(a) Nasia

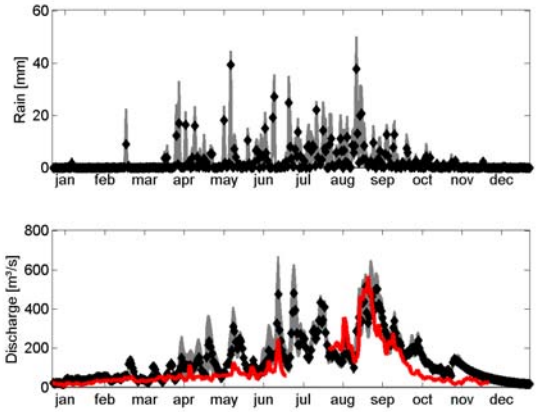

(b) Pwalugu

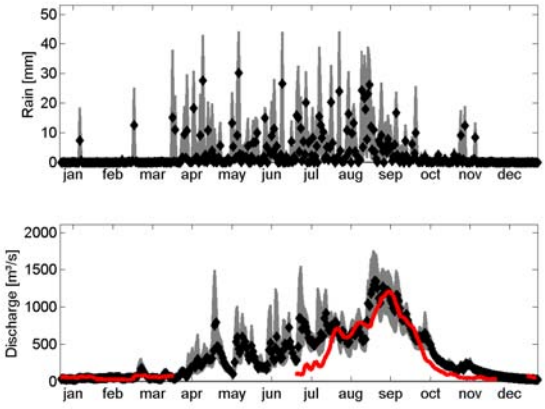

(c) Nawuni

Figure 7.22: Time series of daily range (grey) and mean value (black) for precipitation (top), and routed vs. measured (red) discharge (bottom) for Nasia, Pwalugu and Nawuni for 2004 using turning band simulations as precipitation input

beginning of the rainy season, when simulations overestimate observations. Simulation results for both stations are good, although the range of modelling results using turning band simulations is narrower for Pwalugu and Nawuni compared to Nasia.

In summary, the impact of turning band simulations for precipitation on hydrological modelling results is clearly visible on the spatial distribution and the temporal development of water balance variables. Uncertainties in the precipitation estimation propagate in the spatial and temporal distribution of actual evapotranspiration and total discharge. The width of the bands enclosing all hydrological simulations using turning band results depends on (i) the considered variable and (ii) the location. These bands provide important information on the possible spatial and temporal distribution of water balance variables under consideration of uncertainties, which occur due to the simulation of areal precipitation fields.

7.6 Summary

In this chapter, the propagation of uncertainties, resulting from the calculation of areal precipitation from point measurements, in water balance estimations are investigated. Therefore, different spatial interpolation methods for areal precipitation are applied, and their impact on water balance estimates is analysed. In addition to standard interpolation methods, inverse distance weighting (IDW) and Thiessen polygons, ordinary (OK) and external drift kriging (EDK) are applied for the spatial interpolation. The areal annual precipitation fields show that the application of external drifts supports the spatial interpolation of point measurements. For example, the long-term mean precipitation field provides, in particular in regions with extremely coarse observation networks, important additional information for the spatial interpolation of station data. The performance comparison with cross validation results shows that kriging methods outperform the IDW interpolation. The use of external drifts increases the variance of the areal precipitation fields.

The results of the hydrological simulations show that differences in the areal precipitation fields due to the selected interpolation method, impact the temporal and spatial distribution of water balance variables. For spatially aggregated variables and the corresponding time series the differences are small. However, the selected interpolation method affects the spatial distribution of water balance variables. The differences are very heterogeneous in space, but the impact of the applied external drift can be detected.

In addition to the different interpolation methods, geostatistical simulations for areal precipitation are performed for the investigation of the propagation

of uncertainties in water balance estimations. Compared to the spatial interpolation methods, turning band simulations increase the spatial variability of precipitation fields. This leads to an increase in spatial variability for actual evapotranspiration and a decrease of variability for total discharge, which is in good agreement with the kriging results. The entirety of all hydrological simulations results, driven by equally probable precipitation fields from the turning band simulations, provides ranges of the temporal and spatial distribution of water balance variables. These ranges are the consequence of uncertainties from the calculation of areal precipitation from station data. The propagation of uncertainties in the precipitation estimation in the spatially distributed results for actual evapotranspiration and total runoff is clearly visible. The same applies for the time series of spatially aggregated water balance variables. The range of possible daily precipitation amounts is large, which affects in particular the total runoff time series with a wide range of possible realizations. The comparison of turning band results for routed discharge for the gauges Nasia, Pwalugu and Nawuni shows, that the width of possible realizations varies considerable depending on the location of the subcatchment and the uncertainties of the upstream subcatchments.

8 Summary and conclusions

The main objective of this work is to provide estimations of the current water resources and fluxes in a poorly gauged basin. This is a central task to support water management authorities and stakeholders in operational irrigation, water supply and running hydro-power strategies. In this summary, the integration, potentials and limitations of the applied methods in hydro-meteorological decision support are discussed.

In poorly gauged basins, where no automatic data recorders with online transmission are available, other meteorological data sources for near real time estimations of the terrestrial water balance have to be used to overcome the temporal delay and/or the insufficient spatial resolution. Therefore, a model-based, operational water flow and balance system for the White Volta basin is developed which provides the required information. Near real time water balance estimations, which are available with approximately 48 h delay, require the results of a meteorological model as input data source. This joint atmospheric-hydrological modelling system can also be used in forecast mode where, instead of global analysis data, global forecasts are dynamically downscaled to regional scale. An operational 5-day numerical weather prediction for the Volta basin (http://imk-ifu.fzk.de/de/wetter/index_wetter_africa.htm) is performed at IMK-IFU.

With the results of joint atmospheric-hydrological simulations, near real time estimations of (i) atmospheric variables and (ii) the terrestrial water balance are available. The results of the joint atmospheric-hydrological simulations in ex-post hindcasting mode (Chapter 5.1) have shown that the meteorological model *MM5* is able to provide the required meteorological input data for near real time hydrological simulations in reasonable quality. The joint *MM5-WaSiM* results show a good performance for 2004 and a weaker one for 2005 due to precipitation overestimations. Scaling the *MM5* results with observed, gridded precipitation data from *GPCC* improves the joint *MM5-WaSiM* results considerably for 2005. The scaled *MM5* precipitation fields are available with one month delay, comparable to the scaled *TRMM* product 3B42, whose performance is discussed in the following paragraph.

The performance of the hydrological simulations using the scaled *TRMM* product 3B42 are good. However, the simulations with real time and scaled *MM5* output for 2004 and scaled *MM5* output for 2005 perform better. Due to the fact that the *TRMM* product 3B42 only provides gridded precipitation

data, other data sources for the remaining required meteorological variables have to be used.

Using station data as the meteorological data source, the delay can increase up to one year or more in regions with weak infrastructure and without automatic data recorders. Furthermore, the availability of basin-wide station data is hampered in basins which are shared by several countries. The use of station data as meteorological data source leads to good and often best model efficiencies in this study.

In order to increase the level of detail in the spatial and temporal dimension of land surface properties in hydrological modelling, satellite derived land surface properties are imported into the hydrological model. In this study, the *MODIS* products for albedo and leaf area index *LAI* are used. Both variables have an impact on potential evapotranspiration, which is calculated using the Penman-Monteith approach. In Chapter 6 it has been shown that the comparison between static tabulated values from standard literature and dynamic *MODIS* estimates shows, for albedo, a comparable spatial distribution with an increased level of detail in the spatial dimension for the White Volta basin. For the *LAI*, the temporal development is not sufficiently represented by two seasons with the static tabulated approach in the classic hydrological model setup. In comparison to *MODIS LAI*, the tabulated values overestimate the *LAI* during the dry season and underestimate it during the rainy season in the southern part of the catchment. The assimilation of dynamic *MODIS* estimates of albedo and *LAI* in hydrological modelling show a minor impact on spatially aggregated, daily time series of water balance variables. However, the sum curves of daily differences identify slightly higher values for potential evapotranspiration during the complete year using *MODIS* estimates for albedo. The use of *MODIS* estimates for *LAI* leads to lower potential evapotranspiration values during the dry and equal to slightly higher ones during the rainy season. This agrees well with the differences of albedo and *LAI* grids using static tabulated or dynamic *MODIS* values. The comparison of the impact of interannual variations of *MODIS* albedo and *LAI* shows, that for all water balance variables the temporal development of the sum of differences curves is similar, but the magnitude differs. The impact of dynamic *MODIS* estimates of albedo and *LAI* on the spatial distribution of water balance variables in the White Volta basin is clearly visible. The calculated differences of water balance variables, using *MODIS* estimates or static tabulated values, are very heterogeneous in space with positive and negative signs in almost all subcatchments. Overall, the use of dynamic *MODIS* estimates leads to slightly higher evapotranspiration and runoff values in the North and lower ones in the South of the White Volta basin. Furthermore, the use of dynamic *MODIS* estimates decreases standard deviation values of evapotranspiration and total runoff on sub and catchment scale compared to tabulated static ones for albedo and *LAI*. Despite similar differences with respect to static tabulated values, the impact of

interannual variations of *MODIS* estimates for albedo and *LAI* on the spatial distribution of all water balance variables is clearly visible.

Short-term sustainable decisions in water resources management require the current spatial distribution of water resources like actual evapotranspiration, groundwater recharge, soil moisture, and total runoff. For near real time water balance estimations, discharge time series have been mainly shown as hydrological modelling results in Section 5.3, due to the fact that only discharge measurements are available for validation purposes. According to the long-term (1961-2000) water balance simulation results in Section 5.2.2, *WaSiM* provides additional information about the temporal and spatial distribution of further important water balance variables. For the following results, hydrological simulations are driven by *MM5* results for domain 3 and the year 2004, and dynamic *MODIS* estimates are used for albedo and *LAI*. Hence, these simulations use near real time available meteorological input data and derived land surface properties from remote sensing data.

Spatially distributed results of the expost hindcasting simulations for 2004 are shown for actual evapotranspiration, groundwater recharge, soil moisture, and total runoff as annual sums or mean (for soil moisture) for 2004 in Figure 8.1. The results show, additionally to the large scale distribution, a high spatial variability on smaller scales, except for soil moisture. The spatial resolution of soil moisture is dominated by the coarse-resolution soil texture discretization. This means that a finer discretization of the soil texture will probably increase the spatial resolution of soil moisture. The coupling of a two-dimensional groundwater flow module to the unsaturated zone module provides spatially distributed hydraulic head estimations, which determine the groundwater flow (see Figure 8.2).

The spatial distribution of water balance variables, which are shown in Figure 8.1 and Figure 8.2 as aggregated annual sums or means, are available for each time step, i.e. in this study for each day. Therefore, near real time estimations are available basin wide and spatially distributed for each day. This provides the physical basis needed to support economically and ecologically sound water management decision-making. In this study, the performance of hydrological simulations driven by different meteorological and land surface data sources has been investigated and validated on catchment scale (White Volta basin) and a few subcatchments, where validation data were available. For water management decisions in other subcatchment and on local scales this setup has to be validated before application.

For sustainable decisions in water resources management, in addition to the modelling result itself, the reliability or uncertainty of the result has to be quantified. Due to the fact that the spatial variability of rainfall is often termed as the major source of error in investigations of rainfall-runoff processes and modelling, the propagation of uncertainties, resulting from the calculation of areal

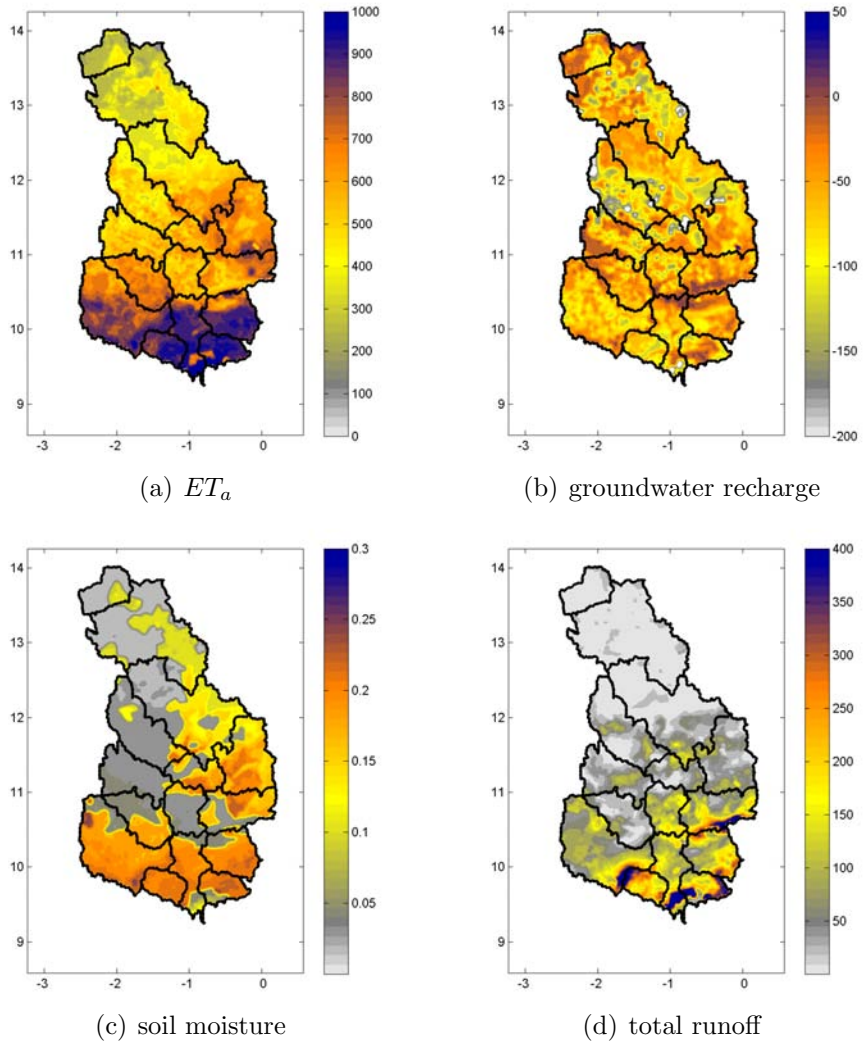

(a) ET_a (b) groundwater recharge

(c) soil moisture (d) total runoff

Figure 8.1: Spatial distribution of annual (a) actual evapotranspiration [mm], (b) groundwater recharge [mm], (c) soil moisture [-], and (d) total runoff [mm] for 2004

precipitation from point measurements, in water balance estimations have been investigated in Chapter 7. In this study, station data are used as the meteorological input data source. First, different spatial interpolation methods for areal precipitation are applied, and their impact on water balance estimates is analysed. Additionally to the standard interpolation methods inverse distance weighting (IDW) and Thiessen polygons, ordinary (OK) and external drift kriging (EDK) are applied for the spatial interpolation. The areal annual precipitation fields show that the application of external drifts supports the spatial interpolation of point measurements. The long-term mean precipitation field provides, in particular in regions with extremely coarse observation networks, important additional information for the spatial interpolation of station data.

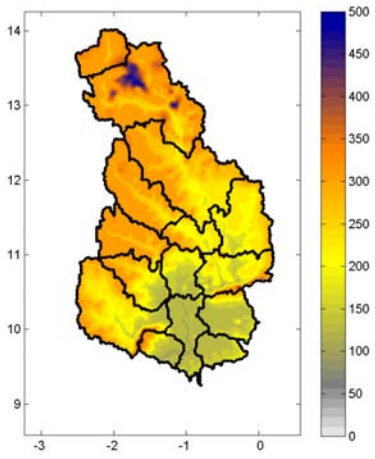

Figure 8.2: Mean annual hydraulic head [m] for 2004

The cross validation results show that kriging methods outperform the *IDW* interpolation. Thereby, the use of external drifts increases the variance of the areal precipitation fields. The impact of the selected spatial interpolation method for areal precipitation on hydrological modelling results is minor for spatially aggregated variables and the corresponding time series. However, the selected interpolation method affects the spatial distribution of water balance variables. Although the differences are very heterogeneous in space, the impact of the applied external drift is clearly visible. Second, geostatistical simulations for areal precipitation are performed in order to investigate the propagation of uncertainties in water balance estimations. Turning band simulations increase the spatial variability of the precipitation fields, which leads to an increase of spatial variability for actual evapotranspiration and a decrease of variability for total discharge. This is in good agreement with the kriging results.

For sustainable decisions in water resources management, the entirety of all hydrological simulation results, driven by equally probable precipitation fields from the turning band simulations, provides ranges of the temporal and spatial distribution of water balance variables (see Figure 7.20 and Figure 7.21). These ranges are the consequence of uncertainties from the calculation of areal precipitation from station data. The propagation of uncertainties from the areal estimation of precipitation in the spatial and temporal distribution of water balance variables is clearly visible. The partially large range of possible daily precipitation amounts leads to a wide range of possible realizations, in particular for the total runoff time series. The comparison of turning band results for routed discharge shows that the width of possible realizations varies considerably depending on the location of the subcatchment and the uncertainties of the upstream subcatchments.

Altogether it was shown that the integration of atmospheric modelling and

satellite derived land surface data provides a significant benefit for hydrological modelling, especially in regions with weak infrastructure and coarse-resolution observation networks. The prerequisite of world wide available data sources and public domain models allows a transfer of the methodological approach of a model based water balance monitoring system to other basins and regions in the world.

Outlook The developed system will be further applied and validated for current years. This will be done by local water management institutions and stakeholders in Ghana and Burkina Faso. For this purpose, the developed system was transferred to Ghana and Burkina Faso, and users will be trained during workshops in January 2008.

The *MM5* simulations are performed with one data set of global analysis fields which is available at real time. Further global analysis fields and particularly reanalysis data may improve the meteorological modelling results with the limitation that they cannot be used for near real time estimations. The joint atmospheric-hydrological simulations are performed in the one-way coupling approach. For a higher degree of consistency between the atmospheric and hydrological part, a two-way coupling approach can be thought to combine the advantages of both models.

In addition to dynamic *MODIS* estimates for albedo and *LAI*, further land surface properties, e.g. roughness length and emissivity, can be assimilated in hydrological and also in meteorological modelling. This allows a more detailed spatial and temporal representation of the land surface properties in the modelling process.

The validation of hydrological simulations was restricted to observed discharge only. If observations become available, the validation should be extended to ground water measurements and spatially distributed information, for example satellite derived evapotranspiration estimations.

The propagation of uncertainties, resulting from the calculation of areal precipitation, in water balance estimations is performed with station data in this work. This can be extended to gridded precipitation data, like meteorological modelling results and the *TRMM* product 3B42. For example, disaggregations of the coarser meteorological fields to the resolution of the hydrological simulations, and the consideration of geostatistical characteristics of the gridded data, could further improve the representation of precipitation and hence estimations of the terrestrial water balance.

Bibliography

Abbott, M.B., & Refsgaard, J.C. (eds). 1996. *Distributed Hydrological Modelling*. Kluwer Academic Publishers.

Adams, W.M., Goudie, A.S., & Orme, A.R. (eds). 1996. *The Physical Geography of Africa*. Oxford University Press.

Agyare, W. A. 2004. *Soil characterization and modeling of spatial distribution of saturated hydraulic conductivity at two sites in the Volta Basin of Ghana*. Ecology and Development Series, vol. 17. Cuvillier Verlag Goettingen.

Ahmed, S., & de Marsily, G. 1987. Comparison of geostatistical methods for estimating transmissivity using data on transmissivity and specific capacity. *Water Resources Research*, **23**(9), 1717–1737.

Amani, A. 2001. *Assessment of precipitation and resources variability across the Sahelian region*. Gash, J.H.C., Odada, E.O., Oyebande, L. Schulz, R.E.; Report of the International Workshop on Africas Water Resources, Nairobi, October 1999 (BAHC).

Amisigo, B. A. 2005. *Modeling riverflow in the Volta Basin of West Africa: A data driven framework*. Ph.D. thesis, University of Delft.

Andreini, M., Giesen, N. Van De, Edig, A. Van, Fosu, M., & Andah, W. 2000. Volta Basin Water Balance. *ZEF - discussion papers on development policy 21*.

Arnell, N. W., Hudson, D. A., & Jones, R. G. 2003. Climate change scenarios from a regional climate model: Estimating change in runoff in southern Africa. *Journal of Geophysical Research*, **108**(D16), 1–17.

Ashrit, R. G., Kumar, K. R., & Kumar, K. K. 2001. ENSO-Monsoon relationships in a greenhouse warming scenario. *Geophysical Research Letters*, **28**, 1727–1730.

Ashton, P. J. 2002. Avoiding conflicts over Africas water resources. *Ambio*, **31**, 236–242.

Asner, G., Scurlock, J., & Hicke, J. 2003. Global synthesis of leaf area index observations: implications for ecological and remote sensing studies. *Global Ecology and Biogeography*, **12**, 191–205.

Bader, J. 2005. *The role of the tropical indian ocean in global climate*. Ph.D. thesis, University of Hamburg.

Bárdossy, A. 2003. Concepts of geostatistics and stochastic modelling. *Lecture notes, University of Stuttgart, Germany*.

Bárdossy, A. 2006. *Personal conversation*.

Bárdossy, A., & Das, T. 2006. Influence on rainfall observation network on model calibration and application. *HESSD*, **3**, 3691–3726.

Bárdossy, A., & Plate, E. 1992. Space-Time Model for Daily Rainfall using Atmospheric Circulation Patterns. *Water Resources Research*, **28**(5), 1247–1259.

Barry, B., Obuobie, E., Andreini, M., Andah, W., & Pluquet, M. 2005. *The Volta River Basin*. Comprehensive Assessment of Water Management in Agriculture, IWMI.

Betts, A. K. 1986. A new convective adjustment scheme. Part I: Observation and theoretical basis. *Quarterly Journal of the Royal Meteorological Society*, **112**, 677–691.

Beven, K. 1989. Changing ideas in hydrology - the case of physically-based models. *Journal of Hydrology*, **105**, 157–172.

Beven, K. J. 2001. *Rainfall-Runoff Modelling*. The Primer. John Wiley and Sons, Chichester.

Boegh, E., Kunstmann, H., Wagener, T., Hall, A., Bastidas, L., Franks, S., Gupta, H., Rosbjerg, D., & Schaake, J. (eds). 2007. *Quantification and Reduction of Predictive Uncertainty for Sustainable Water Resources Management*. IAHS Publication, vol. 313. IAHS Press.

Bougeault, P. 1983. A non-reflective upper boundary condition for limited-height hydrostatic models. *Monthly Weather Review*, **111**, 420–429.

Brath, A., Montanari, A., & Toth, E. 2004. Analysis of the effects of different scenarios of historical data availability on the calibration of a spatially-distributed hydrological model. *Journal of Hydrology*, **291**, 232–253.

Brommundt, J., & Bárdossy, A. 2007. Regionalisation of Cross Correlation of Daily Rain Gauge Data. *Journal of Hydrology*, submitted.

Brutsaert, W. 1982. *Evaporation into the Atmosphere*. Kluwer Academic Publishers.

Burpee, R. 1972. The origin and structure of easterly waves in the lower troposphere of North Africa. *Journal of Atmospheric Sciences*.

Chen, F., & Dudhia, J. 2001. Coupling an Advanced Land-Surface/Hydrology Model with the Penn State/NCAR MM5 Modeling System. Part I: Model Implementation and Sensitivity. *Monthly Weather Review*, **129**, 569–585.

Chevallier, P., & Planchon, O. 1993. Hydrological processes in a small humid savanna basin (Ivory Coast). *Journal of Hydrology*, **151**, 173–191.

Colditz, R. R., Conrad, C., Wehrmann, T., Schmidt, M., & Dech, S. W. 2006. Generation and assessment of MODIS time series using quality information. *IEEE International Conference on Geoscience and Remote Sensing, IGARSS 2006*, 779–782.

Colditz, R. R., Conrad, C., Wehrmann, T., Schmidt, M., & Dech, S. W. 2007. TiSeG - A flexible software tool for time series generation of MODIS data utilizing the quality assessment science data set. *IEEE Transactions on Geoscience and Remote Sensing, in review*.

Cressie, N. A. 1991. *Statistics for Spatial Data*. Wiley series in Probability and Mathematical Statistics. John Wiley and Sons, Inc.

Das, T. 2006. The Impact of Spatial Variability of Precipitation on the Predictive Uncertainty of Hydrological Models. *Institut für Wasserbau, Mitteilungen*.

Deutsch, C. V., & Journel, A. G. 1998. *GSLIB: Geostatistical Software Library and User's Guide*. Oxford University Press, New York.

Dingman, S. L. 2002. *Physical Hydrology*. 2nd Edition. Prentice-Hall, Inc.

Druyan, L. M. 1991. The sensitivity of sub-Saharan precipitation to Atlantic SST. *Climate Change*, **18**, 17–36.

Dudhia, J., Gill, D., Manning, K., Wang, W., Bruyere, C., Wilson, J., & Kelly, S. 2003. *PSU/NCAR Mesoscale Modelling System Tutorial Class Notes and User's Guide, MM5 Modeling System Version 3*.

Ebert, E. E. 2005. *Satellite vs. model rainfall - Which one to use?* Fifth Int. Scientific Conf. on the Global Energy and Water Cycle Experiment (GEWEX), Orange County.

Ezzedine, S. M. 2005. *Stochastic modeling of Flow and Transport in Porous and Fractured Media*. Encyclopedia of Hydrological Sciences. John Wiley and Sons, Ltd.

FAO. 1971-81. *Soil Map of the World*. United Nations Food and Agriculture Organization, UNESCO, Paris.

Fensholt, R., Sandholt, I., & Rasmussen, M. Schultz. 2004. Evaluation of MODIS LAI, fAPAR and the relation between fAPAR and NDVI in a semi-arid environment using in situ measurements. *Remote Sensing of Environment*, **91**, 490–507.

Geiger, R., Robert, H. A., & Todhunter, P. 1995. *The Climate Near the Ground*. Friedr. Vieweg und Sohn Verlagsgesellschaft, Braunschweig.

Genuchten, M. T. Van. 1976. A closed-form equation for predicting the hydraulic conductivity of unsaturated soils. *American Journal of Soil Sciences*, **44**(5), 892–898.

Giesen, N. Van De. 2001. Characterization of west african shallow flood plains with L- and C- band radar. *Remote Sensing and Hydrology*, **267**, 365–367.

Giorgi, F., Hewitson, B., Christensen, J., Hulme, M., Storch, H. V., Whetton, P., Jones, R., Mearns, L., & Fu, C. 2001. Climate Change 2001: The scientific basis. *In: Regional climate information - evaluation and projections*. Cambridge University Press.

Govaerts, Y., & Lattanzio, A. 2007. Surface albedo response to sahel precipitation changes. *EOS Trans. AGU*, **88**(3), 24–25.

Grayson, R. B., & Blöschl, G. (eds). 2000. *Spatial Patterns in Catchment Hydrology: Observations and Modeling*. Cambridge University Press.

Grell, G. A., & Kuo, Y.-H. 1991. Semiprognostic tests of cumulus parametrization schemes in the middle latitudes. *Monthly Weather Review*, **119**, 5–31.

Grell, G. A., Dudhia, J., & Stauffer, D. R. 1995. *A description of the Fifth-Generation Penn State/NCAR Mesoscale Model (MM5)*. Tech. rept.

Guenther, B., Xiong, X., Salomonson, V. V., Barnes, W. L., & Young, J. 2002. On-orbit performance of the Earth Observing System Moderate Resolution Imaging Spectroradiometer; first year of data. *Remote Sensing of Environment*, **83**(1-2), 16–30.

Haberlandt, U. 2007. Geostatistical interpolation of hourly precipitation from rain gauges and radar for a large-scale extreme rainfall events. *Journal of Hydrology*, **332**, 144–157.

Hayward, D., & Oguntoyinbo, J. 1987. *Climatology of West Africa*. Hutchindson.

Hodnet, M. G., & Tomasella, J. 2002. Marked differences between van Genuchten soil-water retention parameters for temperate and tropical soils: New water-retention pedo-functions developed for tropical soils. *Geoderma*, **108**, 155–180.

Hong, S.-Y., & Pan, H. L. 1996. Nonlocal boundary layer vertical diffusion in a medium range forecast model. *Monthly Weather Review*, **124**, 2322–2339.

Houghton, J. T., Ding, Y., Griggs, D. J., Noguer, M., Linden, P. J. Van Der, Dai, X., Maskell, K., & Johnson, C. A. 2001. *Climate Change 2001: The scientific basis*. Cambridge University Press.

Huffman, G. J., Adler, R. F., Rudolph, B., Schneider, U., & Keehn, P. 1995. Global Precipitation Estimates Based on a Technique for Combining Satellite-Based Estimates, Rain Gauge Analysis, and NWP Model Precipitation Information. *Journal of Climate*, **8**, 1284–1295.

Huffman, G. J., Adler, R. F., Bolvin, D. T., Gu, G., Nelkin, E. J., Bowman, K. P., Hong, Y., Stocker, E. F., & Wolff, D. B. 2007. The TRMM Multisatellite Precipitation Analysis (TMPA): Quasi-Global, Multiyear, Combined-Sensor Precipitation Estimates at Fine Scales. *Journal of Hydrometeorology*, **8**, 38–55.

Hulme, M., Doherty, R., Ngara, T., New, M., & Lister, D. 2001. African climate change: 1900-2100. *Climate Research*, **17**, 145–168.

Isaaks, E. H., & Srivastava, R. M. 1989. *Applied Geostatistics*. Oxford University Press, New York.

Jacobson, M. Z. (ed). 2005. *Fundamentals of Atmospheric Modeling*. Cambridge University Press.

Jones, R. G., Murphy, J. M., & Noguer, M. 1995. Simulation of climate change over Europe using a nested regional-climate model. Part I: Assessment of control climate, including sensitivity to location of lateral boundaries. *Quarterly Journal of the Royal Meteorological Society*, **121**, 1413–1449.

Jung, G. 2006. *Regional Climate Change and the Impact on Hydrology in the Volta Basin of West Afrika.* Ph.D. thesis, Forschungszentrum Karlsruhe and University of Augsburg.

Jung, G., & Kunstmann, H. 2007. High-resolution Regional Climate Modelling for the Volta Basin of West Africa. *Journal of Geophysical Research - Atmosphere*, in press.

Justice, C. O., Vermote, E. F., Townshend, J. R. G., DeFries, R. S., Roy, D. P., Hall, D. K., Salomonson, V. V., Privette, J. L., Riggs, G., Strahler, A. H., Lucht, W., Myneni, R. B., Knyazikhin, Y., Running, S. W., Nemani, R. R., Wan, Z., Huete, A. R., van Leeuwen, W. J. D., Wolfe, R. E., Giglio, L., Muller, J.-P., Lewis, P., & Barnsley, M. J. 1998. The Moderate Resolution Imaging Spectroradiometer (MODIS): land remote sensing for global change research. *IEEE Transactions on Geoscience and Remote Sensing*, **36**(4), 1228–1249.

Justice, C. O., Townshend, J. R. G., Vermote, E. F., Masuoka, E., Wolfe, R. E., el Saleous, N. Z., Roy, D. P., & Morisette, J. T. 2002. An overview of MODIS Land data processing and product status. *Remote Sensing of Environment*, **83**(1-2), 3–15.

Kalnay, E. 2003. *Atmospheric Modelling, Data Assimilation and Predictability*. Cambridge University Press.

Kitanidis, P. K. 1997. *Introduction to Geostatistics*. Cambridge University Press.

Kleinn, J. 2002. *Climate change and runoff statistics in the Rhine Basin: A process study with a coupled climate-runoff model*. Ph.D. thesis, ETH Zuerich.

Klemp, J. B., & Durran, D. R. 1983. An upper boundary condition permitting internal gravity wave radiation in numerical mesoscale models. *Monthly Weather Review*, **111**, 430–444.

Klemp, J. B., & Wilhelmson, R. B. 1978. The simulation of three-dimensional convective storm dynamics. *Journal of the Atmospheric Sciences*, **35**, 1070–1096.

Knyazikhin, Y., Martonchik, J. V., Diner, D. J., Myneni, R. B., Verstraete, M. M., Pinty, B., & Gobron, N. 1998. Estimation of vegetation canopy leaf area index and fraction of absorbed photosynthetically active radiation from atmosphere-corrected MISR data. *Journal of Geophysical Research*, **103**(D24), 32239–32256.

Kottegoda, N. T., & Kassim, A.H.M. 1991. The turning bands method with the fast-Fourier transform as an aid to the determination of storm movement. *Journal of Hydrology*, **127**, 55–69.

Krause, P., Boyle, D. P., & Bäse, F. 2005. Comparison of different efficiency criteria for hydrological model assessment. *Advances in Geosciences*, **5**, 89–97.

Kunstmann, H., & Jung, G. 2003. Water Resources Systems - Water Availability and Global Change. *In: Investigation of feedback mechanisms between soil moisture, Land use and precipitation in West Africa*, vol. 280. IAHS Publications.

Kunstmann, H., Schneider, K., Forkel, R., & Knoche, R. 2004. Impact analysis of climate change for an Alpine catchment using high resolution dynamic downscaling of ECHAM4 time slices. *Hydrology and Earth System Sciences*, **8**(6), 1030–1043.

Kunstmann, H., Jung, G., Wagner, S., & Clottey, H. 2007. Integration of atmospheric sciences and hydrology for the development of decision support systems in sustainable water management. *Physics and Chemistry of the Earth*.

Lebarbé, L., & Lebel, T. 1997. Rainfall climatology of the HAPEX-Sahel region during the years 1950-1990. *Journal of Hydrology*, **188-189**, 43–73.

Lebarbé, L., Lebel, T., & Tapsoba, D. 2002. Rainfall variability in West Africa during the years 1950-90. *Journal of Climate*, **15**, 187–202.

Liang, S. 2000. Narrowband to broadband conversions of land surface albedo: I Algorithms. *Remote Sensing of Environment*, **76**(2), 213–238.

Loughlin, G. O., Huber, W., & Chocat, B. 1996. Rainfall-runoff processes and modelling. *Journal of Hydraulic Research*, **34**(6), 733–751.

Lucht, W., Schaaf, C. B., & Strahler, A. H. 2000. An algorithm for the retrieval of albedo from space using semiempirical BRDF models. *IEEE Transactions on Geoscience and Remote Sensing*, **38**(2), 977–998.

Maidment, D. R. 1993. *Handbook of Hyrology*. McGraw Hill Inc.

Mantheron, G. 1973. The intrinsic random functions and their applications. *Advances in Applied Probability*, **5**, 439–468.

Mantoglou, A., & Wilson, J. L. 1982. The Turning Bands Method for Simulation of Random Fields Using Line Generation by a Spectral Method. *Water Resources Research*, **18(5)**, 1379–1394.

Martin, N., & Giesen, N. Van De. 2005. Spatial distribution of groundwater production and development potential in the vVlta river basin of Ghana and Burkina Faso. *Water International*, **30**(2), 239–249.

Martonne, E. De. 1920. L'indice d'aridité. 3rd edn. Géographie Physique.

Marx, A. 2007. Einsatz gekoppelter Modelle und Wetterradar zur Abschätzung von Niederschlagsintensitäten und zur Abflussvorhersage. *Institut für Wasserbau, Mitteilungen*, **160**.

Monteith, J. L. 1975. *Vegetation and the atmosphere, vol. 1: Principles.* Academic Press.

MWH. 1998. *Information in the Volta Basin System.* Ministry of Works and Housing: Water Resources Management Study; Accra.

Myneni, R. B., Nemani, R. R., & Running, S. W. 1997. Estimation of global leaf area index and absorbed PAR using radiative transfer models. *IEEE Transactions on Geoscience and Remote Sensing*, **35**(6), 1380–1393.

Myneni, R. B., Hoffman, S., Knyazikhin, Y., Privette, J. L., Glassy, J., Tian, Y., Wang, Y., Song, X., Zhang, Y., Smith, G. R., Lotsch, A., Friedl, M. A., Morisette, J. T., Votava, P., Nemani, R. R., & Running, S. W. 2002. Global products of vegetation leaf area and fraction absorbed PAR from year one of MODIS data. *Remote Sensing of Environment*, **83**(1-2), 214–231.

Nash, J. E., & Sutcliffe, J. V. 1970. River flow forecasting through conceptual models. Part I - a discussion of principles. *Journal of Hydrology*, **10**(3).

Neumann, R., Jung, G., Laux, P., & Kunstmann, H. 2007. Climate trends of temperature, precipitation and river discharge in the Volta Basin of West Africa. *Journal of River Basin Management*, **5**(1), 17–30.

Nicholson, S. E. 1993. An overview of African rainfall fluctuations of the last decade. *Journal of Climate*, **6**, 1463–1466.

Nicholson, S. E. 2001. Climatic and environmental change in Africa during the last two centuries. *Climate Research*, **17**, 123–144.

Obeng-Asiedu, P. 2004. *Allocating water resources for agricultural and economic development in the Volta river basin.* Ph.D. thesis, University of Bonn.

Oguntunde, P. G. 2004. *Evapotranspiration and complimentary relations in the water balance of the Volta basin: field measurements and GIS-based regional estimates.* Ph.D. thesis, Cuvillier Verlag Goettingen.

Oke, T. R. 1987. *Boundary Layer Climates.* Routledge.

ORSTOM. 1996. *Afrique de'l Ouest et Centrale Précipitations Moyennes Annuelles (Période 1951-1989).* Laboratoire d'Hydrologie.

Parry, M. L., Canziani, O. F., Palutikof, J. P., van der Linden, P. J., & Hanson, C. E. (eds). 2007. *Climate Change 2007: Impacts, Adaptation and Vulnerability. Contribution of Working Group II to the Fourth Assessment Report of the Intergovernmental Panel on Climate Change.* Cambridge University Press, UK.

Pichler, H. 1997. *Dynamic der Atmosphäre*. Spektrum Akademischer Verlag GmbH.

Pielke, R. A. 2002. *Mesoscale Meteorological Modeling.* Academic Press.

Pinty, B., Verstraete, M. M., Gobron, N., Roveda, F., & Govaerts, Y. 2000. Do man-made fires affect Earth's surface reflectance at continental scales? *EOS Trans. AGU*, **81**(34), 381,388–389.

Privette, J. L., Myneni, R. B., Knyazikhin, Y., Mukelabai, M., Roberts, G., Tian, Y., Wang, Y., & Leblanc, S. G. 2002. Early spatial and temporal validation of MODIS LAI product in the Southern Africa Kalahari. *Remote Sensing of Environment*, **83**(1-2), 232–243.

Quante, M., & Matthias, V. 2006. Water in the Earth's atmosphere. *J. Phys. IV France*, **139**, 37–61.

Reisner, J., Rasmussen, R. M., & Bruintjes, R. T. 1998. Explicit forecasting of supercooled liquid water in winter storms using the MM5 mesoscale model. *Quarterly Journal of the Royal Meteorological Society*, **100**, 239–265.

Richards, L. 1931. Capillary Conduction of liquids through porous medium. *Physics*, **1**, 318–333.

Robinson, M. 2005. *Precipitation measurement: gauge development.* Encyclopedia of Hydrological Sciences. John Wiley and Sons, Ltd.

Rosbjerg, D., & Madsen, H. 2005. *Concepts of Hydrologic Modeling.* Encyclopedia of Hydrological Sciences. John Wiley and Sons, Ltd.

Roy, D. P., Borak, J. S., Devadiga, S., Wolfe, R. E., Zheng, M., & Descloitres, J. 2002. The MODIS Land product quality assessment approach. *Remote Sensing of Environment*, **83**(1-2), 62–76.

Rudolf, B. 1996. *Global Precipitation Climatology Center activities.* GEWEX News, 6(1).

Schaaf, C. B., Gao, F., Strahler, A. H., Lucht, W., Li, X., Tsang, T., Strugnell, N. C., Zhang, X., Jin, Y., Muller, J.-P., Lewis, P., Barnsley, M. J., Hobson, P. D., Disney, M., Roberts, G., Dunderdale, M., Doll, C., d'Entremont, R. P., Hug, B., Liang, S., Privette, J. L., & Roy, D. P. 2002. First operational BRDF, albedo nadir reflectance products from MODIS. *Remote Sensing of Environment*, **83**(1-2), 135–148.

Schafmeister, M.-Th. 1999. *Geostatistik für die hydrogeologische Praxis.* Springer Verlag.

Schulla, J. 2006. *Personal conversation.*

Schulla, J., & Jasper, K. 2000. *Model Description WaSiM-ETH.* Tech. rept. ETH Zuerich.

Schultz, G. A. 1998. Remote sensing in hydrology. *Journal of Hydrology*, **124**, 1071–1107.

Shahin, M. 2002. *Hydrology and water resources of Africa.* Water Science and Technology Library, vol. 41. Kluwer Academic Publisher.

Singh, V. P. (ed). 1995. *Computer Models of Watershed Hydrology.* Water Resources Publications.

Skamarok, W. C., & Klemp, J. B. 1994. The stability of time-split numerical methods for the hydrostatic and nonhydrostatic elastic equations. *Monthly Weather Review*, **120**, 2109–2127.

Sommen, J. J. Van Der, & Geirnaert, W. 1988. Estimation of natural groundwater recharge. *In: On the continuity of aquifer systems on the crystalling basement of Burkina Faso.* D. Reidel Publishing Company.

Stehlýk, J., & Bárdossy, A. 2002. Multivariate stochastic downscaling model for generating daily precipitation series based on atmospheric circulation. *Journal of Hydrology*, **256**, 120–141.

Syed, K. H., Goodrich, D. C., Myers, D. E., & Sorooshian, S. 2003. Spatial characteristics of thunderstorm rainfall fields and their relation to runoff. *Journal of Hydrology*, **271**, 1–21.

Talagrand, O. 1997. Assimilation of observations, an introduction. *J. Met. Soc. Japan*, **Special Issue 75**(1B), 191–209.

Unesco. 1978. *World water balance and water resources of the earth.* Studies and Reports in Hydrology 25, Prepared by the USSR Committee for the International Hydrological Decade, Paris.

Unesco. 1992. *The Dublin Statement on Water and Sustainable Development.* International Conference on Water and Environment, Dublin, Ireland.

Vescovi, F. D. 2001. Classification of African complex environments based on a contextual spatial approach (SPARK). *International workshop on Geo-Spatial Knowledge Processing for Natural Resources Management.*

Wagner, S., Kunstmann, H., & Bárdossy, A. 2006. Model based distributed water balance monitoring of the White Volta catchment in West Africa through coupled meteorological-hydrological simulations. *Advances in Geosciences*, **9**, 39–44.

Wagner, S., Kunstmann, H., & Bárdossy, A. 2007. Uncertainties in water balance estimations due to scarce meteorological information: A case study for the White Volta catchment in West Africa. *IAHS publication*, **313**, 86–97.

Wagner, S., Kunstmann, H., Bárdossy, A., Conrad, C., & Colditz, R. R. 2008. Water balance estimations of poorly gauged catchments in West Africa using dynamical downscaling of meteorological fields and remote sensing information. *J. Phys. Chem. Earth*, **doi:10.1016/j.pce.2008.04.002**.

Wang, Y., Leung, L. R., McGregor, J. L., Lee, D.-K., Wang, W.-C., Ding, Y., & Kimura, F. 2004. Regional climate modeling: progress, challenges and prospects. *Journal of the Meteorological Society of Japan*, **82**(6), 1599–1628.

Warner, T. T., Peterson, R. A., & Treadon, R. E. 1997. A tutorial on lateral boundary conditions as a basic and potentially serious limitation to regional numerical weather prediction. *Bulletin of the American Meteorological Society*, **78**, 2599–2617.

Wolfe, R. E., Nishihama, M., Fleig, A. J., Kuyper, J. A., Roy, D. P., Storey, J. C., & Patt, F. S. 2002. Achieving sub-pixel geolocation accuracy in support of MODIS land science. *Remote Sensing of Environment*, **83**(1-2), 31–49.

Worldbank. 2006. *Ghana and Burkina Faso Data Profile*. http://devdata.worldbank.org.

Zehe, E., Becker, R., Bárdossy, A., & Plate, E. 2005. Uncertainty of simulated catchment runoff response in the presence of threshold processes: role of initial soil moisture and precipitation. *Journal of Hydrology*, **315**, 183–202.

A Appendix

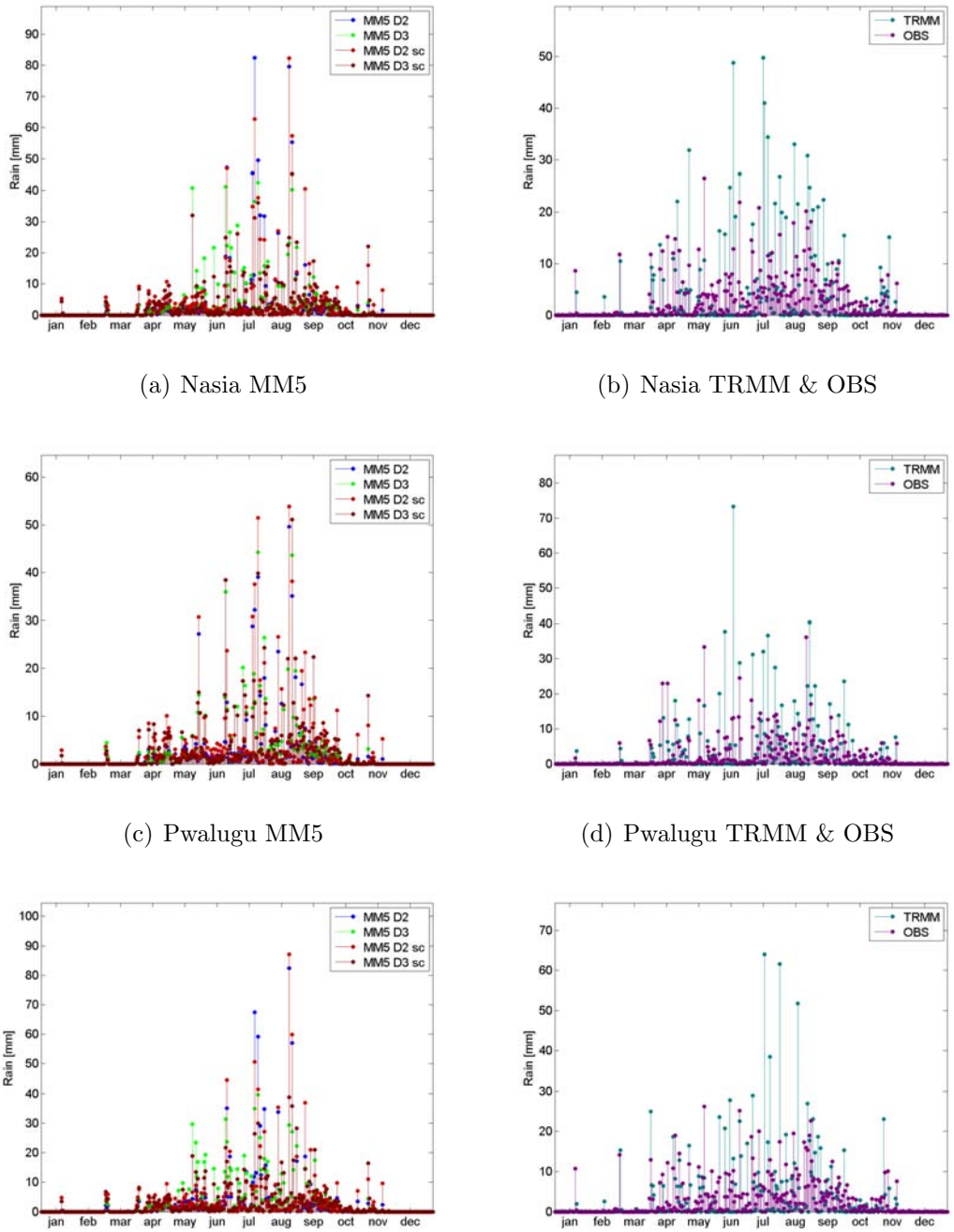

(a) Nasia MM5

(b) Nasia TRMM & OBS

(c) Pwalugu MM5

(d) Pwalugu TRMM & OBS

(e) Nawuni MM5

(f) Nawuni TRMM & OBS

Figure A.1: Daily precipitation [mm] for 2004 for the subcatchments Nasia, Pwalugu, and Nawuni using different meteorological data sources: (i) gridded, real time *MM5* results (MM5 D2 and MM5 D3), (ii) gridded, scaled *MM5* results (MM5 D2 sc and MM5 D3 sc), (iii) the gridded, scaled *TRMM* product 3B42, and (iv) station data

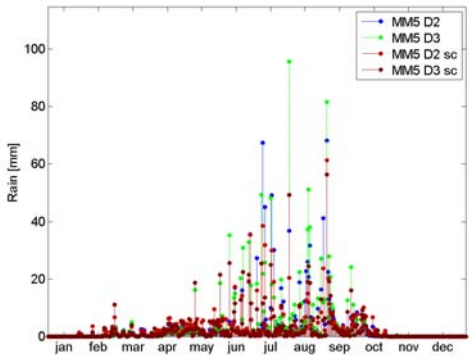

(a) Nasia MM5

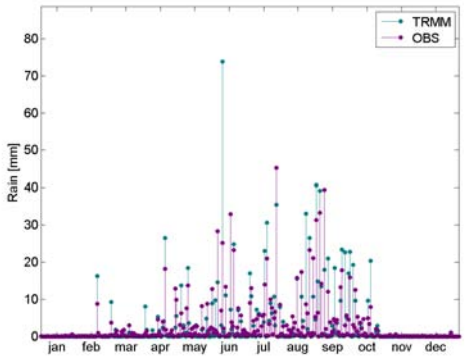

(b) Nasia TRMM & OBS

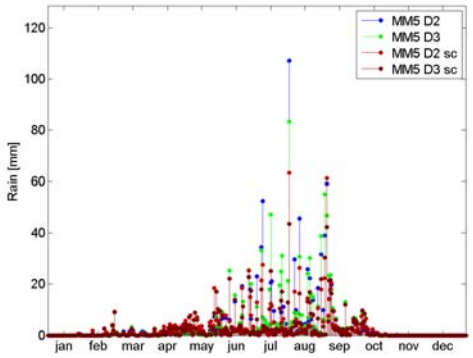

(c) Pwalugu MM5

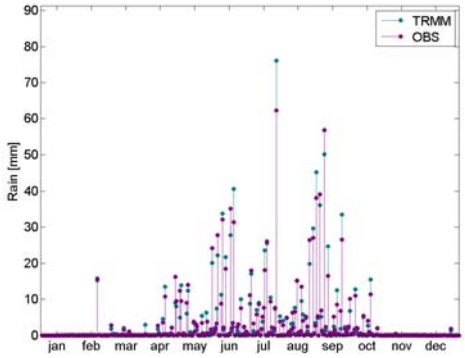

(d) Pwalugu TRMM & OBS

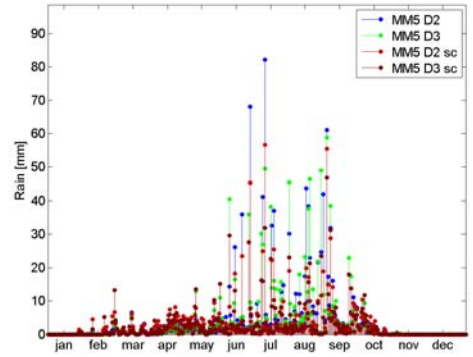

(e) Nawuni MM5

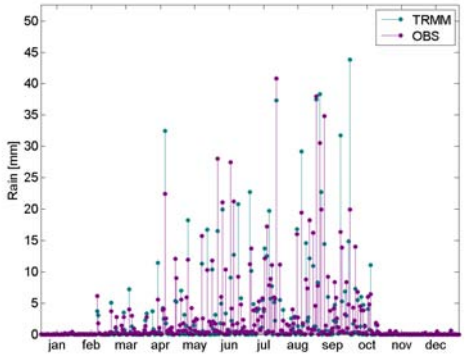

(f) Nawuni TRMM & OBS

Figure A.2: Daily precipitation [mm] for 2005 for the subcatchments Nasia, Pwalugu, and Nawuni using different meteorological data sources: (i) gridded, real time *MM5* results (MM5 D2 and MM5 D3), (ii) gridded, scaled *MM5* results (MM5 D2 sc and MM5 D3 sc), (iii) the gridded, scaled *TRMM* product 3B42, and (iv) station data

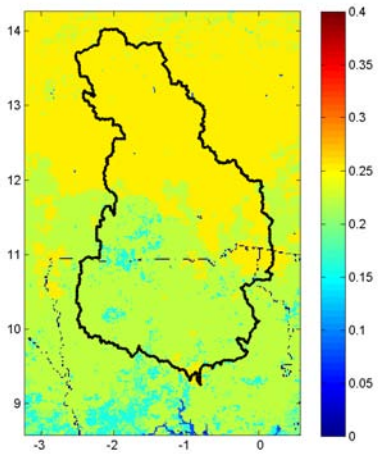

(a)

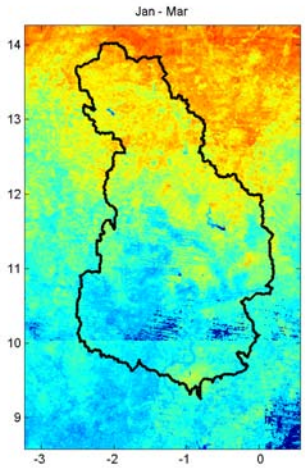

(b) MODIS: Jan-Mar

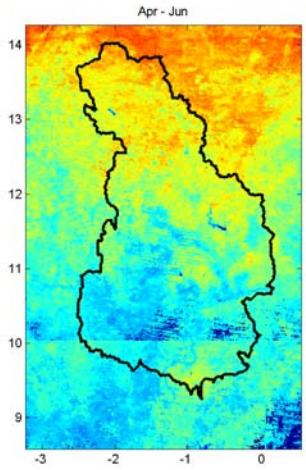

(c) MODIS: Apr-Jun

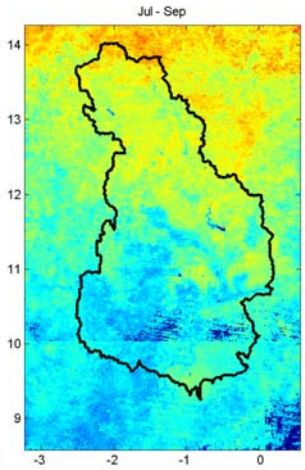

(d) MODIS: Jul-Sep

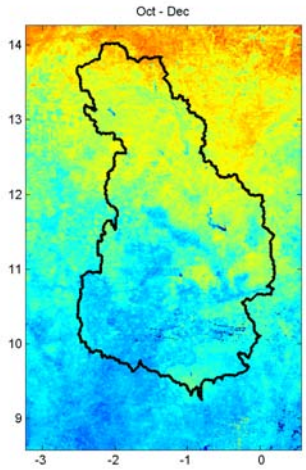

(e) MODIS: Oct-Dec

Figure A.3: Albedo grid of the White Volta basin using (a) static tabulated values and (b)-(e) dynamic *MODIS* estimates averaged to 3-month means for 2005

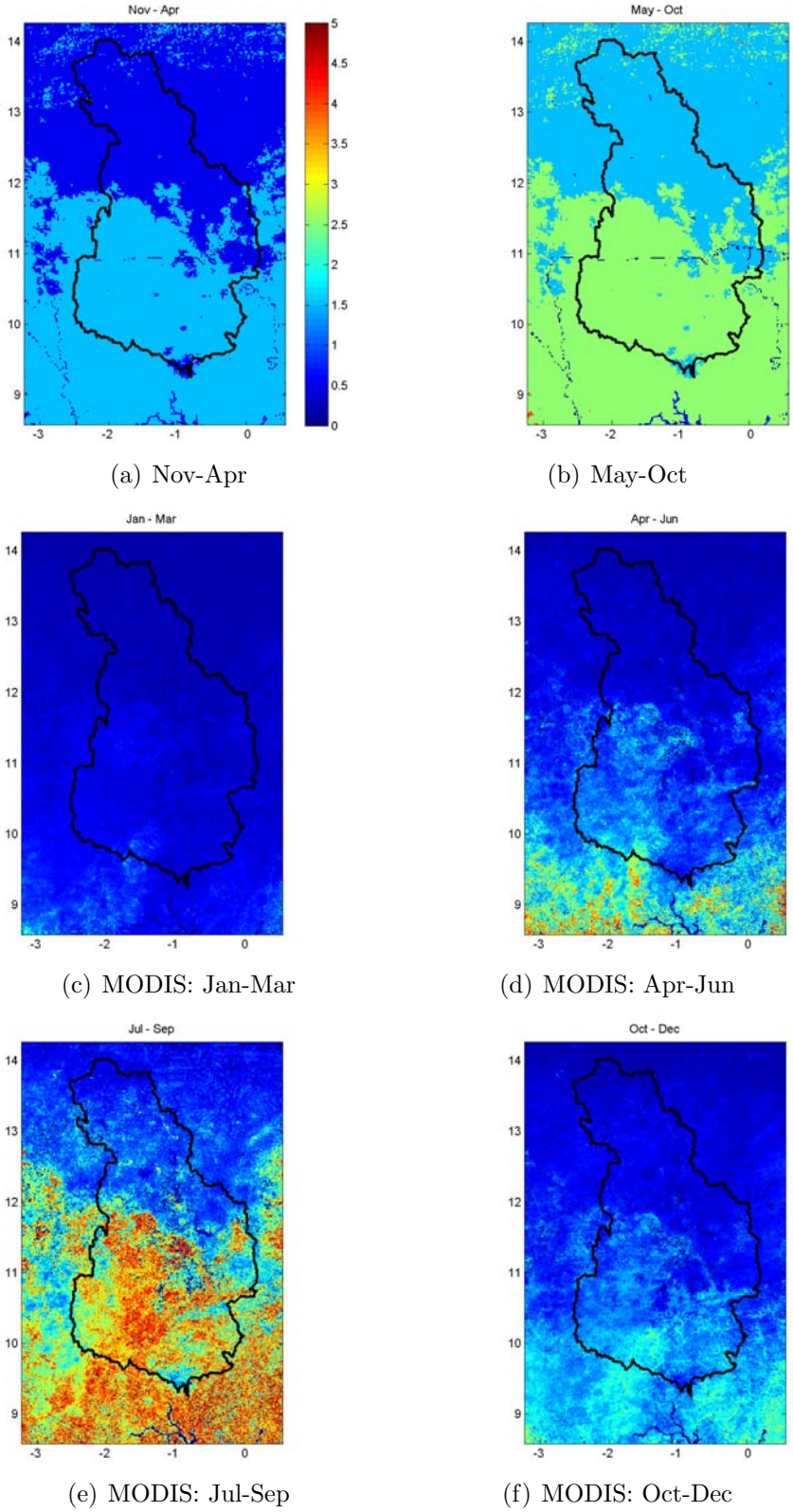

(a) Nov-Apr (b) May-Oct

(c) MODIS: Jan-Mar (d) MODIS: Apr-Jun

(e) MODIS: Jul-Sep (f) MODIS: Oct-Dec

Figure A.4: *LAI* grid of the White Volta basin using (a)-(b) static tabulated values and (c)-(f) dynamic *MODIS* estimates averaged to 3-month means for 2005

Curriculum vitae

15. July 1976	born in Weingarten, Germany
1987 - 1996	Welfen-Gymnasium in Ravensburg, Germany
1997 - 2003	Environmental Engineering Study (Dipl.-Ing.), University Stuttgart, Germany
2001 - 2002	Exchange student at the Department of Earth Science, University of Waterloo, Canada
2000 - 2003	Master of Science (M.Sc.) in Water Resources Engineering and Management (WAREM), University Stuttgart, Germany
2003	Master thesis at Institute for Hydraulic Engineering, University of Stuttgart, Germany
2004 - 2008	Research Assistant at the Institute for Meteorology and Climate Research in Garmisch-Partenkirchen, Forschungszentrum Karlsruhe GmbH, Germany

Institut für Wasserbau
Universität Stuttgart

Pfaffenwaldring 61
70569 Stuttgart (Vaihingen)
Telefon (0711) 685 - 64717/64749/64752/64679
Telefax (0711) 685 - 67020 o. 64746 o. 64681
E-Mail: iws@iws.uni-stuttgart.de
http://www.iws.uni-stuttgart.de

Verzeichnis der Mitteilungshefte

5 Plate, Erich: *Beitrag zur Bestimmung der Windgeschwindigkeitsverteilung in der durch eine Wand gestörten bodennahen Luftschicht*,
und
Röhnisch, Arthur; Marotz, Günter: *Neue Baustoffe und Bauausführungen für den Schutz der Böschungen und der Sohle von Kanälen, Flüssen und Häfen; Gestehungskosten und jeweilige Vorteile*, sowie Unny, T.E.: *Schwingungsuntersuchungen am Kegelstrahlschieber*, 1967

6 Seiler, Erich: *Die Ermittlung des Anlagenwertes der bundeseigenen Binnenschiffahrtsstraßen und Talsperren und des Anteils der Binnenschiffahrt an diesem Wert*, 1967

7 *Sonderheft anläßlich des 65. Geburtstages von Prof. Arthur Röhnisch mit Beiträgen von* Benk, Dieter; Breitling, J.; Gurr, Siegfried; Haberhauer, Robert; Honekamp, Hermann; Kuz, Klaus Dieter; Marotz, Günter; Mayer-Vorfelder, Hans-Jörg; Miller, Rudolf; Plate, Erich J.; Radomski, Helge; Schwarz, Helmut; Vollmer, Ernst; Wildenhahn, Eberhard; 1967

8 Jumikis, Alfred: *Beitrag zur experimentellen Untersuchung des Wassernachschubs in einem gefrierenden Boden und die Beurteilung der Ergebnisse*, 1968

9 Marotz, Günter: *Technische Grundlagen einer Wasserspeicherung im natürlichen Untergrund*, 1968

10 Radomski, Helge: *Untersuchungen über den Einfluß der Querschnittsform wellenförmiger Spundwände auf die statischen und rammtechnischen Eigenschaften*, 1968

11 Schwarz, Helmut: *Die Grenztragfähigkeit des Baugrundes bei Einwirkung vertikal gezogener Ankerplatten als zweidimensionales Bruchproblem*, 1969

12 Erbel, Klaus: *Ein Beitrag zur Untersuchung der Metamorphose von Mittelgebirgsschneedecken unter besonderer Berücksichtigung eines Verfahrens zur Bestimmung der thermischen Schneequalität*, 1969

13 Westhaus, Karl-Heinz: *Der Strukturwandel in der Binnenschiffahrt und sein Einfluß auf den Ausbau der Binnenschiffskanäle*, 1969

14 Mayer-Vorfelder, Hans-Jörg: *Ein Beitrag zur Berechnung des Erdwiderstandes unter Ansatz der logarithmischen Spirale als Gleitflächenfunktion*, 1970

15 Schulz, Manfred: *Berechnung des räumlichen Erddruckes auf die Wandung kreiszylindrischer Körper*, 1970

16 Mobasseri, Manoutschehr: *Die Rippenstützmauer. Konstruktion und Grenzen ihrer Standsicherheit*, 1970

17 Benk, Dieter: *Ein Beitrag zum Betrieb und zur Bemessung von Hochwasserrückhaltebecken*, 1970

18 Gàl, Attila: *Bestimmung der mitschwingenden Wassermasse bei überströmten Fischbauchklappen mit kreiszylindrischem Staublech*, 1971, vergriffen

19 Kuz, Klaus Dieter: *Ein Beitrag zur Frage des Einsetzens von Kavitationserscheinungen in einer Düsenströmung bei Berücksichtigung der im Wasser gelösten Gase*, 1971, vergriffen

20 Schaak, Hartmut: *Verteilleitungen von Wasserkraftanlagen*, 1971

21 *Sonderheft zur Eröffnung der neuen Versuchsanstalt des Instituts für Wasserbau der Universität Stuttgart mit Beiträgen von* Brombach, Hansjörg; Dirksen, Wolfram; Gàl, Attila; Gerlach, Reinhard; Giesecke, Jürgen; Holthoff, Franz-Josef; Kuz, Klaus Dieter; Marotz, Günter; Minor, Hans-Erwin; Petrikat, Kurt; Röhnisch, Arthur; Rueff, Helge; Schwarz, Helmut; Vollmer, Ernst; Wildenhahn, Eberhard; 1972

22 Wang, Chung-su: *Ein Beitrag zur Berechnung der Schwingungen an Kegelstrahlschiebern*, 1972

23 Mayer-Vorfelder, Hans-Jörg: *Erdwiderstandsbeiwerte nach dem Ohde-Variationsverfahren*, 1972

24 Minor, Hans-Erwin: *Beitrag zur Bestimmung der Schwingungsanfachungsfunktionen überströmter Stauklappen*, 1972, vergriffen

25 Brombach, Hansjörg: *Untersuchung strömungsmechanischer Elemente (Fluidik) und die Möglichkeit der Anwendung von Wirbelkammerelementen im Wasserbau*, 1972, vergriffen

26 Wildenhahn, Eberhard: *Beitrag zur Berechnung von Horizontalfilterbrunnen*, 1972

27 Steinlein, Helmut: *Die Eliminierung der Schwebstoffe aus Flußwasser zum Zweck der unterirdischen Wasserspeicherung, gezeigt am Beispiel der Iller*, 1972

28 Holthoff, Franz Josef: *Die Überwindung großer Hubhöhen in der Binnenschiffahrt durch Schwimmerhebewerke*, 1973

29 Röder, Karl: *Einwirkungen aus Baugrundbewegungen auf trog- und kastenförmige Konstruktionen des Wasser- und Tunnelbaues*, 1973

30 Kretschmer, Heinz: *Die Bemessung von Bogenstaumauern in Abhängigkeit von der Talform*, 1973

31 Honekamp, Hermann: *Beitrag zur Berechnung der Montage von Unterwasserpipelines*, 1973

32 Giesecke, Jürgen: *Die Wirbelkammertriode als neuartiges Steuerorgan im Wasserbau*, und Brombach, Hansjörg: *Entwicklung, Bauformen, Wirkungsweise und Steuereigenschaften von Wirbelkammerverstärkern*, 1974

33 Rueff, Helge: *Untersuchung der schwingungserregenden Kräfte an zwei hintereinander angeordneten Tiefschützen unter besonderer Berücksichtigung von Kavitation*, 1974

34 Röhnisch, Arthur: *Einpreßversuche mit Zementmörtel für Spannbeton - Vergleich der Ergebnisse von Modellversuchen mit Ausführungen in Hüllwellrohren*, 1975

35 *Sonderheft anläßlich des 65. Geburtstages von Prof. Dr.-Ing. Kurt Petrikat mit Beiträgen von*: Brombach, Hansjörg; Erbel, Klaus; Flinspach, Dieter; Fischer jr., Richard; Gàl, Attila; Gerlach, Reinhard; Giesecke, Jürgen; Haberhauer, Robert; Hafner Edzard; Hausenblas, Bernhard; Horlacher, Hans-Burkhard; Hutarew, Andreas; Knoll, Manfred; Krummet, Ralph; Marotz, Günter; Merkle, Theodor; Miller, Christoph; Minor, Hans-Erwin; Neumayer, Hans; Rao, Syamala; Rath, Paul; Rueff, Helge; Ruppert, Jürgen; Schwarz, Wolfgang; Topal-Gökceli, Mehmet; Vollmer, Ernst; Wang, Chung-su; Weber, Hans-Georg; 1975

36 Berger, Jochum: *Beitrag zur Berechnung des Spannungszustandes in rotationssymmetrisch belasteten Kugelschalen veränderlicher Wandstärke unter Gas- und Flüssigkeitsdruck durch Integration schwach singulärer Differentialgleichungen*, 1975

37 Dirksen, Wolfram: *Berechnung instationärer Abflußvorgänge in gestauten Gerinnen mittels Differenzenverfahren und die Anwendung auf Hochwasserrückhaltebecken*, 1976

38 Horlacher, Hans-Burkhard: *Berechnung instationärer Temperatur- und Wärmespannungsfelder in langen mehrschichtigen Hohlzylindern*, 1976

39 Hafner, Edzard: *Untersuchung der hydrodynamischen Kräfte auf Baukörper im Tiefwasserbereich des Meeres*, 1977, ISBN 3-921694-39-6

40 Ruppert, Jürgen: *Über den Axialwirbelkammerverstärker für den Einsatz im Wasserbau*, 1977, ISBN 3-921694-40-X

41 Hutarew, Andreas: *Beitrag zur Beeinflußbarkeit des Sauerstoffgehalts in Fließgewässern an Abstürzen und Wehren*, 1977, ISBN 3-921694-41-8, vergriffen

42 Miller, Christoph: *Ein Beitrag zur Bestimmung der schwingungserregenden Kräfte an unterströmten Wehren*, 1977, ISBN 3-921694-42-6

43 Schwarz, Wolfgang: *Druckstoßberechnung unter Berücksichtigung der Radial- und Längsverschiebungen der Rohrwandung*, 1978, ISBN 3-921694-43-4

44 Kinzelbach, Wolfgang: *Numerische Untersuchungen über den optimalen Einsatz variabler Kühlsysteme einer Kraftwerkskette am Beispiel Oberrhein*, 1978, ISBN 3-921694-44-2

45 Barczewski, Baldur: *Neue Meßmethoden für Wasser-Luftgemische und deren Anwendung auf zweiphasige Auftriebsstrahlen*, 1979, ISBN 3-921694-45-0

46 Neumayer, Hans: *Untersuchung der Strömungsvorgänge in radialen Wirbelkammerverstärkern*, 1979, ISBN 3-921694-46-9

47 Elalfy, Youssef-Elhassan: *Untersuchung der Strömungsvorgänge in Wirbelkammerdioden und -drosseln*, 1979, ISBN 3-921694-47-7

48 Brombach, Hansjörg: *Automatisierung der Bewirtschaftung von Wasserspeichern*, 1981, ISBN 3-921694-48-5

49 Geldner, Peter: *Deterministische und stochastische Methoden zur Bestimmung der Selbstdichtung von Gewässern*, 1981, ISBN 3-921694-49-3, vergriffen

50 Mehlhorn, Hans: *Temperaturveränderungen im Grundwasser durch Brauchwassereinleitungen*, 1982, ISBN 3-921694-50-7, vergriffen

51 Hafner, Edzard: *Rohrleitungen und Behälter im Meer*, 1983, ISBN 3-921694-51-5

52 Rinnert, Bernd: *Hydrodynamische Dispersion in porösen Medien: Einfluß von Dichteunterschieden auf die Vertikalvermischung in horizontaler Strömung*, 1983, ISBN 3-921694-52-3, vergriffen

53 Lindner, Wulf: *Steuerung von Grundwasserentnahmen unter Einhaltung ökologischer Kriterien*, 1983, ISBN 3-921694-53-1, vergriffen

54 Herr, Michael; Herzer, Jörg; Kinzelbach, Wolfgang; Kobus, Helmut; Rinnert, Bernd: *Methoden zur rechnerischen Erfassung und hydraulischen Sanierung von Grundwasserkontaminationen*, 1983, ISBN 3-921694-54-X

55 Schmitt, Paul: *Wege zur Automatisierung der Niederschlagsermittlung*, 1984, ISBN 3-921694-55-8, vergriffen

56 Müller, Peter: *Transport und selektive Sedimentation von Schwebstoffen bei gestautem Abfluß*, 1985, ISBN 3-921694-56-6

57 El-Qawasmeh, Fuad: *Möglichkeiten und Grenzen der Tropfbewässerung unter besonderer Berücksichtigung der Verstopfungsanfälligkeit der Tropfelemente*, 1985, ISBN 3-921694-57-4, vergriffen

58 Kirchenbaur, Klaus: *Mikroprozessorgesteuerte Erfassung instationärer Druckfelder am Beispiel seegangsbelasteter Baukörper*, 1985, ISBN 3-921694-58-2

59 Kobus, Helmut (Hrsg.): *Modellierung des großräumigen Wärme- und Schadstofftransports im Grundwasser*, Tätigkeitsbericht 1984/85 (DFG-Forschergruppe an den Universitäten Hohenheim, Karlsruhe und Stuttgart), 1985, ISBN 3-921694-59-0, vergriffen

60 Spitz, Karlheinz: *Dispersion in porösen Medien: Einfluß von Inhomogenitäten und Dichteunterschieden*, 1985, ISBN 3-921694-60-4, vergriffen

61 Kobus, Helmut: *An Introduction to Air-Water Flows in Hydraulics*, 1985, ISBN 3-921694-61-2

62 Kaleris, Vassilios: *Erfassung des Austausches von Oberflächen- und Grundwasser in horizontalebenen Grundwassermodellen*, 1986, ISBN 3-921694-62-0

63 Herr, Michael: *Grundlagen der hydraulischen Sanierung verunreinigter Porengrundwasserleiter*, 1987, ISBN 3-921694-63-9

64 Marx, Walter: *Berechnung von Temperatur und Spannung in Massenbeton infolge Hydratation*, 1987, ISBN 3-921694-64-7

65 Koschitzky, Hans-Peter: *Dimensionierungskonzept für Sohlbelüfter in Schußrinnen zur Vermeidung von Kavitationsschäden*, 1987, ISBN 3-921694-65-5

66 Kobus, Helmut (Hrsg.): *Modellierung des großräumigen Wärme- und Schadstofftransports im Grundwasser*, Tätigkeitsbericht 1986/87 (DFG-Forschergruppe an den Universitäten Hohenheim, Karlsruhe und Stuttgart) 1987, ISBN 3-921694-66-3

67 Söll, Thomas: *Berechnungsverfahren zur Abschätzung anthropogener Temperaturanomalien im Grundwasser*, 1988, ISBN 3-921694-67-1

68 Dittrich, Andreas; Westrich, Bernd: *Bodenseeufererosion, Bestandsaufnahme und Bewertung*, 1988, ISBN 3-921694-68-X, vergriffen

69 Huwe, Bernd; van der Ploeg, Rienk R.: *Modelle zur Simulation des Stickstoffhaushaltes von Standorten mit unterschiedlicher landwirtschaftlicher Nutzung*, 1988, ISBN 3-921694-69-8, vergriffen

70 Stephan, Karl: *Integration elliptischer Funktionen*, 1988, ISBN 3-921694-70-1

71 Kobus, Helmut; Zilliox, Lothaire (Hrsg.): *Nitratbelastung des Grundwassers, Auswirkungen der Landwirtschaft auf die Grundwasser- und Rohwasserbeschaffenheit und Maßnahmen zum Schutz des Grundwassers*. Vorträge des deutsch-französischen Kolloquiums am 6. Oktober 1988, Universitäten Stuttgart und Louis Pasteur Strasbourg (Vorträge in deutsch oder französisch, Kurzfassungen zweisprachig), 1988, ISBN 3-921694-71-X

72 Soyeaux, Renald: *Unterströmung von Stauanlagen auf klüftigem Untergrund unter Berücksichtigung laminarer und turbulenter Fließzustände*,1991, ISBN 3-921694-72-8

73 Kohane, Roberto: *Berechnungsmethoden für Hochwasserabfluß in Fließgewässern mit überströmten Vorländern*, 1991, ISBN 3-921694-73-6

74 Hassinger, Reinhard: *Beitrag zur Hydraulik und Bemessung von Blocksteinrampen in flexibler Bauweise*, 1991, ISBN 3-921694-74-4, vergriffen

75 Schäfer, Gerhard: *Einfluß von Schichtenstrukturen und lokalen Einlagerungen auf die Längsdispersion in Porengrundwasserleitern*, 1991, ISBN 3-921694-75-2

76 Giesecke, Jürgen: *Vorträge, Wasserwirtschaft in stark besiedelten Regionen; Umweltforschung mit Schwerpunkt Wasserwirtschaft*, 1991, ISBN 3-921694-76-0

77 Huwe, Bernd: *Deterministische und stochastische Ansätze zur Modellierung des Stickstoffhaushalts landwirtschaftlich genutzter Flächen auf unterschiedlichem Skalenniveau*, 1992, ISBN 3-921694-77-9, vergriffen

78 Rommel, Michael: *Verwendung von Kluftdaten zur realitätsnahen Generierung von Kluftnetzen mit anschließender laminar-turbulenter Strömungsberechnung*, 1993, ISBN 3-92 1694-78-7

79 Marschall, Paul: *Die Ermittlung lokaler Stofffrachten im Grundwasser mit Hilfe von Einbohrloch-Meßverfahren*, 1993, ISBN 3-921694-79-5, vergriffen

80 Ptak, Thomas: *Stofftransport in heterogenen Porenaquiferen: Felduntersuchungen und stochastische Modellierung*, 1993, ISBN 3-921694-80-9, vergriffen

81 Haakh, Frieder: *Transientes Strömungsverhalten in Wirbelkammern,* 1993, ISBN 3-921694-81-7

82 Kobus, Helmut; Cirpka, Olaf; Barczewski, Baldur; Koschitzky, Hans-Peter: *Versucheinrichtung zur Grundwasser und Altlastensanierung VEGAS, Konzeption und Programmrahmen*, 1993, ISBN 3-921694-82-5

83 Zang, Weidong: *Optimaler Echtzeit-Betrieb eines Speichers mit aktueller Abflußregenerierung*, 1994, ISBN 3-921694-83-3, vergriffen

84 Franke, Hans-Jörg: *Stochastische Modellierung eines flächenhaften Stoffeintrages und Transports in Grundwasser am Beispiel der Pflanzenschutzmittelproblematik*, 1995, ISBN 3-921694-84-1

85 Lang, Ulrich: *Simulation regionaler Strömungs- und Transportvorgänge in Karstaquiferen mit Hilfe des Doppelkontinuum-Ansatzes: Methodenentwicklung und Parameteridentifikation*, 1995, ISBN 3-921694-85-X, vergriffen

86 Helmig, Rainer: *Einführung in die Numerischen Methoden der Hydromechanik*, 1996, ISBN 3-921694-86-8, vergriffen

87 Cirpka, Olaf: *CONTRACT: A Numerical Tool for Contaminant Transport and Chemical Transformations - Theory and Program Documentation* -, 1996, ISBN 3-921694-87-6

88 Haberlandt, Uwe: *Stochastische Synthese und Regionalisierung des Niederschlages für Schmutzfrachtberechnungen*, 1996, ISBN 3-921694-88-4

89 Croisé, Jean: *Extraktion von flüchtigen Chemikalien aus natürlichen Lockergesteinen mittels erzwungener Luftströmung*, 1996, ISBN 3-921694-89-2, vergriffen

90 Jorde, Klaus: *Ökologisch begründete, dynamische Mindestwasserregelungen bei Ausleitungskraftwerken*, 1997, ISBN 3-921694-90-6, vergriffen

91 Helmig, Rainer: *Gekoppelte Strömungs- und Transportprozesse im Untergrund - Ein Beitrag zur Hydrosystemmodellierung-*, 1998, ISBN 3-921694-91-4

92 Emmert, Martin: *Numerische Modellierung nichtisothermer Gas-Wasser Systeme in porösen Medien,* 1997, ISBN 3-921694-92-2

93 Kern, Ulrich: *Transport von Schweb- und Schadstoffen in staugeregelten Fließgewässern am Beispiel des Neckars*, 1997, ISBN 3-921694-93-0, vergriffen

94 Förster, Georg: *Druckstoßdämpfung durch große Luftblasen in Hochpunkten von Rohrleitungen 1997*, ISBN 3-921694-94-9

95 Cirpka, Olaf: *Numerische Methoden zur Simulation des reaktiven Mehrkomponententransports im Grundwasser*, 1997, ISBN 3-921694-95-7, vergriffen

96 Färber, Arne: *Wärmetransport in der ungesättigten Bodenzone: Entwicklung einer thermischen In-situ-Sanierungstechnologie*, 1997, ISBN 3-921694-96-5

97 Betz, Christoph: *Wasserdampfdestillation von Schadstoffen im porösen Medium: Entwicklung einer thermischen In-situ-Sanierungstechnologie*, 1998, ISBN 3-921694-97-3

98 Xu, Yichun: *Numerical Modeling of Suspended Sediment Transport in Rivers*, 1998, ISBN 3-921694-98-1, vergriffen

99 Wüst, Wolfgang: *Geochemische Untersuchungen zur Sanierung CKW-kontaminierter Aquifere mit Fe(0)-Reaktionswänden,* 2000, ISBN 3-933761-02-2

100 Sheta, Hussam: *Simulation von Mehrphasenvorgängen in porösen Medien unter Einbeziehung von Hysterese-Effekten*, 2000, ISBN 3-933761-03-4

101 Ayros, Edwin: *Regionalisierung extremer Abflüsse auf der Grundlage statistischer Verfahren*, 2000, ISBN 3-933761-04-2, vergriffen

102 Huber, Ralf: *Compositional Multiphase Flow and Transport in Heterogeneous Porous Media*, 2000, ISBN 3-933761-05-0

103 Braun, Christopherus: *Ein Upscaling-Verfahren für Mehrphasenströmungen in porösen Medien*, 2000, ISBN 3-933761-06-9

104 Hofmann, Bernd: *Entwicklung eines rechnergestützten Managementsystems zur Beurteilung von Grundwasserschadensfällen*, 2000, ISBN 3-933761-07-7

105 Class, Holger: *Theorie und numerische Modellierung nichtisothermer Mehrphasenprozesse in NAPL-kontaminierten porösen Medien,* 2001, ISBN 3-933761-08-5

106 Schmidt, Reinhard: *Wasserdampf- und Heißluftinjektion zur thermischen Sanierung kontaminierter Standorte*, 2001, ISBN 3-933761-09-3

107 Josef, Reinhold:, *Schadstoffextraktion mit hydraulischen Sanierungsverfahren unter Anwendung von grenzflächenaktiven Stoffen*, 2001, ISBN 3-933761-10-7

108 Schneider, Matthias: *Habitat- und Abflussmodellierung für Fließgewässer mit unscharfen Berechnungsansätzen*, 2001, ISBN 3-933761-11-5

109 Rathgeb, Andreas: *Hydrodynamische Bemessungsgrundlagen für Lockerdeckwerke an überströmbaren Erddämmen*, 2001, ISBN 3-933761-12-3

110 Lang, Stefan: *Parallele numerische Simulation instätionärer Probleme mit adaptiven Methoden auf unstrukturierten Gittern*, 2001, ISBN 3-933761-13-1

111 Appt, Jochen; Stumpp Simone: *Die Bodensee-Messkampagne 2001, IWS/CWR Lake Constance Measurement Program 2001*, 2002, ISBN 3-933761-14-X

112 Heimerl, Stephan: *Systematische Beurteilung von Wasserkraftprojekten,* 2002, ISBN 3-933761-15-8

113 Iqbal, Amin: *On the Management and Salinity Control of Drip Irrigation,* 2002, ISBN 3-933761-16-6

114 Silberhorn-Hemminger, Annette: *Modellierung von Kluftaquifersystemen: Geostatistische Analyse und deterministisch-stochastische Kluftgenerierung,* 2002, ISBN 3-933761-17-4

115 Winkler, Angela: *Prozesse des Wärme- und Stofftransports bei der In-situ-Sanierung mit festen Wärmequellen,* 2003, ISBN 3-933761-18-2

116 Marx, Walter: *Wasserkraft, Bewässerung, Umwelt - Planungs- und Bewertungsschwerpunkte der Wasserbewirtschaftung,* 2003, ISBN 3-933761-19-0

117 Hinkelmann, Reinhard: *Efficient Numerical Methods and Information-Processing Techniques in Environment Water,* 2003, ISBN 3-933761-20-4

118 Samaniego-Eguiguren, Luis Eduardo: *Hydrological Consequences of Land Use / Land Cover and Climatic Changes in Mesoscale Catchments*, 2003, ISBN 3-933761-21-2

119 Neunhäuserer, Lina: *Diskretisierungsansätze zur Modellierung von Strömungs- und Transportprozessen in geklüftet-porösen Medien*, 2003, ISBN 3-933761-22-0

120 Paul, Maren: *Simulation of Two-Phase Flow in Heterogeneous Poros Media with Adaptive Methods*, 2003, ISBN 3-933761-23-9

121 Ehret, Uwe: *Rainfall and Flood Nowcasting in Small Catchments using Weather Radar*, 2003, ISBN 3-933761-24-7

122 Haag, Ingo: *Der Sauerstoffhaushalt staugeregelter Flüsse am Beispiel des Neckars - Analysen, Experimente, Simulationen -,* 2003, ISBN 3-933761-25-5

123 Appt, Jochen: *Analysis of Basin-Scale Internal Waves in Upper Lake Constance,* 2003, ISBN 3-933761-26-3

124 Hrsg.: Schrenk, Volker; Batereau, Katrin; Barczewski, Baldur; Weber, Karolin und Koschitzky, Hans-Peter: *Symposium Ressource Fläche und VEGAS - Statuskolloquium 2003, 30. September und 1. Oktober 2003,* 2003, ISBN 3-933761-27-1

125 Omar Khalil Ouda: *Optimisation of Agricultural Water Use: A Decision Support System for the Gaza Strip,* 2003, ISBN 3-933761-28-0

126 Batereau, Katrin: *Sensorbasierte Bodenluftmessung zur Vor-Ort-Erkundung von Schadensherden im Untergrund*, 2004, ISBN 3-933761-29-8

127 Witt, Oliver: *Erosionsstabilität von Gewässersedimenten mit Auswirkung auf den Stofftransport bei Hochwasser am Beispiel ausgewählter Stauhaltungen des Oberrheins*, 2004, ISBN 3-933761-30-1

128 Jakobs, Hartmut: *Simulation nicht-isothermer Gas-Wasser-Prozesse in komplexen Kluft-Matrix-Systemen*, 2004, ISBN 3-933761-31-X

129 Li, Chen-Chien: *Deterministisch-stochastisches Berechnungskonzept zur Beurteilung der Auswirkungen erosiver Hochwasserereignisse in Flussstauhaltungen,* 2004, ISBN 3-933761-32-8

130 Reichenberger, Volker; Helmig, Rainer; Jakobs, Hartmut; Bastian, Peter; Niessner, Jennifer: *Complex Gas-Water Processes in Discrete Fracture-Matrix Systems: Upscaling, Mass-Conservative Discretization and Efficient Multilevel Solution,* 2004, ISBN 3-933761-33-6

131 Hrsg.: Barczewski, Baldur; Koschitzky, Hans-Peter; Weber, Karolin; Wege, Ralf: *VEGAS - Statuskolloquium 2004,* Tagungsband zur Veranstaltung am 05. Oktober 2004 an der Universität Stuttgart, Campus Stuttgart-Vaihingen, 2004, ISBN 3-933761-34-4

132 Asie, Kemal Jabir: *Finite Volume Models for Multiphase Multicomponent Flow through Porous Media*. 2005, ISBN 3-933761-35-2

133 Jacoub, George: *Development of a 2-D Numerical Module for Particulate Contaminant Transport in Flood Retention Reservoirs and Impounded Rivers,* 2004, ISBN 3-933761-36-0

134 Nowak, Wolfgang: *Geostatistical Methods for the Identification of Flow and Transport Parameters in the Subsurface,* 2005, ISBN 3-933761-37-9

135 Süß, Mia: *Analysis of the influence of structures and boundaries on flow and transport processes in fractured porous media*, 2005, ISBN 3-933761-38-7

136 Jose, Surabhin Chackiath: *Experimental Investigations on Longitudinal Dispersive Mixing in Heterogeneous Aquifers,* 2005, ISBN: 3-933761-39-5

137 Filiz, Fulya: *Linking Large-Scale Meteorological Conditions to Floods in Mesoscale Catchments,* 2005, ISBN 3-933761-40-9

138 Qin, Minghao: *Wirklichkeitsnahe und recheneffiziente Ermittlung von Temperatur und Spannungen bei großen RCC-Staumauern*, 2005, ISBN 3-933761-41-7

139 Kobayashi, Kenichiro: *Optimization Methods for Multiphase Systems in the Subsurface - Application to Methane Migration in Coal Mining Areas*, 2005, ISBN 3-933761-42-5

140 Rahman, Md. Arifur: *Experimental Investigations on Transverse Dispersive Mixing in Heterogeneous Porous Media,* 2005, ISBN 3-933761-43-3

141 Schrenk, Volker: *Ökobilanzen zur Bewertung von Altlastensanierungsmaßnahmen,* 2005, ISBN 3-933761-44-1

142 Hundecha, Hirpa Yeshewatesfa: *Regionalization of Parameters of a Conceptual Rainfall-Runoff Model*, 2005, ISBN: 3-933761-45-X

143 Wege, Ralf: *Untersuchungs- und Überwachungsmethoden für die Beurteilung natürlicher Selbstreinigungsprozesse im Grundwasser,* 2005, ISBN 3-933761-46-8

144 Breiting, Thomas: *Techniken und Methoden der Hydroinformatik - Modellierung von komplexen Hydrosystemen im Untergrund*, 2006, 3-933761-47-6

145 Hrsg.: Braun, Jürgen; Koschitzky, Hans-Peter; Müller, Martin: *Ressource Untergrund: 10 Jahre VEGAS: Forschung und Technologieentwicklung zum Schutz von Grundwasser und Boden,* Tagungsband zur Veranstaltung am 28. und 29. September 2005 an der Universität Stuttgart, Campus Stuttgart-Vaihingen, 2005, ISBN 3-933761-48-4

146 Rojanschi, Vlad: *Abflusskonzentration in mesoskaligen Einzugsgebieten unter Berücksichtigung des Sickerraumes,* 2006, ISBN 3-933761-49-2

147 Winkler, Nina Simone: *Optimierung der Steuerung von Hochwasserrückhaltebecken-systemen,* 2006, ISBN 3-933761-50-6

148 Wolf, Jens: *Räumlich differenzierte Modellierung der Grundwasserströmung alluvialer Aquifere für mesoskalige Einzugsgebiete*, 2006, ISBN: 3-933761-51-4

149 Kohler, Beate: *Externe Effekte der Laufwasserkraftnutzung*, 2006, ISBN 3-933761-52-2

150 Hrsg.: Braun, Jürgen; Koschitzky, Hans-Peter; Stuhrmann, Matthias: *VEGAS-Statuskolloquium 2006,* Tagungsband zur Veranstaltung am 28. September 2006 an der Universität Stuttgart, Campus Stuttgart-Vaihingen, 2006, ISBN 3-933761-53-0

151 Niessner, Jennifer: *Multi-Scale Modeling of Multi-Phase - Multi-Component Processes in Heterogeneous Porous Media*, 2006, ISBN 3-933761-54-9

152 Fischer, Markus: *Beanspruchung eingeerdeter Rohrleitungen infolge Austrocknung bindiger Böden,* 2006, ISBN 3-933761-55-7

153 Schneck, Alexander: *Optimierung der Grundwasserbewirtschaftung unter Berücksichtigung der Belange der Wasserversorgung, der Landwirtschaft und des Naturschutzes*, 2006, ISBN 3-933761-56-5

154 Das, Tapash: *The Impact of Spatial Variability of Precipitation on the Predictive Uncertainty of Hydrological Models,* 2006, ISBN 3-933761-57-3

155 Bielinski, Andreas: *Numerical Simulation of CO_2 sequestration in geological formations*, 2007, ISBN 3-933761-58-1

156 Mödinger, Jens: *Entwicklung eines Bewertungs- und Entscheidungsunterstützungssystems für eine nachhaltige regionale Grundwasserbewirtschaftung*, 2006, ISBN 3-933761-60-3

157 Manthey, Sabine: *Two-phase flow processes with dynamic effects in porous media - parameter estimation and simulation,* 2007, ISBN 3-933761-61-1

158 Pozos Estrada, Oscar: *Investigation on the Effects of Entrained Air in Pipelines,* 2007, ISBN 3-933761-62-X

159 Ochs, Steffen Oliver: *Steam injection into saturated porous media – process analysis including experimental and numerical investigations*, 2007, ISBN 3-933761-63-8

160 Marx, Andreas: *Einsatz gekoppelter Modelle und Wetterradar zur Abschätzung von Niederschlagsintensitäten und zur Abflussvorhersage, 2007,* ISBN 3-933761-64-6

161 Hartmann, Gabriele Maria: *Investigation of Evapotranspiration Concepts in Hydrological Modelling for Climate Change Impact Assessment*, 2007, ISBN 3-933761-65-4

162 Kebede Gurmessa, Tesfaye: *Numerical Investigation on Flow and Transport Characteristics to Improve Long-Term Simulation of Reservoir Sedimentation*, 2007, ISBN 3-933761-66-2

163 Trifković, Aleksandar: *Multi-objective and Risk-based Modelling Methodology for Planning, Design and Operation of Water Supply Systems*, 2007, ISBN 3-933761-67-0

164 Götzinger, Jens: *Distributed Conceptual Hydrological Modelling - Simulation of Climate, Land Use Change Impact and Uncertainty Analysis*, 2007, ISBN 3-933761-68-9

165 Hrsg.: Braun, Jürgen; Koschitzky, Hans-Peter; Stuhrmann, Matthias: *VEGAS – Kolloquium 2007,* Tagungsband zur Veranstaltung am 26. September 2007 an der Universität Stuttgart, Campus Stuttgart-Vaihingen, 2007, ISBN 3-933761-69-7

166 Freeman, Beau: *Modernization Criteria Assessment for Water Resources Planning; Klamath Irrigation Project, U.S.*, 2008, ISBN 3-933761-70-0

167 Dreher, Thomas: *Selektive Sedimentation von Feinstschwebstoffen in Wechselwirkung mit wandnahen turbulenten Strömungsbedingungen*, 2008, ISBN 3-933761-71-9

168 Yang, Wei: *Discrete-Continuous Downscaling Model for Generating Daily Precipitation Time Series*, 2008, ISBN 3-933761-72-7

169 Kopecki, Ianina: *Calculational Approach to FST-Hemispheres for Multiparametrical Benthos Habitat Modelling,* 2008*,* ISBN 3-933761-73-5

170 Brommundt, Jürgen: *Stochastische Generierung räumlich zusammenhängender Niederschlagszeitreihen*, 2008, ISBN 3-933761-74-3

171 Papafotiou, *Alexandros: Numerical Investigations of the Role of Hysteresis in Heterogeneous Two-Phase Flow Systems*, 2008, ISBN 3-933761-75-1

172 He, Yi: *Application of a Non-Parametric Classification Scheme to Catchment Hydrology*, 2008, ISBN 3-933761-76-X

173 Wagner, Sven: *Water Balance in a Poorly Gauged Basin in West Africa Using Atmospheric Modelling and Remote Sensing Information*, 2008, ISBN 3-933761-77-8

Die Mitteilungshefte ab dem Jahr 2005 stehen als pdf-Datei über die Homepage des Instituts: www.iws.uni-stuttgart.de zur Verfügung.